STRATEGIES FOR CONTROLLING PHYSICOCHEMICAL CHARACTERISTICS OF NANOMATERIALS TOWARD PERSONALIZED MEDICINE

A Dissertation

by

YEN-NAN LIN

Submitted to the Graduate and Professional School of
Texas A&M University
in partial fulfillment of the requirements for the degree of

DOCTOR OF PHILOSOPHY

Chair of Committee,	Karen L. Wooley
Committee Members,	Kevin Burgess
	Carolyn L. Cannon
	James C. Sacchettini
Head of Department,	Simon W. North

May 2022

Major Subject: Chemistry

ABSTRACT

Nanomedicine holds great potential for effective treatment against life-threatening diseases by providing efficient transport and controlled release of significant quantities of therapeutic agents to the target sites of the diseased tissue. Despite promising laboratory results, many nanomedicine formulations failed in clinical trials, in part due to heterogeneity in diseased individuals. Individual heterogeneity leads to heterogeneous outcome of nanomedicine treatments, and thus presents a great challenge for clinical translation of nanomedicine. Personalized nanocarriers, with tailored physicochemical properties for a specific individual's genetic and disease profile, can overcome such a challenge. Therefore, the future of nanomedicine will depend on customization and personalization, and the development of next-generation nanomedicine requires more precise control of the physicochemical characteristics of nanomaterials. Consequently, effective approaches that reduce burdens for controlling physicochemical characteristic of nanomaterials would facilitate bench-to-bedside translation of nanomedicine.

First, we reported co-assembly of two degradable glucose-based amphiphilic block polymers is demonstrated to control nanoparticle size, surface charge, and stimuli-responsive properties, allowing optimization of these constructs for cytosolic drug delivery applications. The accessible procedures presented here for engineering highly tunable nanoparticles from glucose-based, functional, degradable polymers offer

versatile strategies for accelerating the development and clinical implementation of such stimuli-responsive, tailored nanocarriers.

Second, we reported a facile fabrication of cell membrane-camouflaged nanocarriers (CMNs) that exhibit tunable paclitaxel (PTX) release kinetics *via* altering macromolecular stereostructure. Biomimetic-cell-membrane-camouflaged polymeric nanocarriers, possessing advantages related to the functional diversity of natural cell membranes and the physicochemical tailorability of synthetic polymers, serve as promising candidates for a therapeutic platform. This work represents fundamental advances toward a potential personalized nanocarrier technology that would be capable of employing an individual's RBCs for membrane isolation, together with tuning of cargo loading and release simply via alteration of the biocompatible PLA stereoisomer feed ratio.

Third, we investigated the role that reversible covalent loading of a hydrophobic drug exerts on intra-nanoparticle physical properties and explore the utility of this payload control strategy for tuning the access of active agents and, thereby, the stimuli sensitivity of smart nanomaterials. Interactions between drug molecules, nanocarrier components, and surrounding media influence the properties and therapeutic efficacies of nanomedicines. In this study, glutathione sensitivity was controlled via altering the degree of hydrophobic payload loading of disulfide-linked camptothecin-conjugated sugar-based nanomaterials. This work represents an advancement in drug carrier design by demonstrating the importance of controlling the amount of drug loading on the overall payload and its availability.

DEDICATION

This work is dedicated to my beloved parents, Chia-Chuan Lin and Hsiu-Hui Lin Chang.

They made an immense sacrifice for my educational opportunities.

ACKNOWLEDGEMENTS

I would first like to thank my advisor, Professor Karen L. Wooley. She is a kind, supportive, passionate, diligent, and considerate role model. Her encouragement and support have allowed me to pursue my passion, curiosity, and science. Besides tremendous knowledge of science, Karen encouraged me to ask questions all the time and, most importantly, to be constantly curious. She never stopped providing me with freedom, support, and suggestions to explore anything I deem interesting and exciting. I cannot express all my gratitude for having her as my supervisor with these limited words.

Secondly, I would like to thank my dissertation committee members, Professors Kevin Burgess, Carolyn L. Cannon, James C. Sacchettini, for their technical expertise, valuable advice, and simulating discussions, which improved research toward the completion of this dissertation.

Within the Wooley group, I am incredibly thankful for my mentor and colleague, Dr. Lu Su, for numerous valuable discussions on science and life. I would also like to thank other past and present members of the Wooley group, Dr. Yingchao Chen, Ben Demor, Mei Dong, Dr. Mahmoud F. A. Elsabahy, Dr. Simcha E. Felder, Dr. Jeniree A. Flores Delgado, Dr. Marco Giles, Jessica H. Huang, Dr. Ashlee A. Jahnke, Dr. Nari Kang, Sarosh Khan, Dr. Christopher H. Komatsu, Dr. Gyu Seong Heo, Dr. Samantha L. Kristufek, Dr. Eric E. Leonhardt, Dr. Rachel A. Letteri, Mahsa Minaeian, Shota Osumi, Randinu Pulukkody, Dr. Yue Song, Dr. Guorong Sun, David K. Tran, Mariela Vazquez, Brooke A. Versaw, Dr. Hai Wang, Dr. Fuwu Zhang, Dr. Xiang Zhu, and Dr. Jennifer S. Zigmond, who created a friendly and safe work environment and supported my research. Finally, I would like to thank the Wooley staff and managers (Sherry Melton and Justin A. Smolen) for all their help, not just in teaching but in keeping the Wooley lab going. I am thankful for their support, direction, and patience in teaching me.

Additionally, I would be remiss to not acknowledge all Administrative and Support Staff in the Chemistry Department, particularly the Graduate Office (Sandy Horton, Valerie A. McLaughlin, Dr. Joanna Goodey-Pellois, and Dr. Simon W. North), Business Operations (Ron G. Carter, Curtis Lee, Angie T. Stickley, Judy R. Ludwig, Julie A. Zercher, Angie T. Medina, and Melvin C. William), NMR facilities (Drs. Greg P. Wylie, Vladimir Bakhmoutov, and Douglas W. Elliott), Mass Spectrometry (Drs. Bo Wang, Doyong Kim, Yohannes Rezenom, and Vanessa Santiago), Electronics (Tim P. Pehl), Glass Blowing (Bill C. Merka), Machine Shops (Bill T. Seward), and IT (Steve Tran and Mike D. Green) — I am thankful for all that you have done, especially the work that often goes unnoticed by the students but keeps the Department of Chemistry at Texas A&M running.

I must acknowledge my parents, who made an immense sacrifice for my educational opportunities. I vividly remember an incident in 2003 when we immigrated to the USA from Taiwan. We encountered a bomb alert as we entered the US border while waiting for the transfer flight in California. People still vividly remembered the World Trade Center's collapse, so everyone panicked at the airport. We were evacuated to the outside of the airport, and spent our first night at the United States on the street. It was a cold, windy night. We waited on the street without luggage along with hundreds, if not thousands, of travelers. All flights were suspended. It was a tough night, and I was mentally exhausted as a typical 12-year-old. Yet my racing heart was tranquilized after seeing my father, who remained calm throughout the event. His composure provided reassurance for our family.

I would like to thank many of my lifelong friends in the Taiwanese Gospel Fellowship for their spiritual support and friendships.

Lastly, I acknowledge my wife, Jiayi Lu. I am so fortunate to met her in the graduate statistics course. We can talk endlessly for hours. I treasure our time together gardening in the backyard, strolling in the neighborhood, and feeding birds at local parks. Her endless support and companionship are essential for completing my physician-scientist training.

CONTRIBUTORS AND FUNDING SOURCES

Contributors

This work was supervised by a dissertation committee consisting of Professor Karen L. Wooley (advisor) of the Departments of Chemistry, Chemical Engineering, and Materials Science and Engineering; Professor James Sacchettini (committee member) of the Departments of Biochemistry and Biophysics, and Chemistry; and Professor Kevin Burgess (committee member) of the Department of Chemistry; Professor Carolyn L. Cannon (committee member) of the Department of Microbial Pathogenesis and Immunology.

In Chapter III, the wide-angle X-ray diffraction experiments were performed by Dr. Joseph Reibenspies at the Texas A&M University. The cytotoxicity experiments were performed with the help by Mrs. Sarosh Khan. The immunotoxicity experiments were performed by Sarosh Khan and Dr. Mahmoud Elsabahy.

In Chapter IV, the cytotoxicity experiments were performed with the help with Mrs. Sarosh Khan.

All other experiments were carried out independently by the student.

Funding Sources

The work in Chapter II was made possible by the financial support from the National Science Foundation (CHE-1610311, DMREF-1629094, and DMR-1507429) and the Robert A. Welch Foundation through the W. T. Doherty-Welch Chair in Chemistry (A-0001).

The work in Chapter III and IV was made possible by the financial support from the National Science Foundation (CHE-1610311 and DMREF-1629094), and the Robert A. Welch Foundation through the W. T. Doherty-Welch Chair in Chemis-try (A-0001).

These contents are solely the responsibility of the authors and do not necessarily represent the official views of the National Science Foundation and the Welch Foundation.

NOMENCLATURE

AFM	Atomic force microscopy
ATR	Attenuated total reflection
D_{av}	Average diameters
HBTU	2-(1*H*-Benzotriazole-1-yl)-1,1,3,3-tetramethylaminium hexafluorophosphate
CPT	Camptothecin
MCNs	Cell membrane-camouflaged nanocarriers
ΔH	Changes in enthalpies
δ	Chemical shift
f_{CPT}	Degree of CPT conjugation
DP_n	Degrees of polymerization
D/H	Diameter-to-height
DCM	Dichloromethane
DSC	Differential scanning calorimetry
DIPEA	*N,N*-Diisopropylethylamine
DMF	*N,N*-Dimethyl formamide
DMSO	Dimethyl sulfoxide
Đ	Dispersity
DTT	Dithiothreitol
DMEM	Dulbecco's Modified Eagle's Medium
DLS	Dynamic light scattering

EPR	Enhanced permeability and retention
RBC-MCNs	Erythrocyte membrane-camouflaged nanocarriers
FTIR	Fourier transform infrared
T_g	Glass transitions
GSH	Glutathione
GM-CSF	Granulocyte macrophage-colony-stimulating factor
G-CSF	Granulocyte-colony-stimulating factor
IC_{50}	Half maximal inhibitory concentration
HPLC	High-performance liquid chromatography
IFN	Interferon
IL	Interleukin
IR	Irinotecan
KC	Keratinocyte-derived chemokine
MIP	Macrophage inflammatory protein
T_m	Melting transition
GC(EPC)	Methyl-2-*O*-ethyloxycarbonyl-3-*O*-propargyloxycarbonyl-4,6-*O*-carbonyl-α-D-glucopyranoside
MWCO	Molecular weight cut-off
MCP	Monocyte chemotactic protein
MOPS	3-(*N*-Morpholino)propanesulfonic acid
NP	Nanoparticle
$D_{h(number)}$	Number-average hydrodynamic diameter
M_n	Number-averaged molar mass

PTX	Paclitaxel
ppm	Parts per million
PBS	Phosphate-buffered saline
PTA	Phosphotungstic acid
PDGC	Poly(D-glucose carbonate)
PDLA	Poly(D-lactide)
PDLLA	Poly(DL-lactide)
PEG	Poly(ethylene glycol)
PLLA	Poly(L-lactide)
PLA	Polylactide
RBC	Red blood cell
RANTES	Regulated upon activation normal T-cell expressed, and presumably secreted
ROP	Ring-opening polymerizations
SI	Selective Index
SEC	Size exclusion chromatography
scPLA	Stereocomplex polylactides
THF	Tetrahydrofuran
TGA	Thermogravimetric analysis
TEM	Transmission electron microscopy
TBD	1,5,7-Triazabicyclo[4.4.0]dec-5-ene
TNF-α	Tumor necrosis factor-α
WAXD	Wide-angle powder X-ray diffraction

TABLE OF CONTENTS

Page

LIST OF FIGURES

LIST OF TABLES

1. INTRODUCTION

Nanomedicine holds great potential for effective treatment against life-threatening diseases by providing efficient transport and controlled release of significant quantities of therapeutic agents to the diseased tissue. Despite promising laboratory results, many nanomedicine formulations failed in clinical trials, in part due to heterogeneity in diseased individuals. Individual heterogeneity leads to heterogeneous outcome of nanomedicine treatments, and thus presents a great challenge for clinical translation of nanomedicine. Personalized nanocarriers, with tailored physicochemical properties for a specific individual's genetic and disease profile, can overcome such a challenge. Therefore, the future of nanomedicine will depend on customization and personalization, and the development of next-generation nanomedicine requires more precise control of the physicochemical characteristics of nanomaterials. Consequently, effective approaches that reduce burdens for controlling physicochemical characteristic of nanomaterials would facilitate bench-to-bedside translation of nanomedicine.

Due to the complexity of biological systems, several challenges influence success of nanomedicine, including potential adverse effects of long-term accumulations of the nanocarriers, off-target toxicity of the therapeutics to normal tissues, and the limited ability of nanomedicines to penetrate target tissues at a potentially lethal concentration. Upon systemic administration, nanocarrier will encounter a series of biological challenges, including protein adhesion, mononuclear phagocytes uptakes, immunotoxicity, reticuloendothelial clearance, off-site accumulation, off-site drug release, cell membrane traversal, lysosomal drug degradation, drug efflux, and excretion. Nanocarriers must avoid these obstacles in order to maximize bioavailability of drugs to target sites and reduce off-target toxicity. Several physicochemical parameters of the nanomaterials contribute to their ability to achieve these goals; therefore, careful physicochemical control of the nanomaterials is essential.

Nanocarrier size and surface charge significantly influence their biological interactions during the course of delivery. Particle size substantially affects the circulation time, clearance, and biodistribution of the carriers. Nanoparticles with diameters ranging from 20–200 nm are well poised to avoid renal clearance by filtration, in which particles < 10 nm are filtered and cleared, reduce entrapment of hepatic and splenic fenestrations, in which particles >1 μm are cleared, and accumulate passively in tumor tissues *via* the enhanced permeability and retention (EPR) effect. Besides particle size, the surface charge also substantially impacts the pharmacokinetics and performance of drug carriers. During blood circulation, positive-charge particulates interact with plasma components and consequently facilitate aggregation, opsonization, and clearance. Precise size and surface charge controls of the nanomaterials is essential.

Controlled drug release significantly impacts drug efficacy and biodistribution while mitigating off-target toxicity, therefore, is an important attribute for designing drug carriers. Tuning cargo release kinetics is particularly crucial for drug delivery to maintain optimal drug concentration duration, reduce side-effects, and improve therapeutic efficacy.[1] Altering core compositions of the nanocarrier can influence drug release kinetics,[2-4] yet many tailor-made materials have unknown toxicity profiles in humans, increasing the uncertainty for clinical translation of the resulting nanomaterials. Expanding control over the drug release kinetics for nanocarriers using biocompatible materials with simple approach is, therefore, desirable.

In addition to drug release kinetics, various types of endogenous and exogenous stimuli, including pH, redox, enzyme, temperature, and radiation, have been utilized in designing smart nanocarriers for drug delivery. Stimuli-responsive nanocarriers alter their physicochemical properties in response to specific stimuli, and accordingly change spatial/temporal drug release profiles and pharmacokinetics of drugs. Since different drugs have different optimal release profiles, they would benefit from different level of stimuli sensitivity of nanocarriers in response to stimuli of a diseased area. While encouraging progress in stimuli-responsive formulation has been achieved, very few formulations have been approved by Food and Drug Administration (FDA) due to individual heterogeneity in clinical responses. Therefore, facile strategies for controlling stimuli-responsive sensitivity of nanomaterials would facilitate optimization and clinical translation of personalized smart drug carrier formulations.

Tailoring polymeric nanocarriers requires careful control over the physicochemical properties of these constructs, yet synthesis and optimization of individual material for each unique situation is a time-consuming, expensive, and labor-intensive process, impeding the clinical translation of designer nanomaterials. It is imperative to reduce the burden associated with nanomaterials development in order to accelerate the clinical implementation of nanomedicine. To this end, this thesis focuses on the development of facile fabrication strategies and novel nanomaterials to address the above-mentioned challenges, enabling facile controls over the physicochemical characteristics of nanomaterials.

2. CO-ASSEMBLY OF SUGAR-BASED AMPHIPHILIC BLOCK POLYMERS TO ACHIEVE NANOPARTICLES WITH TUNABLE MORPHOLOGY, SIZE, SURFACE CHARGE, AND ACID-RESPONSIVE BEHAVIOR[*]

2.1. Introduction

Polymeric nanocarriers, especially those that respond to endogenous or exogenous stimuli, have tremendous potential in medicine.[5-9] Tailoring polymeric nanocarriers to target specific tissues or mediate controlled release of therapeutics requires careful control over the physicochemical properties of these constructs.[10-21] To this end, assembly of amphiphilic block copolymers has enabled the fabrication of nanomaterials with diverse morphologies and behaviors.[8, 22-30] However, synthesis and optimization of individual polymers for each unique situation is a time-consuming, expensive, and labor-intensive process, impeding the clinical translation of designer nanoparticles. It is imperative to reduce the burden associated with the development of smart nanomaterials to accelerate their development and clinical implementation.

Due to the complexity of biological systems, several aspects need to be considered in the design of drug carriers.[31] Nanocarrier size and surface charge significantly influence their biological interactions during the course of delivery.[32] Particle size substantially affects the circulation time, clearance, and biodistribution of

---

[*] Reprinted (adapted) with permission from "Co-assembly of sugar-based amphiphilic block polymers to achieve nanoparticles with tunable morphology, size, surface charge, and acid-responsive behavior" by Lin, Y.-N.; Su, L.; Smolen, J.; Li, R.; Song, Y.; Wang, H.; Dong, M.; Wooley, K. L., *Mater. Chem. Front.* **2018,** *2* (12), 2230-2238. Copyright 2018 The Royal Society of Chemistry.

the carriers.[10] Nanoparticles with diameters ranging from 20–200 nm are well poised to avoid renal clearance by filtration, in which particles <10 nm are filtered and cleared, reduce entrapment of hepatic and splenic fenestrations, in which particles >1 μm are cleared, and accumulate passively in tumor tissues *via* the enhanced permeability and retention (EPR) effect.[10, 33] Besides particle size, the surface charge also substantially impacts the pharmacokinetics and performance of drug carriers.[34] During circulation in the blood stream, positively-charged particulates interact with plasma components and consequently facilitate aggregation, opsonization, and clearance.[10] Carriers that passively deposit into tissues often enter cells *via* endocytosis;[10] as endosomes mature into lysosomes, the lysosomal degradative enzymes can destroy encapsulated active drugs. Further, drugs such as paclitaxel and doxorubicin must reach cellular components outside of the endolysosomal compartments. Paclitaxel binds to beta-tubulin subunits of microtubules located in the cytosol, thereby preventing disassembly of the microtubules.[35] Doxorubicin intercalates DNA and stabilizes the topoisomerase II complex located in the nucleus, preventing DNA replication needed for cell division.[36-37] Since molecular targets of these drugs are located outside of the endolysosome, endolysosomal escape is crucial for these drugs. To facilitate cytosolic drug delivery, nanocarriers should exhibit optimal size, non-cationic surface charge, and colloidal stability during circulation, and then undergo charge-reversal to display cationic surfaces in response to acidification of endosomes (pH = 5.0–6.5) to induce rupture of endosomes and release of nanocarriers into the cytoplasm.[7, 38-42]

Co-assembly of multiple polymeric components has been demonstrated to yield an array of functional composite nanoparticles with a range of properties without the need for synthesis of individual polymers for each nanoparticle.[6, 30, 43-44] Co-assembly has also been applied to control the surface characteristics of DNA-conjugated nanocarriers, thereby tuning cellular uptake, nuclease resistance, and antisense activity.[43] In addition, physical blending of different temperature-responsive polymers was employed to fine-tune the transition temperature of elastin-based materials.[45] Advances in synthetic chemistry have enabled precise tuning of the physicochemical properties of natural product-based polymeric materials, which are particularly beneficial for biomedical applications owing to their biocompatibility.[46-49] Co-assembly of sugar-based amphiphilic nonionic and cationic amphiphilic block polymers afforded nanocarriers for delivery of chemotherapeutics with tunable size, toxicity, and drug release kinetics.[6] Taken together, these studies showcase the potential of co-assembly as a versatile approach to fine-tune the stimuli-responsive behavior and physicochemical properties of natural product-based nanocarriers.

Herein, co-assembly of acid- and histamine-modified hydrolytically degradable glucose-based block copolymers was explored as a means to control the size, surface charge, and acid-responsive profile of polymer nanomaterials, enabling optimization for drug delivery and other potential applications. In designing the nanocarriers, poly(DL-lactide)-*b*-poly(D-glucose carbonate) (PDLLA-*b*-PDGC) building blocks were selected based upon their biocompatibility, functionality, and ability to assemble into versatile nanostructures with varying sizes, charges, and functions.[6, 50-51] The alkyne-containing

PDGC block has been employed to enable facile post-polymerization modification *via* thiol-yne and copper(I)-catalyzed azide alkyne cycloaddition reactions, affording a variety of multi-functional polymeric systems.[6, 50-51] In addition, we recently demonstrated that poly(L-lactide)-*b*-poly(D-glucose carbonate) PLLA-*b*-PDGC degrades into low molar mass hydrophilic molecules,[51] including lactic acid and carbon dioxide, which are anticipated to be easily eliminated to reduce systemic accumulation.[51] Acid- and histamine-modified PDLLA-*b*-PDGC are anticipated to display complementary properties for drug delivery applications. Histamine-modification imparts pH-responsive properties to polymer systems, due to the presence of imidazole groups, which are expected to facilitate a neutral-to-positive charge transformation when pH values below the pK_a of the imidazole conjugate acid ($pK_a = 6.95$)[52-53] are experienced, for instance in acidic endolysosomal environments. Besides charge switching, the buffering capacity of the imidazole groups close to endosomal pH is known to trigger hydrochloric acid influx into endosomes, leading to osmotic swelling and rupture of endolysosomes and cytosolic release of the contents through the proton-sponge effect.[7, 53-54] Such delivery mechanisms are especially beneficial for drugs having destinations in the cytoplasm (*e.g.*, paclitaxel). While histamine-functionalized PDLLA-*b*-PDGC is anticipated to provide pH-responsive behavior and afford endosomal escape, these materials may also exhibit limited hydrophilicity, particularly at blood pH where the imidazoles are deprotonated, which may hinder the formation of colloidally-stable nanostructures. On the other hand, acid-functionalized PDLLA-*b*-PDGC is anticipated to impart colloidal stability and anionic character, but lack pH-responsive character in the physiological-relevant pH range desired to promote endosomal rupture. Therefore, here we describe the co-assembly of the acid- and histamine-modified PDLLA-*b*-PDGC to achieve highly tunable nanomaterials, enabling facile optimization of smart sugar-based nanoparticles for drug delivery applications. This work represents fundamental advances in the fabrication of multi-functional nanostructures from glucose-derived acid-responsive amphiphilic block polymeric materials, with potential for these constructs to be useful in drug delivery applications.

2.2. Results and Discussions

Polymer nanoparticles with controllable size, zeta potential, and pH-responsive behavior allow optimization towards specific drug delivery applications, such as drug release in the cytoplasm. Intravenous cytosolic drug carriers should exhibit the following criteria: 1) 20–200 nm diameter during blood circulation to minimize renal clearance, reduce reticuloendothelial clearance, and, for cancer drug delivery, passively accumulate into tumor tissue by the EPR effect; 2) non-cationic surfaces to impart colloidal stability during circulation; and 3) charge-reversal capabilities to promote escape from endosomal compartments into the cytoplasm upon acidification to *ca.* pH 5.0–6.5. To this end, alkyne-functionalized, sugar-based block polymers were synthesized by ring-opening polymerization and modified to afford acid- and histamine-modified block polymers for co-assembly into nanoparticles with tunable sizes, surface compositions and pH-responsive properties. Organocatalyzed sequential ring-opening polymerization of cyclic DL-lactide and bicyclic, glucose-based GC(EPC) yielded alkyne-containing block polymers. The polymers were modified to append carboxylates *via* photo-initiated thiol-yne click chemistry, and the acid-functionalized polymers were further modified by amidation to afford histamine-modified polymers. Histamine was selected due to its pH-responsiveness and endosomal escape capability, which is desirable for cytosolic delivery.[7, 10, 15] Co-assembly of these polymers in different weight ratios enabled fabrication of nanoparticles with tunable size, surface charge, and pH-responsive profiles well suited for cytosolic drug delivery.

The functional and degradable diblock $PDLLA_{290}$-*b*-$PDGC_{20}$, was synthesized by organocatalyzed sequential ring-opening polymerization of cyclic DL-lactide, followed by bicyclic GC(EPC) at −78 °C in DCM with 4-methylbenzyl alcohol as the initiator and TBD as the organocatalyst, according to previously-reported procedures.[6, 50-51] The degree of polymerization and compositions of the lactide and glucose carbonate blocks were controlled by varying the monomer-initator ratio. The number-average degree of polymerization and corresponding M_n (49.2 kDa) were determined by end group analysis using ^1H NMR spectroscopy (Figure 1). SEC revealed $PDLLA_{290}$-*b*-$PDGC_{20}$ to have a narrow molar mass distribution, with dispersity ($Đ < 1.20$) and $M_n = 42.6$ kDa determined relative to polystyrene standards (Figure 2).

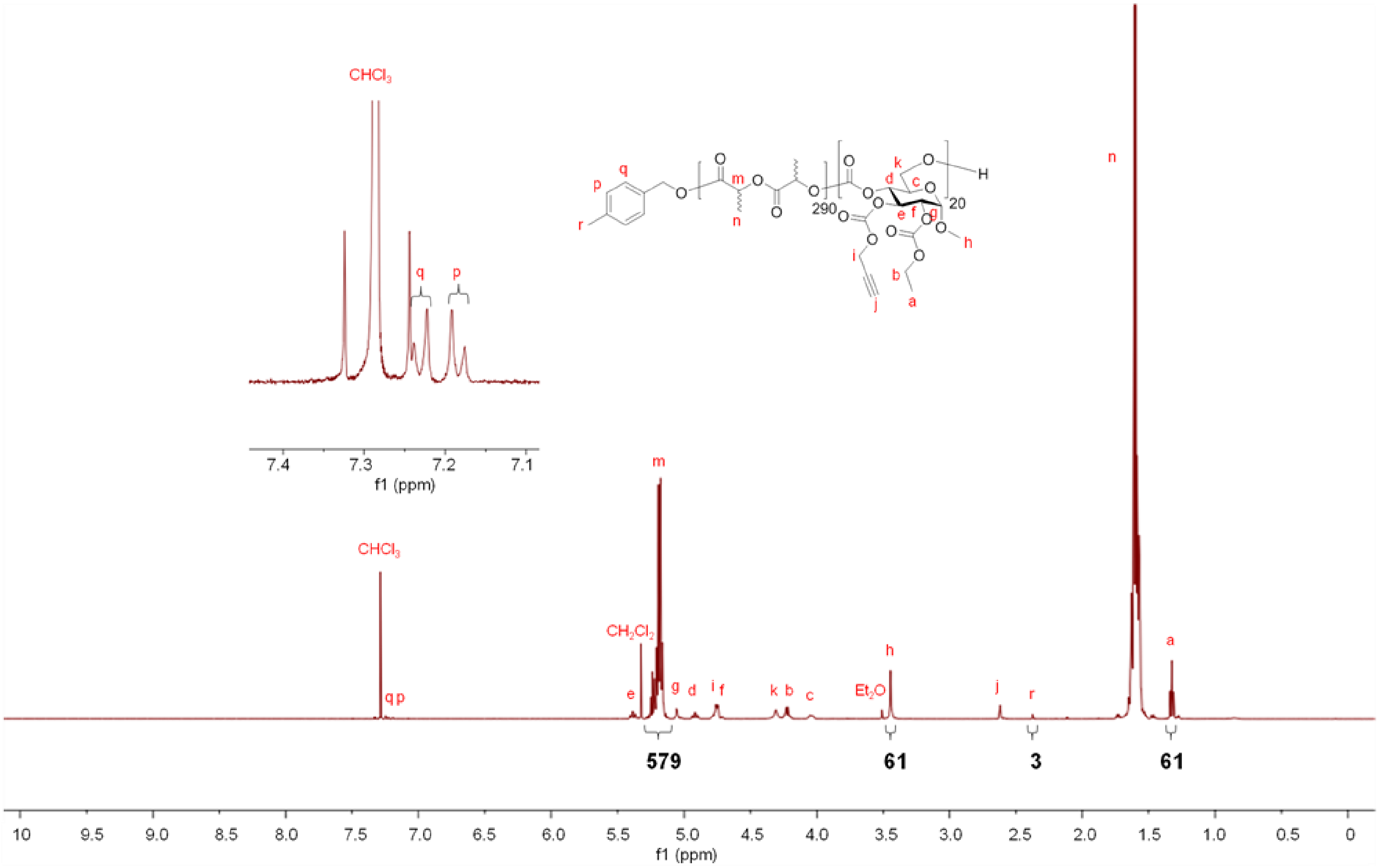

Figure 1. ^{1}H NMR spectrum (500 MHz) of PDLLA$_{290}$-*b*-PDGC$_{20}$ in CDCl$_3$, with the inset expanding the region to show the resonance signals for the aromatic protons of the α-chain end. Reprinted with permission from "Co-assembly of sugar-based amphiphilic block polymers to achieve nanoparticles with tunable morphology, size, surface charge, and acid-responsive behavior" by Lin, Y.-N.; Su, L.; Smolen, J.; Li, R.; Song, Y.; Wang, H.; Dong, M.; Wooley, K. L., *Mater. Chem. Front.* **2018**, *2* (12), 2230-2238. Copyright 2018 The Royal Society of Chemistry

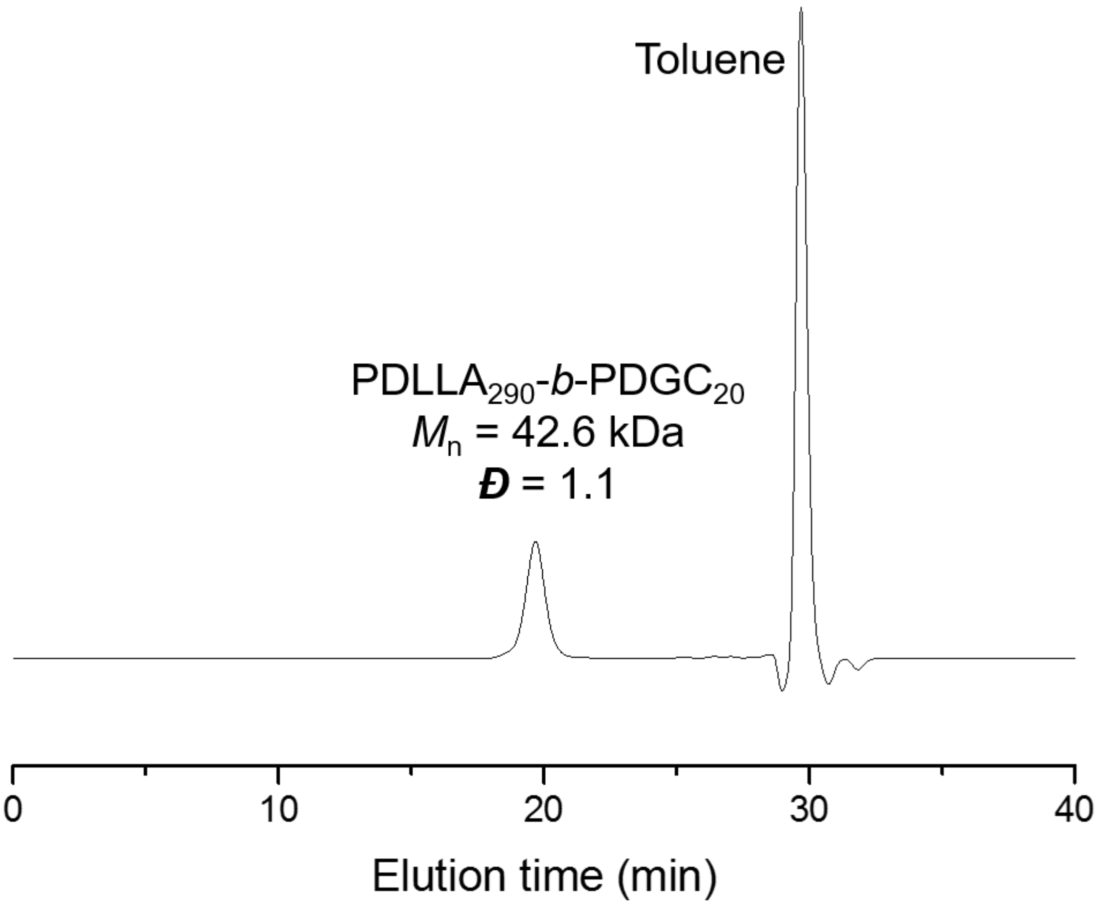

Figure 2. SEC trace of PDLLA$_{290}$-*b*-PDGC$_{20}$ in THF. Reprinted with permission from "Co-assembly of sugar-based amphiphilic block polymers to achieve nanoparticles with tunable morphology, size, surface charge, and acid-responsive behavior" by Lin, Y.-N.; Su, L.; Smolen, J.; Li, R.; Song, Y.; Wang, H.; Dong, M.; Wooley, K. L., *Mater. Chem. Front.* **2018**, *2* (12), 2230-2238. Copyright 2018 The Royal Society of Chemistry.

The anionic PDLLA$_{290}$-*b*-PDGC(COOH)$_{20}$, was prepared by post-polymerization modification of PDLLA$_{290}$-*b*-PDGC$_{20}$ *via* photo-initiated thiol-yne click reaction with a large excess of 3-mercaptopropionic acid (100 molar equivalents relative to alkyne groups). 3-Mercaptopropionic acid was selected due to its hydrophilicity and anionic character, which is desirable for preventing aggregation in physiological environments. In addition, the carboxylic acid groups allowed further polymer modification, which was particularly appealing for installation of histamine moieties that are incompatible with thiol-yne reactions. Successful addition of 3-mercaptopropionic acid to PDLLA$_{290}$-*b*-PDGC$_{20}$ was supported by ^{1}H NMR spectroscopic analysis of the polymer in DMSO-d_6, noting the appearance of proton resonances at δ 3.09 and 2.70 ppm (Figure 3), and by FTIR spectroscopy, with the appearance of peaks characteristic of O-H stretching in the carboxylic acid between 3600 and 2300 cm^{-1} after modification (Figure 4).

The pH-responsive PDLLA$_{290}$-*b*-PDGC(His)$_{20}$, was prepared by post-polymerization modification of PDLLA$_{290}$-*b*-PDGC(COOH)$_{20}$ *via* amidation with an excess of histamine (4 molar equivalents relative to carboxylic acid groups) (Scheme 1). Histamine was conjugated *via* amidation with the carboxylic acid groups of PDLLA$_{290}$-*b*-PDGC(COOH)$_{20}$ since photo-initiated thiol-yne click chemistry was not suitable for histamine due to the presence of the radical-sensitive imidazole groups.[55-56] Successful conjugation of histamine to PDLLA$_{290}$-*b*-PDGC(COOH)$_{20}$ was supported by ^{1}H NMR spectroscopic analysis of the polymer in DMSO-d_6, noting the appearance of imidazole proton resonances at δ 8.06 and 7.40 ppm (Figure 5). FTIR spectroscopy further revealed the disappearance of O-H stretching in carboxylic acid between 3600 and 2300 cm^{-1} after modification (Figure 4).

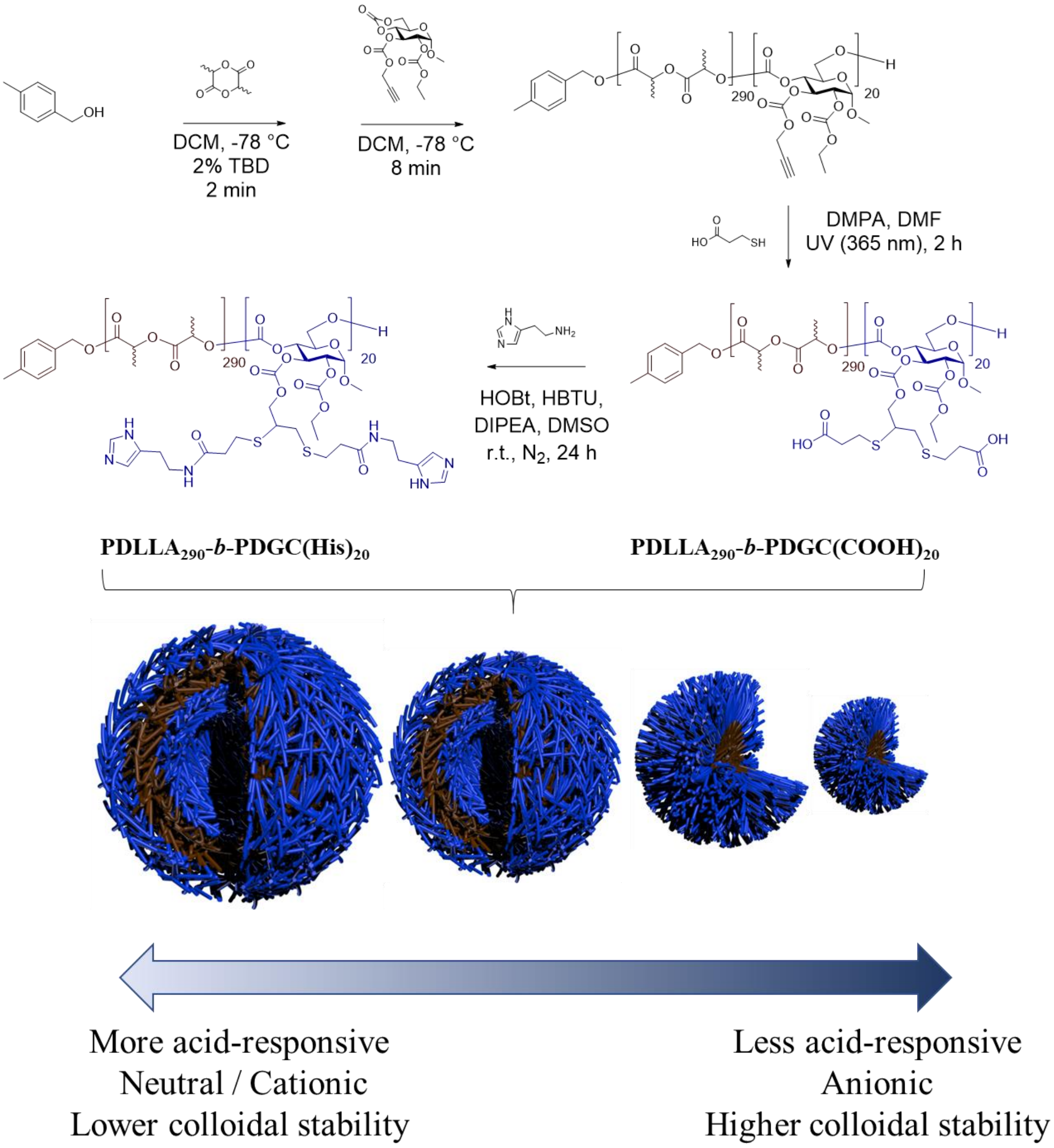

Scheme 1. Synthesis and aqueous assembly of acid- (PDLLA$_{290}$-*b*-PDGC(COOH)$_{20}$) and histamine-modified (PDLLA$_{290}$-*b*-PDGC(His)$_{20}$) PLA-*b*-PDGC. Reprinted with permission from "Co-assembly of sugar-based amphiphilic block polymers to achieve nanoparticles with tunable morphology, size, surface charge, and acid-responsive behavior" by Lin, Y.-N.; Su, L.; Smolen, J.; Li, R.; Song, Y.; Wang, H.; Dong, M.; Wooley, K. L., *Mater. Chem. Front.* **2018**, *2* (12), 2230-2238. Copyright 2018 The Royal Society of Chemistry.

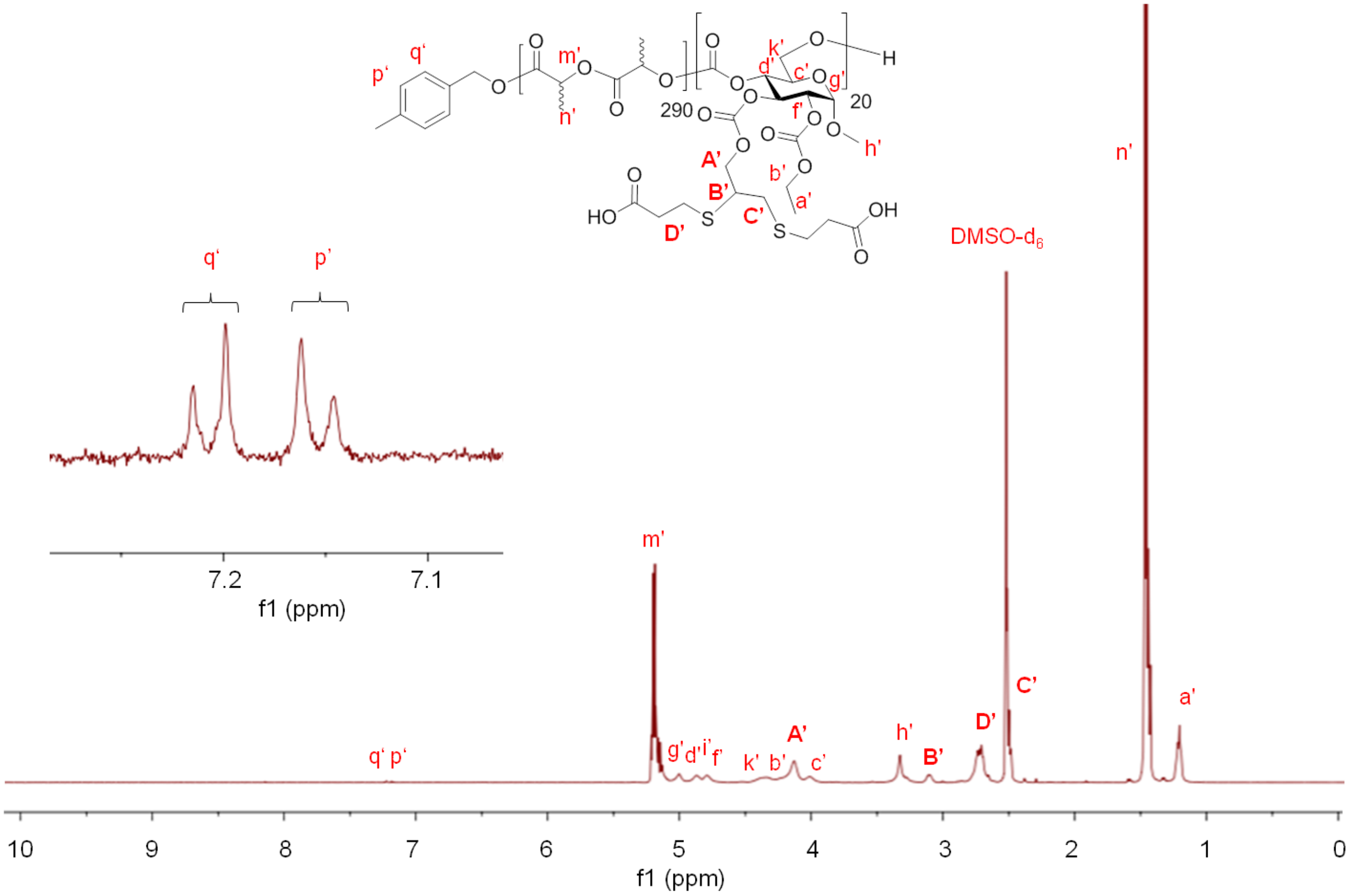

Figure 3. ^{1}H NMR spectrum (500 MHz) of PDLLA$_{290}$-*b*-PDGC(COOH)$_{20}$ in DMSO-*d*$_6$, with the inset expanding the region to show the resonance signals for the aromatic protons of the α-chain end. Reprinted with permission from "Co-assembly of sugar-based amphiphilic block polymers to achieve nanoparticles with tunable morphology, size, surface charge, and acid-responsive behavior" by Lin, Y.-N.; Su, L.; Smolen, J.; Li, R.; Song, Y.; Wang, H.; Dong, M.; Wooley, K. L., *Mater. Chem. Front.* **2018**, *2* (12), 2230-2238. Copyright 2018 The Royal Society of Chemistry.

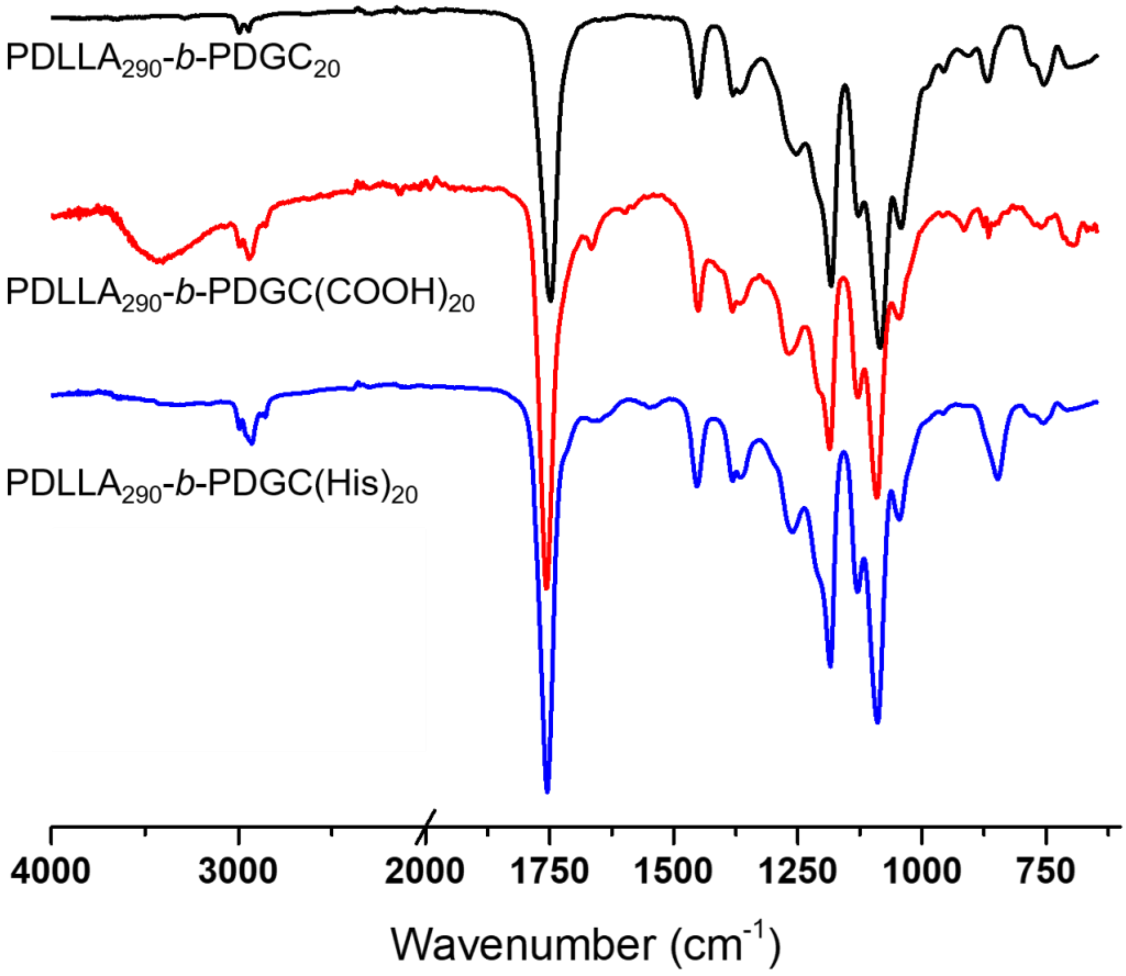

Figure 4. FT-IR spectra of PDLLA$_{290}$-*b*-PDGC$_{20}$, PDLLA$_{290}$-*b*-PDGC(COOH)$_{20}$ and PDLLA$_{290}$-*b*-PDGC(His)$_{20}$. Reprinted with permission from "Co-assembly of sugar-based amphiphilic block polymers to achieve nanoparticles with tunable morphology, size, surface charge, and acid-responsive behavior" by Lin, Y.-N.; Su, L.; Smolen, J.; Li, R.; Song, Y.; Wang, H.; Dong, M.; Wooley, K. L., *Mater. Chem. Front.* **2018**, *2* (12), 2230-2238. Copyright 2018 The Royal Society of Chemistry.

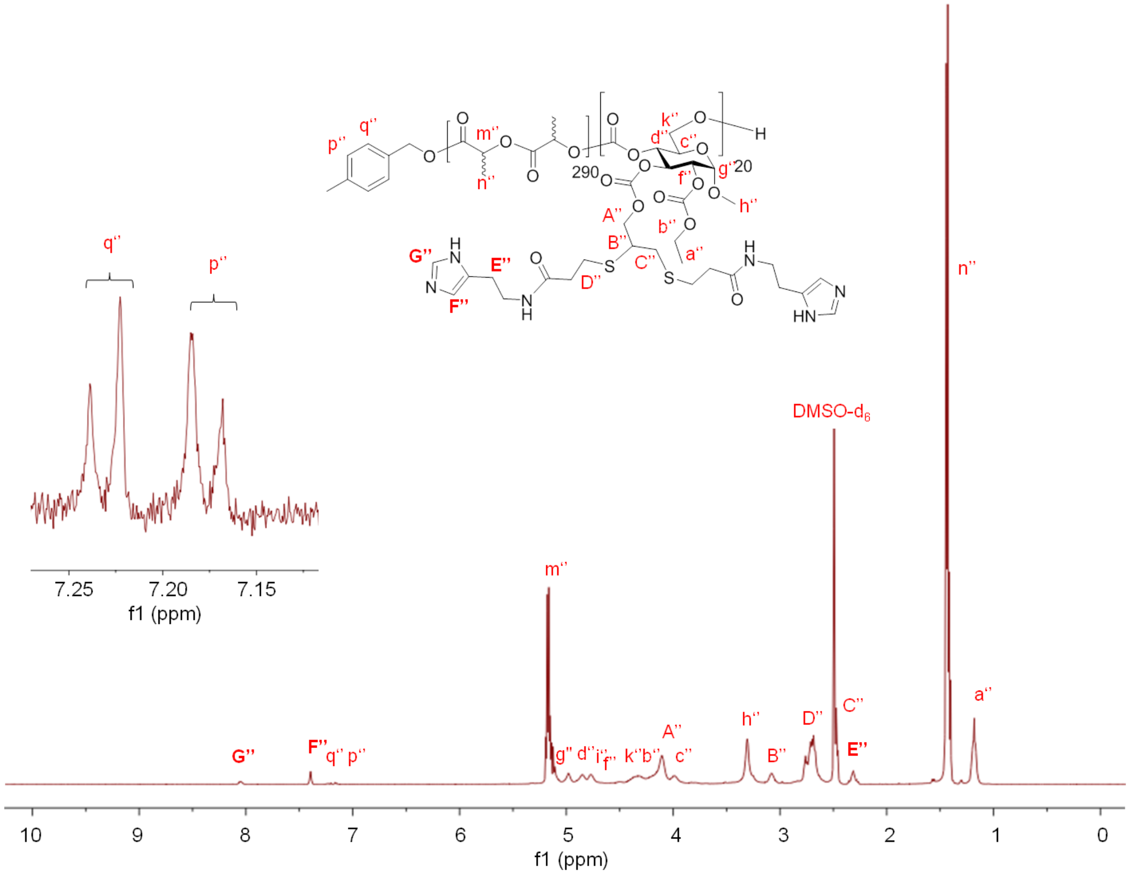

Figure 5. ^{1}H NMR spectrum (500 MHz) of PDLLA$_{290}$-*b*-PDGC(His)$_{20}$ in DMSO-*d*$_{6}$, with the inset expanding the region to show the resonance signals for the aromatic protons of the α-chain end. Reprinted with permission from "Co-assembly of sugar-based amphiphilic block polymers to achieve nanoparticles with tunable morphology, size, surface charge, and acid-responsive behavior" by Lin, Y.-N.; Su, L.; Smolen, J.; Li, R.; Song, Y.; Wang, H.; Dong, M.; Wooley, K. L., *Mater. Chem. Front.* **2018**, *2* (12), 2230-2238. Copyright 2018 The Royal Society of Chemistry.

To gauge the properties of nanoparticles formed from the acid- and histamine-modified block polymers, $PDLLA_{290}$-*b*-$PDGC(COOH)_{20}$ and $PDLLA_{290}$-*b*-$PDGC(His)_{20}$ were first assembled individually in aqueous solution using a nanoprecipitation method.[23, 29, 43] Briefly, the polymers were dissolved in acetone (500 µL, 2 mg/mL), and then added drop-wise to nanopure water (1 mL), followed by stirring in air for 24 h to allow for evaporation of acetone. The final polymer concentration was then adjusted to 1 mg/mL using nanopure water. DLS revealed that upon assembly in nanopure water (pH = *ca.* 6), $PDLLA_{290}$-*b*-$PDGC(COOH)_{20}$ formed nanoparticles with hydrodynamic diameters ($D_{h(number)}$) < 50 nm, while $PDLLA_{290}$-*b*-$PDGC(His)_{20}$ formed micron-sized aggregates (Figure 6 and Figure 7). The differences between the two polymeric particles were attributed to the different functional side chains affording varying degrees of electrostatic stabilization in nanopure water, with anionic carboxylates on $PDLLA_{290}$-*b*-$PDGC(COOH)_{20}$ and neutral or cationic imidazoles on $PDLLA_{290}$-*b*-$PDGC(His)_{20}$. The aggregation of the histamine-functionalized polymers into larger particles is attributed to the lower hydrophilic character imparted by the imidazole-containing pendant groups compared to the carboxylate-containing pendant groups in nanopure water at pH = *ca.* 6. Amphiphilic polymers with less hydrophilic character tend to assemble into larger particle sizes to minimize the energetically unfavorable contact of hydrophobic regions with water molecules, since larger particles have smaller surface area-to-volume ratios.[57] $PDLLA_{290}$-*b*-$PDGC(COOH)_{20}$ nanoparticles displayed anionic surfaces with zeta potentials of *ca.* -36 mV, whereas electrophoretic light scattering of $PDLLA_{290}$-*b*-$PDGC(His)_{20}$ aqueous assemblies could only be conducted after centrifugation of large aggregates with the remaining particles displaying neutral surfaces with zeta potentials of *ca.* -1.6 mV in nanopure water (Figure 7 and Figure 8), consistent with the aggregation observed for PDLLA$_{290}$-*b*-PDGC(His)$_{20}$ (Figure 7). Although neither PDLLA$_{290}$-*b*-PDGC(COOH)$_{20}$ nor PDLLA$_{290}$-*b*-PDGC(His)$_{20}$ alone was anticipated to yield assemblies suitable for cytosolic drug delivery, we hypothesized that blending the two polymers would enable the fabrication of co-assemblies with highly tunable particle sizes and surface charges to tailor degradable, smart sugar-based nanoparticle drug carriers.

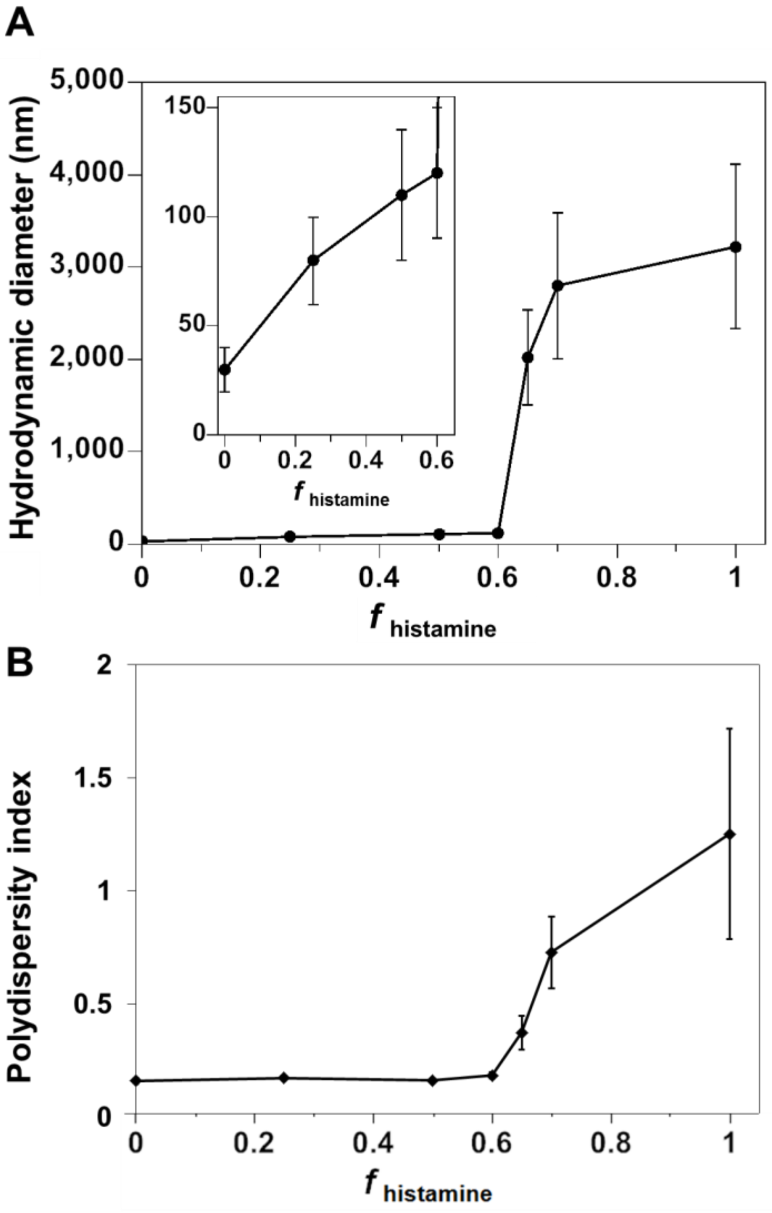

Figure 6. A) Hydrodynamic diameter and B) polydispersity index of polymer co-assemblies, measured by DLS, as a function of the weight fraction of PDLLA$_{290}$-*b*-PDGC(His)$_{20}$ ($f_{\text{histamine}}$) in nanopure water. Reprinted with permission from "Co-assembly of sugar-based amphiphilic block polymers to achieve nanoparticles with tunable morphology, size, surface charge, and acid-responsive behavior" by Lin, Y.-N.; Su, L.; Smolen, J.; Li, R.; Song, Y.; Wang, H.; Dong, M.; Wooley, K. L., *Mater. Chem. Front.* **2018**, *2* (12), 2230-2238. Copyright 2018 The Royal Society of Chemistry.

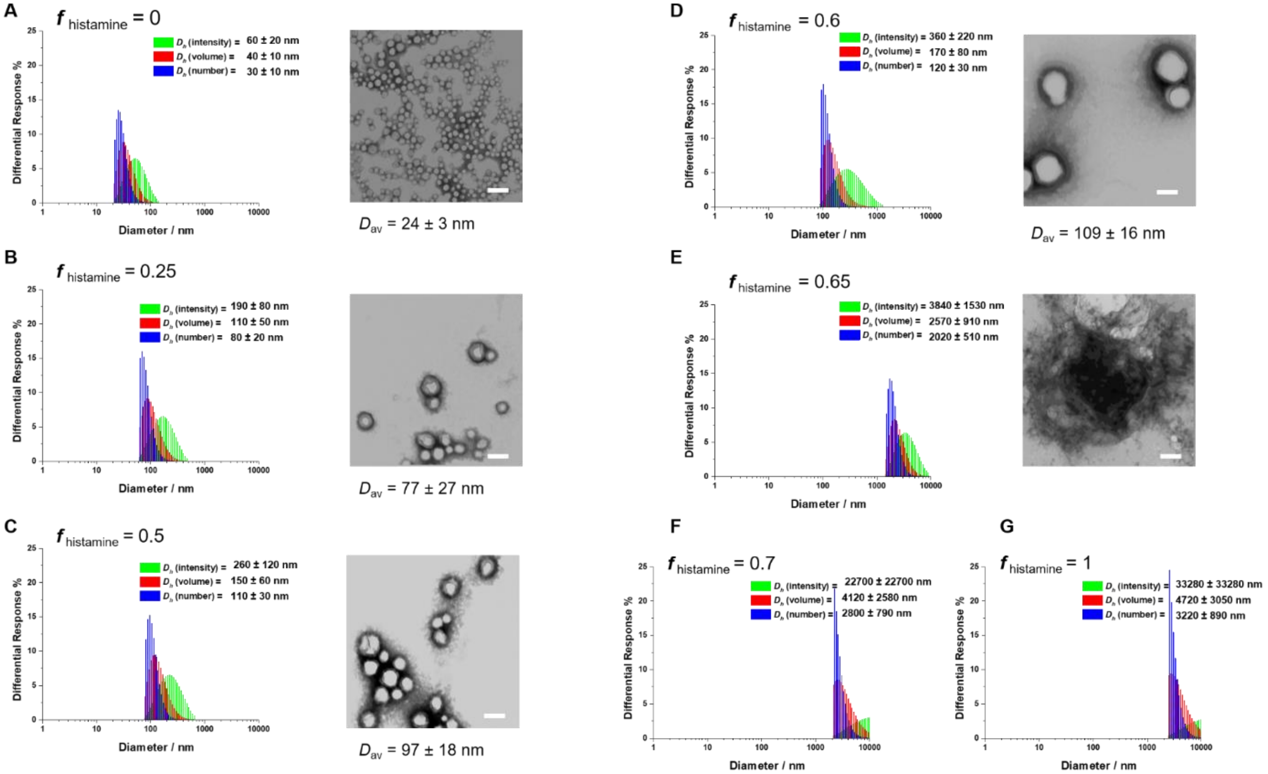

Figure 7. Dynamic light scattering (DLS) and transmission electron microscopy (TEM) of nanoparticles prepared by co-assembly of PDLLA$_{290}$-*b*-PDGC(COOH)$_{20}$ and PDLLA$_{290}$-*b*-PDGC(His)$_{20}$ in nanopure water at different PDLLA$_{290}$-*b*-PDGC(His)$_{20}$ contents, $f_{\text{histamine}}$ = (A) 0, (B) 0.25, (C) 0.5, (D) 0.6, (E) 0.65, (F) 0.7, (G) 1.0. TEM samples were negatively stained by 1 wt % phosphotungstic acid aqueous solution. The scale bars in the TEM images represent 100 nm. Visible precipitates were observed in samples with high $f_{\text{histamine}}$ (*i.e.*, E-G). Reprinted with permission from "Co-assembly of sugar-based amphiphilic block polymers to achieve nanoparticles with tunable morphology, size, surface charge, and acid-responsive behavior" by Lin, Y.-N.; Su, L.; Smolen, J.; Li, R.; Song, Y.; Wang, H.; Dong, M.; Wooley, K. L., *Mater. Chem. Front.* **2018**, *2* (12), 2230-2238. Copyright 2018 The Royal Society of Chemistry.

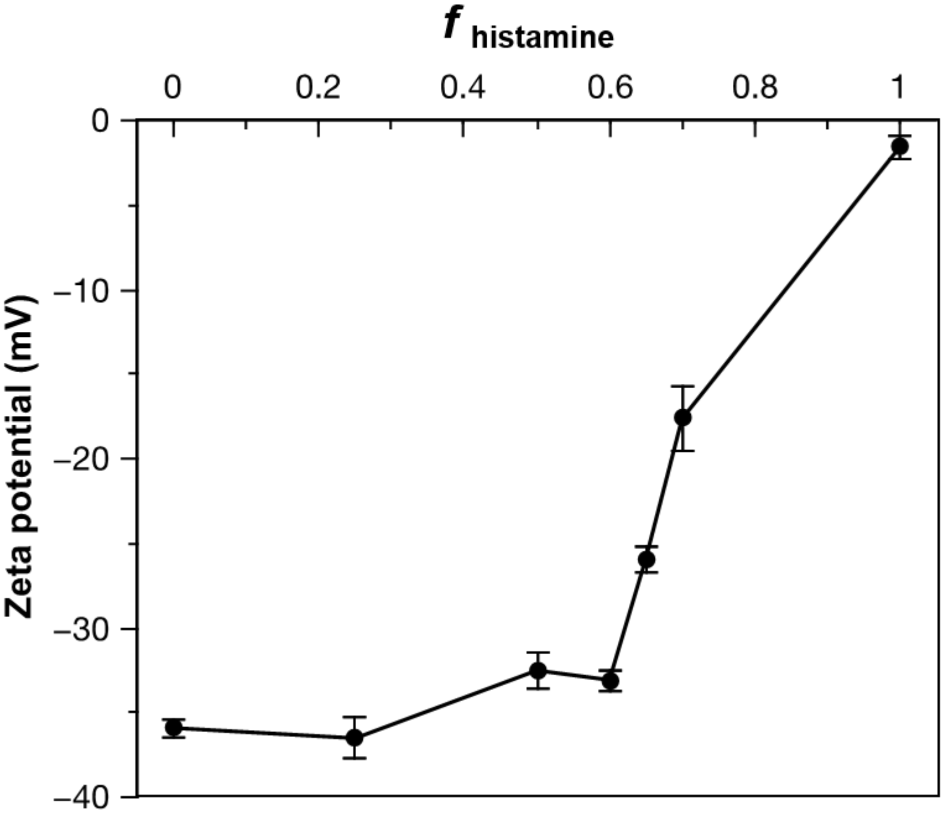

Figure 8. Zeta potential of the co-assemblies in nanopure water as a function of $f_{\text{histamine}}$. Reprinted with permission from "Co-assembly of sugar-based amphiphilic block polymers to achieve nanoparticles with tunable morphology, size, surface charge, and acid-responsive behavior" by Lin, Y.-N.; Su, L.; Smolen, J.; Li, R.; Song, Y.; Wang, H.; Dong, M.; Wooley, K. L., *Mater. Chem. Front.* **2018**, *2* (12), 2230-2238. Copyright 2018 The Royal Society of Chemistry.

Co-assemblies of PDLLA$_{290}$-*b*-PDGC(COOH)$_{20}$ and PDLLA$_{290}$-*b*-PDGC(His)$_{20}$ were fabricated in aqueous solution (1 mg/mL in nanopure water) at predetermined weight fractions using a similar nanoprecipitation method as for the single-component assemblies,[23, 29, 43] affording particles with a variety of sizes and surface compositions. As depicted in Figure 7, DLS data revealed unimodal size distributions of all nanocarriers, suggesting the incorporation of PDLLA$_{290}$-*b*-PDGC(COOH)$_{20}$ and

$PDLLA_{290}$-*b*-$PDGC(His)_{20}$ into the same nanostructures. The size of the co-assemblies increased from $D_{h(\mathrm{number})} = 30 \pm 10$ nm to $D_{h(\mathrm{number})} = 120 \pm 30$ nm (Figure 6 and Figure 7) as the weight fraction of the histamine-modified $PDLLA_{290}$-*b*-$PDGC(His)_{20}$ ($f_{\mathrm{histamine}}$) increased from 0 to 0.6, owing to the decrease in hydrophilic content of the assemblies in nanopure water (pH = *ca.* 6). Co-assemblies with $f_{\mathrm{histamine}} = 0.6$ were found to be at a threshold composition, above which the particle diameter increased from nanoscale to microscale (Figure 6 and Figure 7).

An initial postulate as to the mechanism of assembly and rationale for the variations in particle sizes is based upon several factors. $PDLLA_{290}$-*b*-$PDGC(COOH)_{20}$ is more hydrophilic compared to $PDLLA_{290}$-*b*-$PDGC(His)_{20}$ in nanopure water, due to the presence of the carboxylate side-chains instead of imidazole side-chains. The increased hydrophilicity is supported by the ability to form stable supramolecular assemblies comprised of only $PDLLA_{290}$-*b*-$PDGC(COOH)_{20}$ in water, whereas stable co-assemblies could only be formed when the weight fraction of $PDLLA_{290}$-*b*-$PDGC(His)_{20}$ was maintained at ≤ 60% ($f_{\mathrm{histamine}} \leq 0.60$). With the greater hydrophilicity and water solubility for the $PDGC(COOH)_{20}$ coronal segments, the hydrophilic volume fraction is larger in $PDLLA_{290}$-*b*-$PDGC(COOH)_{20}$ assemblies compared to co-assemblies containing $PDLLA_{290}$-*b*-$PDGC(His)_{20}$. Furthermore, acid-base attractive interactions between the carboxylic acids of the $PDGC(COOH)_{20}$ segments and the histamines of the $PDGC(His)_{20}$ segments would further reduce the hydrophilic volume fraction in the co-assesmblies. Reduction in hydrophilic volume fraction would change the average molecular shape of the polymer chain in aqueous solution, resulting in different morphology of the assemblies in order to minimize the total free energy of the system.[58-59] TEM images of Figure 7 suggest that assemblies of PDLLA$_{290}$-*b*-PDGC(COOH)$_{20}$ are primarily micelles, whereas the larger co-assembled particles may be vesicular. Micelle-to-vesicle transformations upon reduction of hydrophilic volume fraction is consistent with other polymeric assemblies reported in the literature.[60-61] Polymer co-assembly further allowed fabrication of particles with controllable particle surface charge depending on the feed ratio of two sugar-based copolymers. Particles with zeta potentials ranging from *ca.* -36 to -1.6 mV were formed simply by altering the $f_{\text{histamine}}$ (Figure 7 and Figure 8**)**. When $f_{\text{histamine}} \leq 0.6$, the zeta potential of the co-assemblies remained relatively constant, as the overall particle surfaces were dominated by the hydrophilic anionic carboxylates of PDLLA$_{290}$-*b*-PDGC(COOH)$_{20}$. As $f_{\text{histamine}}$ increased, the surface density of the acid groups decreased, yielding a corresponding decrease in the magnitude of the negative zeta potential (Figure 7 and Figure 8). Interparticle repulsion decreased with the decreasing magnitude of zeta potential, consistent with the marked increase in co-assembly diameter at $f_{\text{histamine}} > 0.6$.

The histamine moieties within the co-assemblies imparted highly tunable pH-dependent charge-switching profiles to the polymeric particles. While the surface charge of PDLLA$_{290}$-*b*-PDGC(COOH)$_{20}$ assemblies remained relatively constant with zeta potentials of *ca.* -35 mV, PDLLA$_{290}$-*b*-PDGC(His)$_{20}$ assemblies underwent a cationic-to-anionic surface charge transformation (*ca.* +22 mV to -15 mV) as pH was increased from 5 to 8, with an apparent isoelectric point (pH(I)) of *ca.* 7 (Figure 9 and Figure 10). The pH-dependent charge transformation of PDLLA$_{290}$-*b*-PDGC(His)$_{20}$ was in agreement with the reported pK_a of the imidazole conjugate acid (pK_a = 6.95).[52] Interestingly, the apparent isoelectric point of PDLLA$_{290}$-*b*-PDGC(His)$_{20}$ was *ca.* 7, where PDLLA$_{290}$-*b*-PDGC(His)$_{20}$ was expected to be partially positive due to protonation of *ca.* 50% of the imidazoles at pH 7. The neutralization may result from the surface charge balance between protonated PDLLA$_{290}$-*b*-PDGC(His)$_{20}$ and adsorbed anionic hydroxyl ions on the surface of the assemblies. Since oxygen atoms of water molecules preferentially orient toward the hydrophobic particle surface,[62,63] hydrogen atoms of the interfacial-adsorbed water molecules can facilitate adsorption of anionic hydroxyl ions (from self-ionization of water), leading to negative surface zeta potentials for hydrophobic polymeric particles.[62-63]

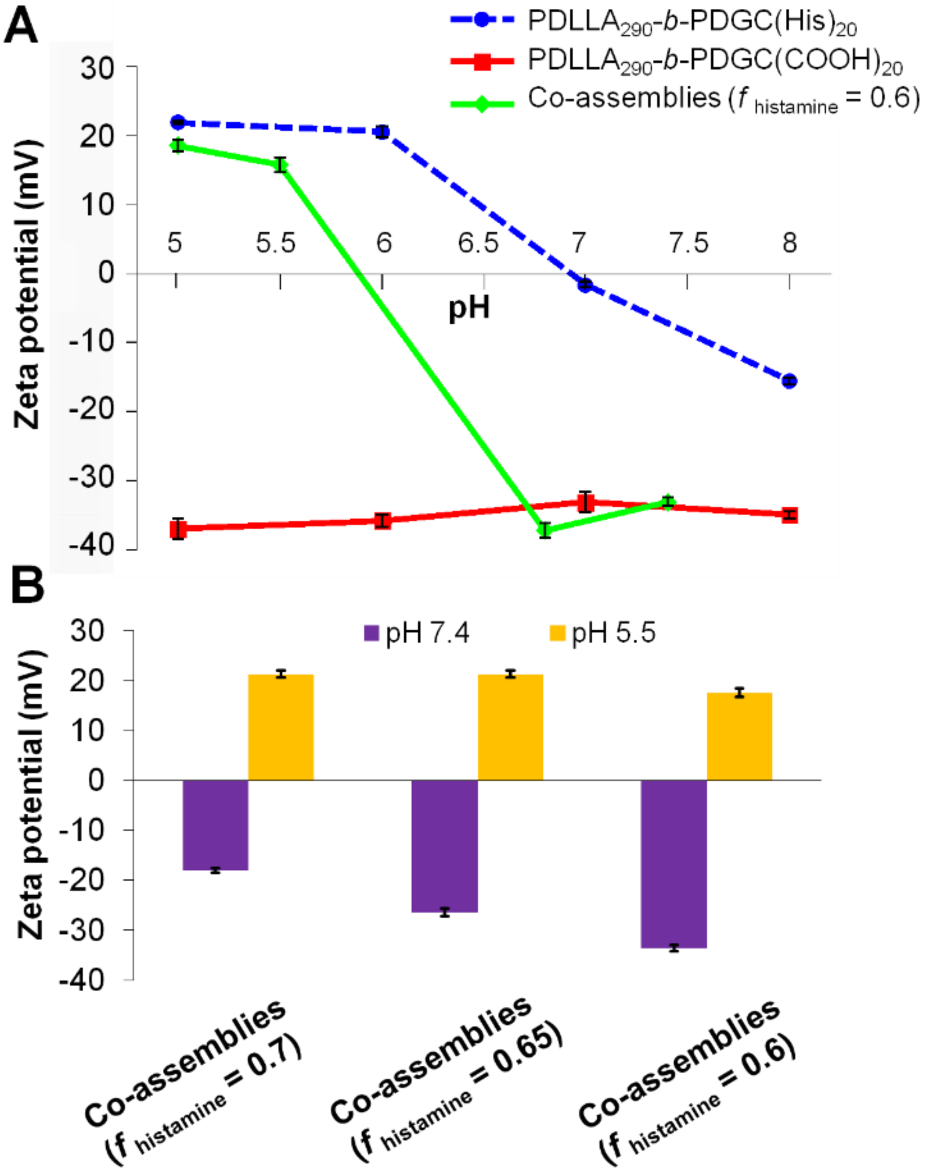

Figure 9. pH-Responsive properties of acid- and histamine-modified, sugar-based block copolymers and their co-assemblies: A) pH-Dependent zeta potential of nanoparticles comprised of PDLLA$_{290}$-*b*-PDGC(COOH)$_{20}$, PDLLA$_{290}$-*b*-PDGC(His)$_{20}$, and co-assemblies ($f_{\text{histamine}}$ = 0.6) in MOPS buffer (20 mM); B) acid-induced charge reversal of PDLLA$_{290}$-*b*-PDGC(COOH)$_{20}$ and PLA$_{290}$-*b*-PDGC(His)$_{20}$ co-assemblies. Reprinted with permission from "Co-assembly of sugar-based amphiphilic block polymers to achieve nanoparticles with tunable morphology, size, surface charge, and acid-responsive behavior" by Lin, Y.-N.; Su, L.; Smolen, J.; Li, R.; Song, Y.; Wang, H.; Dong, M.; Wooley, K. L., *Mater. Chem. Front.* **2018**, *2* (12), 2230-2238. Copyright 2018 The Royal Society of Chemistry.

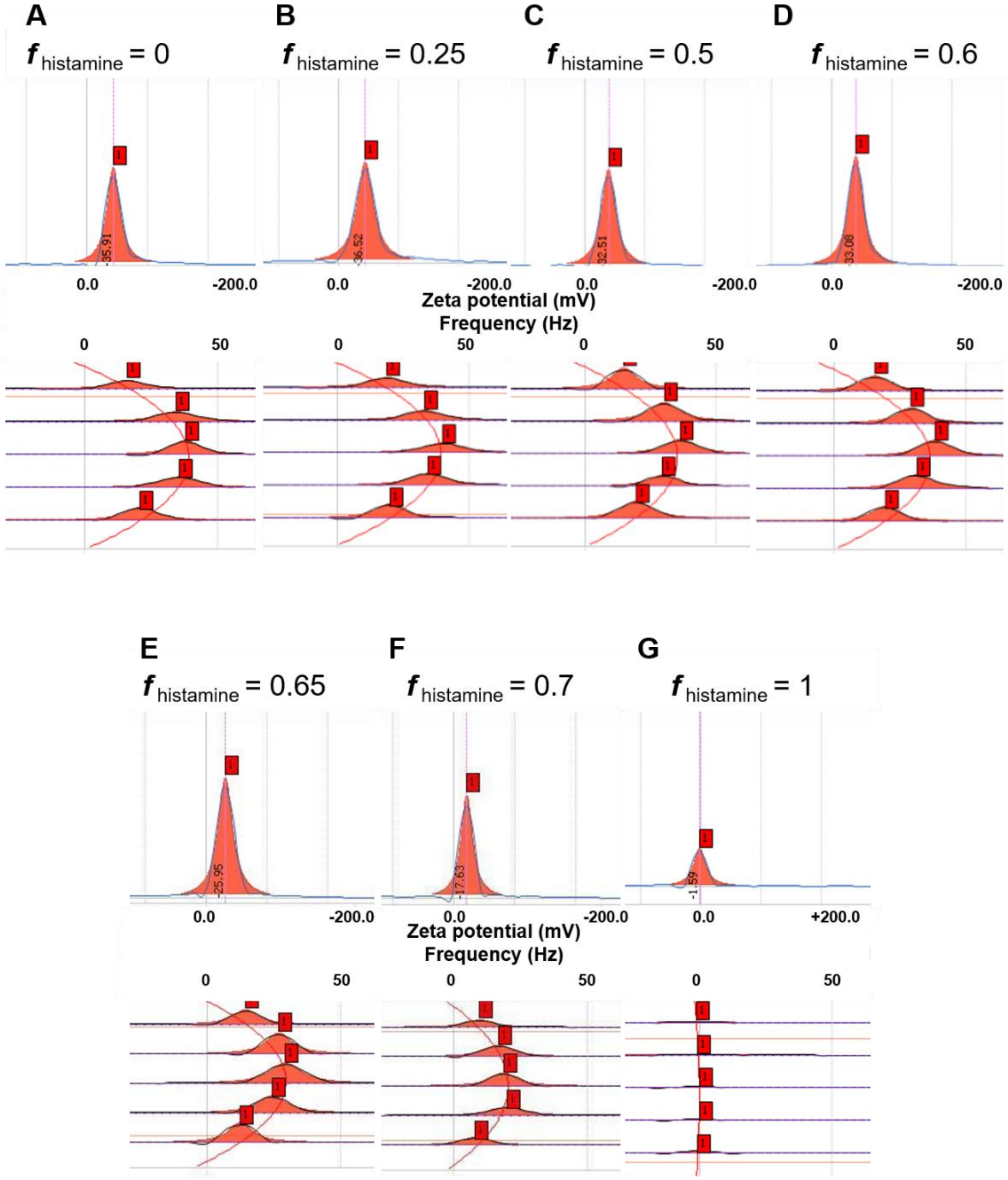

Figure 10. Zeta potential characterization of the nanoparticles in nanopure water prepared by co-assembly of PDLLA$_{290}$-*b*-PDGC(COOH)$_{20}$ and PDLLA$_{290}$-*b*-PDGC(His)$_{20}$ with $f_{\text{histamine}}$ = (A) 0, (B) 0.25, (C) 0.5, (D) 0.6, (E) 0.65, (F) 0.7, and (G) 1. Zeta potential Lorentzian peak (upper) and top view of frequency distribution (lower) as a function of position across the cell during the electrophoretic light scattering measurement. Reprinted with permission from “Co-assembly of sugar-based amphiphilic block polymers to achieve nanoparticles with tunable morphology, size, surface charge, and acid-responsive behavior” by Lin, Y.-N.; Su, L.; Smolen, J.; Li, R.; Song, Y.; Wang, H.; Dong, M.; Wooley, K. L., *Mater. Chem. Front.* **2018**, *2* (12), 2230-2238. Copyright 2018 The Royal Society of Chemistry.

Polymeric co-assemblies exhibited different pH-dependent charge-switching profiles compared to particles comprised only of PDLLA$_{290}$-*b*-PDGC(COOH)$_{20}$ or PDLLA$_{290}$-*b*-PDGC(His)$_{20}$. Aqueous co-assemblies with $f_{\text{histamine}}$ from 0.6–0.7 underwent anionic-to-cationic surface charge transformations as the solution pH was decreased from 7.4 to 5.5, (Figure 9 and Figure 11). The pH-dependent zeta potential change upon acidification was more pronounced for polymer co-assemblies ($f_{\text{histamine}}$ = 0.6, *ca.* +55 mV) compared to PDLLA$_{290}$-*b*-PDGC(His)$_{20}$ assemblies (*ca.* +35 mV) (Figure 9 and Figure 10). In addition, polymer co-assemblies ($f_{\text{histamine}}$ = 0.6) underwent charge-reversal within a narrower pH range of 1.3 (*i.e.*, from pH 5.5 to 6.8), compared to the wider pH range of 2 (from pH 6 to 8) required for the transformation of PDLLA$_{290}$-*b*-PDGC(His)$_{20}$ assemblies. Additionally, the isoelectric point of the polymer co-assemblies ($f_{\text{histamine}}$ = 0.6) was lower (pH(I) = *ca.* 6) than that of the PDLLA$_{290}$-*b*-PDGC(His)$_{20}$ assemblies (pH(I) = *ca.* 7). The tunability of the pH-responsive properties by this co-assembly procedure was further demonstrated in co-assemblies with varying $f_{\text{histamine}}$. Co-assemblies with higher $f_{\text{histamine}}$ exhibited less pronounced charge transformations compared to co-assemblies with lower $f_{\text{histamine}}$, with surface compositions dominated by the carboxylates of the PDLLA$_{290}$-*b*-PDGC(COOH)$_{20}$ at pH 7.4. Therefore, the overall surface charge of the co-assemblies could be modulated both by pH and by the relative ratio of carboxylate and imidazole functionalities in the nanostructures (Figure 9 and Figure 11).

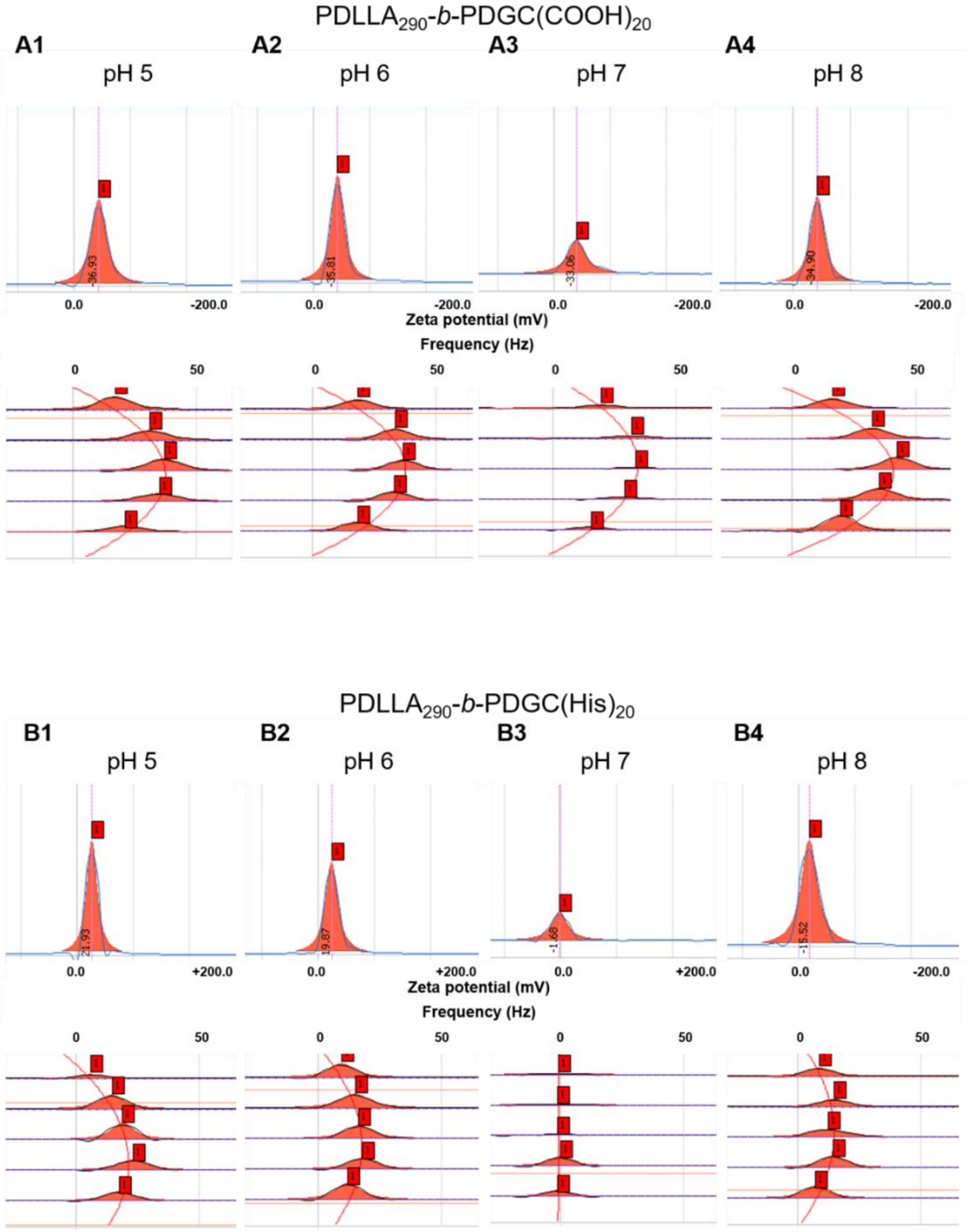

Figure 11. Zeta potential characterization of the nanoparticles prepared by self-assembly of (A) PDLLA$_{290}$-*b*-PDGC(COOH)$_{20}$ and (B) PDLLA$_{290}$-*b*-PDGC(His)$_{20}$ in MOPS buffer (20 mM) as a function of pH. Zeta potential Lorentzian peak (upper) and frequency distribution as a function of position across the cell during the electrophoretic light scattering measurement (lower). Reprinted with permission from "Co-assembly of sugar-based amphiphilic block polymers to achieve nanoparticles with tunable morphology, size, surface charge, and acid-responsive behavior" by Lin, Y.-N.; Su, L.; Smolen, J.; Li, R.; Song, Y.; Wang, H.; Dong, M.; Wooley, K. L., *Mater. Chem. Front.* **2018**, *2* (12), 2230-2238. Copyright 2018 The Royal Society of Chemistry.

In addition to tuning particle size and pH-dependent surface charge, co-assembly altered the morphology of the polymeric nanoparticles as a function of pH and composition. PDLLA$_{290}$-*b*-PDGC(COOH)$_{20}$ aqueous assemblies remained relatively constant in size (Figure 12 and Figure 13), whereas PDLLA$_{290}$-*b*-PDGC(His)$_{20}$ assemblies decreased in size and the co-assemblies ($f_{\text{histamine}}$ = 0.6) increased in size with decreasing pH (Figure 12, Figure 13, and Figure 14). At pH = 5.5, a majority of the imidazole groups were protonated and PDLLA$_{290}$-*b*-PDGC(His)$_{20}$ assemblies exhibited cationic surfaces, imparting hydrophilicity and affording colloidally-stable nano-sized assemblies. The imidazole groups of PDLLA$_{290}$-*b*-PDGC(His)$_{20}$ were deprotonated at pH = 7.4, increasing the hydrophobic character and, consequently, the diameter of the assemblies, which eventually aggregated into micron-sized precipitates.

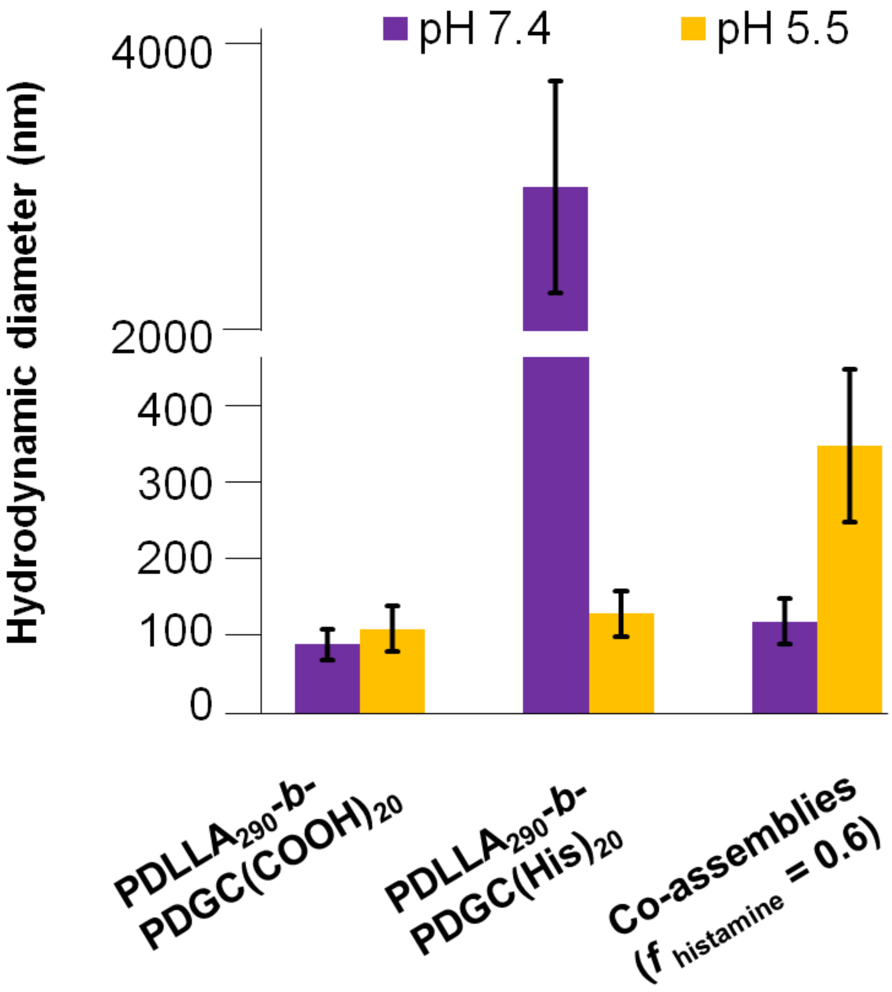

Figure 12. Hydrodynamic diameter of assemblies comprised of PDLLA$_{290}$-*b*-PDGC(COOH)$_{20}$, PDLLA$_{290}$-*b*-PDGC(His)$_{20}$, and co-assemblies ($f_{\text{histamine}}$ = 0.6) in MOPS buffer (20 mM) at pH = 5.5 and 7.4. Reprinted with permission from "Co-assembly of sugar-based amphiphilic block polymers to achieve nanoparticles with tunable morphology, size, surface charge, and acid-responsive behavior" by Lin, Y.-N.; Su, L.; Smolen, J.; Li, R.; Song, Y.; Wang, H.; Dong, M.; Wooley, K. L., *Mater. Chem. Front.* **2018**, *2* (12), 2230-2238. Copyright 2018 The Royal Society of Chemistry.

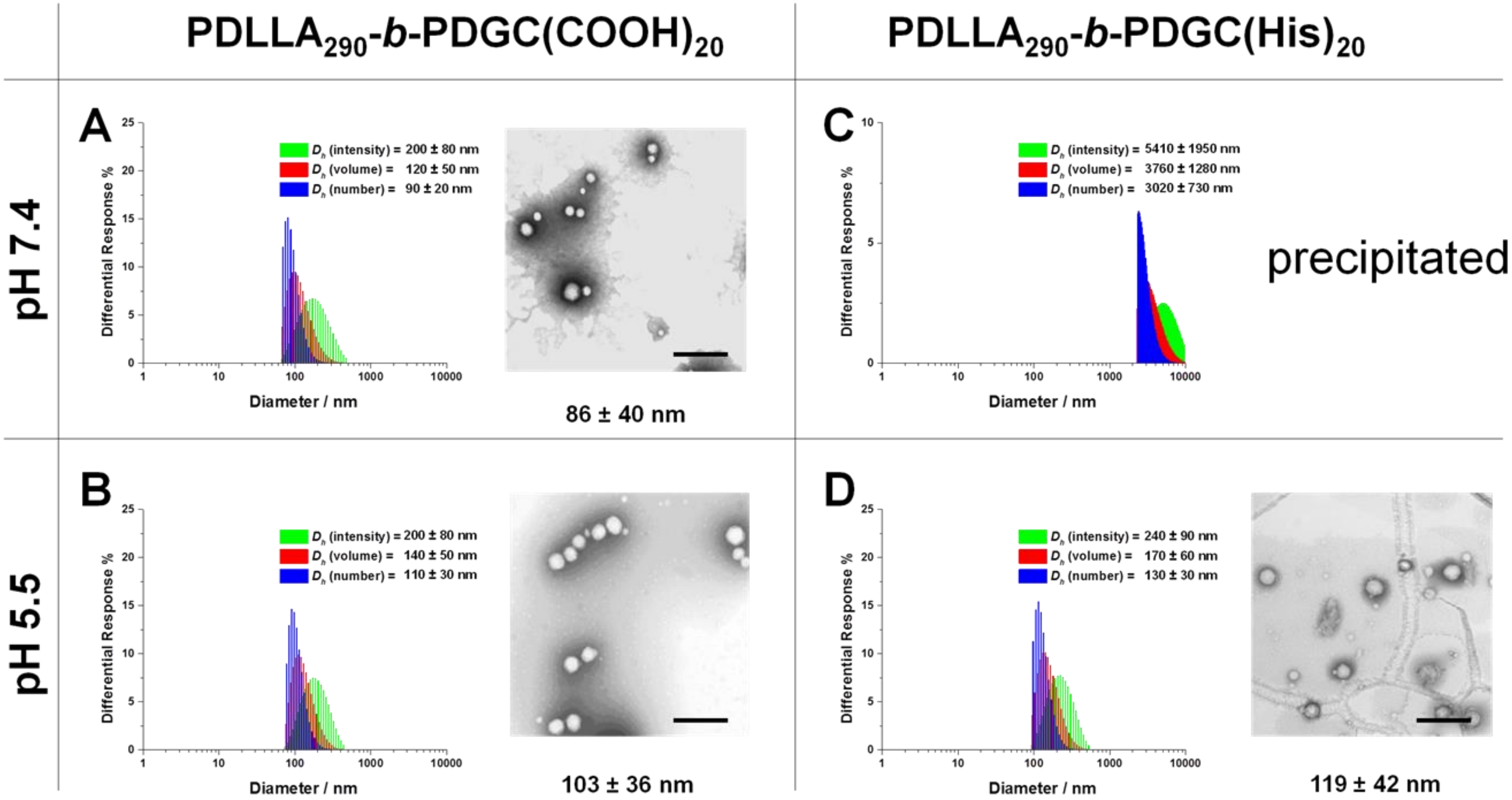

Figure 13. DLS and TEM of nanoparticles prepared by self-assembly of PDLLA$_{290}$-*b*-PDGC(COOH)$_{20}$ and PDLLA$_{290}$-*b*-PDGC(His)$_{20}$ in MOPS buffer (20 mM) at pH 5.5 and 7.4. TEM samples were negatively stained by 1 wt % phosphotungstic acid aqueous solution. The scale bars in the TEM images represent 500 nm. PDLLA$_{290}$-*b*-PDGC(His)$_{20}$ precipitated during assembly at pH 7.4. Reprinted with permission from "Co-assembly of sugar-based amphiphilic block polymers to achieve nanoparticles with tunable morphology, size, surface charge, and acid-responsive behavior" by Lin, Y.-N.; Su, L.; Smolen, J.; Li, R.; Song, Y.; Wang, H.; Dong, M.; Wooley, K. L., *Mater. Chem. Front.* **2018**, *2* (12), 2230-2238. Copyright 2018 The Royal Society of Chemistry.

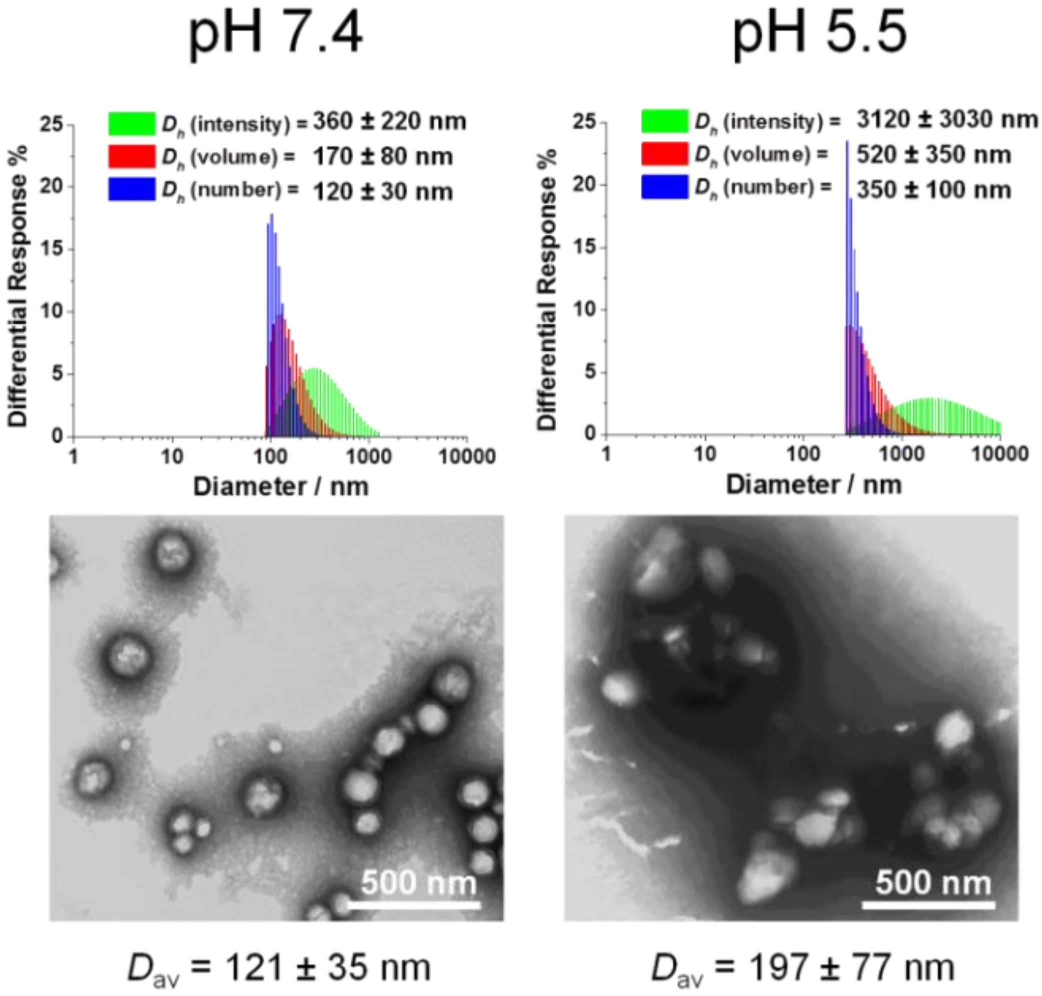

Figure 14. Morphological characterization of co-assemblies ($f_{\text{histamine}}$ = 0.6) at pH 7.4 and pH 5.5 using DLS and TEM. TEM samples were negatively stained by 1 wt % phosphotungstic acid aqueous solution. Reprinted with permission from "Co-assembly of sugar-based amphiphilic block polymers to achieve nanoparticles with tunable morphology, size, surface charge, and acid-responsive behavior" by Lin, Y.-N.; Su, L.; Smolen, J.; Li, R.; Song, Y.; Wang, H.; Dong, M.; Wooley, K. L., *Mater. Chem. Front.* **2018**, *2* (12), 2230-2238. Copyright 2018 The Royal Society of Chemistry.

In contrast, co-assemblies ($f_{\text{histamine}}$ = 0.6) exhibited acid-triggered swelling behavior. We speculated that, at pH 7.4, unprotonated imidazole groups were primarily localized within the hydrophobic core, whereas the acid groups dominated the surface of the particles. With decreasing pH and imidazole protonation, the hydrophilicity of the protonated imidazole groups resulted in swelling of the co-assemblies. Interestingly, $PDLLA_{290}$-*b*-$PDGC(COOH)_{20}$ formed different morphologies when assembled in nanopure water *vs.* MOPS buffer (pH 7.4). The $PDLLA_{290}$-*b*-$PDGC(COOH)_{20}$ formed micelles *ca.* 30 nm in diameter in nanopure water but formed vesicles *ca.* 90 nm in diameter in MOPS buffer (pH 7.4, Figure 7 and Figure 13). The difference may arise from charge shielding by the buffer ions, reducing the electrostatic repulsion between carboxylates, thereby reducing the hydrophilic volume fraction and giving rise to different morphologies compared to those formed in nanopure water. Such results suggested the potential tunability in morphology by altering the salt composition of the aqueous solution.

Despite the successful charge-switching ability of the imidazole-containing pH-responsive $PDLLA_{290}$-*b*-$PDGC(His)_{20}$, the micron-size self-assemblies (Figure 13) at physiological pH of 7.4 would reduce the circulation time and diminish the EPR effect. It was, therefore, imperative to reduce particle size while maintaining the charge-switching capability of the imidazole-containing polymer. TEM images of co-assemblies ($f_{\text{histamine}} = 0.6$) at pH 7.4 showed vesicular structures with average diameters of 121 ± 35 nm (Figure 14), in good agreement with the DLS results ($D_{h(\text{number})} = 120 \pm 30$ nm). These multicomponent polymeric co-assemblies ($f_{\text{histamine}} = 0.6$) are well poised for cytosolic delivery, being within the optimal size range (20–200 nm) to minimize renal clearance, reduce reticuloendothelial clearance, and affording passive accumulation in tumor tissue by the EPR effect. The co-assemblies displayed carboxylate-dominated anionic surfaces (with zeta potentials of *ca.* -34 mV) at pH 7.4 and underwent charge-reversal to imidazole-dominated cationic surfaces (*ca.* +15 mV) at endolysosomal pH (5.5) (Figure 9). During the charge-reversal process, the hydrophobic-to-hydrophilic transformation associated with the protonation of imidazole moities swelled the polymeric co-assemblies, as shown in the increase in $D_{h(\mathrm{number})}$ from 120 nm to 350 nm with decreasing pH (Figure 14). TEM images of co-assemblies ($f_{\mathrm{histamine}}$ = 0.6) also indicated swelling in acidic environments, by an increase in particle diameter from 121 ± 35 nm at pH 7.4 to 197 ± 77 nm at pH 5.5. This acid-induced swelling was further associated with a broadening of the size distribution and the observation of non-spherical morphologies, as evidenced by discrepancy between DLS and TEM size measurements at endolysosomal pH. In conjunction with the endosomal escape capabilities expected from these co-assemblies, the acid-triggered swelling is expected to facilitate cytosolic delivery of therapeutics.[7, 10, 15, 54, 64]

2.3. Experimental Section

2.3.1. Materials

DL-Lactide was purchased from TCI America (Portland, OR) and purified by recrystallization from ethyl acetate. 1,5,7-Triazabicyclo[4.4.0]dec-5-ene (TBD) was used as received from TCI America (Portland, OR). Hydroxybenzotriazole (HOBt) and 2-(1*H*-Benzotriazole-1-yl)-1,1,3,3-tetramethylaminium hexafluorophosphate (HBTU) were used as received from Chem-Impex International, Inc. (Wood Dale, IL). Dichloromethane (DCM) and *N*,*N*-dimethyl formamide (DMF) were dried using a solvent purification system (J. C. Meyer Solvent Systems, Inc., Laguna Beach, CA). Hydrochloric acid (HCl, 36.5–38.0 wt%) was purchased from Thermo-Fisher Scientific. Nanopure water (18.2 MΩ·cm) was obtained from a Milli-Q water filtration system (Millipore Corp, USA). The alkyne-substituted glucose carbonate monomer, methyl-2-*O*-ethyloxycarbonyl-3-*O*-propargyloxycarbonyl-4,6-*O*-carbonyl-α-D-glucopyranoside (GC(EPC)), was synthesized according to a previously published procedure.[50] 3-(*N*-Morpholino)propanesulfonic acid (MOPS) was acquired from Sigma-Aldrich (St. Louis, MO). MOPS buffers were prepared according to the Cold Spring Harbor protocols. Briefly, MOPS (4.19 g), sodium acetate (410 mg), and disodium ethylenediaminetetraacetate dihydrate ($Na_2EDTA \cdot 2H_2O$, 372 mg) were dissolved in nanopure water (1 L), and the pH was adjusted using sodium hydroxide and hydrochloric acid solutions. All other chemicals were purchased from Sigma-Aldrich (St. Louis, MO) and used without further purification unless otherwise noted. Spectra/Por dialysis membranes (MWCO 12–14 kDa) were purchased from Spectrum Laboratories, Inc. (Rancho Dominguez, CA).

2.3.2. Instrumentation

^{1}H NMR and ^{13}C NMR spectra were recorded on a Varian 500 spectrometer (Varian, Inc., Palo Alto, CA) interfaced to a UNIX computer using VNMR-J software. All NMR experiments were performed at ambient temperature. Chemical shifts were referenced to the solvent residual signals. All ^{1}H NMR chemical shifts are reported in parts per million (ppm) downfield of tetramethylsilane and relative to the signals for residual $CHCl_3$ (7.26 ppm). All ^{13}C NMR spectra are reported in ppm relative to $CDCl_3$ (77.23 ppm) and were obtained with ^{1}H decoupling.

Fourier transform infrared (FTIR) spectra were recorded on an IR Prestige 21 system equipped with a diamond attenuated total reflection (ATR) lens (Shimadzu Corp., Japan) and analyzed using IRsolution v. 1.40 software.

Size exclusion chromatography (SEC) eluting with tetrahydrofuran (THF) was performed on a Waters Chromatography, Inc. (Milford, MA) system equipped with an isocratic pump (model 1515), a differential refractometer (model 2414), and column set comprised of a PLgel 5 μm guard column (50 × 7.5 mm), a PLgel 5 μm Mixed C column (300 × 7.5 mm, Agilent Technologies) and two Styragel® columns (500 Å and 104 Å, 300 × 7.5 mm, Waters Chromatography, Inc.). The system was operated at 40 °C with a flow rate of 1 mL/min. Data were analyzed using Breeze software from Waters Chromatography, Inc. (Milford, MA). Molar masses were determined relative to polystyrene standards (580–3,250,000 Da) purchased from Polymer Laboratories, Inc. (Amherst, MA). Polymer solutions were prepared at a concentration of *ca.* 3 mg/mL with 0.05 vol% toluene as the flow rate marker; an injection volume of 200 μL was used.

Thermogravimetric analysis (TGA) was performed under Ar atmosphere using a Mettler-Toledo TGA2/1100/464, with a heating rate of 10 °C/min, from 25 to 500 °C. Data were analyzed using Mettler-Toledo STAR^{e} v. 15.00a software.

Glass transition (T_g) and melting (T_m) temperatures were measured by differential scanning calorimetry (DSC) on a Mettler-Toledo DSC3/700/1190 (Mettler-Toledo, Inc., Columbus, OH) under $N_{2(g)}$. The T_g was taken as the midpoint of the inflection tangent of the second heating scan. The T_m was taken as the maximum of the endothermic peak of the second heating scan. Measurements were performed with a heating rate of 10 °C/min and the data were analyzed using Mettler-Toledo STAR^e v. 15.00a software.

Dynamic light scattering (DLS) measurements were conducted using a Delsa Nano C instrument (Beckman Coulter, Inc., Fullerton, CA) equipped with a laser diode operating at 658 nm. Scattered light was detected at 165° and analyzed using a log correlator over 70 accumulations for a 0.5 mL of sample in a glass size cell (capacity = 0.9 mL). The photomultiplier aperture and attenuator were adjusted automatically to obtain a photon count rate of *ca.* 10 kcps. The particle size distribution and distribution averages were calculated using CONTIN particle size distribution analysis routines in Delsa Nano 2.31 software. The average diameter of the particles is reported as the intensity-, volume- and number-average particle diameter from 70 accumulations. All measurements were repeated 10 times.

The zeta potentials of the nanoparticles were determined by a Delsa Nano C particle analyzer (Beckman Coulter Inc., Fullerton, CA) equipped with a 30 mW dual laser diode at 658 nm. The zeta potential of the particles in suspension was obtained by measuring the electrophoretic mobility of the charged particles. Scattered light was detected at a 30° angle at 25 °C. The zeta potential was measured at five regions in the flow cell and a weighted mean was calculated. These five measurements were used to correct for electroosmotic flow induced in the cell due to the surface charge of the cell wall. The zeta potential is reported as the average and standard deviation of three measurements.

Transmission electron microscopy (TEM) images were collected on a JEOL 1200EX operated at 100 kV, and micrographs were recorded using a SIA-15C CCD camera. Samples for TEM were prepared as follows: 20 µL of aqueous polymer solution (0.5 mg/mL) was deposited onto a carbon-coated copper grid, and after 1 min, excess solution was quickly wicked away by a piece of filter paper. The samples were then negatively stained with a 1 wt% phosphotungstic acid (PTA) aqueous solution (20 µL). After 30 s, excess stain solution was quickly wicked away by a piece of filter paper and the samples were left to dry under ambient conditions prior to imaging.

2.3.3. Synthesis

2.3.3.1. Synthesis of PDLLA$_{290}$-*b*-PDGC$_{20}$

A solution of DL-lactide (1.00 g, 6.94 mmol) and 4-methylbenzyl alcohol (0.10 mL, 24 mg/mL in DCM, 2.4 mg, 0.020 mmol) was prepared in anhydrous DCM (1.00 mL) and transferred to a vial equipped with a stir bar and a rubber septum in an argon-filled glovebox. The vial was then removed from the glovebox and connected *via* a needle inlet to a Schlenk line. A solution of TBD in DCM (0.10 mL, 14 mg/mL, 0.010 mmol) was injected quickly into the vial of DL-lactide at −78 °C (acetone-dry ice bath). After stirring for 2 min, a solution of GC(EPC) (200 mg, 0.54 mmol) in DCM (1.00 mL) was added *via* syringe to the reaction mixture. The reaction was stirred for an additional 6 min at −78 °C and then quenched by addition of excess acetic acid. Precipitation from DCM into methanol three times and drying under vacuum yielded PDLLA$_{290}$-*b*-PDGC$_{20}$ as a white powder (952 mg, 79% yield). ^{1}H NMR (500 MHz, CDCl$_3$, ppm): δ 7.20 and

7.17 (AB_q, J = 8 Hz), 5.36 (dd, J = 10, 10 Hz), 5.11–5.24 (m), 5.03 (d, J = 5 Hz), 4.89 (dd, J = 10, 10 Hz), 4.79–4.68 (m), 4.28 (s), 4.20 (dq, J = 8, 3 Hz), 4.01 (m), 3.42 (s), 2.59 (t, J = 3 Hz), 2.35 (s), 1.62–1.53 (m), 1.30 (t, J = 7 Hz). ^{13}C NMR (126 MHz, $CDCl_3$, ppm): δ 169.7, 154.1, 153.7, 153.6, 129.4, 128.5, 96.5, 77.3, 77.0, 76.3, 74.2, 73.6, 69.3, 69.1, 66.7, 65.8, 64.9, 56.0, 55.9, 16.8, 16.7, 14.2. FTIR: 3270, 2990, 2970, 1750, 1455, 1375, 1255, 1090, 1025, 905, 870, 750 cm^{-1}. SEC (THF): M_n = 42.6 kDa, $Đ$ = 1.10. TGA in Ar: 316–379 °C, 95% mass loss. T_g = 60 °C.

2.3.3.2. Synthesis of $PDLLA_{290}$-*b*-$PDGC(COOH)_{20}$

A solution of $PDLLA_{290}$-*b*-$PDGC_{20}$ (600 mg, 0.21 mmol alkyne), 3-mercaptopropionic acid (2255 mg, 21 mmol), and 2,2-dimethoxy-2-phenylacetophenone (DMPA, 53.8 mg, 0.21 mmol) was prepared in anhydrous DMF (50 mL), deoxygenated under $N_{2(g)}$ for 30 min, and irradiated under UV light (365 nm) for 2 h. The reaction mixture was precipitated into diethyl ether twice and dissolved in DMF. The resulting copolymer solution was transferred to dialysis tubing (MWCO 6-8 kDa) and dialyzed against nanopure water at 4 °C for 3 d to remove DMF, excess thiol and photo-initiator. The solution was then lyophilized to give the anionic polymer as a white powder (620 mg, 93% yield). ^1H NMR (500 MHz, DMSO-d_6, ppm): δ 7.20 and 7.17 (AB_q, J = 8 Hz), 5.32 (br), 5.20–5.08 (m), 4.98 (br), 4.85 (br), 4.77 (br), 4.32 (br), 4.19 (br), 4.11 (br), 3.31 (br), 3.09 (br), 2.70 (br), 2.48 (br), 1.43 (m), 1.18 (br). ^{13}C NMR (126 MHz, DMSO-d_6, ppm): δ 172.9, 169.1, 153.8, 153.4, 153.2, 95.6, 68.9, 68.6, 66.3, 64.5, 62.9, 54.9, 43.8, 34.8, 34.6, 33.6, 27.3, 25.9, 16.4, 13.9. FTIR: 3670-3090, 2995, 2940, 2850, 1750, 1665, 1455, 1380, 1265, 1185, 1130, 1090, 1050, 920, 865, 760 cm^{-1}. TGA in Ar: 240–290 °C, 17% mass loss; 290–323 °C, 69% mass loss. T_g = 60 °C, 106 °C.

2.3.3.3. Synthesis of PDLLA$_{290}$-*b*-PDGC(His)$_{20}$

A solution of PDLLA$_{290}$-*b*-PDGC(COOH)$_{20}$ (326 mg, 0.22 mmol acid), HOBt (44 mg, 0.33 mmol), and HBTU (130 mg, 0.34 mmol) was prepared in dimethyl sulfoxide (DMSO, 2.50 mL) and stirred at ambient temperature for 0.5 h. Histamine (97 mg, 0.87 mmol) and *N*,*N*-diisopropylethylamine (DIPEA, 42 mg, 0.33 mmol) were dissolved in DMSO (0.50 mL), then added to the reaction mixture and stirred for 24 h. The solution was transferred to dialysis tubing (MWCO 6-8 kDa) and dialyzed against nanopure water at 4 °C for 3 d to remove excess histamine and coupling agents. The solution was then lyophilized to give the histamine-modified polymer, PDLLA$_{290}$-*b*-PDGC(His)$_{20}$, as a white powder (281 mg, 80% yield). ^{1}H NMR (500 MHz, DMSO-d_6, ppm): δ 8.06 (br), 7.40 (br), 7.20 and 7.17 (AB$_q$, J = 8 Hz), 5.33 (br), 5.20–5.08 (m), 4.99 (br), 4.86 (br), 4.78 (br), 4.34 (br), 4.19 (br), 4.11 (br), 3.99 (br), 3.31 (br), 3.08 (br), 2.77 (br), 2.72 (br), 2.48 (br), 2.32 (br), 1.44 (m), 1.19 (br). ^{13}C NMR (126 MHz, DMSO-d_6, ppm): δ 173.0, 169.2, 153.8, 153.5, 153.3, 134.6, 259.0, 68.9, 68.7, 64.5, 54.9, 43.8, 35.8, 34.6, 33.5, 27.9, 26.0, 16.5, 13.9. FTIR: 3670-3090, 2995, 2940, 2850, 1750, 1665, 1455, 1380, 1265, 1185, 1130, 1090, 1050, 920, 865, 760 cm^{-1}. TGA in Ar: 240–290 °C, 17% mass loss; 290–323 °C, 69% mass loss. T_g = 58 °C.

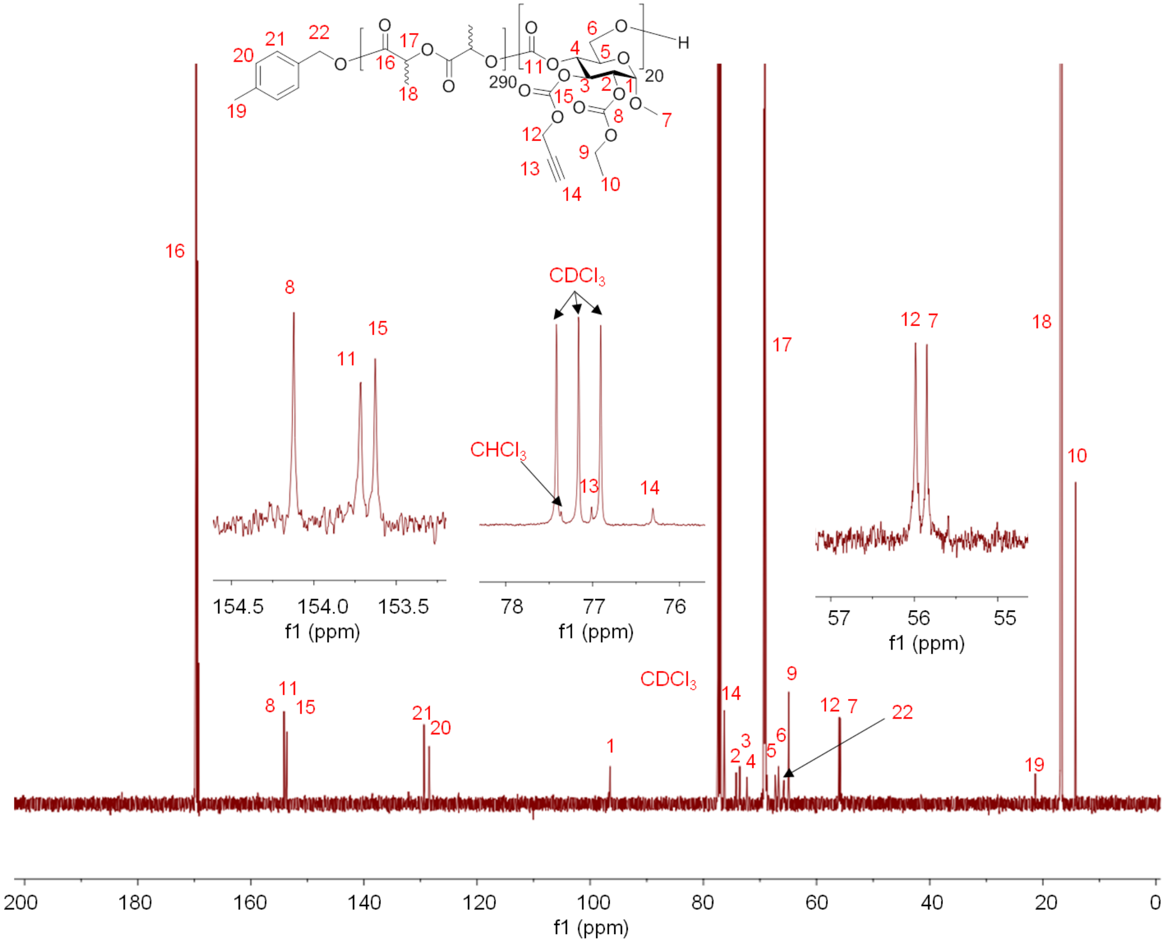

Figure 15. ^{13}C NMR spectrum (126 MHz) of PDLLA$_{290}$-*b*-PDGC$_{20}$ in CDCl$_3$. Reprinted with permission from "Co-assembly of sugar-based amphiphilic block polymers to achieve nanoparticles with tunable morphology, size, surface charge, and acid-responsive behavior" by Lin, Y.-N.; Su, L.; Smolen, J.; Li, R.; Song, Y.; Wang, H.; Dong, M.; Wooley, K. L., *Mater. Chem. Front.* **2018**, *2* (12), 2230-2238. Copyright 2018 The Royal Society of Chemistry.

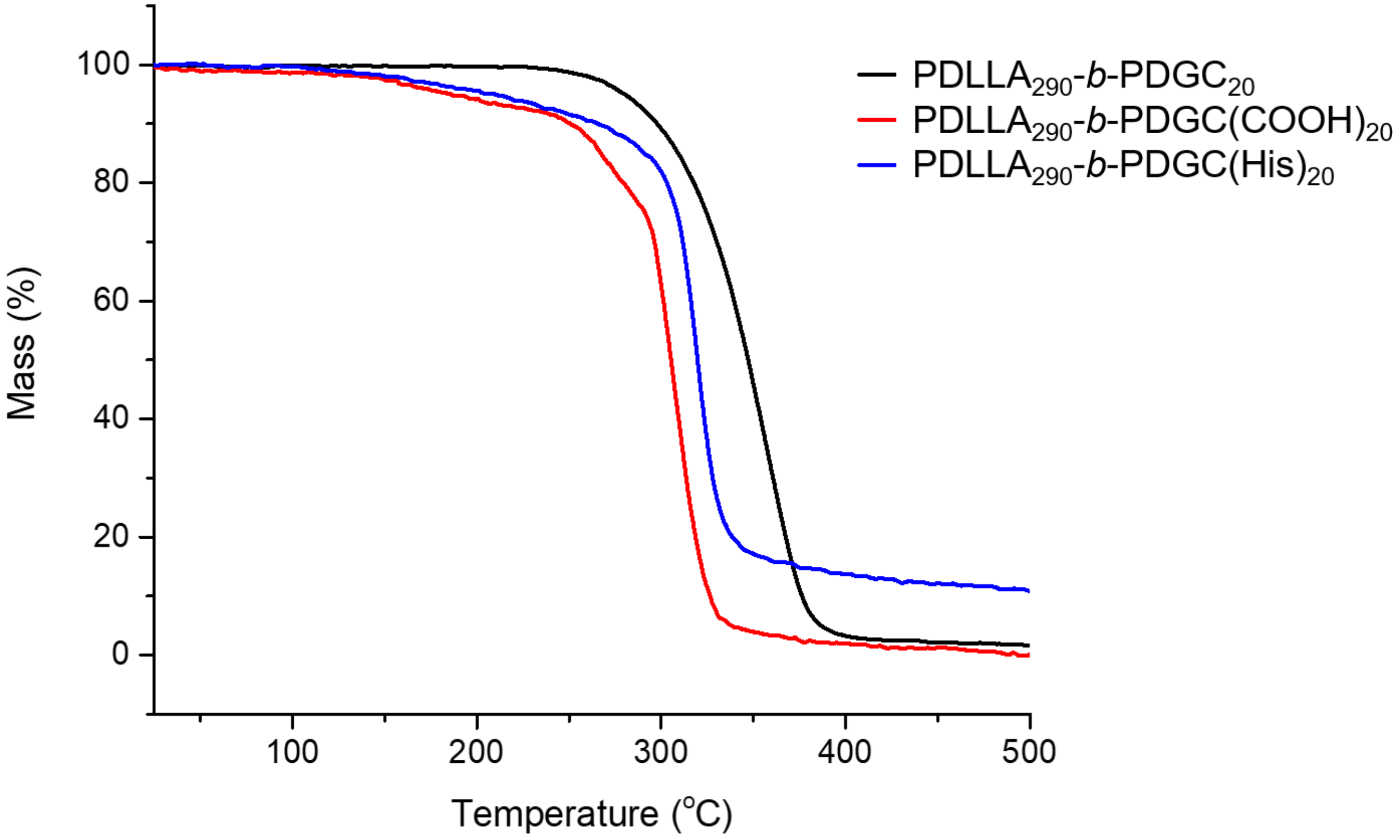

Figure 16. TGA traces of PDLLA$_{290}$-*b*-PDGC$_{20}$, PDLLA$_{290}$-*b*-PDGC(COOH)$_{20}$, and PDLLA$_{290}$-*b*-PDGC(His)$_{20}$. Reprinted with permission from "Co-assembly of sugar-based amphiphilic block polymers to achieve nanoparticles with tunable morphology, size, surface charge, and acid-responsive behavior" by Lin, Y.-N.; Su, L.; Smolen, J.; Li, R.; Song, Y.; Wang, H.; Dong, M.; Wooley, K. L., *Mater. Chem. Front.* **2018**, *2* (12), 2230-2238. Copyright 2018 The Royal Society of Chemistry.

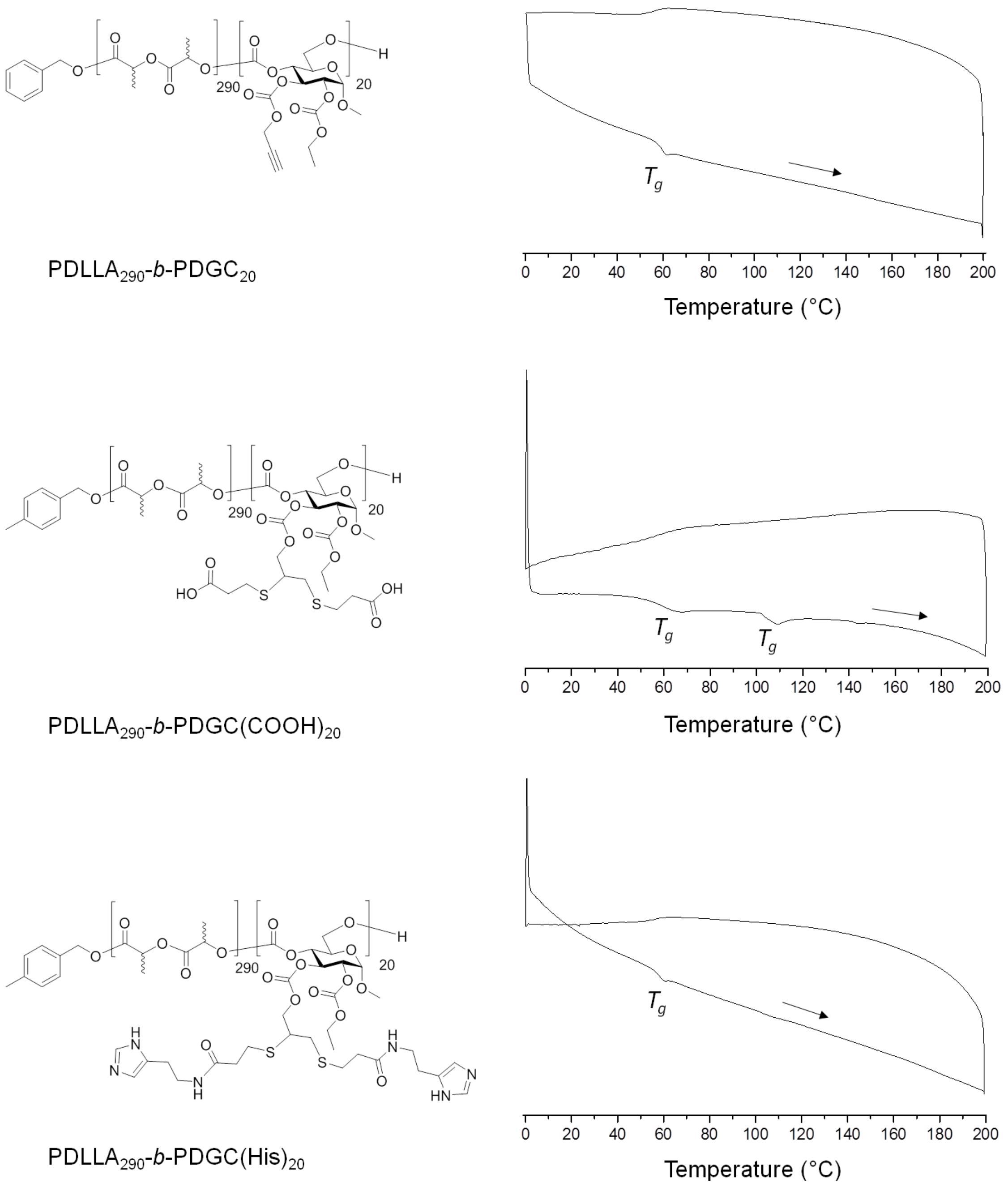

Figure 17. DSC curves for PDLLA$_{290}$-*b*-PDGC$_{20}$, PDLLA$_{290}$-*b*-PDGC(COOH)$_{20}$, and PDLLA$_{290}$-*b*-PDGC(His)$_{20}$. Glass transitions (T_g) are labeled on the thermograms. Arrows indicate the direction of temperature ramping. Reprinted with permission from "Co-assembly of sugar-based amphiphilic block polymers to achieve nanoparticles with tunable morphology, size, surface charge, and acid-responsive behavior" by Lin, Y.-N.; Su, L.; Smolen, J.; Li, R.; Song, Y.; Wang, H.; Dong, M.; Wooley, K. L., *Mater. Chem. Front.* **2018**, *2* (12), 2230-2238. Copyright 2018 The Royal Society of Chemistry.

2.3.4. Procedures

2.3.4.1. General procedure for co-assembly

$PDLLA_{290}$-*b*-$PDGC(COOH)_{20}$ and $PDLLA_{290}$-*b*-$PDGC(His)_{20}$ were assembled in aqueous solution at predetermined weight ratios using a nanoprecipitation method.[23, 29, 43] Briefly, the polymers (1 mg) were dissolved in acetone (500 µL), and then added drop-wise to aqueous solution (1 mL, nanopure water or MOPS buffer), followed by stirring in air for 24 h to allow evaporation of acetone. The final polymer concentration was adjusted to 1 mg/mL using nanopure water. The polymer assemblies were characterized in solution by dynamic light scattering (DLS) and zeta potential measurements, and in the dry state by transmission electron microscopy (TEM).

2.3.4.2. Evaluation of the pH-responsive behavior of the co-assemblies

Block copolymers (2 mg) were first dissolved in acetone (1 mL) with a predetermined polymer weight ratio, and then added drop-wise to nanopure water (2 mL) followed by stirring in air for 24 h. The polymer co-assemblies were transferred to dialysis tubing (MWCO 6-8 kDa) and dialyzed against 1x MOPS buffer (pH = 5.5 or 7.4) for 12 h, and the resulting structures were characterized by DLS, zeta potential measurements, and TEM.

2.4. Conclusions

In summary, polymer co-assembly has been shown to be a versatile approach to coincidentally tune the size, shape and surface charge of nanoscopic supramolecular assemblies in water, to optimize the stimuli-responsive properties of nanostructures. Sequential ring opening polymerizations of lactide and an alkynyl-bearing glucose-carbonate monomer afforded reactive block polymers that were conveniently transformed into amphiphilic derivatives having carboxylic acid or histamine side chain groups. Assembly and co-assembly of these block polymers yielded nanoparticles with highly tunable size, zeta potential, and pH-responsive behaviors, while bypassing tedious and time-consuming synthesis. The tailorability derived from co-assembly enables the facile optimization of nanomaterials for different biomedical applications. This work represents a fundamental advance in the design and preparation of glucose-derived acid-responsive amphiphilic block polymeric materials, with potential for these constructs to be useful in a broad range of drug delivery applications. For instance, it is anticipated that the acid-induced swelling of the assemblies will facilitate acid-triggered drug release in endolysosomal environments (pH 4.5–6.5). Ongoing studies are determining the fundamental behaviors of these co-assembled polymer mixtures *in vitro*, with an aim to pursue practical strategies for their utilization in biomedical applications.

3. ERYTHROCYTE MEMBRANE-CAMOUFLAGED NANOCARRIERS WITH TUNABLE PACLITAXEL RELEASE KINETICS *VIA* MACROMOLECULAR STEREOCOMPLEXATION[¥]

3.1. Introduction

Cell-membrane-camouflaged polymeric nanocarriers (MCNs) combine advantages related to the functional diversity of natural cell membranes and the physicochemical tailorability of synthetic polymers.[65-68] Many studies have focused on utilizing diverse cell-derived membranes to functionalize nanocarrier surfaces, leading to biomimetic nanocarriers with different surface properties toward various applications, including drug delivery,[69] vaccination,[70] toxin neutralization,[71-73] anti-inflammatory agents,[74] photothermal therapy,[75] and cancer immunotherapy.[76-78] Erythrocyte (red blood cell, RBC)-membrane-camouflaged nanoparticles (RBC-MCNs) have been shown to decrease protein adsorption, reduce immune response, and prolong blood circulation times, compared to uncloaked nanoparticle counterparts.[65, 79]

Controlling cargo release kinetics is essential for the optimization of MCNs toward various applications. Tuning cargo release kinetics is particularly crucial for drug delivery to maintain optimal drug concentration duration, reduce side-effects, and improve therapeutic efficacy.[1] Altering core compositions of the nanocarrier can influence drug release kinetics, [3-4, 80] yet many tailor-made materials have unknown toxicity profiles in humans, increasing the

---

[¥] Reprinted (adapted) with permission from “Erythrocyte-Membrane-Camouflaged Nanocarriers with Tunable Paclitaxel Release Kinetics *via* Macromolecular Stereocomplexation” by Lin, Y.-N.; Elsabahy, M.; Khan, S.; Zhang, F.; Song, Y.; Dong, M.; Li, R.; Smolen, J.; Letteri, R. A.; Su, L.; Wooley, K. L., *ACS Mater. Lett.* **2020,** *2*, 595-601. Copyright 2020 American Chemical Society.

uncertainty for clinical translation of the resulting MCNs. Expanding control over the drug release kinetics for MCNs using biocompatible materials is, therefore, desirable.

Non-covalent polylactide (PLA) stereocomplex interactions can provide a versatile strategy to tune the drug release kinetics, while the surface chemistry is also important in the overall characteristics and performance of MCNs as drug delivery devices. PLA homopolymer, a biocompatible and biodegradable aliphatic polyester, has been FDA-approved as a medical implant material for anchors, screws, plates, pins, rods, and meshes. [81-82] Physical blending of isotactic and enantiomeric poly(d-lactide) (PDLA) and poly(l-lactide) (PLLA) forms regular stereocomplexes with increased crystallinity, leading to higher melting transition temperatures and greater mechanical strength, compared to the isotactic counterparts.[83-85] PLA crystalline domains are analogous to non-covalent cross-linking within a polymer matrix. Core cross-linked polymer nanoconstructs reduce drug release rates by hindering drug diffusion.[86-87] Tuning drug release kinetics with PLA stereocomplexation has been reported in PEG–PLA platforms for drugs, such as doxorubicin,[88] camptothecin,[89] and rifampin.[90-91] However, with replacement of PEG by a RBC-membrane-based coating material, MCNs outperformed PEGylated counterparts in recent literature, with double blood circulation half-life.[65, 79] MCNs also offer diverse biointerfaces by employing different biological membrane components, beyond those found on RBCs, to exhibit affinities to various biological targets that range from toxins,[71] to damaged vasculature,[92] to cancer cells,[75] and to microbes.[92] In contrast, installing such a variety of biomimetic moieties onto a PEGylated surface could be a costly and labor-intensive process. Furthermore, PEGylated nanoparticles (NPs) can elicit an immune response, leading to accelerated blood clearance with repeated administrations.[93-94] The present study combines these two concepts and provides a facile fabrication method for MCNs with tunable drug release kinetics via internal macromolecular stereostructure using biocompatible amorphous, crystalline, and stereocomplexed PLA materials and external surface chemistry derived from RBC membranes (Scheme 2).

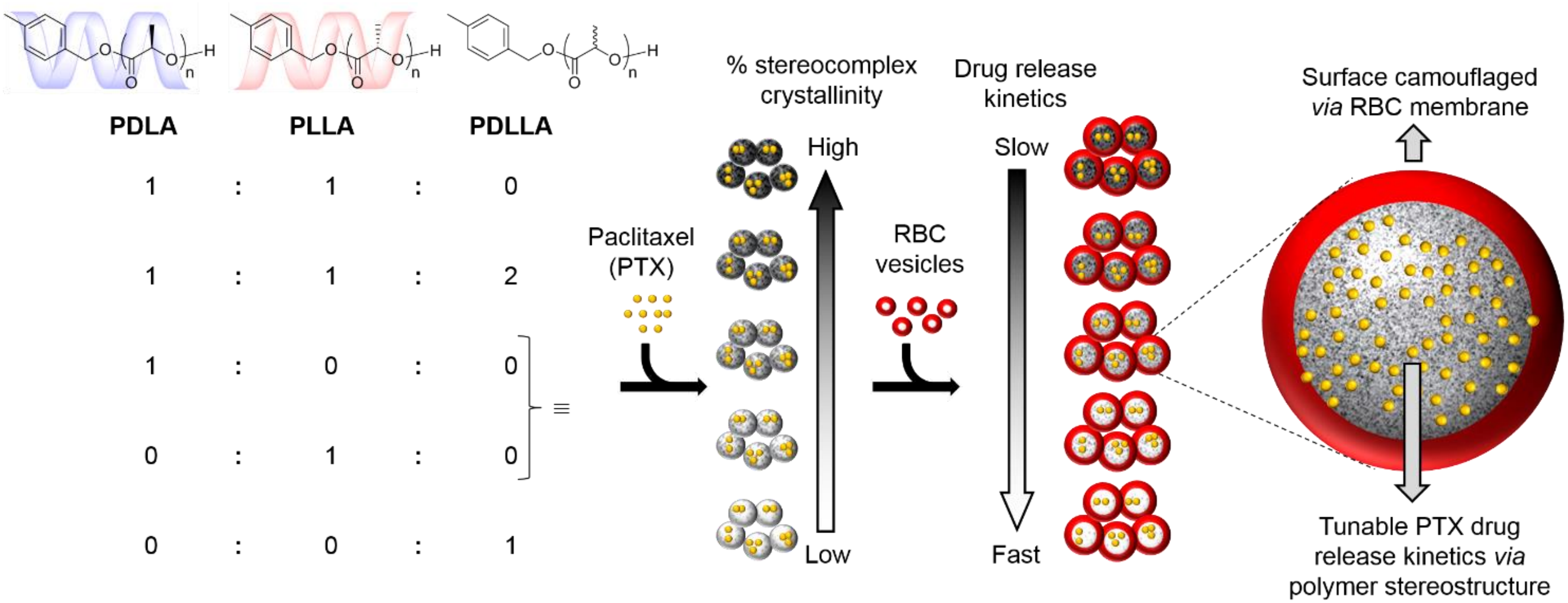

Scheme 2. Design of the RBC membrane-camouflaged nanocarriers with tunable drug release kinetics. Reprinted with permission from "Erythrocyte-Membrane-Camouflaged Nanocarriers with Tunable Paclitaxel Release Kinetics *via* Macromolecular Stereocomplexation" by Lin, Y.-N.; Elsabahy, M.; Khan, S.; Zhang, F.; Song, Y.; Dong, M.; Li, R.; Smolen, J.; Letteri, R. A.; Su, L.; Wooley, K. L., *ACS Mater. Lett.* **2020**, *2*, 595-601. Copyright 2020 American Chemical Society.

3.2. Results and Discussions

Isotactic PDLA, PLLA, and atactic PDLLA were synthesized via organocatalyzed ring-opening polymerizations (ROP) of cyclic lactide (d-lactide, l-lactide, and dl-lactide, respectively) at −78 °C in dichloromethane (DCM) with 4-methylbenzyl alcohol as the initiator and 1,5,7-triazabicyclo[4.4.0]dec-5-ene (TBD) as the organocatalyst. The structures of PLAs were confirmed by ^{1}H NMR (Figure 18), ^{13}C NMR (Figure 19, Figure 20, and Figure 21), and FT-IR (Figure 22) spectroscopies, and the thermal properties were evaluated by thermogravimetric analysis (TGA, Figure 23). Size exclusion chromatography (SEC) indicated a monomodal molar mass distribution with low dispersity ($Đ < 1.1$) of each polymer, demonstrating the well-defined structures (Figure 24). The number-averaged molar mass (M_n) of the polymers and degrees of polymerization (DP_n) were calculated from the ^{1}H NMR spectra (Figure 18), acquired after isolation of the polymer samples by precipitation. For each, comparison of the integral of the methyl protons originating from the initiator at 2.35 ppm with that of methyl groups from the repeating units at 1.58 ppm allowed for calculation of the DP_n, which was then converted to a value of M_n by multiplying the molar mass of the repeat unit (144 Da) by the DP_n and adding the molar mass of the chain ends. The resulting polymers showed comparable M_n (8.4 kDa for PDLA, 8.2 kDa for PLLA, and 8.9 kDa for PDLLA), thus minimizing the effects of molar mass variations in the study.

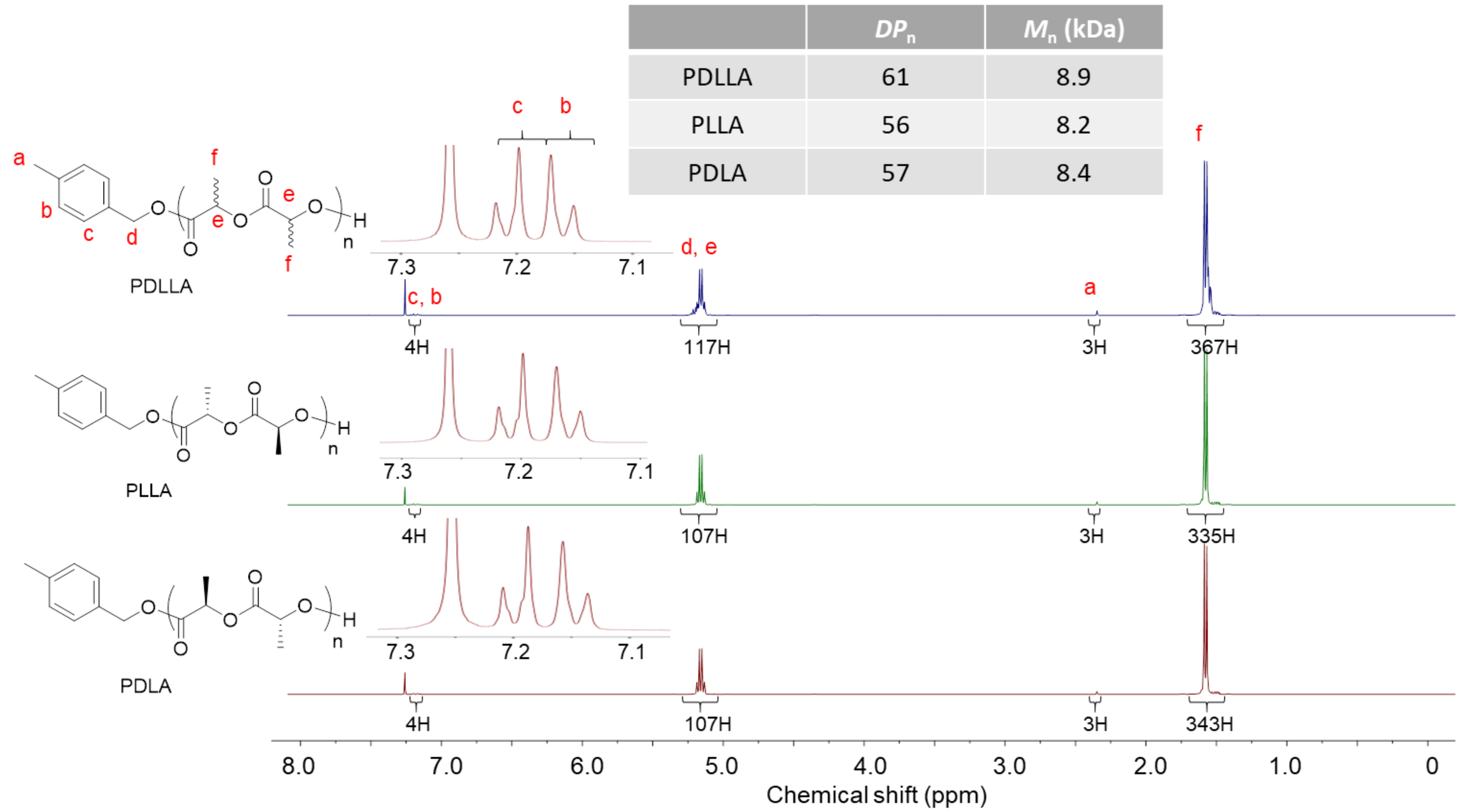

	DP_n	M_n (kDa)
PDLLA	61	8.9
PLLA	56	8.2
PDLA	57	8.4

Figure 18. ^{1}H NMR spectra (500 MHz) of PDLLA, PLLA, PDLA (descending order) in $CDCl_3$, with the inset expanding the region to show the resonance signals for the aromatic protons of the α-chain end. Reprinted with permission from “Erythrocyte-Membrane-Camouflaged Nanocarriers with Tunable Paclitaxel Release Kinetics *via* Macromolecular Stereocomplexation” by Lin, Y.-N.; Elsabahy, M.; Khan, S.; Zhang, F.; Song, Y.; Dong, M.; Li, R.; Smolen, J.; Letteri, R. A.; Su, L.; Wooley, K. L., *ACS Mater. Lett.* **2020,** *2*, 595-601. Copyright 2020 American Chemical Society.

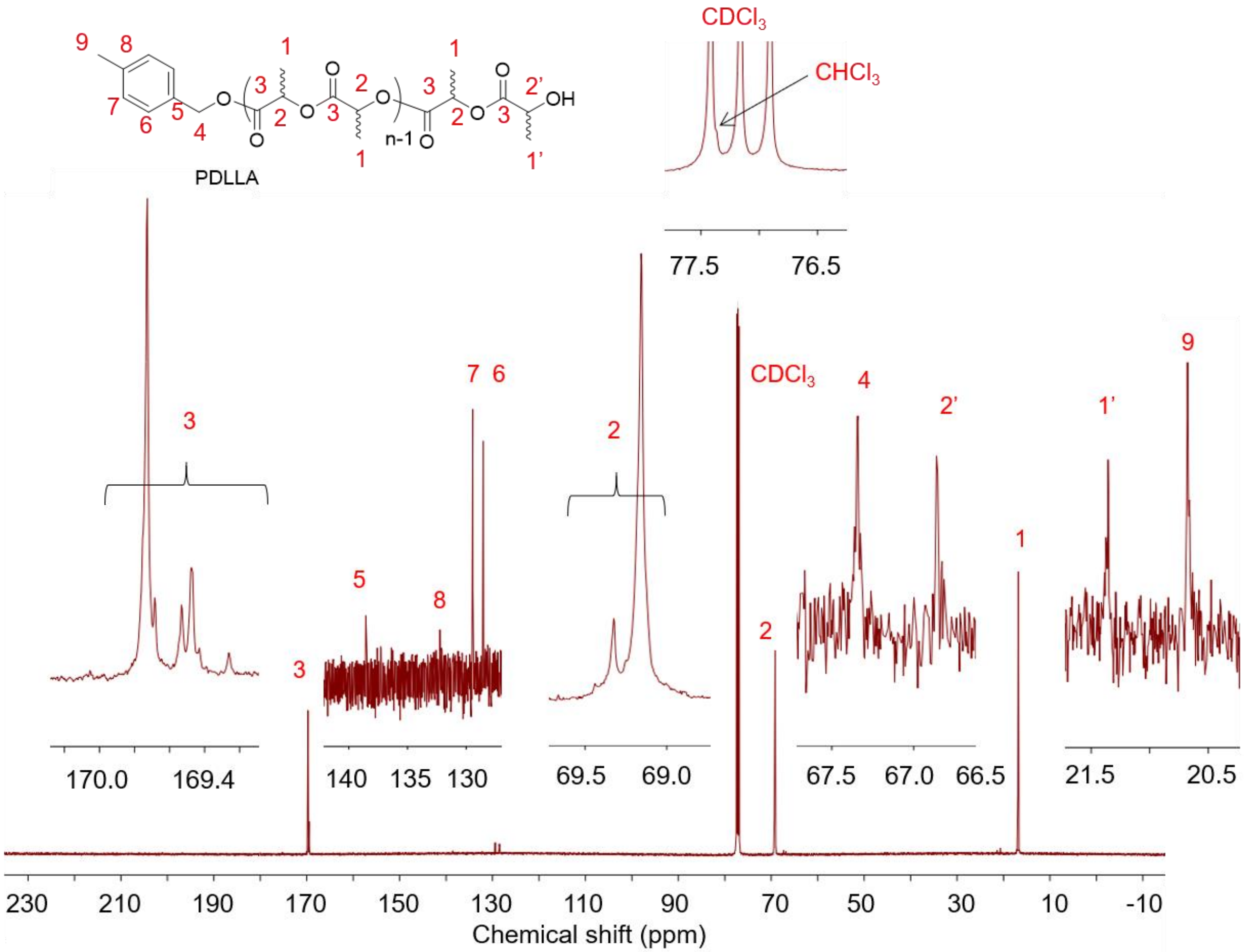

Figure 19. ^{13}C NMR spectrum (126 MHz, $CDCl_3$) of PDLLA. Reprinted with permission from "Erythrocyte-Membrane-Camouflaged Nanocarriers with Tunable Paclitaxel Release Kinetics *via* Macromolecular Stereocomplexation" by Lin, Y.-N.; Elsabahy, M.; Khan, S.; Zhang, F.; Song, Y.; Dong, M.; Li, R.; Smolen, J.; Letteri, R. A.; Su, L.; Wooley, K. L., *ACS Mater. Lett.* **2020,** *2*, 595-601. Copyright 2020 American Chemical Society.

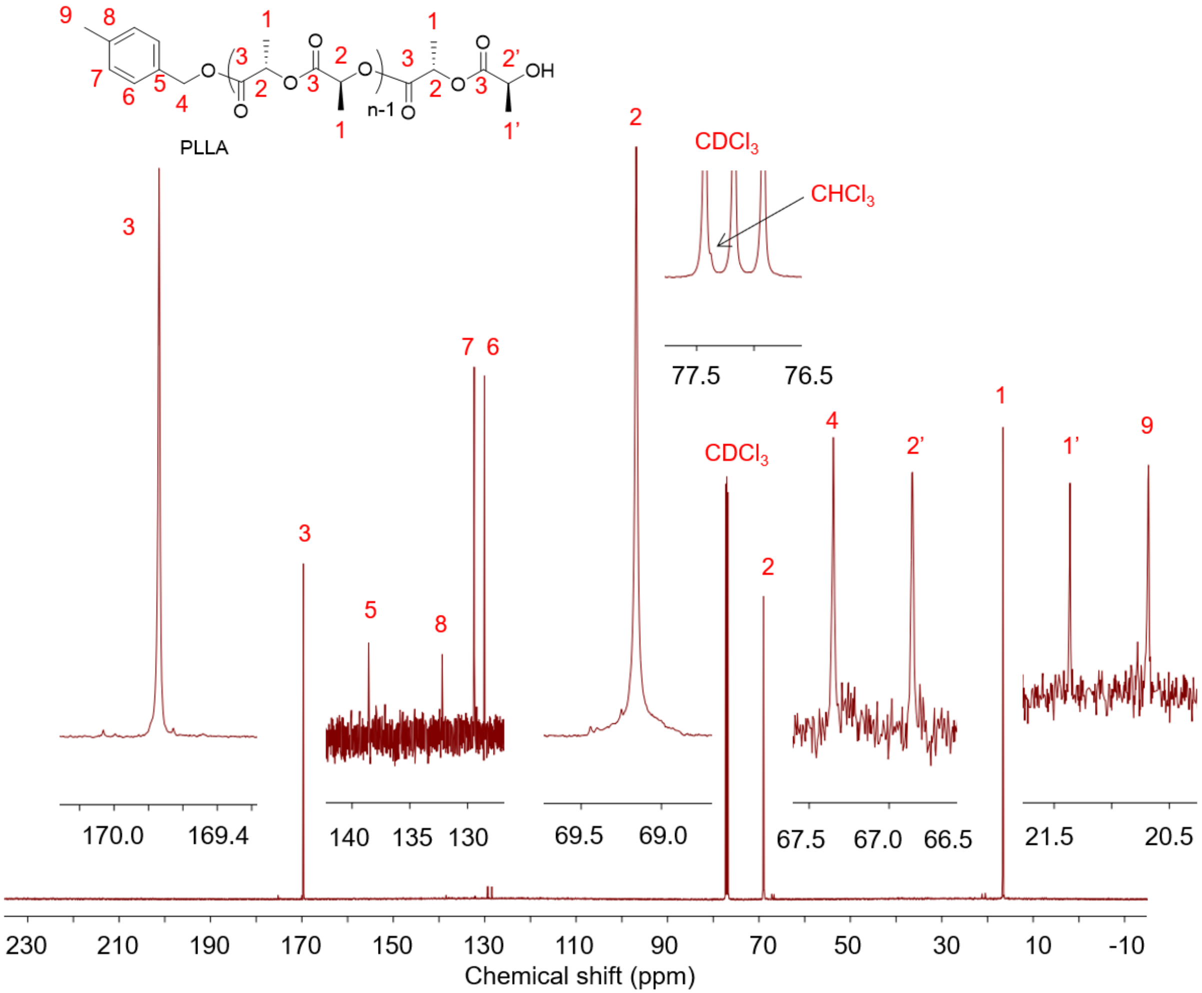

Figure 20. ^{13}C NMR spectrum (126 MHz, $CDCl_3$) of PLLA. Reprinted with permission from "Erythrocyte-Membrane-Camouflaged Nanocarriers with Tunable Paclitaxel Release Kinetics *via* Macromolecular Stereocomplexation" by Lin, Y.-N.; Elsabahy, M.; Khan, S.; Zhang, F.; Song, Y.; Dong, M.; Li, R.; Smolen, J.; Letteri, R. A.; Su, L.; Wooley, K. L., *ACS Mater. Lett.* **2020,** *2*, 595-601. Copyright 2020 American Chemical Society.

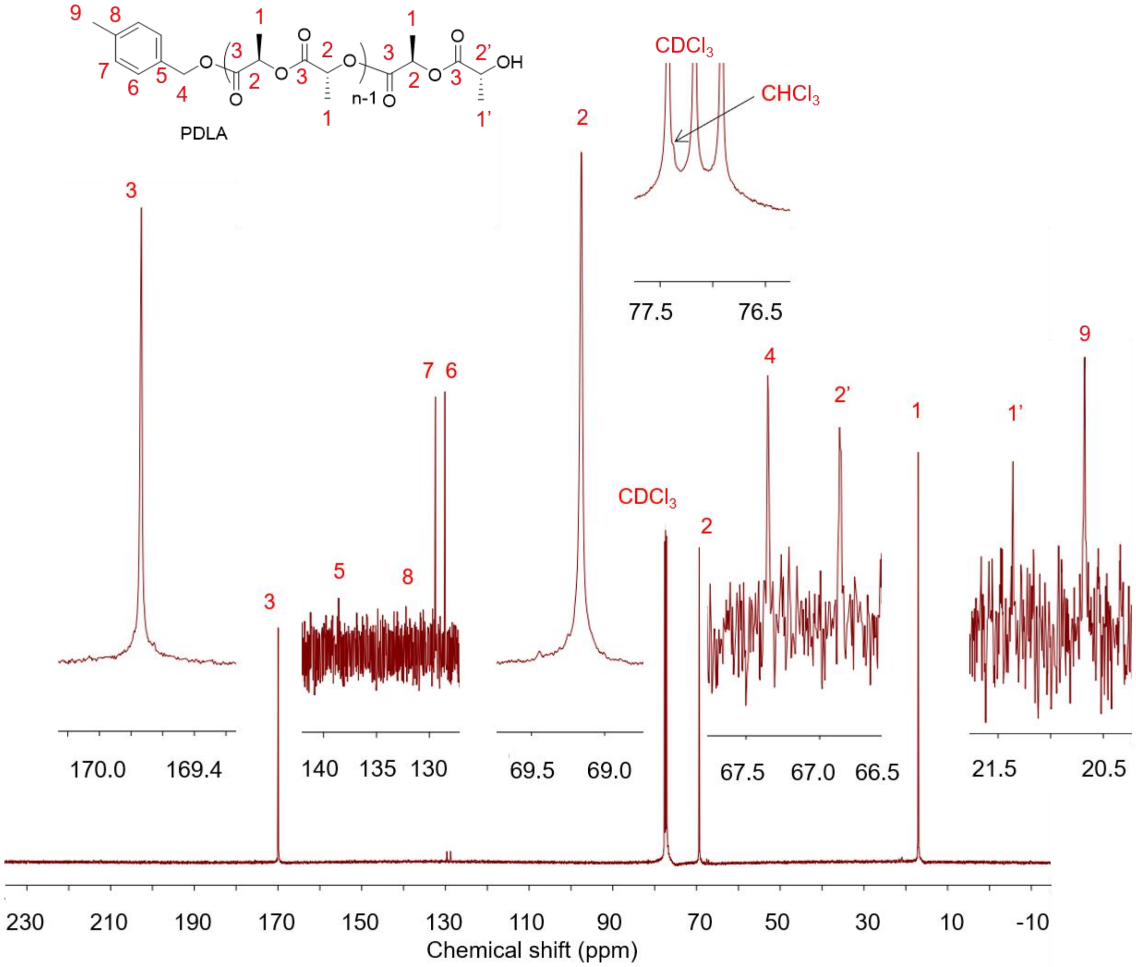

Figure 21. ^{13}C NMR spectrum (126 MHz, CDCl$_3$) of PDLA. Reprinted with permission from "Erythrocyte-Membrane-Camouflaged Nanocarriers with Tunable Paclitaxel Release Kinetics *via* Macromolecular Stereocomplexation" by Lin, Y.-N.; Elsabahy, M.; Khan, S.; Zhang, F.; Song, Y.; Dong, M.; Li, R.; Smolen, J.; Letteri, R. A.; Su, L.; Wooley, K. L., *ACS Mater*. *Lett.* **2020,** *2*, 595-601. Copyright 2020 American Chemical Society.

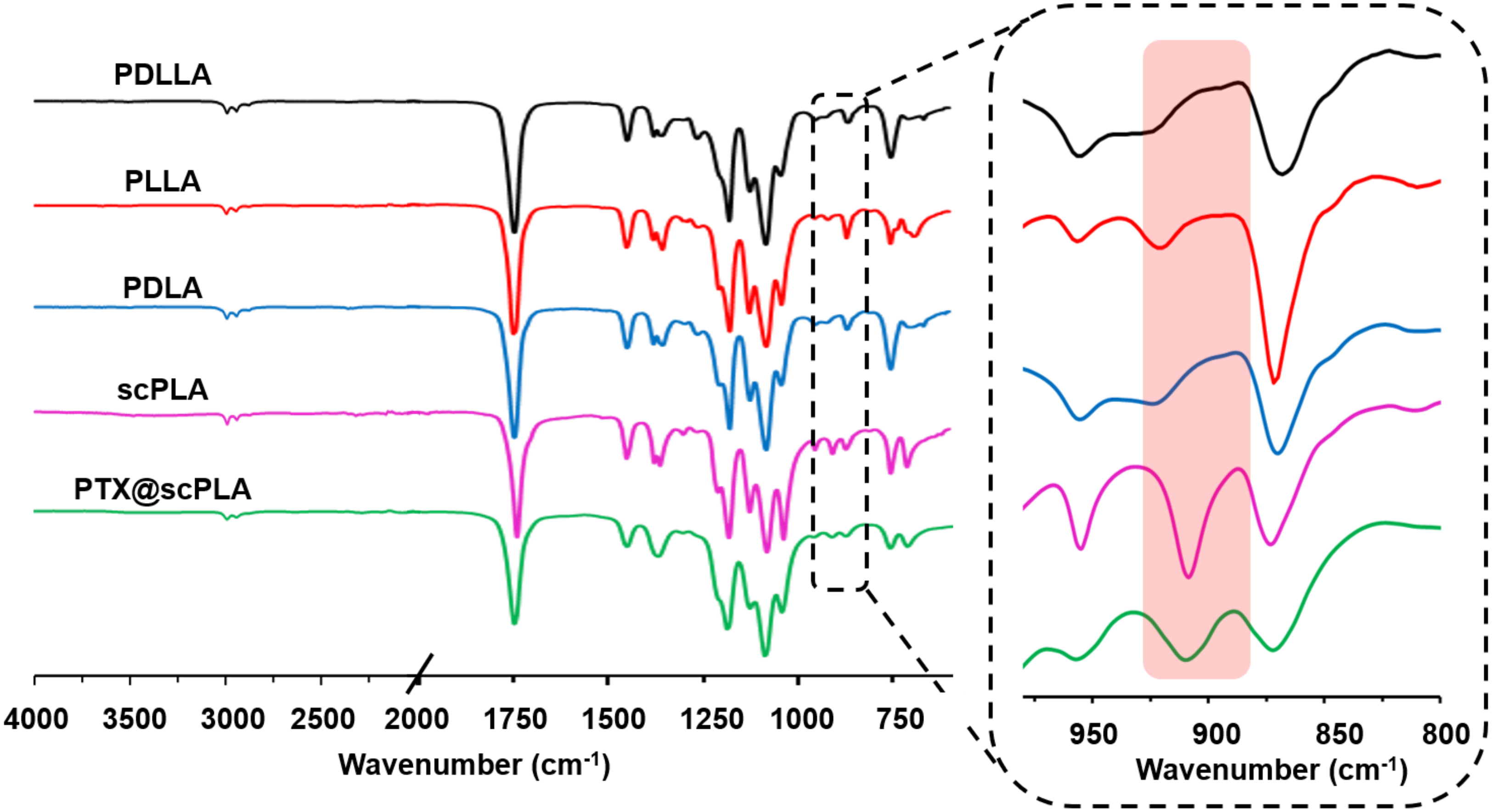

Figure 22. FTIR spectra of lyophilized PDLLA, PLLA, PDLA, and stereocomplex PLA nanoconstructs (descending order). The highlight of the expanding region shows the characteristic band of the PLA stereocomplex (β crystals) at 908 cm^{-1}.[95] Reprinted (adapted) with permission from "Erythrocyte-Membrane-Camouflaged Nanocarriers with Tunable Paclitaxel Release Kinetics *via* Macromolecular Stereocomplexation" by Lin, Y.-N.; Elsabahy, M.; Khan, S.; Zhang, F.; Song, Y.; Dong, M.; Li, R.; Smolen, J.; Letteri, R. A.; Su, L.; Wooley, K. L., *ACS Mater. Lett.* **2020,** *2*, 595-601. Copyright 2020 American Chemical Society.

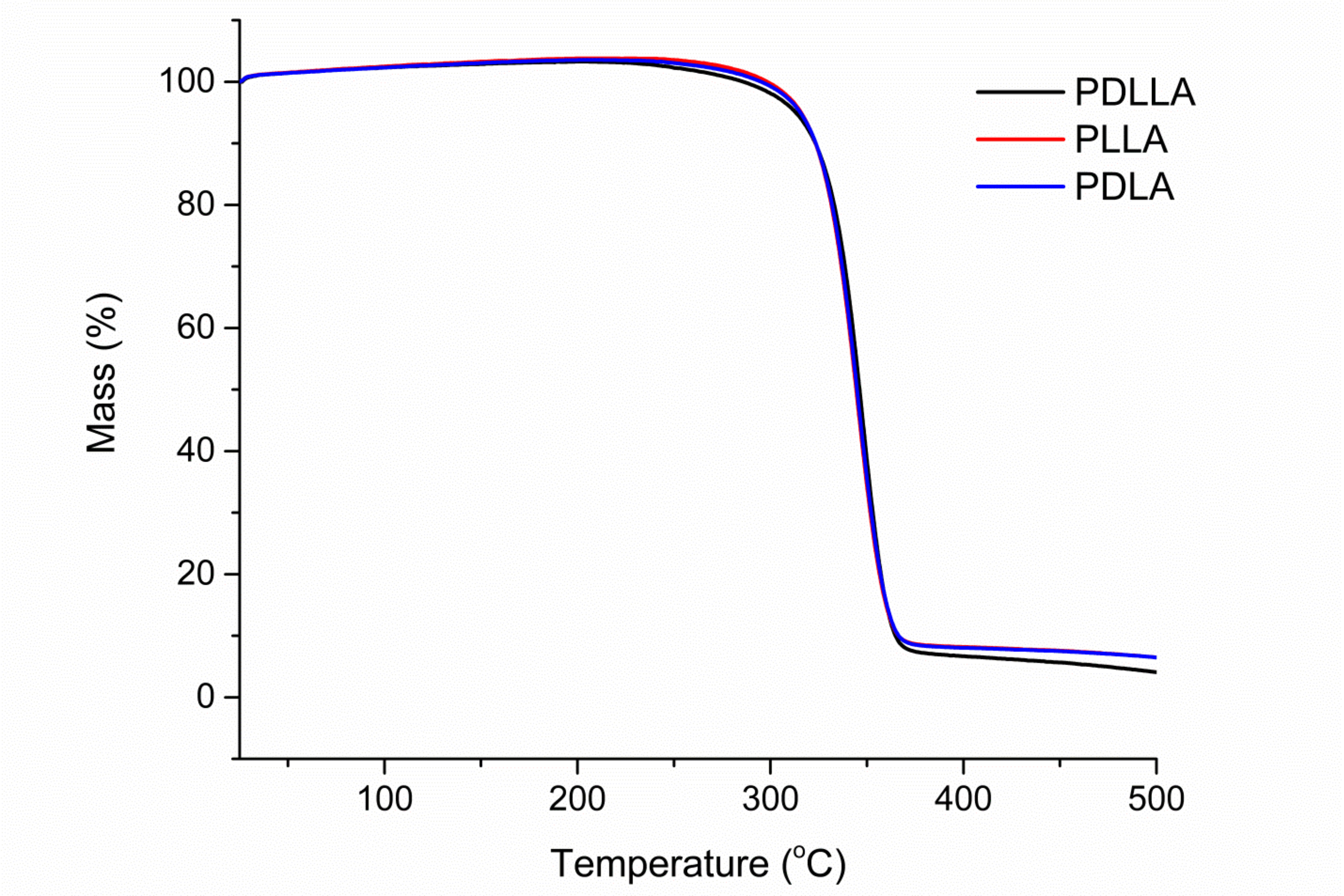

Figure 23. TGA traces of PDLLA, PLLA, and PDLA. Reprinted with permission from "Erythrocyte-Membrane-Camouflaged Nanocarriers with Tunable Paclitaxel Release Kinetics *via* Macromolecular Stereocomplexation" by Lin, Y.-N.; Elsabahy, M.; Khan, S.; Zhang, F.; Song, Y.; Dong, M.; Li, R.; Smolen, J.; Letteri, R. A.; Su, L.; Wooley, K. L., *ACS Mater*. *Lett.* **2020,** *2*, 595-601. Copyright 2020 American Chemical Society.

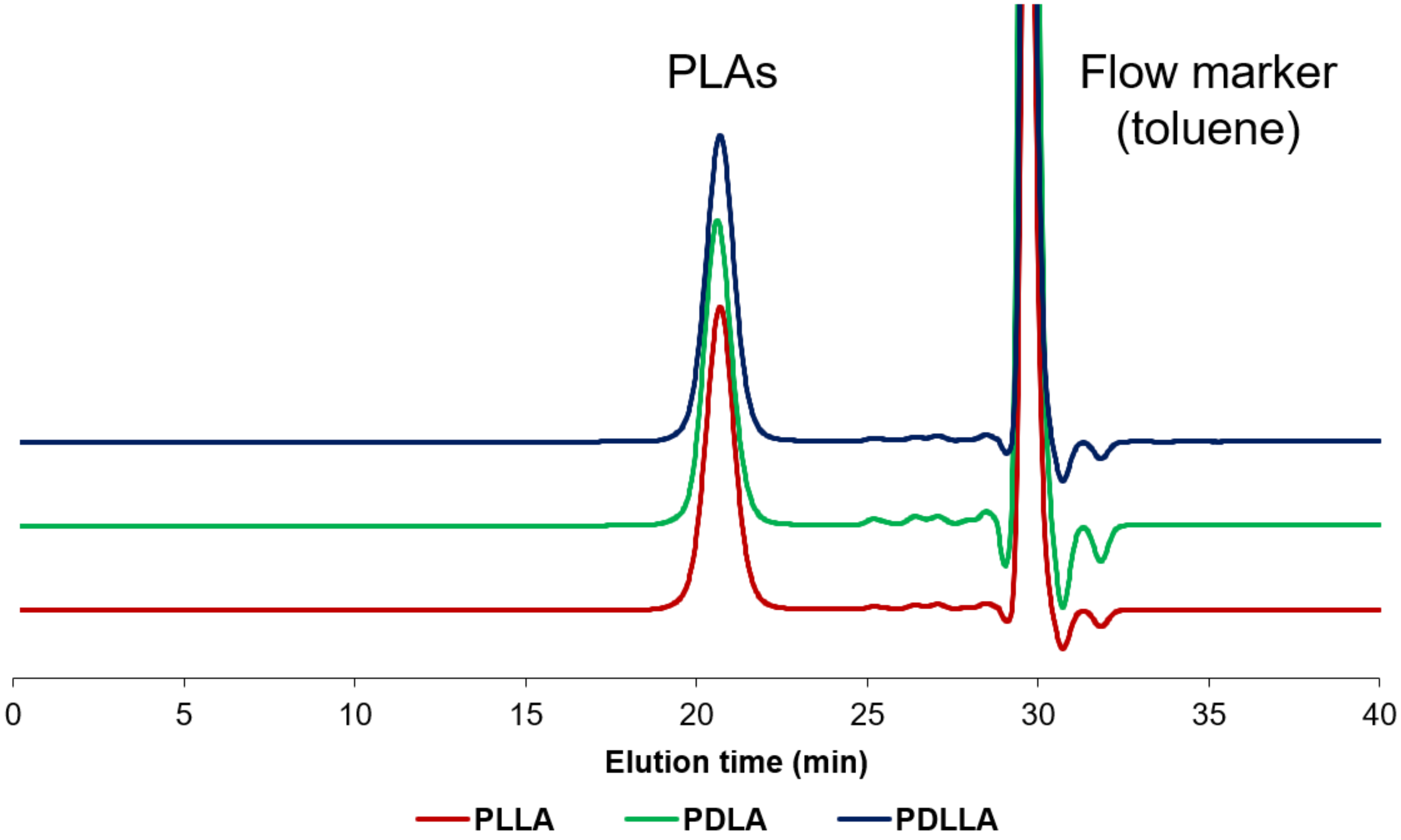

Figure 24. SEC traces of PDLLA, PDLA, and PLLA (descending order) in THF. Reprinted with permission from "Erythrocyte-Membrane-Camouflaged Nanocarriers with Tunable Paclitaxel Release Kinetics *via* Macromolecular Stereocomplexation" by Lin, Y.-N.; Elsabahy, M.; Khan, S.; Zhang, F.; Song, Y.; Dong, M.; Li, R.; Smolen, J.; Letteri, R. A.; Su, L.; Wooley, K. L., *ACS Mater. Lett.* **2020,** *2*, 595-601. Copyright 2020 American Chemical Society.

A series of PLA NPs with varying degrees of stereocomplexation was fabricated through a nanoprecipitation strategy. Briefly, a PLA solution with a predetermined enantiomeric ratio of PDLA vs PLLA vs PDLLA in THF (1 mg/mL) was added dropwise (6 mL/h) into nanopure water under stirring (300 rpm) via a syringe pump. The 100% stereocomplexed PLA (scPLA) NPs contained a 1:1 mass ratio of PDLA and PLLA, whereas 50% stereocomplexed PLA (50%scPLA) NPs contained a 1:1:2 mass ratio of PDLA:PLLA:PDLLA (Table 1). NPs containing neat crystalline PDLA or PLLA and amorphous PDLLA were also prepared. Similarly, the same procedure was conducted for each of the five polymer stereostructure formulations, with PTX (at 5 and 10 wt %) added to the THF solution prior to nanoprecipitation into water. It is noteworthy that the rather low initial THF-to-water volume ratio (1:10) and the fast stirring rate ensured the formation of well-defined nanoscale stereocomplexes.[96] The final polymer concentration was subsequently adjusted to 0.5 mg/mL with nitrogen-flow-promoted evaporation. The resulting PLA NPs were similar in size regardless of the core stereostructures, with the number-average hydrodynamic diameter ($D_{\mathrm{h(number)}}$) ranging from 70 to 90 nm for the neat polymer samples (Figure 25), and slightly larger sizes with PTX loading (*vide infra*).

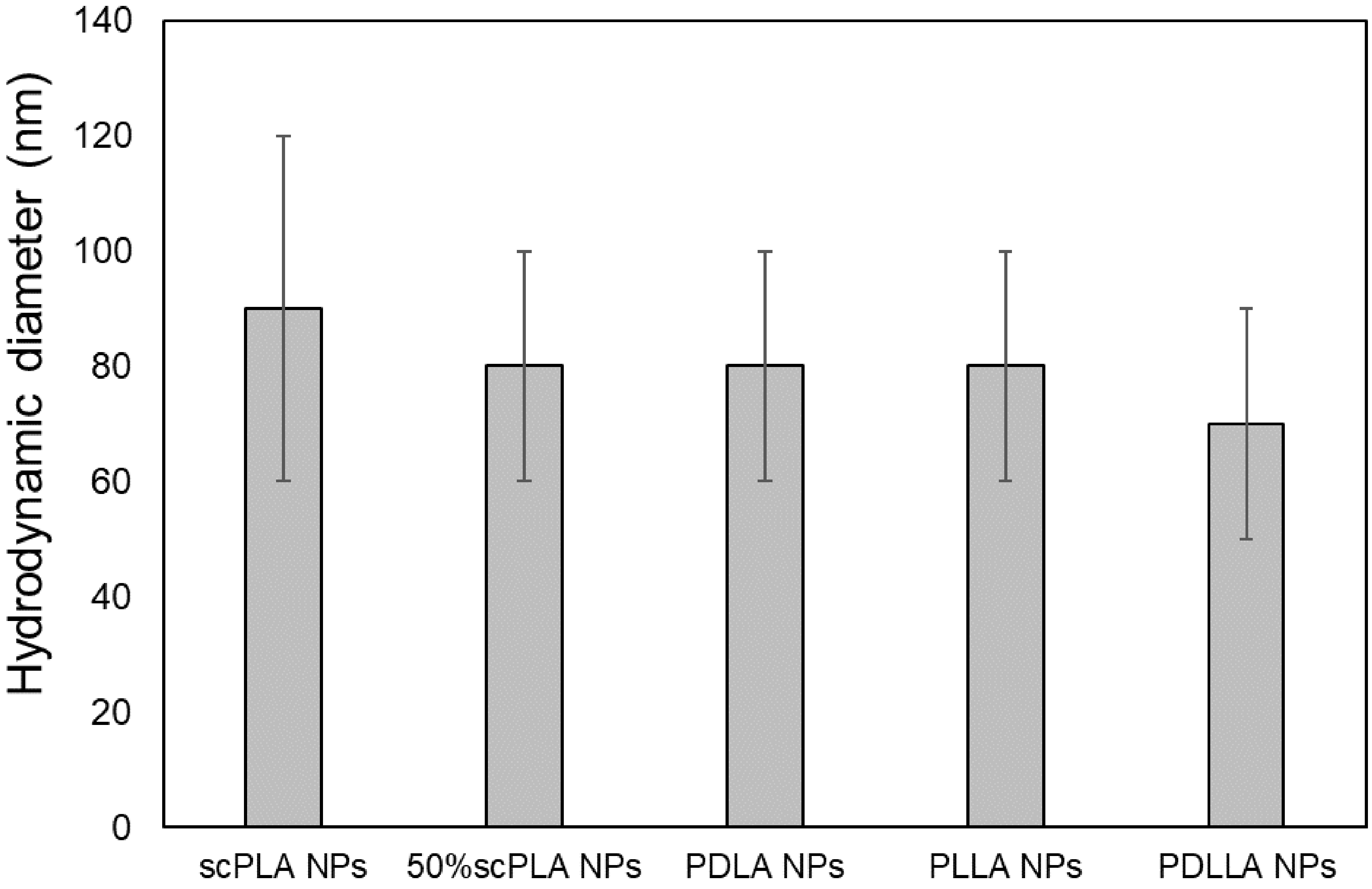

Figure 25. Hydrodynamic diameters of PLA assemblies prepared in nanopure water at different PLLA:PDLA:PDLLA mass ratios – scPLA NPs (1:1:0), 50%scPLA NPs (1:1:2), PDLA NPs (0:1:0), PLLA NPs (1:0:0), and PDLLA NPs (0:0:1). Reprinted with permission from "Erythrocyte-Membrane-Camouflaged Nanocarriers with Tunable Paclitaxel Release Kinetics *via* Macromolecular Stereocomplexation" by Lin, Y.-N.; Elsabahy, M.; Khan, S.; Zhang, F.; Song, Y.; Dong, M.; Li, R.; Smolen, J.; Letteri, R. A.; Su, L.; Wooley, K. L., *ACS Mater. Lett.* **2020,** *2*, 595-601. Copyright 2020 American Chemical Society.

Table 1. Theoretical compositions of different nanoconstructs (in the mass ratio) *via* co-assembly of PLLA, PDLA, and PDLLA with or without PTX. Reprinted with permission from "Erythrocyte-Membrane-Camouflaged Nanocarriers with Tunable Paclitaxel Release Kinetics *via* Macromolecular Stereocomplexation" by Lin, Y.-N.; Elsabahy, M.; Khan, S.; Zhang, F.; Song, Y.; Dong, M.; Li, R.; Smolen, J.; Letteri, R. A.; Su, L.; Wooley, K. L., *ACS Mater. Lett.* **2020,** *2*, 595-601. Copyright 2020 American Chemical Society.

Samples	**PTX (mass ratio)**	**PLLA (mass ratio)**	**PDLA (mass ratio)**	**PDLLA (mass ratio)**
scPLA	0.00%	50.00%	50.00%	0.00%
50%scPLA	0.00%	25.00%	25.00%	50.00%
PDLA	0.00%	0.00%	100.00%	0.00%
PLLA	0.00%	100.00%	0.00%	0.00%
PDLLA	0.00%	0.00%	0.00%	100.00%
10% PTX-scPLA	10.00%	45.00%	45.00%	0.00%
10% PTX-50%scPLA	10.00%	22.50%	22.50%	45.00%
10% PTX-PDLA	10.00%	0.00%	90.00%	0.00%
10% PTX-PLLA	10.00%	90.00%	0.00%	0.00%
10% PTX-PDLLA	10.00%	0.00%	0.00%	90.00%
5% PTX-scPLA	5.00%	47.50%	47.50%	0.00%
5% PTX-50%scPLA	5.00%	23.75%	23.75%	47.50%
5% PTX-PDLA	5.00%	0.00%	95.00%	0.00%
5% PTX-PLLA	5.00%	95.00%	0.00%	0.00%
5% PTX-PDLLA	5.00%	0.00%	0.00%	95.00%

The nature of the PLA as stereocomplexed, crystalline, and/or amorphous structures was confirmed by wide-angle powder X-ray diffraction (WAXD) and Fourier transform infrared (FT-IR) analyses of the lyophilized PLA NPs as a function of the PLA stereochemistries employed during the nanoprecipitation process (Figure 26 and Figure 22). As depicted in Figure 26, atactic PDLLA assemblies did not exhibit distinct diffraction patterns, indicating no significant crystalline domains, as expected for an amorphous structure. Isotactic PDLA and PLLA NPs showed identical diffraction patterns ($2\theta = 15$, 17, 19, and 22.5°), revealing similar crystal packing within the polymer matrix. Stereocomplexed PLA co-assemblies showed differences in X-ray diffraction patterns ($2\theta = 12$, 21, and 24°) compared to those of the isotactic NPs, suggesting changes in crystal structures and formation of PLA stereocomplex equilateral-triangle-shaped crystals.[97-99] PLA stereocomplex formation was further evidenced by FT-IR, with the appearance of the characteristic peak at 908 cm^{-1} (Figure 22).[95]

Colloidal stability upon drug (paclitaxel, PTX) loading was further investigated in both nanopure water and phosphate-buffered saline (PBS, pH 7.4), since the additional hydrophobicity introduced by PTX could have resulted in secondary aggregation or precipitation. Upon loading hydrophobic PTX (5 wt %, 67–86% loading efficiency as measured by HPLC, Table 1), colloidally stable (>1 week) PTX-loaded PLA NPs were obtained with dry-state average diameters (Dav) ranging from 63 to 69 nm, as measured by transmission electron microscopy (TEM), and $D_{h(\text{number})}$ of 110–130 nm, according to DLS, independent of the PLA stereochemistry (Figure 25). However, PTX-loaded bare PLA NPs immediately precipitated in PBS (Figure 26c), and bare PLA NPs were known to be extensively endocytosed by monocytes in plasma,[100] suggesting bare PLA NPs alone cannot serve as drug nanocarriers.

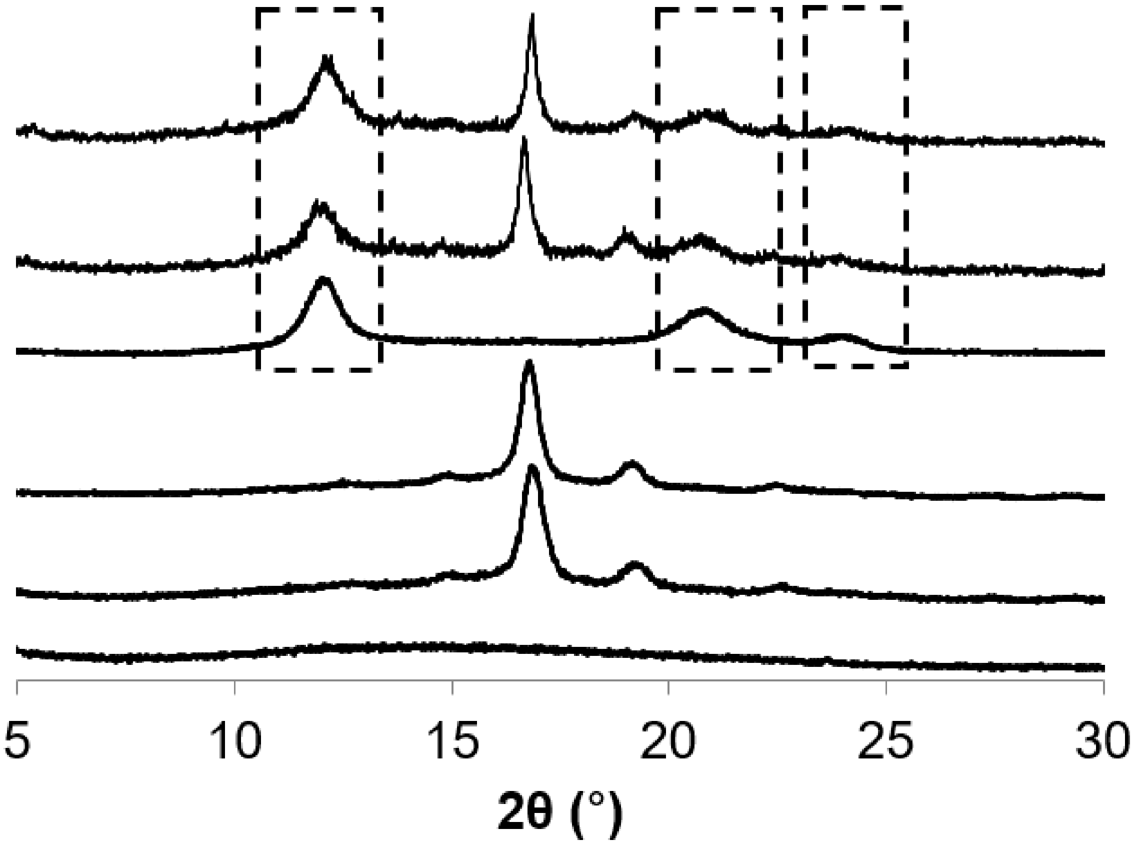

Figure 26. Wide-angle X-ray diffraction of the lyophilized PTX-loaded and empty PLA NPs, indicating partial retention of stereocomplexation upon PTX loading. From top to bottom: 10 *wt*% PTX-loaded scPLA, 5 *wt*% PTX-loaded scPLA, scPLA, PDLA, PLLA, PDLLA NPs. The dashed rectangle encloses XRD peaks that are associated with the PLA stereocomplex crystalline domains. Reprinted with permission from "Erythrocyte-Membrane-Camouflaged Nanocarriers with Tunable Paclitaxel Release Kinetics *via* Macromolecular Stereocomplexation" by Lin, Y.-N.; Elsabahy, M.; Khan, S.; Zhang, F.; Song, Y.; Dong, M.; Li, R.; Smolen, J.; Letteri, R. A.; Su, L.; Wooley, K. L., *ACS Mater. Lett.* **2020,** *2*, 595-601. Copyright 2020 American Chemical Society.

Table 2. PTX loading efficiency and loading capacities of PLA NPs. [a] Mass of PTX loaded within polymer nanoparticles (measured by HPLC) *vs.* mass of PTX added to the mixture. [b] Mass of PTX loaded within polymer nanoparticles (measured by HPLC) *vs.* mass of PTX-loaded polymer nanoparticles. Reprinted with permission from "Erythrocyte-Membrane-Camouflaged Nanocarriers with Tunable Paclitaxel Release Kinetics *via* Macromolecular Stereocomplexation" by Lin, Y.-N.; Elsabahy, M.; Khan, S.; Zhang, F.; Song, Y.; Dong, M.; Li, R.; Smolen, J.; Letteri, R. A.; Su, L.; Wooley, K. L., *ACS Mater. Lett.* **2020,** *2*, 595-601. Copyright 2020 American Chemical Society.

Polymer composition	[Polymer] (mg / mL)	[PTX] Physically loaded (theoretical) (μg / mL)	[PTX] Physically loaded (experimental) (μg / mL)	[a]Physical loading efficiency	[b]Loading capacity
scPLA	0.5	56.28	46.66	82.92%	8.44%
50%scPLA	0.5	56.28	46.44	82.51%	8.40%
PDLA	0.5	56.28	46.55	82.72%	8.42%
PLLA	0.5	56.28	45.37	80.62%	8.22%
PDLLA	0.5	56.28	45.90	81.57%	8.31%
scPLA	0.5	26.31	17.77	67.54%	3.43%
50%scPLA	0.5	26.31	21.13	80.33%	4.06%
PDLA	0.5	26.31	22.55	85.70%	4.32%
PLLA	0.5	26.31	17.75	67.46%	3.43%
PDLLA	0.5	26.31	20.76	78.89%	3.99%

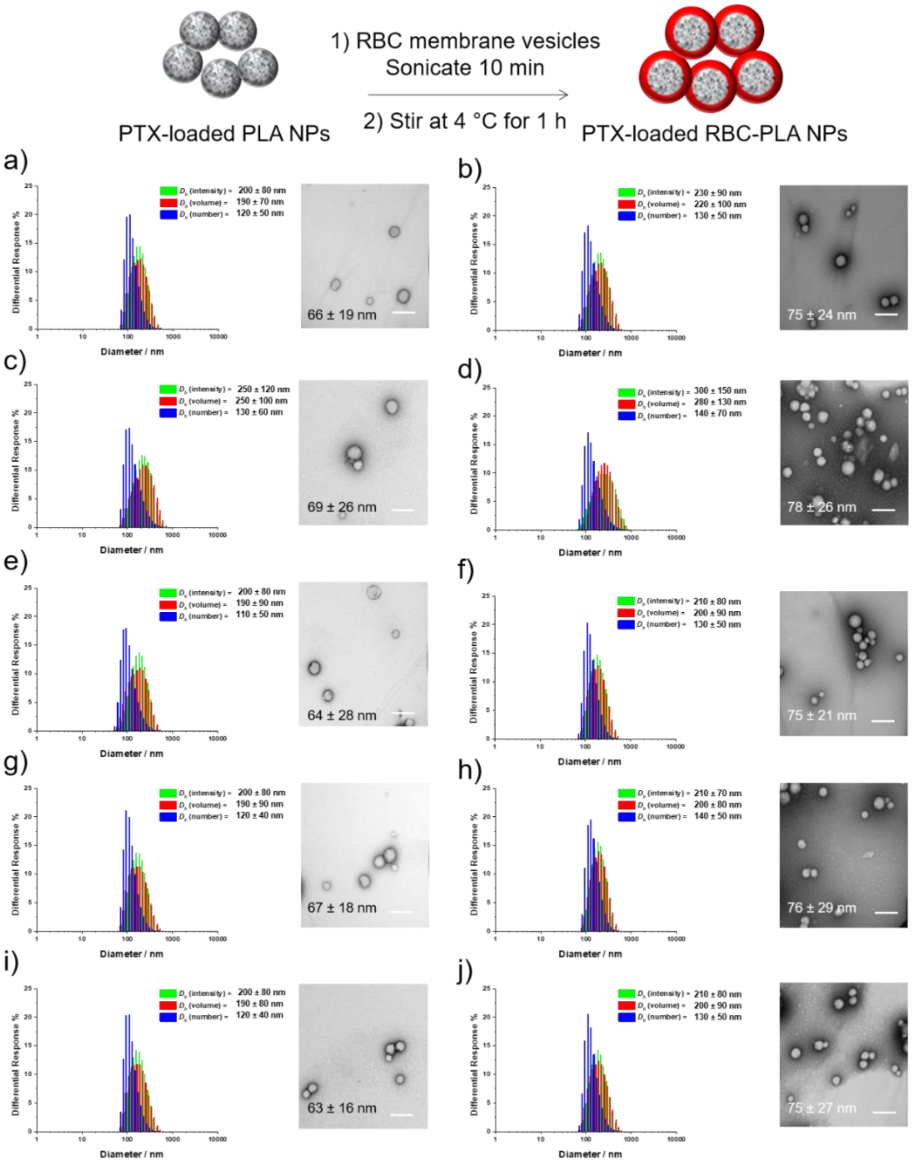

Figure 27. Schematic representation of the PTX-loaded RBC-MCNs formation. DLS and TEM of PTX-loaded nanoconstructs prepared in nanopure water at different PLLA:PDLA:PDLLA mass ratio, (a) scPLA NPs (1:1:0), (c) 50%scPLA NPs (1:1:2), (e) PDLA NPs (0:1:0), (g) PLLA NPs (1:0:0), and (i) PDLLA NPs (0:0:1). PTX-loaded RBC-MCNs with (b) scPLA NPs, (d) 50%scPLA NPs, (f) PDLA NPs, (h) PLLA NPs, and (j). PDLLA NPs. TEM samples were negatively stained by 2% uranyl acetate aqueous solution. The scale bars in the TEM images represent 200 nm. Reprinted with permission from "Erythrocyte-Membrane-Camouflaged Nanocarriers with Tunable Paclitaxel Release Kinetics *via* Macromolecular Stereocomplexation" by Lin, Y.-N.; Elsabahy, M.; Khan, S.; Zhang, F.; Song, Y.; Dong, M.; Li, R.; Smolen, J.; Letteri, R. A.; Su, L.; Wooley, K. L., *ACS Mater. Lett.* **2020,** *2*, 595-601. Copyright 2020 American Chemical Society.

The crystalline properties of the PTX-loaded PLA NPs were subsequent evaluated by WAXD and DSC, since loading hydrophobic drug could potentially disrupt non-covalent intermolecular interactions within the polymer matrix, specifically crystallinity and stereocomplexation crystallinity. As depicted in Figure 26, upon loading PTX in scPLA NPs, the X-ray diffraction analyses revealed the co-existence of the stereocomplex-associated diffraction patterns and the non-stereocomplex-associated diffraction pattern, regardless of PTX loading amount (5 or 10 wt %). This observation indicated partial stereocomplex disruption, resulting in heterogeneous stereocomplex and isotactic PLA crystalline domains in the polymer matrix. DSC analyses of the lyophilized PLA nanoconstructs further supported partial stereocomplex retention upon PTX loading (Figure 28). Since thermal history can be introduced during heating–cooling processes (Figure 29), only the first heating cycle of the DSC traces, which contained relevant information associated with polymer packings of the as-prepared nanoconstructs, was analyzed to decipher the effect of PTX loading on the PLA polymer packing. The atactic PDLLA NPs exhibited a glass transition temperature (T_g) at 56 °C with no melting transition (T_m), as expected for an amorphous material. Isotactic PDLA and PLLA NPs displayed T_m transitions at 167 and 164 °C, respectively, whereas 100% stereocomplex PLA NPs exhibited a single T_m at 232 °C, which was 65–68 °C higher than the T_m of PDLA or PLLA NPs, suggesting the formation of a stereocomplex interaction.[98, 101] The PLA stereocomplex melting transition was retained upon PTX loading (5 and 10 wt %). Upon further analyses of the 135–175 °C regions of the PTX-loaded scPLA thermograms, two small melting transitions were observed corresponding to the isotactic PLLA and PDLA crystalline regions (Figure 28a), indicating the slight interference of the well-defined equilateral-triangle-shaped crystal. However, qualitatively, the melting transition enthalpies of PLA NPs underwent minimal reduction upon hydrophobic PTX loading, suggesting significant crystallinity retention (Figure 28b).

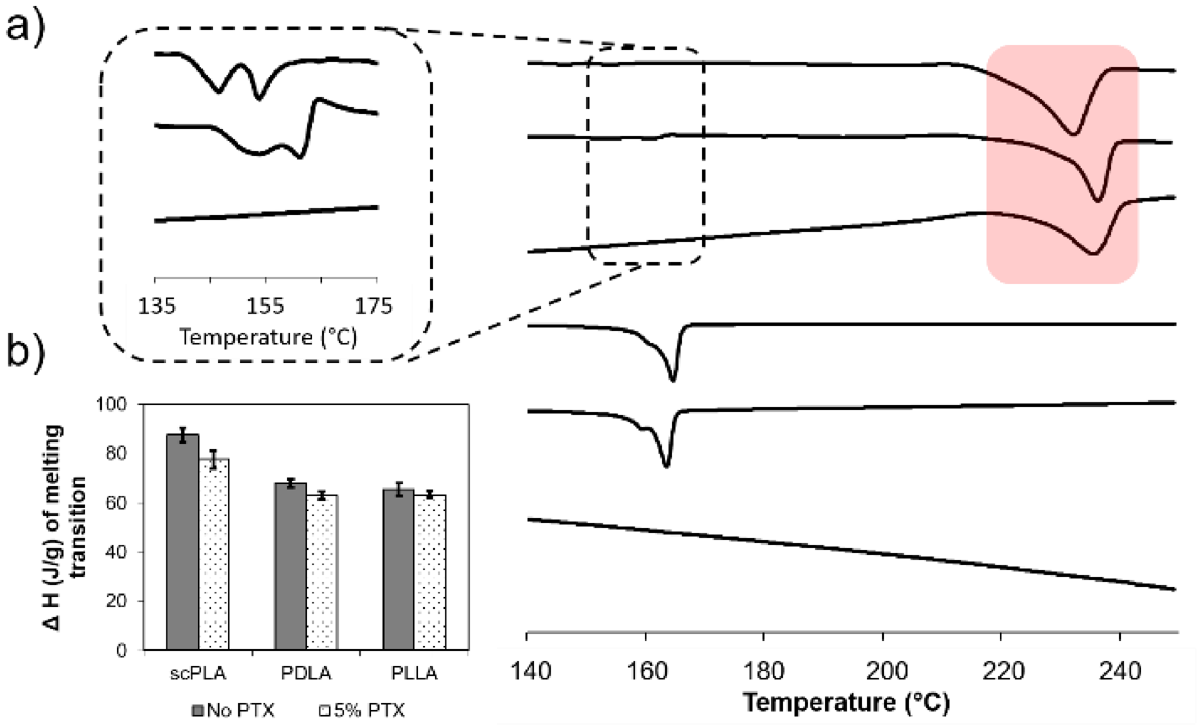

Figure 28. Thermal analysis of the lyophilized PTX-loaded and empty PLA NPs indicated the retention of stereocomplexation upon PTX loading. From top to bottom: 10 *wt*% PTX-loaded scPLA, 5 *wt*% PTX-loaded scPLA, scPLA, PDLA, PLLA, and PDLLA NPs. Traces were taken from the first heating cycle. a) PLA stereocomplex melting transition is highlighted. The dashed rectangle encloses an enlarged view of the non-stereocomplex isotactic PLA melting transition. b) Comparison of the enthalpies (ΔH) of PLAs melting transitions with or without 5 *wt*% PTX loading. Reprinted with permission from "Erythrocyte-Membrane-Camouflaged Nanocarriers with Tunable Paclitaxel Release Kinetics *via* Macromolecular Stereocomplexation" by Lin, Y.-N.; Elsabahy, M.; Khan, S.; Zhang, F.; Song, Y.; Dong, M.; Li, R.; Smolen, J.; Letteri, R. A.; Su, L.; Wooley, K. L., *ACS Mater. Lett.* **2020,** *2*, 595-601. Copyright 2020 American Chemical Society.

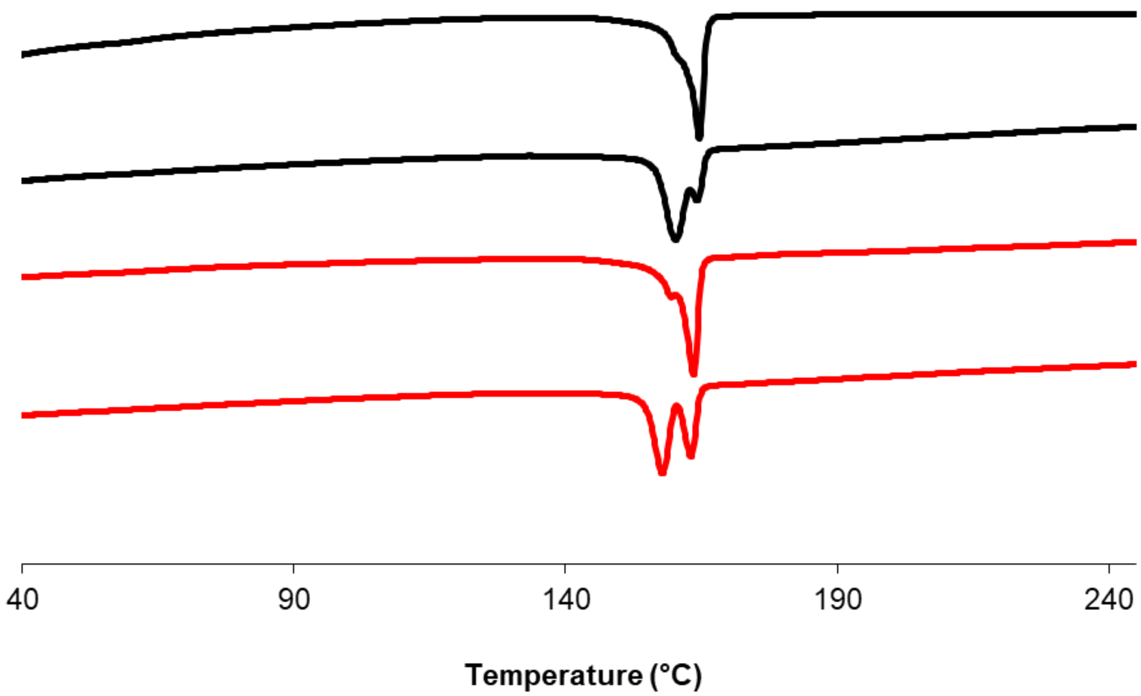

Figure 29. Thermal analysis of the lyophilized PDLA (black) and PLLA (red) NPs. From top to bottom: PDLA (1st heating cycle), PDLA (2nd heating cycle), PLLA (1st heating cycle), and PLLA (2nd heating cycle). Reprinted with permission from "Erythrocyte-Membrane-Camouflaged Nanocarriers with Tunable Paclitaxel Release Kinetics *via* Macromolecular Stereocomplexation" by Lin, Y.-N.; Elsabahy, M.; Khan, S.; Zhang, F.; Song, Y.; Dong, M.; Li, R.; Smolen, J.; Letteri, R. A.; Su, L.; Wooley, K. L., *ACS Mater. Lett.* **2020,** *2*, 595-601. Copyright 2020 American Chemical Society.

To improve solution stability and provide biomimetic surface moieties, RBC membrane vesicles were used to coat PTX-loaded PLA NPs and afford RBC-MCNs with different core tacticities, using reported protocols (Figure 30, Figure 27, Figure 31, and Figure 32).[92, 102] Briefly, PLA NPs (1 mg) and RBC membrane vesicles (derived from 150 µL of human blood) were mixed and sonicated for 10 min in a capped glass vial using a VWR 75T bath sonicator, followed by stirring at 4 °C for 1 h.[79, 103] The resulting PTX-loaded RBC-MCNs showed D_{av} values of 75–78 nm (as measured by TEM) and $D_{h(number)}$ values of 130–140 nm (as measured by DLS, Figure 27). The increase in diameter (ca. 10 nm) indicated the successful coating of two layers of RBC membrane with each layer thickness of 5 nm (Figure 30a and 30b).[104] The zeta potential was changed from ca. −40 mV to ca. −10 mV after RBC membrane coating, owing to the difference in surface charge density between PLA NPs and RBC membrane vesicles (Figure 31). Colloidal stability provided additional evidence for successful PTX-loaded RBC-MCN fabrication. In contrast to the behavior of PTX-loaded PLA NPs, which readily formed precipitates in PBS (pH 7.4) within a few minutes, PTX-loaded RBC-MCNs remained colloidally stable for a prolonged period (>1 week) at 4 °C (Figure 30c).

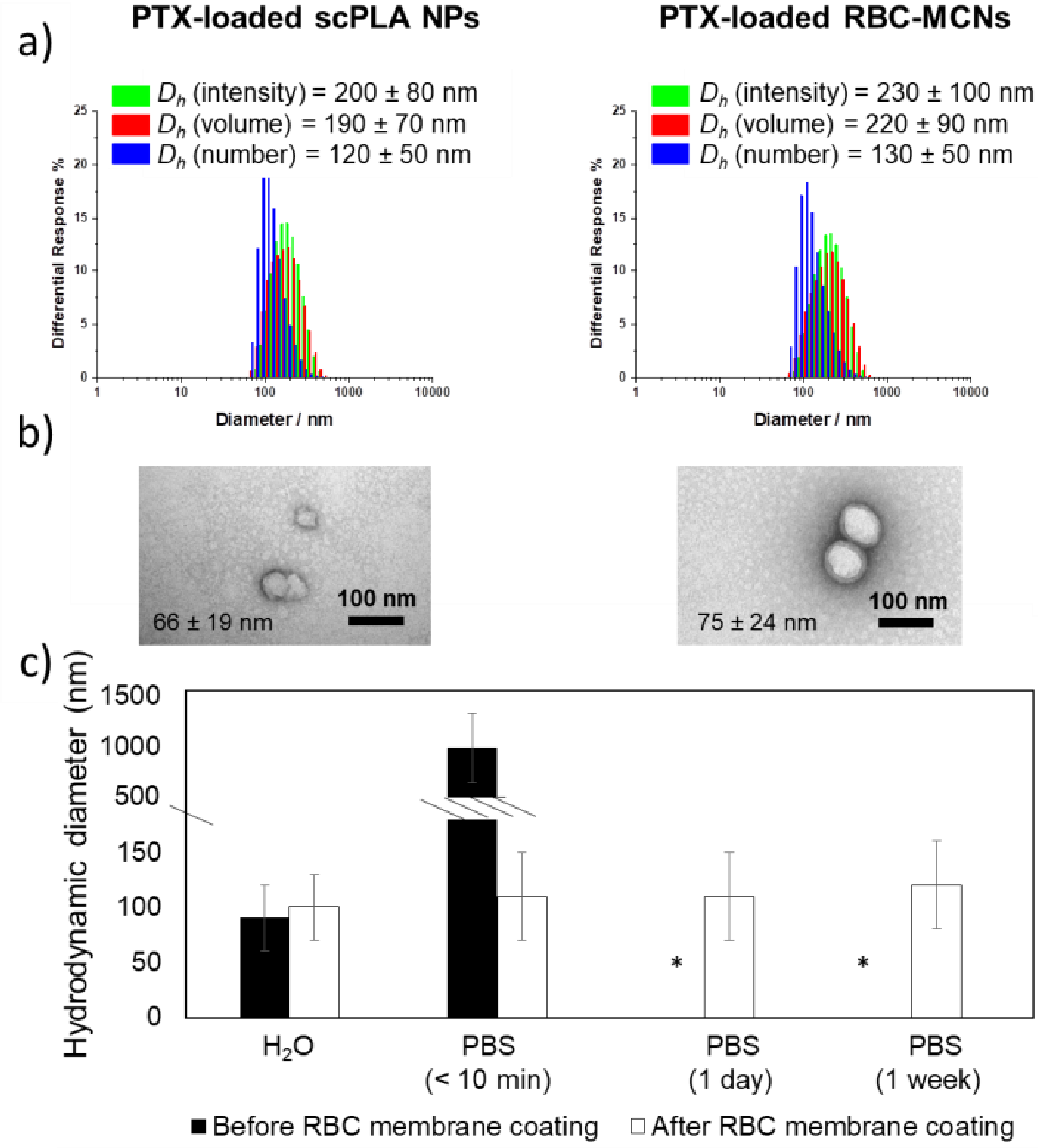

Figure 30. RBC membrane coating of the scPLA NPs was verified by a) DLS, b) TEM (samples negatively stained by 2% uranyl acetate with an average diameter (n = 50), c) colloidal stability in PBS (pH = 7.4) at 4 ºC with * indicating precipitation. Reprinted with permission from "Erythrocyte-Membrane-Camouflaged Nanocarriers with Tunable Paclitaxel Release Kinetics *via* Macromolecular Stereocomplexation" by Lin, Y.-N.; Elsabahy, M.; Khan, S.; Zhang, F.; Song, Y.; Dong, M.; Li, R.; Smolen, J.; Letteri, R. A.; Su, L.; Wooley, K. L., *ACS Mater. Lett.* **2020,** *2*, 595-601. Copyright 2020 American Chemical Society.

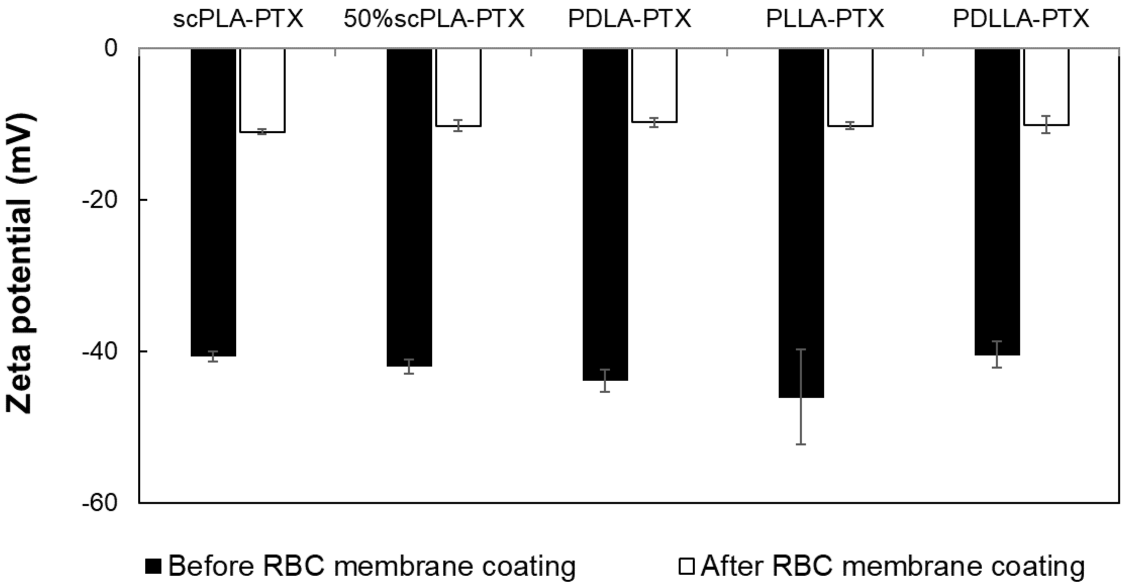

Figure 31. Zeta potential measurements for PTX-loaded PLAs NPs with or without RBC membrane coatings. Reprinted with permission from "Erythrocyte-Membrane-Camouflaged Nanocarriers with Tunable Paclitaxel Release Kinetics *via* Macromolecular Stereocomplexation" by Lin, Y.-N.; Elsabahy, M.; Khan, S.; Zhang, F.; Song, Y.; Dong, M.; Li, R.; Smolen, J.; Letteri, R. A.; Su, L.; Wooley, K. L., *ACS Mater. Lett.* **2020,** *2*, 595-601. Copyright 2020 American Chemical Society.

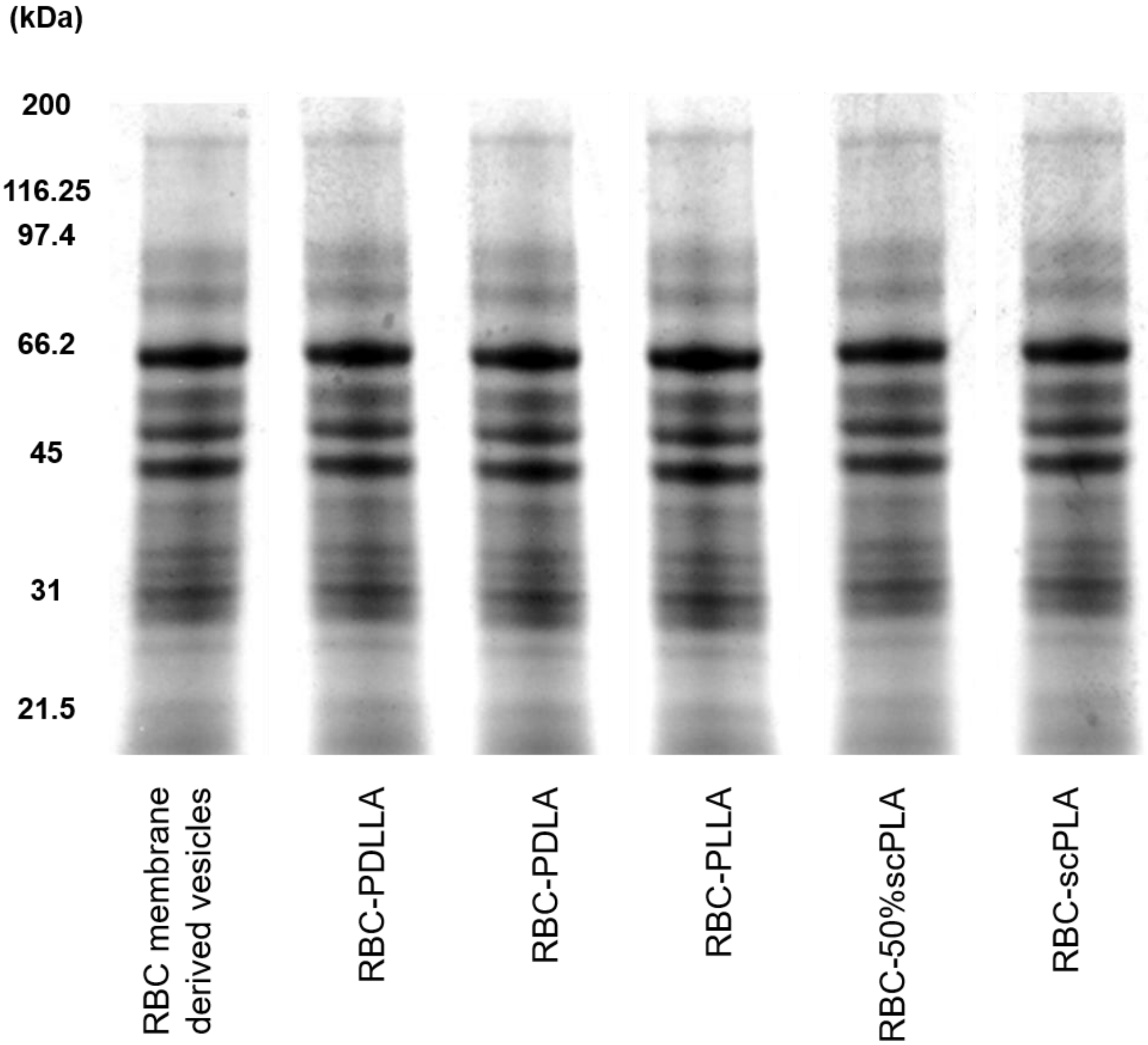

Figure 32. SDS-PAGE electrophoresis of RBC-MCNs and RBC membrane-derived vesicles. Identical protein bands in all lanes indicated minimal protein degradation during the RBC coating process. Reprinted with permission from "Erythrocyte-Membrane-Camouflaged Nanocarriers with Tunable Paclitaxel Release Kinetics *via* Macromolecular Stereocomplexation" by Lin, Y.-N.; Elsabahy, M.; Khan, S.; Zhang, F.; Song, Y.; Dong, M.; Li, R.; Smolen, J.; Letteri, R. A.; Su, L.; Wooley, K. L., *ACS Mater. Lett.* **2020,** *2*, 595-601. Copyright 2020 American Chemical Society.

The structure–property relationships of PTX-loaded RBC-MCNs were evaluated by drug release profiles (Figure 33). An array of PTX-loaded RBC-MCNs was fabricated, and PTX release was monitored in PBS (pH 7.4) at 37 °C using HPLC. Since bare PTX-loaded PLA NPs precipitated immediately in PBS (Figure 30c), only RBC-MCNs were examined in the release study. The PTX-loaded RBC-MCNs showed sustained PTX release, with 100% stereocomplexed PLA RBC-MCNs exhibiting the least PTX release during the first 12 h, compared to 2-, 3-, and 4-fold higher amounts of release for the 50% stereocomplexed, isotactic, and amorphous PLA counterparts, respectively (Figure 33). After 8 days, RBC-MCNs with scPLA, 50%scPLA, PLLA, PDLA, and amorphous PLA cores released 27, 40, 54, 57, and 69% of the loaded PTX, respectively. These data demonstrate that the drug release kinetics of RBC-MCNs were successfully controlled by altering the core stereostructure of the MCNs. The densely packed PLA chains within the stereocomplexed core domains limited PTX diffusion and release; therefore, RBC-scPLA exhibited 10-fold (IC_{50} = 0.50 μM) lower cytotoxicity in human osteosarcoma cells (SJSA-1) compared to free PTX (IC_{50} = 0.05 μM). The faster release of PTX from the amorphous cores of PTX-loaded RBC-PDLLA resulted in only a 5-fold reduction in cytotoxicity (IC_{50} = 0.25 μM) relative to the free small molecule drug (Figure 34). The sustained PTX release over prolonged periods could help maintain a persistent drug concentration in tumor tissues and improve therapeutic efficacy.[1] As a control, empty RBC-MCNs did not show significant cytotoxicity after incubation with SJSA-1 osteosarcoma cells for 72 h at a NP concentration range of 0.17–167 μg/mL (Figure 35).

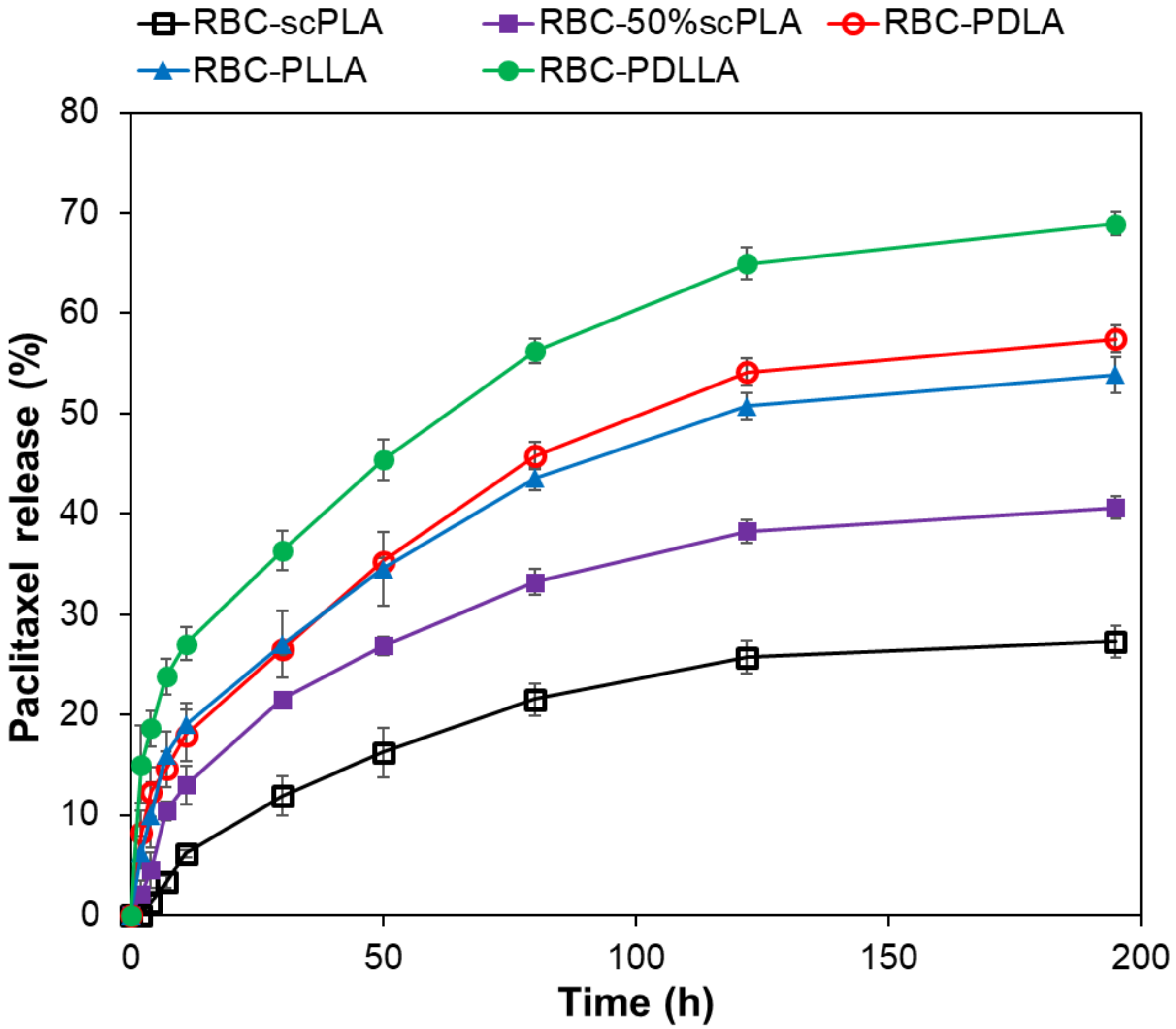

Figure 33. Release of PTX from PTX-loaded RBC-MCNs (5 *wt* %) studied by a dialysis method over 8 days at 37 °C in PBS buffers (pH 7.4), measured in triplicates. Reprinted with permission from "Erythrocyte-Membrane-Camouflaged Nanocarriers with Tunable Paclitaxel Release Kinetics *via* Macromolecular Stereocomplexation" by Lin, Y.-N.; Elsabahy, M.; Khan, S.; Zhang, F.; Song, Y.; Dong, M.; Li, R.; Smolen, J.; Letteri, R. A.; Su, L.; Wooley, K. L., *ACS Mater. Lett.* **2020,** *2*, 595-601. Copyright 2020 American Chemical Society.

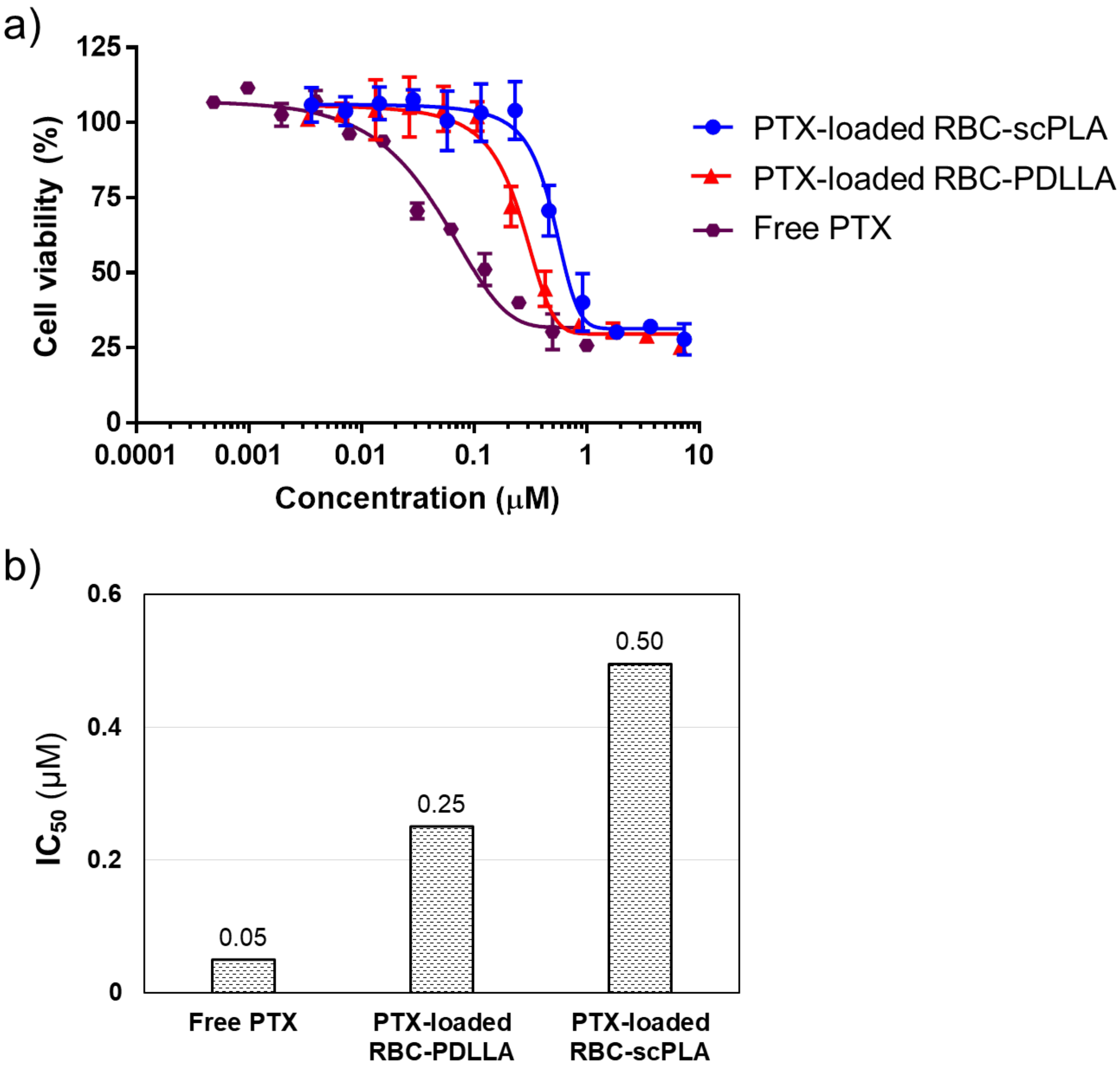

Figure 34. Cytotoxicity of PTX, PTX-loaded RBC-PDLLA, and PTX-loaded RBC-scPLA in SJSA-1 cell line for 72 h. (a) Cell viability as a function of PTX concentration and (b) half maximal inhibitory concentration (IC_{50}) values obtained from the data plotted in (a). Cell viabilities are reported as an average of three measurements, and error bars represent standard deviation. Reprinted with permission from "Erythrocyte-Membrane-Camouflaged Nanocarriers with Tunable Paclitaxel Release Kinetics *via* Macromolecular Stereocomplexation" by Lin, Y.-N.; Elsabahy, M.; Khan, S.; Zhang, F.; Song, Y.; Dong, M.; Li, R.; Smolen, J.; Letteri, R. A.; Su, L.; Wooley, K. L., *ACS Mater. Lett.* **2020,** *2*, 595-601. Copyright 2020 American Chemical Society.

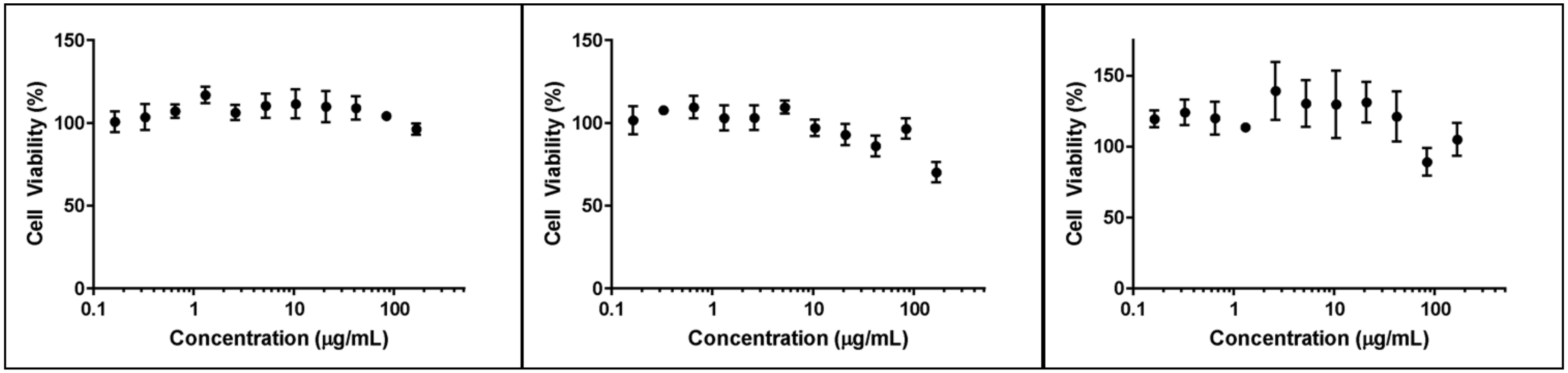

RBC-PLLA **RBC-PDLA** **RBC-50%scPLA**

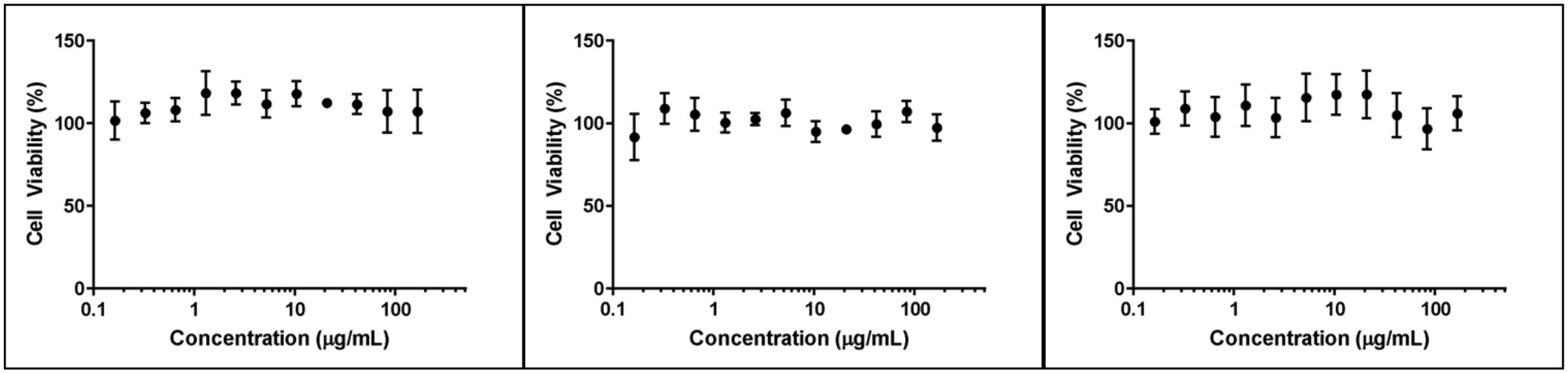

RBC-PDLLA **RBC-scPLA** **RBC membrane vesicles**

Figure 35. RBC-MCNs cytotoxicity in SJSA-1 cell line with polymer concentrations ranging from 0.17–167 μg / mL for 72 h. Cell viabilities are reported as an average of three measurements, and error bars represent standard deviation. Reprinted with permission from "Erythrocyte-Membrane-Camouflaged Nanocarriers with Tunable Paclitaxel Release Kinetics *via* Macromolecular Stereocomplexation" by Lin, Y.-N.; Elsabahy, M.; Khan, S.; Zhang, F.; Song, Y.; Dong, M.; Li, R.; Smolen, J.; Letteri, R. A.; Su, L.; Wooley, K. L., *ACS Mater. Lett.* **2020,** *2*, 595-601. Copyright 2020 American Chemical Society.

The immunotoxicities of the RBC-MCNs were investigated by cytokine expression levels, which can demonstrate the ability of biomaterials to interact with the immune system, either *in vitro* or *in vivo*.[105-106] No significant overexpression of any of the tested 23 cytokines was observed for the PDLLA and scPLA NPs. On the contrary, the human-derived RBC membrane vesicles induced acute immunotoxic reactions in the RAW 264.7 mouse macrophage cell line, possibly due to foreign antigen recognition, as indicated by the significant overexpression ($p = 0.03$) of the G-CSF, IL-10, RANTES, and TNF-α (out of the 23 measured cytokines). Interestingly, acute immunotoxic responses against foreign membrane-associated antigens were reduced after coating the membrane onto the PLA NPs (Figure 36), potentially via altering the interaction of antigens with the surrounding biomolecules and receptors;[107] further study will be conducted to elucidate this phenomenon.

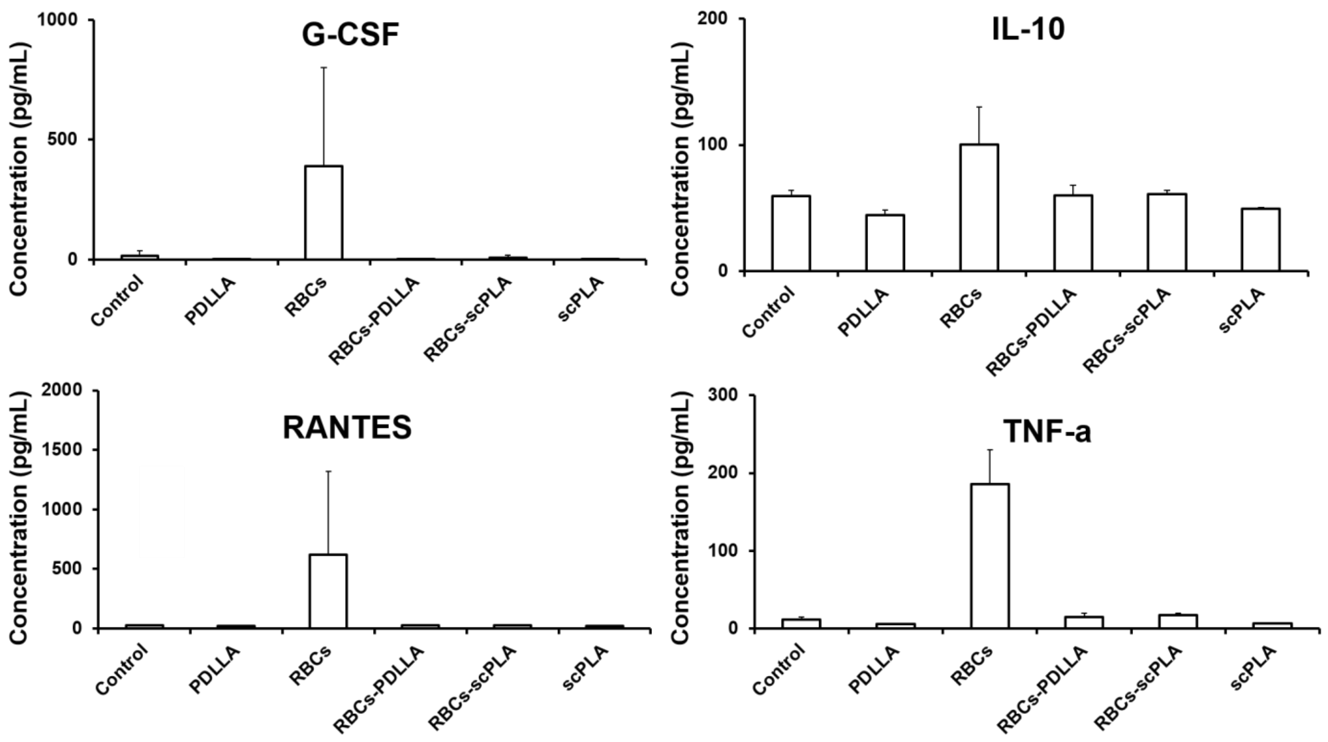

Figure 36. Immunotoxicity assay of RBC-MCNs. The expression of the mouse cytokines, interleukin (IL)-1α, IL-1β, IL-2, IL-3, IL-4, IL-5, IL-6, IL-9, IL-10, IL-12 (P40), IL-12 (P70), IL-13, IL-17, eotaxin, granulocyte-colony-stimulating factor (G-CSF), granulocyte macrophage-colony-stimulating factor (GM-CSF), interferon-γ (IFN-γ), keratinocyte-derived chemokine (KC), monocyte chemotactic protein (MCP)-1, macrophage inflammatory protein (MIP)-1α, MIP-1β, regulated upon activation normal T-cell expressed, and presumably secreted (RANTES) and tumor necrosis factor-α (TNF-α), following the treatment of RAW 264.7 cells with media (control), RBC membrane vesicles, PLAs and RBC-MCNs tested at a concentration of 5 μg/mL for 24h. Reprinted with permission from "Erythrocyte-Membrane-Camouflaged Nanocarriers with Tunable Paclitaxel Release Kinetics *via* Macromolecular Stereocomplexation" by Lin, Y.-N.; Elsabahy, M.; Khan, S.; Zhang, F.; Song, Y.; Dong, M.; Li, R.; Smolen, J.; Letteri, R. A.; Su, L.; Wooley, K. L., *ACS Mater. Lett.* **2020,** *2*, 595-601. Copyright 2020 American Chemical Society.

3.3. Experimental Section

3.3.1. Materials

DL-Lactide, D-lactide, and L-lactide were purified by recrystallization from ethyl acetate. 1,5,7-Triazabicyclo[4.4.0]dec-5-ene (TBD) was purchased from TCI chemicals. Paclitaxel (PTX) was purchased from BIOTANG, Inc. (Lexington, MA). Dichloromethane (DCM) was dried using a solvent purification system from J. C. Meyer Solvent Systems, Inc. (Laguna Beach, CA). Nanopure water (18.2 MΩ cm) was acquired from a Milli-Q water filtration system (Millipore Corp, USA). Human whole blood was obtained from the Gulf Coast Regional Blood Center (Houston, TX). 10x PBS was purchased from MilliporeSigma (Burlington, MA). SDS-PAGE molecular weight standard (broad range), precast Mini-PROTEAN® TGX™ gels, and 10x Tris/Glycine/SDS buffer were purchased from Bio-Rad Laboratories, Inc. (Hercules, CA). Other chemicals and reagents were used as received from Sigma-Aldrich, Co. (St. Louis, MO) unless otherwise noted. Pur-A-Lyzer™ dialysis tubing (6 kDa molecular weight cut-off (MWCO)) were purchased from Sigma-Aldrich (St. Louis, MO). Dulbecco's Modified Eagle's Medium (DMEM) was obtained from the American Type Culture Collection (Manassas, VA), with media additives (10% fetal bovine serum, 1% penicillin/streptomycin) were purchased from Sigma-Aldrich (St. Louis, MO). Osteosarcoma cells (SJSA-1) were provided by Dr. Hughes at MD Anderson Medical Center. The 96-well round-bottom cell culture plates were purchased from Corning Costar Co. (Corning, NY).

3.3.2. Instrumentation

^{1}H NMR and ^{13}C NMR spectra were recorded on a Varian 500 spectrometer (Varian, Inc., Palo Alto, CA) interfaced with a UNIX computer using VNMR-J software. All NMR experiments were performed at ambient temperature. Chemical shifts were referenced to the solvent residual signals. All ^{1}H NMR chemical shifts are reported in parts per million (ppm) downfield of tetramethylsilane and relative to the signals for residual $CHCl_3$ (7.26 ppm). All ^{13}C NMR spectra are reported in ppm relative to $CDCl_3$ (77.23 ppm) and were obtained with ^{1}H decoupling.

Fourier transform infrared (FTIR) spectra were recorded on an IR Prestige 21 system equipped with a diamond attenuated total reflection (ATR) lens (Shimadzu Corp., Japan) and analyzed using IRsolution v. 1.40 software.

Size exclusion chromatography (SEC) eluting with tetrahydrofuran (THF) was performed on a Waters Chromatography, Inc. (Milford, MA) system equipped with an isocratic pump (model 1515), a differential refractometer (model 2414), and a column set comprised of a PLgel 5 μm guard column (50 × 7.5 mm), a PLgel 5 μm Mixed C column (300 × 7.5 mm, Agilent Technologies) and two Styragel® columns (500 Å and 104 Å, 300 × 7.5 mm, Waters Chromatography, Inc.). The system was operated at 40 °C with a flow rate of 1 mL/min. Data were analyzed using Breeze software from Waters Chromatography, Inc. (Milford, MA). Molar masses were determined relative to polystyrene standards (580–3,250,000 Da) purchased from Polymer Laboratories, Inc. (Amherst, MA). Polymer solutions were prepared at a concentration of *ca.* 3 mg/mL with 0.05 vol% toluene as the flow rate marker; an injection volume of 200 μL was used.

Wide-angle X-ray diffraction (WAXD) was performed on a Bruker D8® Bragg-Brentano X-ray powder diffractometer, equipped with a 1 kW Cu tube source (1.54 Å), using an operating voltage of 40 kV and a current of 25 mA. The X-ray optics were set to standard Bragg-Brentano para-focusing mode, with X-rays focusing on the sample from an incident beam divergence-limiting slit (1 mm) and then converging onto a position-sensitive X-ray detector (Lynx-Eye, Bruker-AXS). The sample (*ca*. 10 mg) was placed in the holder of a two-circle goniometer (d = 218 mm) in a radiation safety enclosure, and standard powder θ-2θ diffraction scans were performed at room temperature. Data collection was automated using the COMMANDER program and analyzed with EVA software (Bruker).

Thermogravimetric analysis (TGA) was performed under the Ar atmosphere using a Mettler-Toledo TGA2/1100/464 (Mettler-Toledo, Inc., Columbus, OH), with a heating rate of 10 °C/min, from 25 to 500 °C. Data were analyzed using Mettler-Toledo STAR^e v. 15.00a software.

Glass transition temperature (T_g) and melting temperature (T_m) were measured by differential scanning calorimetry (DSC) on a Mettler-Toledo DSC3/700/1190 (Mettler-Toledo, Inc., Columbus, OH) under $N_{2(g)}$. The T_g was taken as the midpoint of the inflection tangent from the second heating scan. The T_m was taken as the maximum of the endothermic peak from the first and second heating scan. Enthalpies of melting transition (ΔH) were calculated using the area under the melting endotherm. Measurements were performed with a heating rate of 10 °C/min, and the data were analyzed using Mettler-Toledo STAR^e v. 15.00a software.

Dynamic light scattering (DLS) measurements were conducted using a Zetasizer Nano ZS instrument (Malvern Panalytical Inc., Westborough, MA) equipped with a laser diode operating at 632.8 nm. The scattered light was detected at 175° and analyzed using a log correlator for a 0.5 mL sample in a disposable cell (capacity = 0.9 mL). The photomultiplier aperture and attenuator were adjusted automatically. The particle size distribution and distribution averages were calculated using particle size analysis routines in Zetasizer 7.13 software. The measurement duration and number of accumulations were adjusted automatically. The average diameter of the particles was reported as the intensity-, volume-, and number-average hydrodynamic diameter from three measurements.

The zeta potentials of the nanoparticles were determined by electrophoretic light scattering using a Zetasizer Nano ZS instrument (Malvern Panalytical Inc., Westborough, MA) equipped with a laser diode operating at 632.8 nm. The zeta potential of the particles in suspension was obtained by measuring the electrophoretic mobility of the charged particles. Scattered light was detected at a 12.8° angle at 25 °C. The zeta potential is reported as the average and standard deviation of three measurements.

Transmission electron microscopy (TEM) images were collected on a JEOL 1200EX operated at 100 kV, and micrographs were recorded using a SIA-15C CCD camera. Samples for TEM were prepared as follows: aqueous polymer solution (20 μL, 0.5 mg/mL) was deposited onto a carbon-coated copper grid, and after 1 min, excess solution was quickly wicked away by a piece of filter paper. The samples were then negatively stained with a 2% uranyl acetate aqueous solution (20 µL). After 30 s, the excess staining solution was quickly wicked away by a piece of filter paper, and the samples were left to dry under ambient conditions before imaging.

PTX concentrations were determined by high-performance liquid chromatography (HPLC) on a Shimadzu Prominence system equipped with a SPD-20AV prominence UV-Vis detector set to 228 nm and a Waters X Bridge C8 column (4.6 × 150 mm, 5 µM, 100 Å) eluting in 60% acetonitrile and 40% aqueous solution (0.1% trifluoroacetic acid) in isocratic mode. The flow rate was set to 1 mL/min with a run time of 10 min, and the column temperature was set to 40 °C. The HPLC method employed an external calibration of PTX.

3.3.3. Synthesis

3.3.3.1. Synthetic procedure for polylactides

A solution of DL-lactide (301.5 mg, 2.081 mmol) and 4-methylbenzyl alcohol (3.6 mg, 0.030 mmol) was prepared in anhydrous DCM (4.0 mL) and transferred to a vial equipped with a stir bar and a rubber septum in an argon-filled glovebox. The vial was then removed from the glovebox and connected to a Schlenk line. A solution of TBD in DCM (0.1 mL, 10.0 mg/mL, 0.007 mmol) was injected quickly into the vial of lactide solution at −78 °C. After stirring for 2 min, the reaction was quenched by adding excess acetic acid. Precipitation from DCM into methanol three times, and drying under vacuum yielded a white powder, poly(DL-lactide). Poly(D-lactide) and poly(L-lactide) were synthesized using cyclic D-lactide and L-lactide, respectively. **Poly(DL-lactide) (PDLLA)** (268.3 mg, 87%). ^{1}H NMR (500 MHz, $CDCl_3$, ppm): δ 7.21 and 7.16 (AB_q, J = 8 Hz), 5.25-5.11 (m), 2.35 (s), 1.58 (d, J = 8 Hz). ^{13}C NMR (126 MHz, $CDCl_3$, ppm): δ 169.73, 169.68, 169.53, 169.47, 169.26, 138.56, 132.24, 129.43, 128.54, 69.33, 69.15, 67.34, 66.86, 21.36, 20.68, 16.90, 16.80. FTIR: 3000-2900, 1751, 1452, 1381, 1362, 1182, 1128, 1086, 1045, 957, 868, 754 cm^{-1}. T_g = 53 °C. TGA in Ar: 328–360 °C, 96% mass loss. $M_{n\ NMR}$ = 8.9 kDa. $M_{n\ SEC}$ = 19.2 kDa. *Đ = 1.07.* **Poly(L-lactide) (PLLA)** (272.4 mg, 80%). ^{1}H NMR (500 MHz, $CDCl_3$, ppm): δ 7.21 and 7.16 (AB_q, J = 8 Hz), 5.16 (q, J = 8 Hz), 2.35 (s), 1.58 (d, J = 8 Hz). ^{13}C NMR (126 MHz, $CDCl_3$, ppm): δ 169.73, 138.56, 132.19, 129.42, 128.54, 69.14, 67.34, 66.84, 21.35, 20.67, 16.88, 16.79. FTIR: 3000-2900, 1749, 1452, 1383, 1358, 1180, 1126, 1084, 1043, 957, 870, 752 cm^{-1}. T_g = 53 °C, T_m = 158 and 163 °C. TGA in Ar: 326–359 °C, 95% mass loss. $M_{n\ NMR}$ = 8.2 kDa. $M_{n\ SEC}$ = 20.6 kDa. *Đ = 1.09.* **Poly(D-lactide) (PDLA)** (263.7 mg, 83%). ^{1}H NMR (500 MHz, $CDCl_3$, ppm): δ 7.21 and 7.16 (AB_q, J = 8 Hz), 5.16 (q, J = 8 Hz), 2.35 (s), 1.58 (d, J = 8 Hz). ^{13}C NMR (126 MHz, $CDCl_3$, ppm): δ 169.73, 138.56, 132.20, 129.42, 128.53, 69.15, 67.34, 66.85, 21.35, 20.67, 16.89, 16.79. FTIR: 3000-2900, 1751, 1452, 1383, 1360, 1180, 1126, 1084, 1045, 955, 870, 754 cm^{-1}. T_g = 52 °C, T_m = 160 and 164 °C. TGA in Ar: 326–359 °C, 96% mass loss. $M_{n\ NMR}$ = 8.4 kDa. $M_{n\ SEC}$ = 21.4 kDa. *Đ = 1.08.*

3.3.4. Procedures

3.3.4.1. General fabrication procedure for PLA NPs with different stereostructures

Polylactide (PLA, 0.9 mg) was dissolved in THF (0.9 mL), followed by addition to water (9 mL) at the rate of 6 mL/h using a syringe pump while stirring. The organic solvent was removed by nitrogen flow-promoted evaporation, and the final PLA assemblies were concentrated to 0.5 mg/mL. The stereostructures of the PLA nanoconstructs were controlled by altering the mass ratio of PLLA, PDLA, and PDLLA during nanoprecipitation (co)assembly, according to Table 1.

3.3.4.2. General fabrication procedure for PTX-loaded PLA NPs with different stereostructures

PLAs (0.9 mg) and PTX (10 µL or 4.7 µL, 10 mg/mL in THF) were dissolved in THF (0.9 mL), followed by addition to water (9 mL) at the rate of 6 mL/h using a syringe pump while stirring. The organic solvent was removed by nitrogen flow-promoted evaporation, and the final PLA was concentrated to 0.5 mg/mL. PTX concentrations were determined by HPLC equipped with a UV-Vis detector set to 228 nm. The stereostructures of the PLA nanoconstructs were controlled by altering the mass ratio of PLLA, PDLA, and PDLLA during nanoprecipitation (co)assembly, according to Table 1.

3.3.4.3. Preparation of erythrocyte (red blood cell, RBC) membrane-camouflaged nanocarriers (RBC-MCNs)

RBC membrane vesicles were prepared following reported protocols.[65, 103] RBCs were collected from human blood by centrifuging the whole blood at 2000 x *g* for 10 min, following which the supernatant and buffy coat were removed. The collected RBCs were then subject to hypotonic treatment to remove interior contents. The resulting RBC ghosts were extruded through 400 nm polycarbonate porous membranes (11x), then through 100 nm polycarbonate porous membranes (11x) using a hand extruder (Avanti Polar Lipids) to generate RBC membrane vesicles. RBC membrane coating of the polymeric nanoparticle was achieved using reported protocols,[79, 102] with one milligram of polymer NPs mixing with RBC membrane vesicles derived from 150 µL of blood.[4] PLA NP solutions (0.5 mg/mL, 1 mL) and RBC membrane vesicle solutions (deriving from 75 µL of blood) were mixed and sonicated for 10 min in a capped glass vial using a VWR 75T bath sonicator, followed by stirring at 4 °C for 1 h. The resulting RBC-MCN assemblies were characterized by electrophoretic light scattering, DLS, and TEM.

3.3.4.4. Sample preparation for DSC and WAXD analysis

PTX-loaded PLA NP solutions (0.5 mg/mL PLA concentration) were lyophilized to obtain white powders, which were analyzed by DSC and WAXD, as described in the instrumentation section.

3.3.4.5. Colloidal stability investigation of PTX-loaded PLA NPs and RBC-MCNs

PBS (0.1 mL, 10x) was mixed with 0.9 mL of PTX-loaded PLA NPs and RBC-MCNs (0.5 mg/mL PLA concentration). The hydrodynamic sizes of the assemblies were monitored at different time intervals using DLS.

3.3.4.6. Protein characterization using SDS-PAGE

RBC membrane vesicles, PLA NPs, and RBC-MCNs were mixed with Laemmli sample buffer (2x, Bio-Rad) with 200 mM dithiothreitol (DTT). The samples were then run on a Mini-PROTEAN® TGX^{TM} 10-well precast protein gel in Tris/Glycine/SDS running buffer (Bio-Rad) using the Mini-PROTEAN Tetra System (Bio-Rad). The samples were run at 50 V for 30 min, followed by 100 V for 1 h, and the resulting polyacrylamide gel was stained in Coomassie® Violet R 150 (Fiuka Chemie AG) overnight for visualization.

3.3.4.7. *In vitro* drug release studies of the PTX-loaded RBC-MCNs

PTX-loaded RBC-MCN solutions (3 mL, 0.5 mg/mL PLA concentration, 5% *wt* PTX) were transferred into a presoaked dialysis tubing (Pur-A-Lyzer^{TM}, 6 kDa MWCO). The dialysis tubing was stirred in 2.5 L PBS (pH 7.4, 37 °C). Aliquots (100 µL) of the PTX-loaded RBC-MCN solutions were taken at pre-determined times and analyzed by HPLC. The release profiles of the PTX-loaded RBC-MCNs were obtained by monitoring PTX concentration decrease over time. The release study was conducted in triplicate.

3.3.4.8. Cytotoxicity of RBC-MCNs

Osteosarcoma cells SJSA-1 (5 x 10^3 cells/well) were plated in 96-well plates in DMEM medium (10% fetal bovine serum, and 1% penicillin/streptomycin). Cells were incubated at 37 °C in a humidified atmosphere containing 5% CO_2 for 24 h. The culture medium was replaced with serial dilutions of the RBC-MCNs or PTX-loaded RBC-MCNs (100 µL) in fresh medium (final concentrations ranged from 0.17–167 µg/ mL). The cells were incubated with the formulations for 72 h. Then the medium was replaced with 100 µL of the fresh medium before the addition of 20 µL MTS combined reagent to each well (Cell Titer 96® Aqueous Non-Radioactive Cell Proliferation Assay, Promega Co., Madison, WI). The cells were incubated with the reagent for 2 h at 37 °C in a humidified atmosphere containing 5% CO_2 and were protected from light. Absorbance was measured at 490 nm using a SpectraMax M5 spectrometer (Molecular Devices Co., Sunnyvale, CA). The cell viability was calculated based on the relative absorbance to the control untreated cells. The 0% and 100% cell viabilities were considered as the control medium (no cells) and cells with no treatment, respectively.

3.3.4.9. Immunotoxicity of RBC-MCNs

Immunotoxicity was evaluated by incubating RAW 264.7 mouse macrophages with the various formulations at 5 µg/mL for 24 h, followed by measuring the expression levels of 23 cytokines using a previously established multiplexing assay.[34] RAW 264.7 (2 × 10^4 cells/well) mouse macrophages were plated in a 96-well plate in Dulbecco's Modified Eagle Medium (DMEM) (10% fetal bovine serum and 1% penicillin/streptomycin) and incubated at 37 ºC and 5% CO_2 for 24 h. The medium was then replaced with the fresh medium 1 h prior to the addition of 20 µL of each of the samples. After a 24 h incubation, the supernatants were collected and centrifuged for 10 min at 13000 rpm. Serial dilutions of cytokine standards (Bio-Rad Laboratories, Inc., Hercules, CA) were prepared in the cell-culture medium to generate a calibration curve with which to determine cytokine concentration. The cytokine standard and cells treated with culture medium (control, 50 µL) and nanoparticles (50 µL) were incubated with antibody-conjugated magnetic bead solution (50 µL) for 30 min in the dark. After washing, the detection antibody solution (50 µL) was added to the wells and incubated in the dark for 30 min under continuous shaking (300 rpm). After washing, streptavidin-phycoerythrin solution (50 µL) was added to each well and incubated while protected from light for 10 min under continuous shaking (300 rpm). Finally, after several cycles of washing, re-suspension in the assay buffer and shaking, the expression of the mouse cytokines, interleukin (IL)-1α, IL-1β, IL-2, IL-3, IL-4, IL-5, IL-6, IL-9, IL-10, IL-12 (P40), IL-12 (P70), IL-13, IL-17, eotaxin, granulocyte-colony-stimulating factor (G-CSF), granulocyte macrophage-colony stimulating factor (GM-CSF), interferon-γ (IFN-γ), keratinocyte-derived chemokine (KC), monocyte chemotactic protein (MCP)-1, macrophage inflammatory protein (MIP)-1α, MIP-1β, regulated upon activation normal T-cell expressed and presumably secreted (RANTES) and tumor necrosis factor-α (TNF-α) were measured immediately using a Bioplex 200 system, equipped with high-throughput fluidics (HTF) and a Pro II Wash station, and the data were analyzed using Bioplex Data Pro software. Cytokine expression was reported relative to that by cells in the culture medium. Values are presented as means ± SD of at least three independent experiments. Significant differences between the two groups were evaluated by Mann-Whitney or between more than two groups by Kruskal-Wallis test. Differences between different groups were considered significant for p values less than 0.05.

3.4. Conclusions

To conclude, we demonstrated a facile fabrication of RBC-MCNs with tunable PTX release kinetics via controlling the macromolecular stereostructure. Isotactic and atactic PLAs of similar molar masses (M_n = 8.2–8.9 kDa) and dispersities (<1.1) were synthesized via organocatalyzed ROPs. PLA assemblies, with varying polymer tacticity, had comparable hydrodynamic diameters. Significant PLA stereocomplex retention upon loading PTX was evidenced by WAXD and DSC experiments. The PTX release kinetics from the RBC-MCNs was successfully tuned by changing PLA stereochemistry, with a higher degree of stereocomplexation corresponding to slower PTX release. RBC-MCNs were not cytotoxic and displayed lower immunotoxic responses compared to the RBC membrane vesicles. This strategy can be adapted to encapsulate other cargos, such as different chemotherapeutics, radiosensitizers, and growth factors. Although the cytotoxicity against cancer cells was diminished by packaging the drug within the nanoparticle framework, the extended release profile may be attractive for in vivo efficacy. Therefore, this work represents fundamental advances toward a potential personalized nanocarrier technology that would be capable of employing an individual’s RBCs for membrane isolation, together with tuning of cargo loading and release simply via alteration of the biocompatible PLA stereoisomer feed ratio.

4. A TALE OF DRUG-CARRIER OPTIMIZATION: CONTROLLING STIMULI SENSITIVITY VIA NANOPARTICLE HYDROPHOBICITY THROUGH DRUG LOADING [€]

4.1. Introduction

Over the past two decades of development of the field of nanomedicine, large bodies of work have sought to improve the performance of therapeutic agents by using nanoparticle carriers.[108-113] In general, emphasis has been on maximizing the drug payload to achieve transport and accumulation in a targeted tissue;[6, 114-118] however, effects of the properties and extent of drug loading are often neglected. Drug loading may alter a nanocarrier's physiochemical properties in a loading-dependent manner, thereby influencing efficacy. For instance, loading of hydrophobic drug molecules within an amphiphilic nanoparticle framework may affect colloidal stability, size, shape, flexibility, internal accessibility, and other parameters,[10, 118-122] each of which are important attributes affecting circulation time, clearance, biodistribution, and drug release.[10, 123-126] Covalent drug conjugates enable sustained delivery without burst release during circulation, displaying minimized systemic toxicity and increased accumulations in targeted tissue.[110, 116, 122] Furthermore, stimuli-responsive properties provide a preferable spatiotemporal control over payload release, thereby improving therapeutic efficacy while reducing systemic toxicity.[109, 112, 114-115, 127-128] Therefore, a

---

[€] Reprinted (adapted) with permission from "A Tale of Drug-Carrier Optimization: Controlling Stimuli Sensitivity via Nanoparticle Hydrophobicity through Drug Loading" by Lin, Y.-N.; Khan, S.; Song, Y.; Dong, M.; Shen, Y.; Tran, D. K.; Pang, C.; Zhang, F.; Wooley, K. L., *Nano Letters* **2020**, 20 (9), 6563-6571. Copyright 2020 American Chemical Society.

thorough knowledge of the role that therapeutics play on the properties of nanomedicines as a function of payload level is of great importance, and control over drug-carrier-media interactions may provide an additional opportunity to tune physicochemical characteristics and biological performance of nanoformulations. As a proof of concept in this study, hydrophobic drugs were conjugated via stimulus-sensitive linkers along the hydrophobic backbone of amphiphilic block copolymers and assembled into nanoscopic micelles to investigate the importance of payload level on stimulus accessibility, drug release, and therapeutic efficacy and selectivity *in vitro*.

Glutathione (GSH) is an endogenous stimulus for redox-responsive drug carriers, because $[\text{GSH}]_{\text{intracellular}}$ (2–10 mM) > $[\text{GSH}]_{\text{extracellular}}$ (2–20 μM), and $[\text{GSH}]_{\text{tumor-tissue}}$ > $[\text{GSH}]_{\text{healthy-tissue}}$.[129-134] Since different drugs require different optimal release profiles, [111, 135] controlling the sensitivity of GSH-triggered payload release is essential for optimizing redox-responsive carriers.[136] Different strategies have been reported to control the sensitivity of disulfide bonds,[137-141] which undergo reductive cleavage in a high-GSH environment and are commonly incorporated into nanomaterials to bestow redox-responsive properties. [108, 142-147] However, these modulating strategies often require specific chemical structures to achieve discrete GSH sensitivity, thereby elevating barriers for optimizing GSH-responsive drug carriers. For instance, thiol–disulfide exchange kinetics have been modulated by introducing steric or charged groups adjacent to the disulfide bond via precise sequence-controlled solid-phase peptide synthesis.[148-149] The GSH responsiveness of polymeric nanomaterials can be modulated by the placement of disulfide bonds in the backbone,[150-153] side chains,[151, 154] or crosslinks,[155-156] as well as by incorporating multistimuli-responsive properties.[157] Alternatively, substituting disulfide-linkages for other redox-sensitive linkages with different reductive potentials, such as Se–Se bonds,[158-159] can vary GSH sensitivity, yet this strategy is limited by the number of unique redox-labile linkages and potential toxicity of the elements involved.[160-162] Expanding facile approaches to control the sensitivity of nanomaterials toward GSH could be of paramount significance for the development and optimization of redox-responsive drug carriers.

Herein, we describe an approach that uses the active drug molecule directly, for both therapeutic effect and for alteration of nanoparticle physicochemical characteristics that provides for tuning of GSH sensitivity, thereby avoiding the incorporation of extra non-bioactive components, and creating an atom economical design of nanomedicines. To demonstrate this approach, the hydrophobic cancer chemotherapeutic camptothecin (CPT) was used, which, upon release, binds to the DNA topoisomerase I cleavage complex, thereby inhibiting DNA religation and resulting in apoptosis.[117, 163-166] The degree of payload loading was altered by covalent conjugation of CPT via disulfide-linkages onto the backbone of poly(ethylene glycol)-*b*-poly(glucose carbonate) (PEG-*b*-PGC) (Scheme 3). The PEG block provides for hydrophilicity, whereas the sugar-based poly(glucose carbonate) (PGC) was selected for its sustainability, biocompatibility, degradability, multifunctionality for coupling with CPT, and ability to self-assemble into versatile nanostructures.[50, 167-169] We hypothesized that GSH sensitivity could be controlled via tuning the core hydrophobicity of the nanomaterials. It was anticipated that increased CPT loading would result in increased hydrophobicity, thereby decreasing aqueous accessibility and limiting the diffusion of water and water-soluble molecules, leading to reduced access of GSH to disulfide-linkages in the core of PEG-*b*-PGC-based nanocarriers and lowered GSH sensitivity. The degree of CPT conjugation (f_{CPT}) is defined relative to the two carboxylic acids available at each PGC repeat unit, with no, low, medium, and high extents of CPT conjugation being targeted as $f_{\mathrm{CPT}} = 0, 0.15, 0.50$, and 0.85, giving 0, 3, 10, and 17 CPTs per PEG-*b*-PGC chain. Due to the relatively high hydrophobicity of the PGC and CPT-PGC block segments in comparison to that of PEG, we speculated that the sugar segments would be primarily localized in the micelle cores, whereas the PEG segments would dominate the exterior surface of the nanocarriers in an aqueous environment.[6]

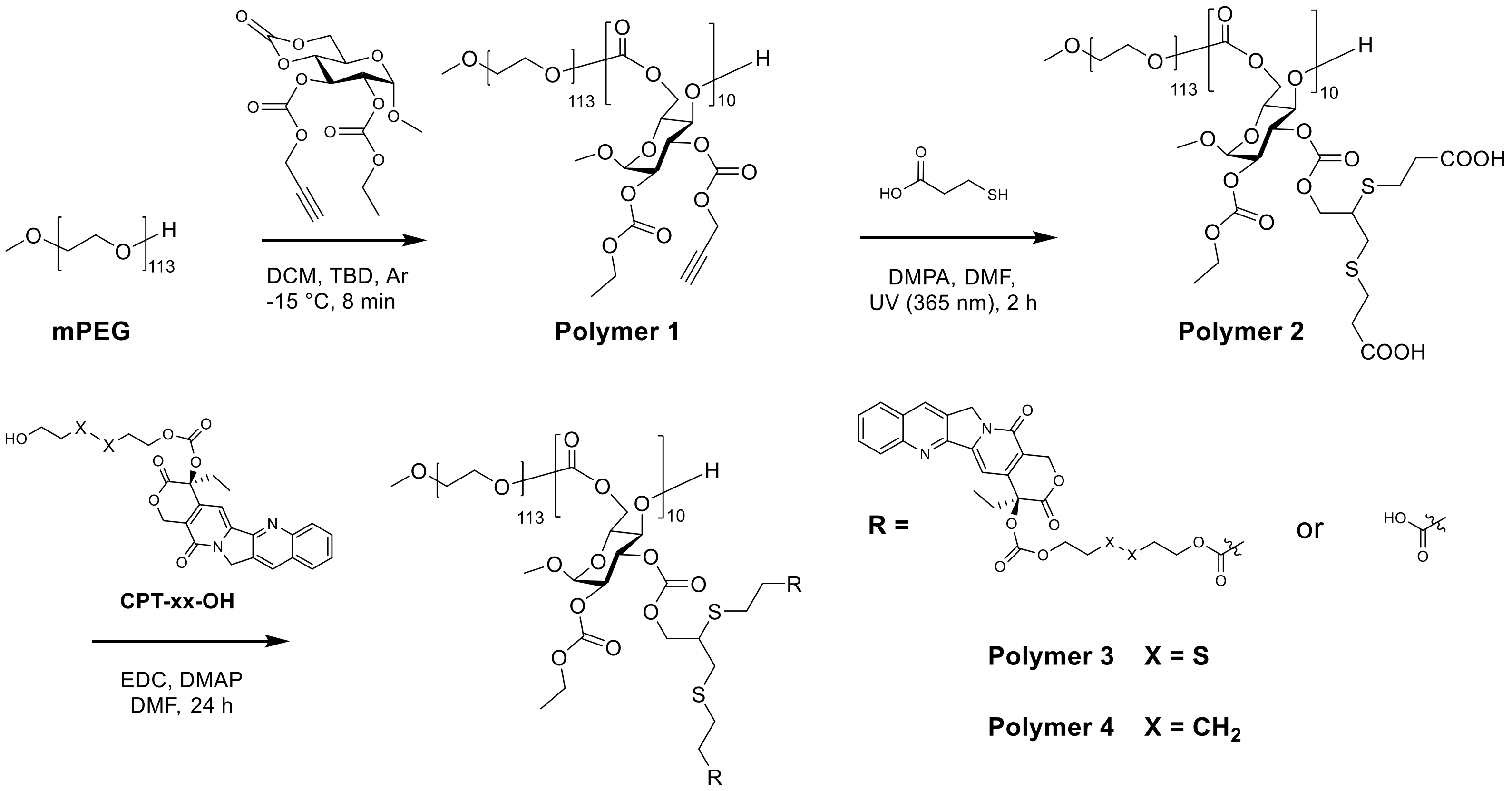

Scheme 3. Synthetic Scheme for the Preparation of CPT-Conjugated PEG-*b*-PDGC. Reprinted with permission from "A Tale of Drug-Carrier Optimization: Controlling Stimuli Sensitivity via Nanoparticle Hydrophobicity through Drug Loading" by Lin, Y.-N.; Khan, S.; Song, Y.; Dong, M.; Shen, Y.; Tran, D. K.; Pang, C.; Zhang, F.; Wooley, K. L., *Nano Letters* **2020**, 20 (9), 6563-6571. Copyright 2020 American Chemical Society.

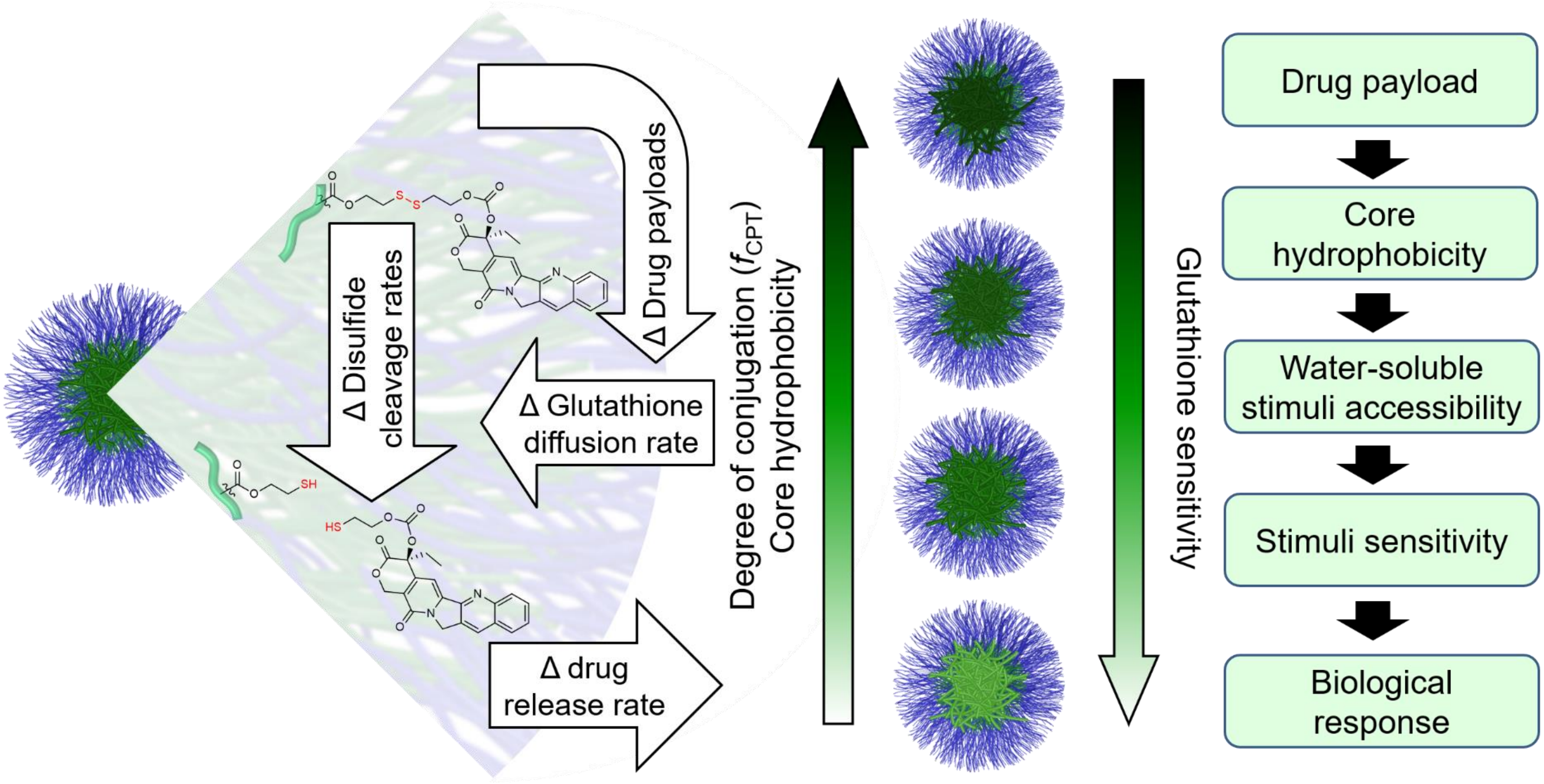

Scheme 4. Scheme for controlling GSH stimuli sensitivity via core hydrophobicity through drug loading. Reprinted with permission from "A Tale of Drug-Carrier Optimization: Controlling Stimuli Sensitivity via Nanoparticle Hydrophobicity through Drug Loading" by Lin, Y.-N.; Khan, S.; Song, Y.; Dong, M.; Shen, Y.; Tran, D. K.; Pang, C.; Zhang, F.; Wooley, K. L., *Nano Letters* **2020**, 20 (9), 6563-6571. Copyright 2020 American Chemical Society.

4.2. Results and Discussions

The CPT-conjugated PEG-*b*-PGCs were prepared by esterification between hydroxyl-functionalized CPT prodrugs (**CPT-xx-OH**) and carboxylic acid-functionalized PEG-*b*-PGC diblock copolymer (**2**). Polymer **2** was constructed by ring-opening polymerization (ROP) of a cyclic glucose carbonate monomer, followed by postpolymerization modification with mercaptopropionic acid (Scheme 3). Briefly, the diblock copolymer **1**, PEG_{113}-*b*-$PGC(EPC)_{10}$, was synthesized by organocatalyzed ROP of the bicyclic glucose carbonate methyl-2-*O*-ethyloxycarbonyl-3-*O*-propargyloxycarbonyl-4,6-*O*-carbonyl-α-d-glucopyranoside (GC(EPC)) at −15 °C in dichloromethane (DCM) with methoxy poly(ethylene glycol) ($mPEG_{113}$) as the macroinitiator and 1,5,7-triazabicyclo[4.4.0]-dec-5-ene (TBD) as the organocatalyst (Figure 37-Figure 39). The carboxylic acid-functionalized polymer **2**, PEG_{113}-*b*-$PGC(COOH)_{20}$, was then prepared by postpolymerization modification of **1** via photoinitiated thiol–yne click reactions using an excess of mercaptopropionic acid (>50 equiv relative to the alkyne groups) with 2,2-dimethoxy-2-phenylacetophenone (DMPA) as the photoinitiator (Figure 40-Figure 41). The CPT-conjugated polymers **3** and **4**, PEG_{113}-*b*-[$PGC(COOH)_{x}$-*co*-$PGC(CPT)_{20-x}$], were generated by postpolymerization modification of block copolymer **2** via 1-ethyl-3-(3-(dimethylamino)propyl)carbodiimide (EDC) mediated coupling reaction with (*S*)-4-ethyl-3,14-dioxo-3,4,12,14-tetrahydro-1*H*-pyrano[3′,4′:6,7]indolizino[1,2-β]quinolin-4-yl (2-((2-hydroxyethyl)disulfanyl)ethyl) carbonate (**CPT-ss-OH**) or (*S*)-4-ethyl-3,14-dioxo-3,4,12,14-tetrahydro-1*H*-pyrano[3′,4′:6,7]indolizino[1,2-β]quinolin-4-yl (6-

hydroxyhexyl) carbonate (**CPT-cc-OH**), respectively (Figure 42-Figure 48).

The f_{CPT} values were calculated from the ^{1}H nuclear magnetic resonance (NMR) spectra via comparison of the integral of the methyl protons originating from the ethyl carbonate side chain on the PGC segment resonating at 1.1–1.2 ppm with that of methyl protons from CPT at 0.91 ppm (Figure 43-Figure **45**, Figure 47). All polymers were rigorously characterized by ^{1}H NMR, ^{13}C NMR, Fourier-transform infrared spectroscopy (FT-IR), thermogravimetric analysis (TGA), and differential scanning calorimetry (DSC) (Figure 38-Figure 51).

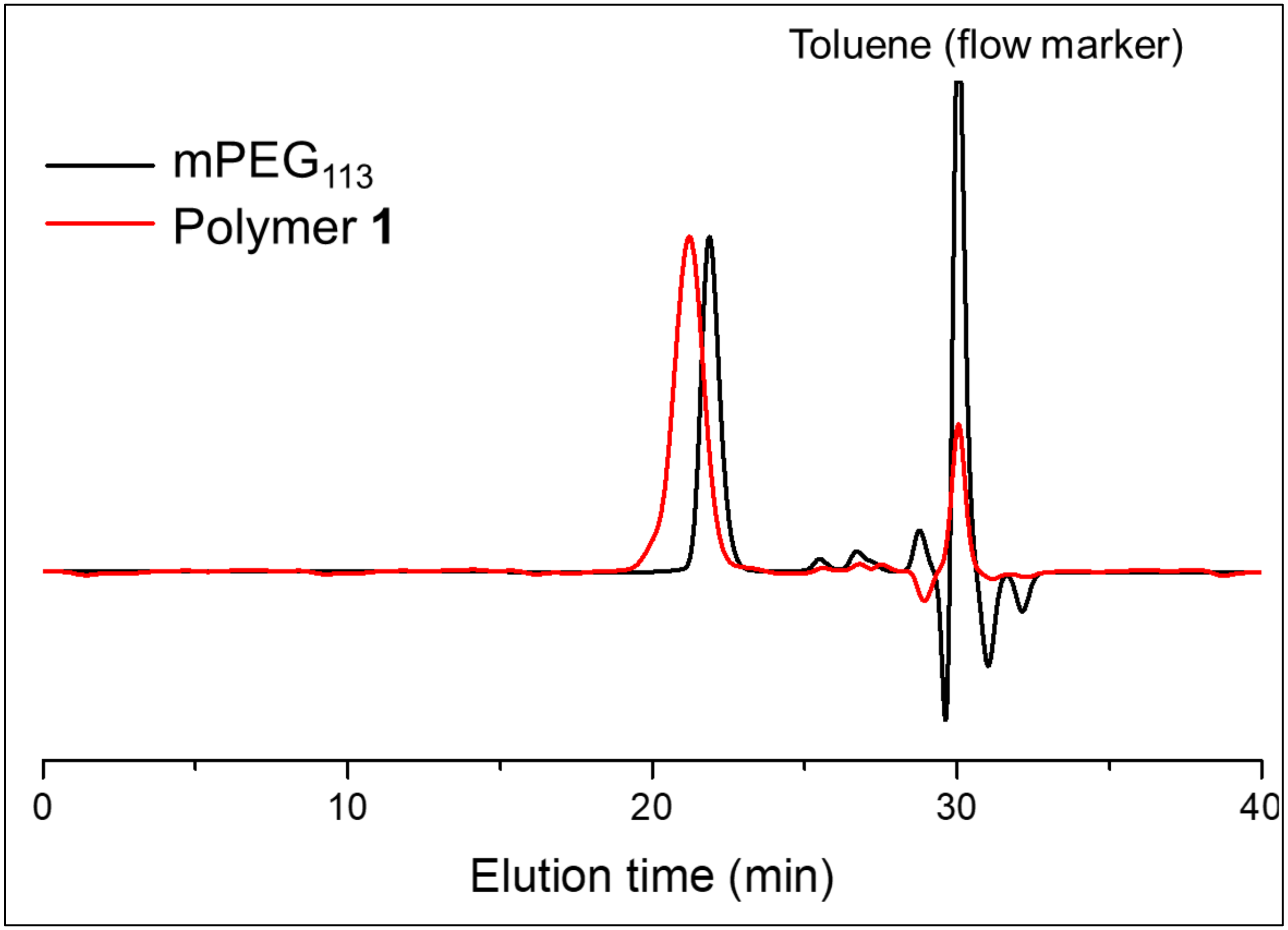

Figure 37. SEC traces of mPEG$_{113}$ and Polymer **1** in THF. Reprinted with permission from "A Tale of Drug-Carrier Optimization: Controlling Stimuli Sensitivity via Nanoparticle Hydrophobicity through Drug Loading" by Lin, Y.-N.; Khan, S.; Song, Y.; Dong, M.; Shen, Y.; Tran, D. K.; Pang, C.; Zhang, F.; Wooley, K. L., *Nano Letters* **2020**, 20 (9), 6563-6571. Copyright 2020 American Chemical Society.

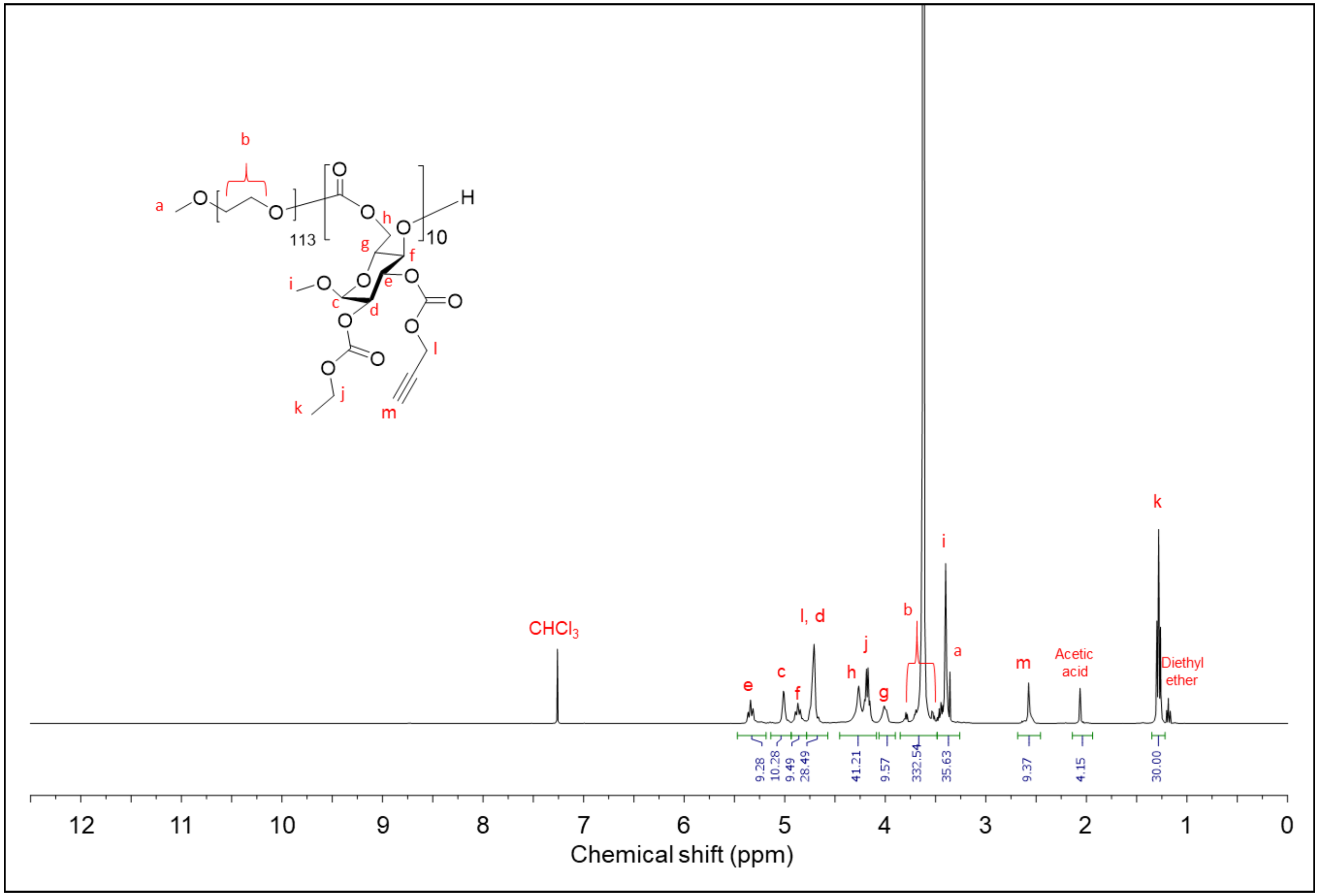

Figure 38. ^{1}H NMR spectrum (500 MHz) of polymer **1** in CDCl$_3$. Reprinted with permission from "A Tale of Drug-Carrier Optimization: Controlling Stimuli Sensitivity via Nanoparticle Hydrophobicity through Drug Loading" by Lin, Y.-N.; Khan, S.; Song, Y.; Dong, M.; Shen, Y.; Tran, D. K.; Pang, C.; Zhang, F.; Wooley, K. L., *Nano Letters* **2020**, 20 (9), 6563-6571. Copyright 2020 American Chemical Society.

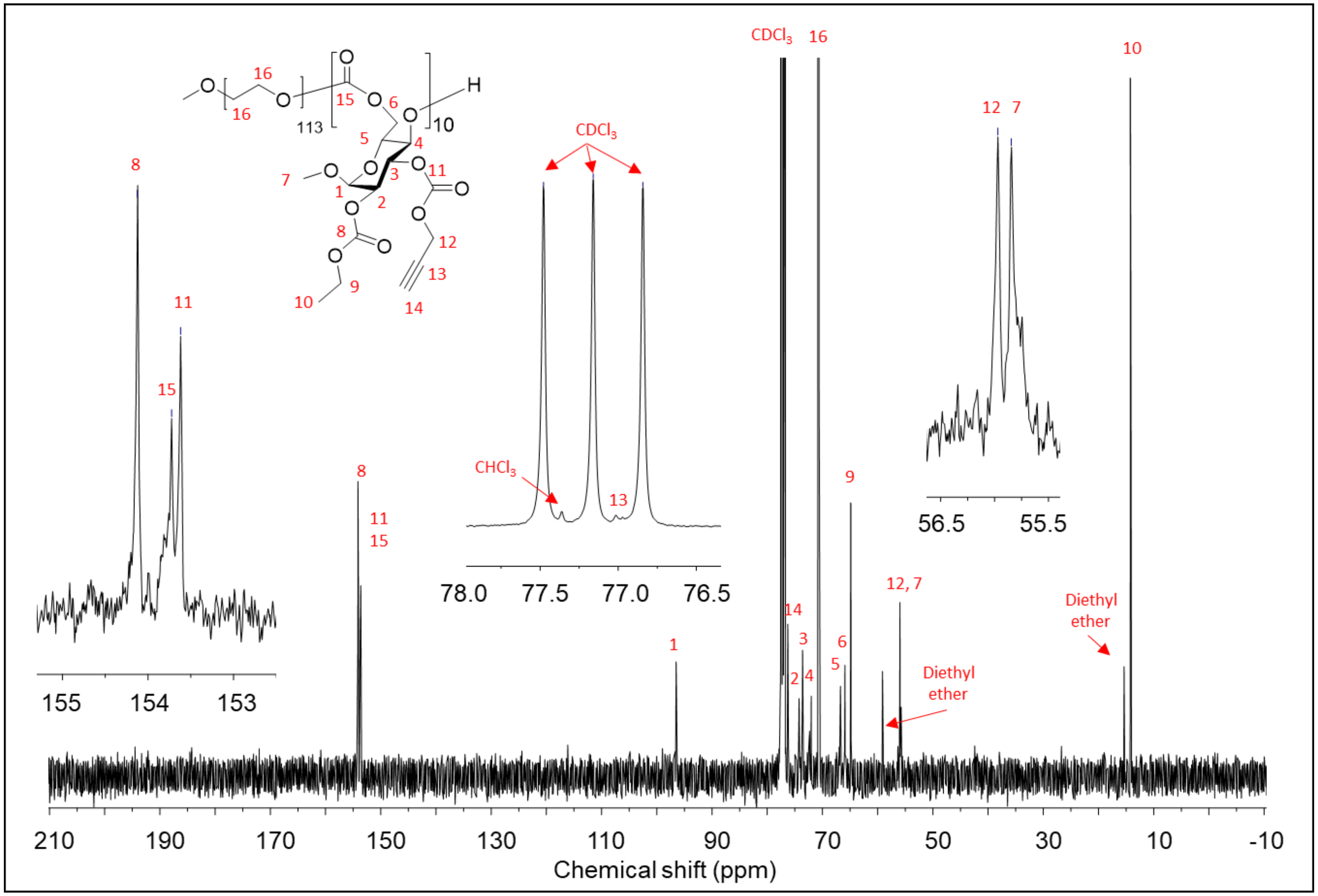

Figure 39. ^{13}C NMR spectrum (126 MHz) of polymer **1** in CDCl$_3$. Reprinted with permission from "A Tale of Drug-Carrier Optimization: Controlling Stimuli Sensitivity via Nanoparticle Hydrophobicity through Drug Loading" by Lin, Y.-N.; Khan, S.; Song, Y.; Dong, M.; Shen, Y.; Tran, D. K.; Pang, C.; Zhang, F.; Wooley, K. L., *Nano Letters* **2020**, 20 (9), 6563-6571. Copyright 2020 American Chemical Society.

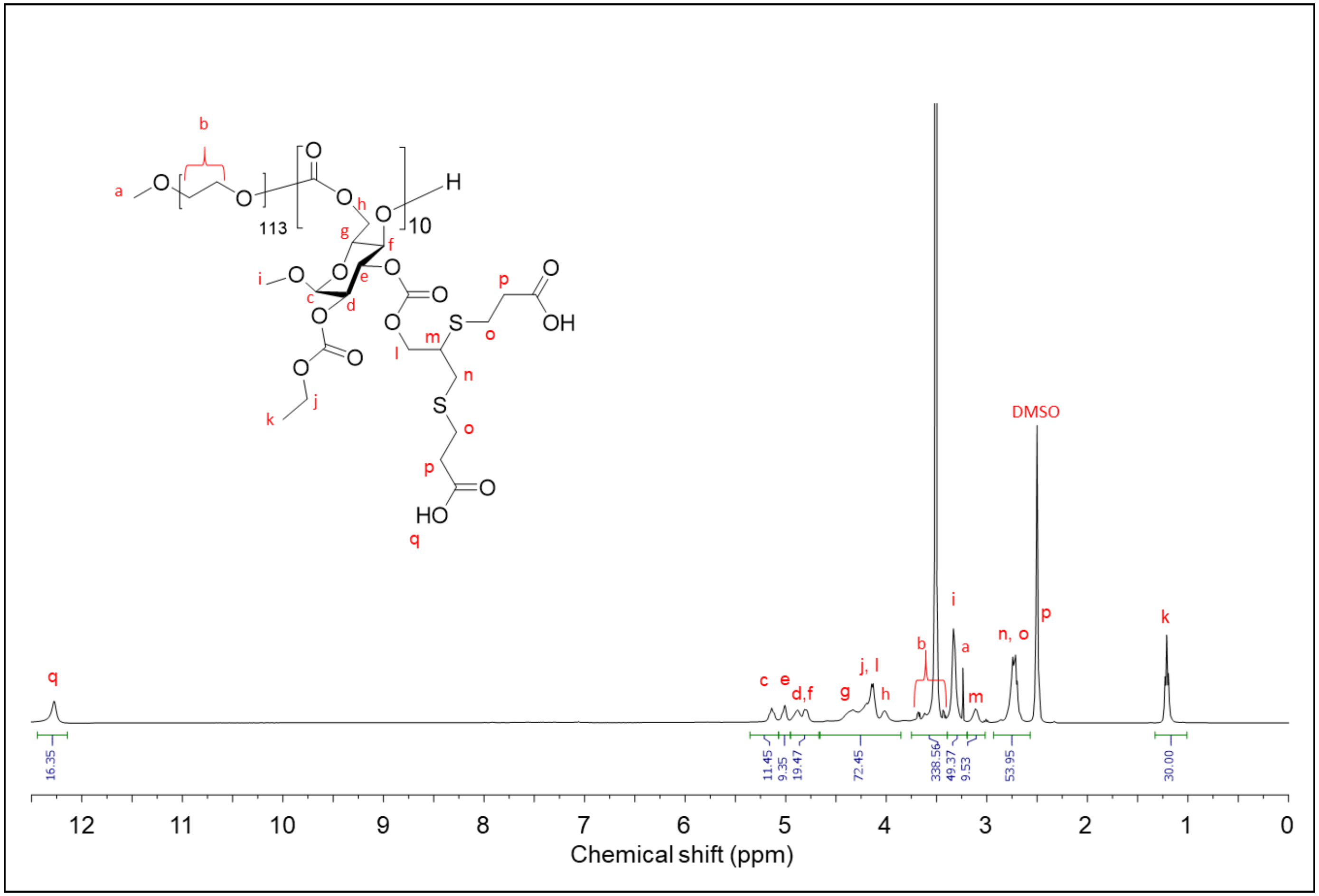

Figure 40. ^{1}H NMR spectrum (500 MHz) of polymer **2** in DMSO-d$_6$. Reprinted with permission from “A Tale of Drug-Carrier Optimization: Controlling Stimuli Sensitivity via Nanoparticle Hydrophobicity through Drug Loading” by Lin, Y.-N.; Khan, S.; Song, Y.; Dong, M.; Shen, Y.; Tran, D. K.; Pang, C.; Zhang, F.; Wooley, K. L., *Nano Letters* **2020**, 20 (9), 6563-6571. Copyright 2020 American Chemical Society.

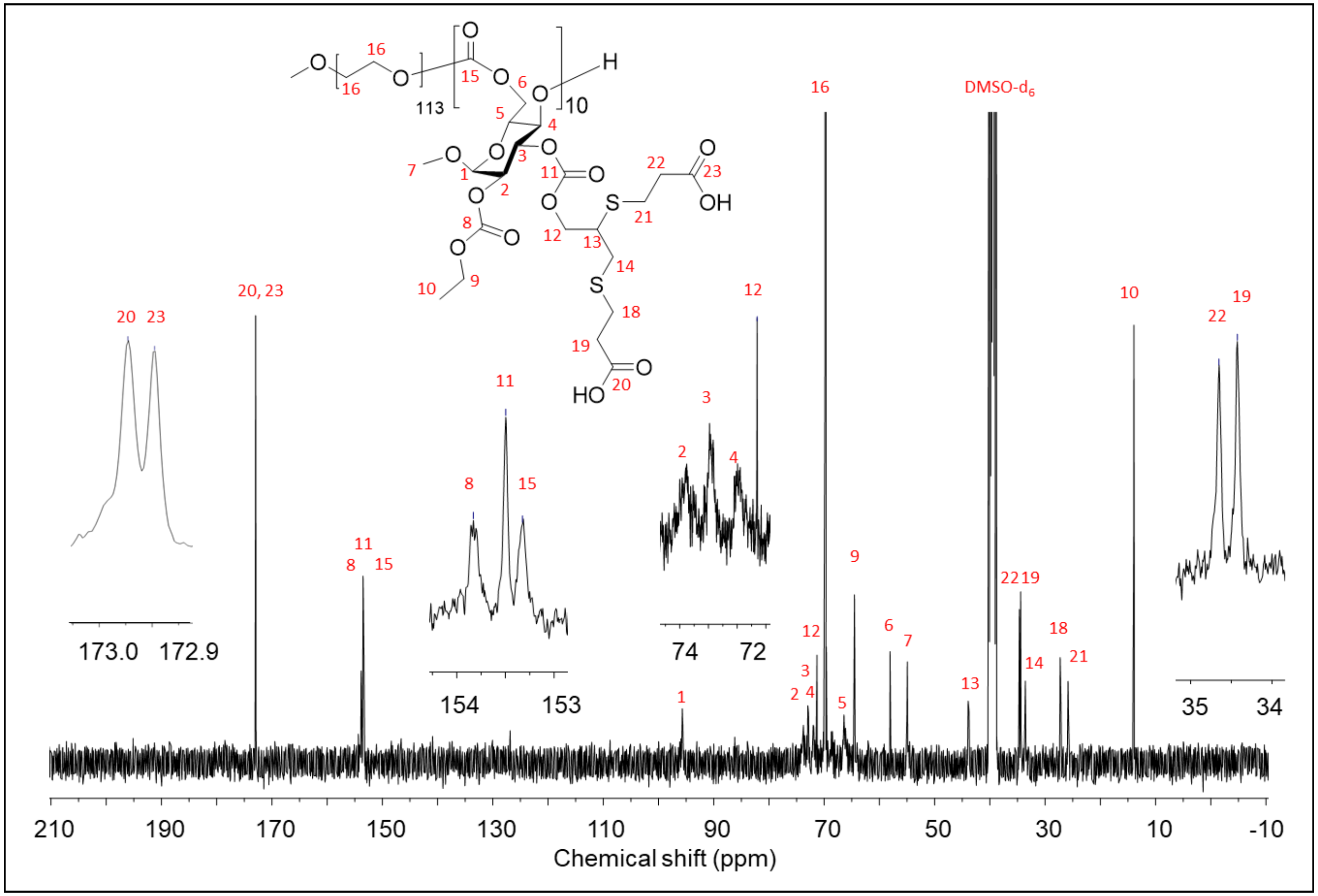

Figure 41. ^{13}C NMR spectrum (126 MHz) of polymer 2 in DMSO-d$_6$. Reprinted with permission from "A Tale of Drug-Carrier Optimization: Controlling Stimuli Sensitivity via Nanoparticle Hydrophobicity through Drug Loading" by Lin, Y.-N.; Khan, S.; Song, Y.; Dong, M.; Shen, Y.; Tran, D. K.; Pang, C.; Zhang, F.; Wooley, K. L., *Nano Letters* **2020**, 20 (9), 6563-6571. Copyright 2020 American Chemical Society.

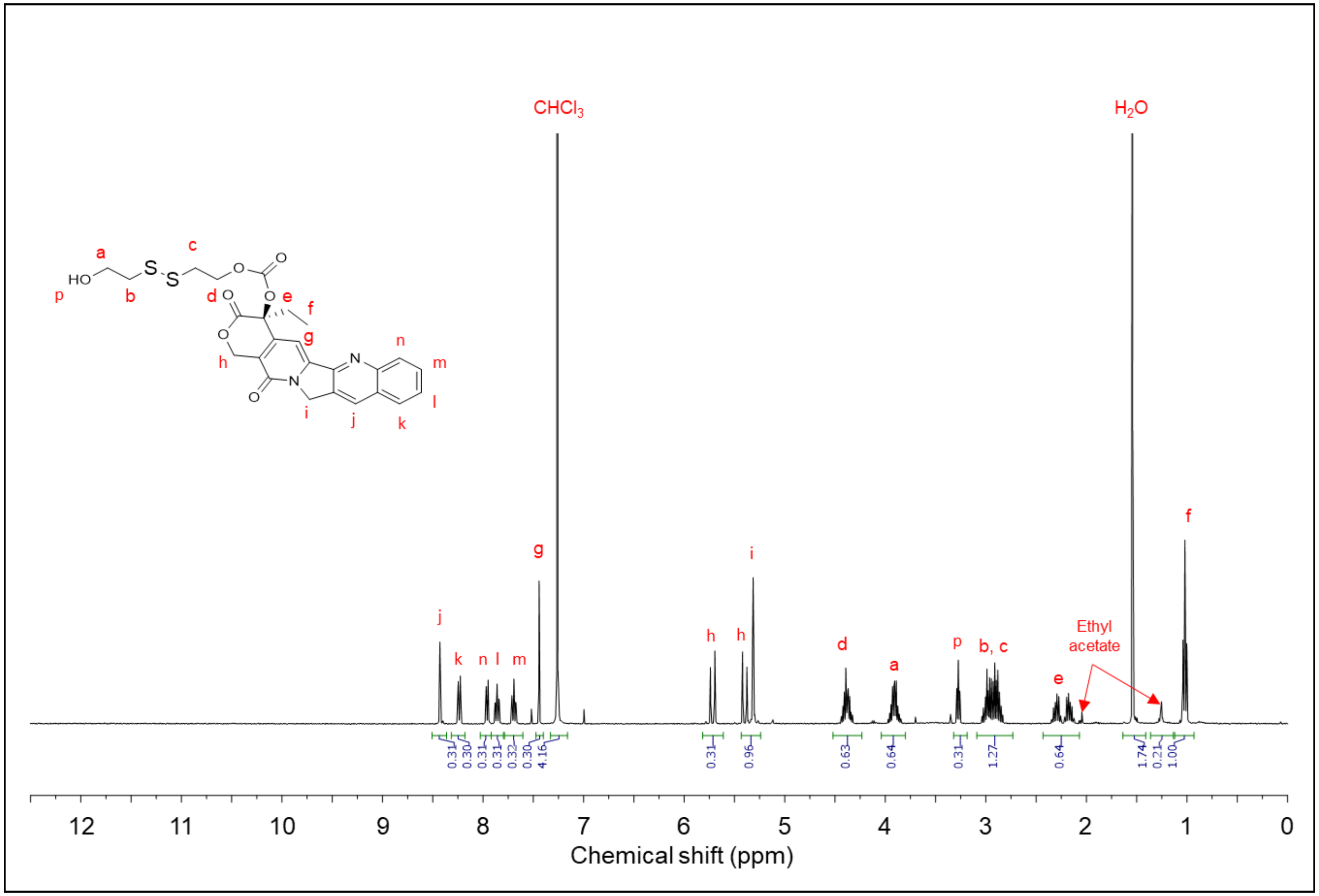

Figure 42. ^{1}H NMR spectrum (500 MHz) of CPT-ss-OH in $CDCl_3$. Reprinted with permission from "A Tale of Drug-Carrier Optimization: Controlling Stimuli Sensitivity via Nanoparticle Hydrophobicity through Drug Loading" by Lin, Y.-N.; Khan, S.; Song, Y.; Dong, M.; Shen, Y.; Tran, D. K.; Pang, C.; Zhang, F.; Wooley, K. L., *Nano Letters* **2020**, 20 (9), 6563-6571. Copyright 2020 American Chemical Society.

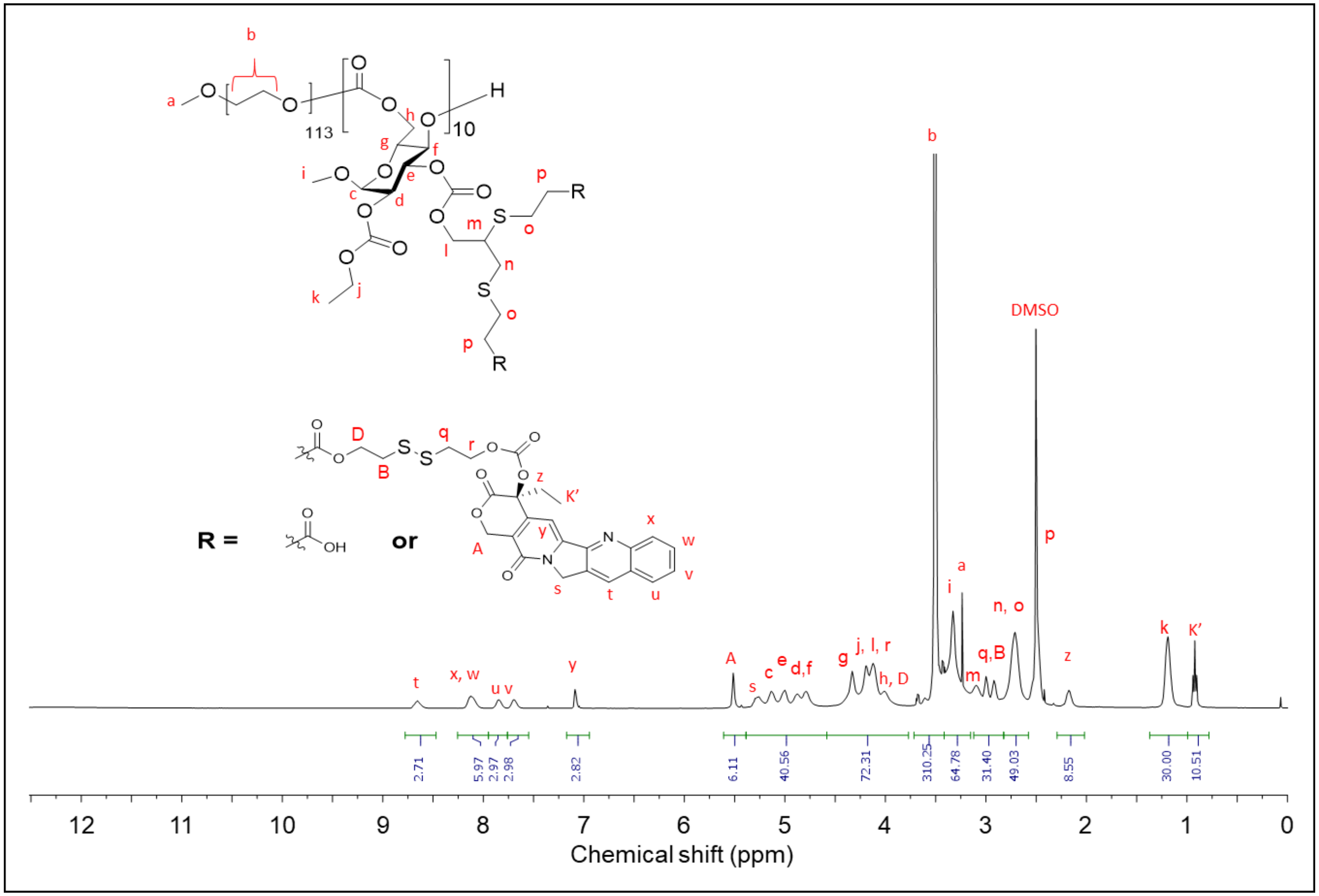

Figure 43. ^{1}H NMR spectrum (500 MHz) of polymer 3 (f_{CPT} = 0.15) in DMSO-d_6. Reprinted with permission from “A Tale of Drug-Carrier Optimization: Controlling Stimuli Sensitivity via Nanoparticle Hydrophobicity through Drug Loading” by Lin, Y.-N.; Khan, S.; Song, Y.; Dong, M.; Shen, Y.; Tran, D. K.; Pang, C.; Zhang, F.; Wooley, K. L., *Nano Letters* **2020**, 20 (9), 6563-6571. Copyright 2020 American Chemical Society.

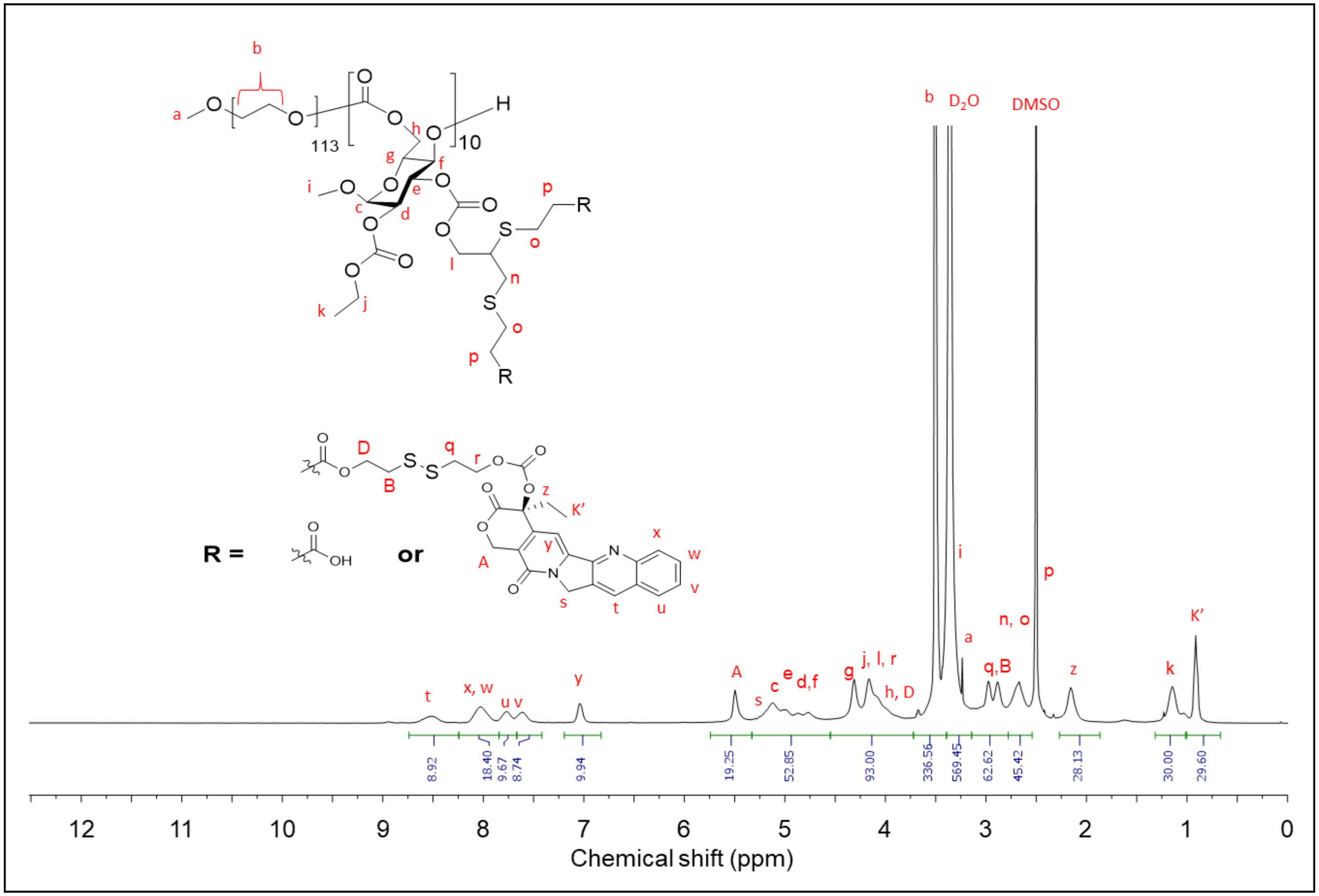

Figure 44. ^{1}H NMR spectrum (500 MHz) of polymer 3 (f_{CPT} = 0.50) in DMSO-d$_6$. Reprinted with permission from "A Tale of Drug-Carrier Optimization: Controlling Stimuli Sensitivity via Nanoparticle Hydrophobicity through Drug Loading" by Lin, Y.-N.; Khan, S.; Song, Y.; Dong, M.; Shen, Y.; Tran, D. K.; Pang, C.; Zhang, F.; Wooley, K. L., *Nano Letters* **2020**, 20 (9), 6563-6571. Copyright 2020 American Chemical Society.

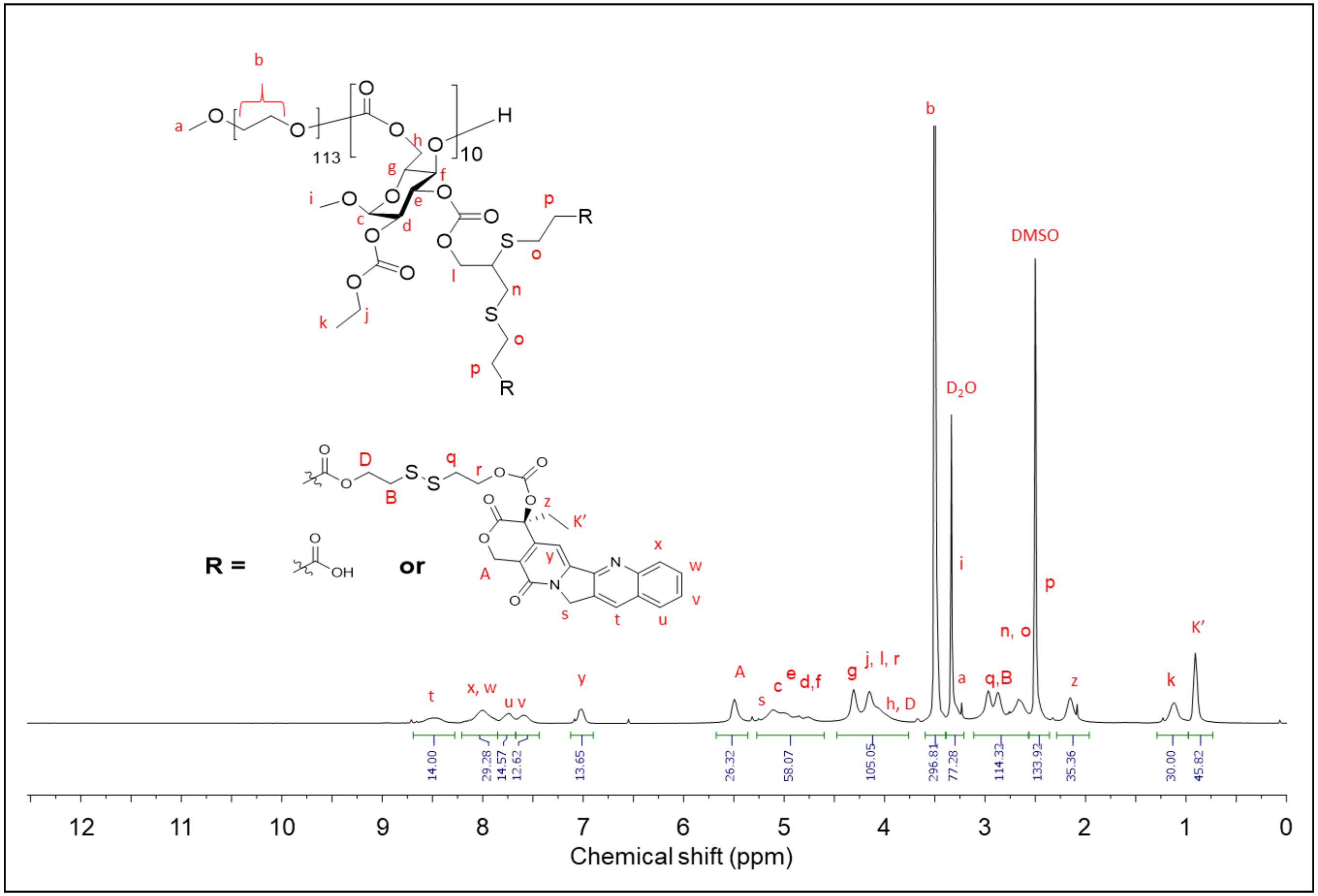

Figure 45. ^{1}H NMR spectrum (500 MHz) of polymer **3** (f_{CPT} = 0.85) in DMSO-d$_6$. Reprinted with permission from "A Tale of Drug-Carrier Optimization: Controlling Stimuli Sensitivity via Nanoparticle Hydrophobicity through Drug Loading" by Lin, Y.-N.; Khan, S.; Song, Y.; Dong, M.; Shen, Y.; Tran, D. K.; Pang, C.; Zhang, F.; Wooley, K. L., *Nano Letters* **2020**, 20 (9), 6563-6571. Copyright 2020 American Chemical Society.

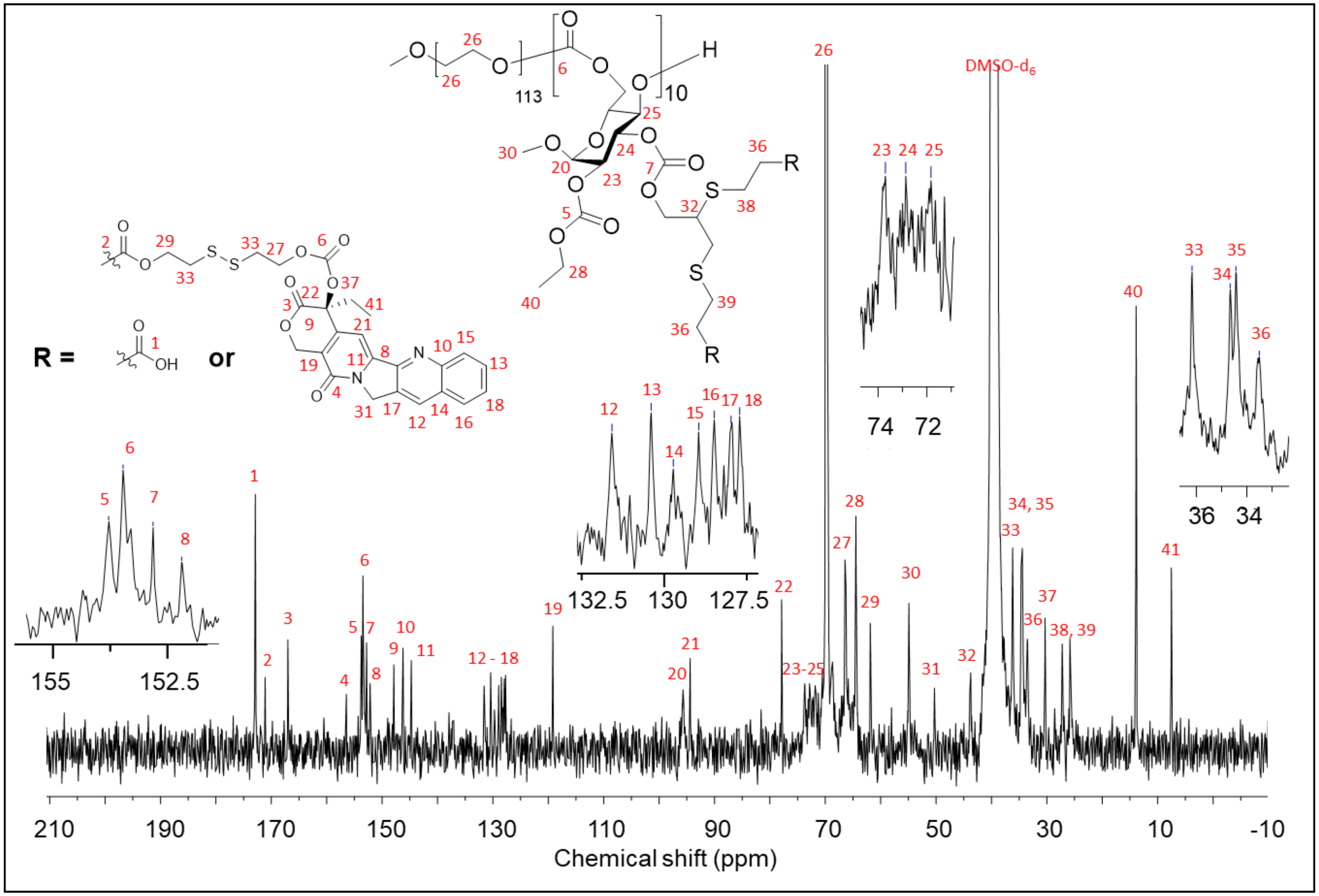

Figure 46. ^{13}C NMR spectrum (126 MHz) of polymer 3 (f_{CPT} = 0.15) in DMSO-d$_6$. Reprinted with permission from “A Tale of Drug-Carrier Optimization: Controlling Stimuli Sensitivity via Nanoparticle Hydrophobicity through Drug Loading” by Lin, Y.-N.; Khan, S.; Song, Y.; Dong, M.; Shen, Y.; Tran, D. K.; Pang, C.; Zhang, F.; Wooley, K. L., *Nano Letters* **2020**, 20 (9), 6563-6571. Copyright 2020 American Chemical Society.

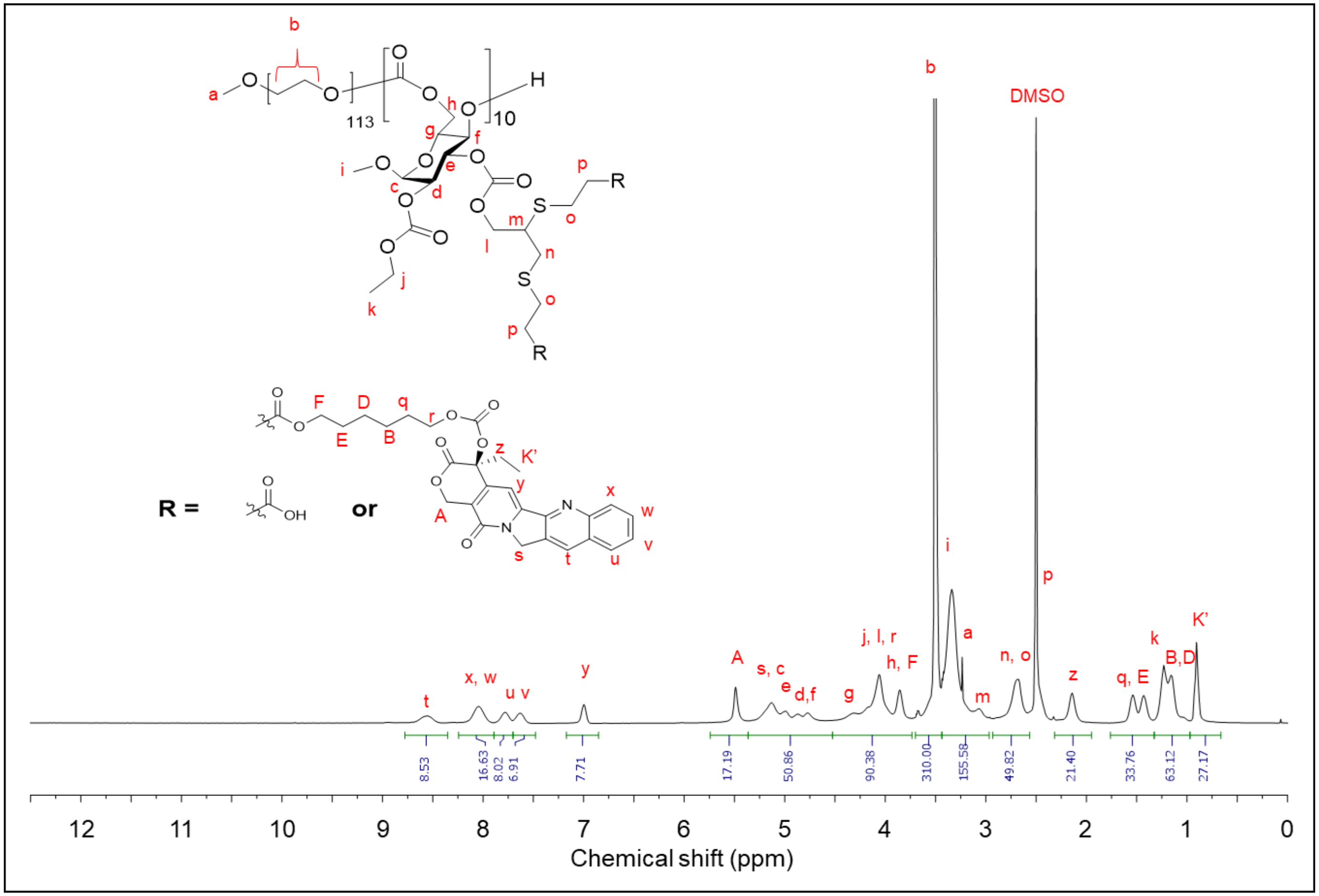

Figure 47. ^{1}H NMR spectrum (500 MHz) of polymer 4 in DMSO-d$_6$. Reprinted with permission from "A Tale of Drug-Carrier Optimization: Controlling Stimuli Sensitivity via Nanoparticle Hydrophobicity through Drug Loading" by Lin, Y.-N.; Khan, S.; Song, Y.; Dong, M.; Shen, Y.; Tran, D. K.; Pang, C.; Zhang, F.; Wooley, K. L., *Nano Letters* **2020**, 20 (9), 6563-6571. Copyright 2020 American Chemical Society.

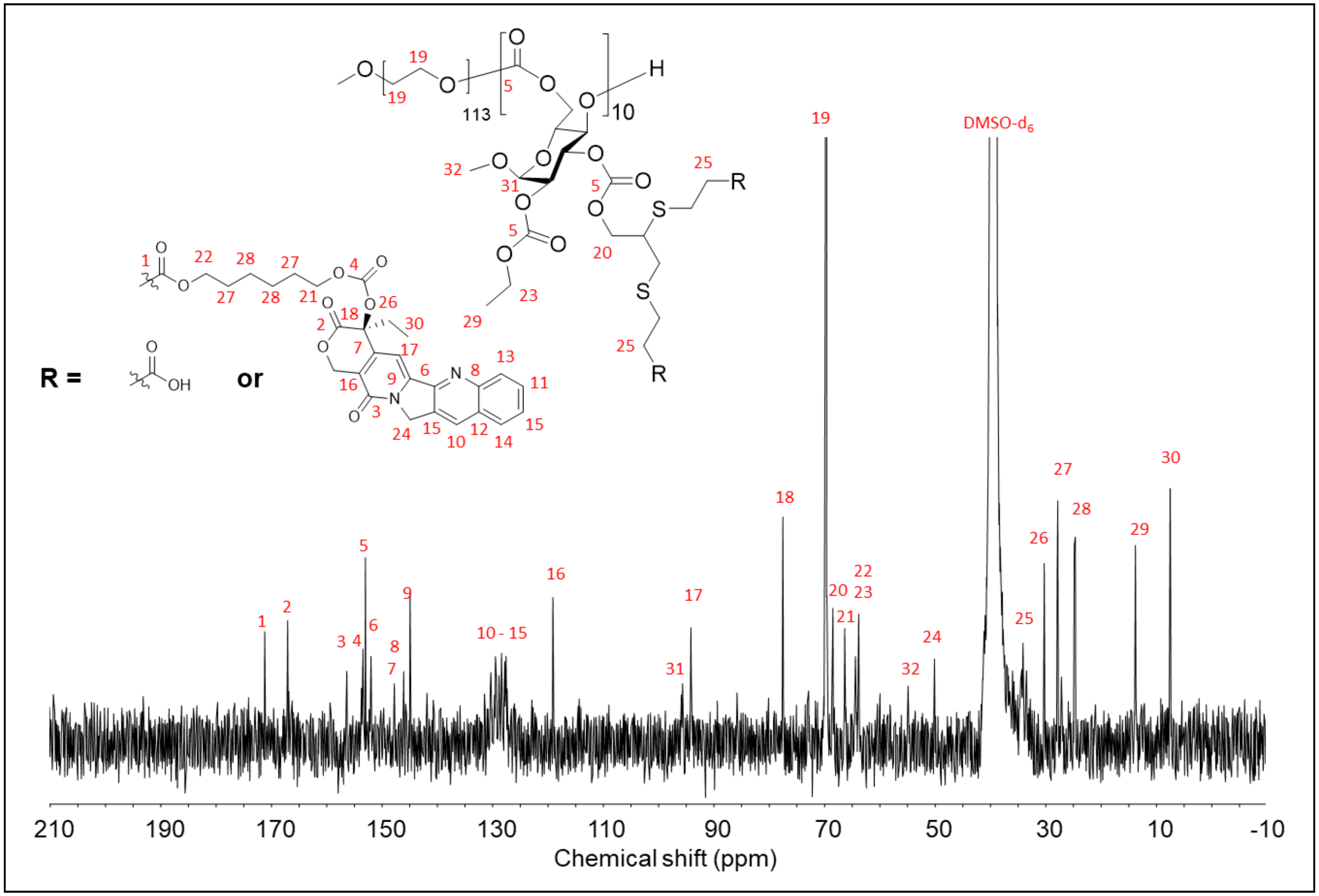

Figure 48. ^{13}C NMR spectrum (126 MHz) of polymer 4 in DMSO-d$_6$. Reprinted with permission from “A Tale of Drug-Carrier Optimization: Controlling Stimuli Sensitivity via Nanoparticle Hydrophobicity through Drug Loading” by Lin, Y.-N.; Khan, S.; Song, Y.; Dong, M.; Shen, Y.; Tran, D. K.; Pang, C.; Zhang, F.; Wooley, K. L., *Nano Letters* **2020**, 20 (9), 6563-6571. Copyright 2020 American Chemical Society.

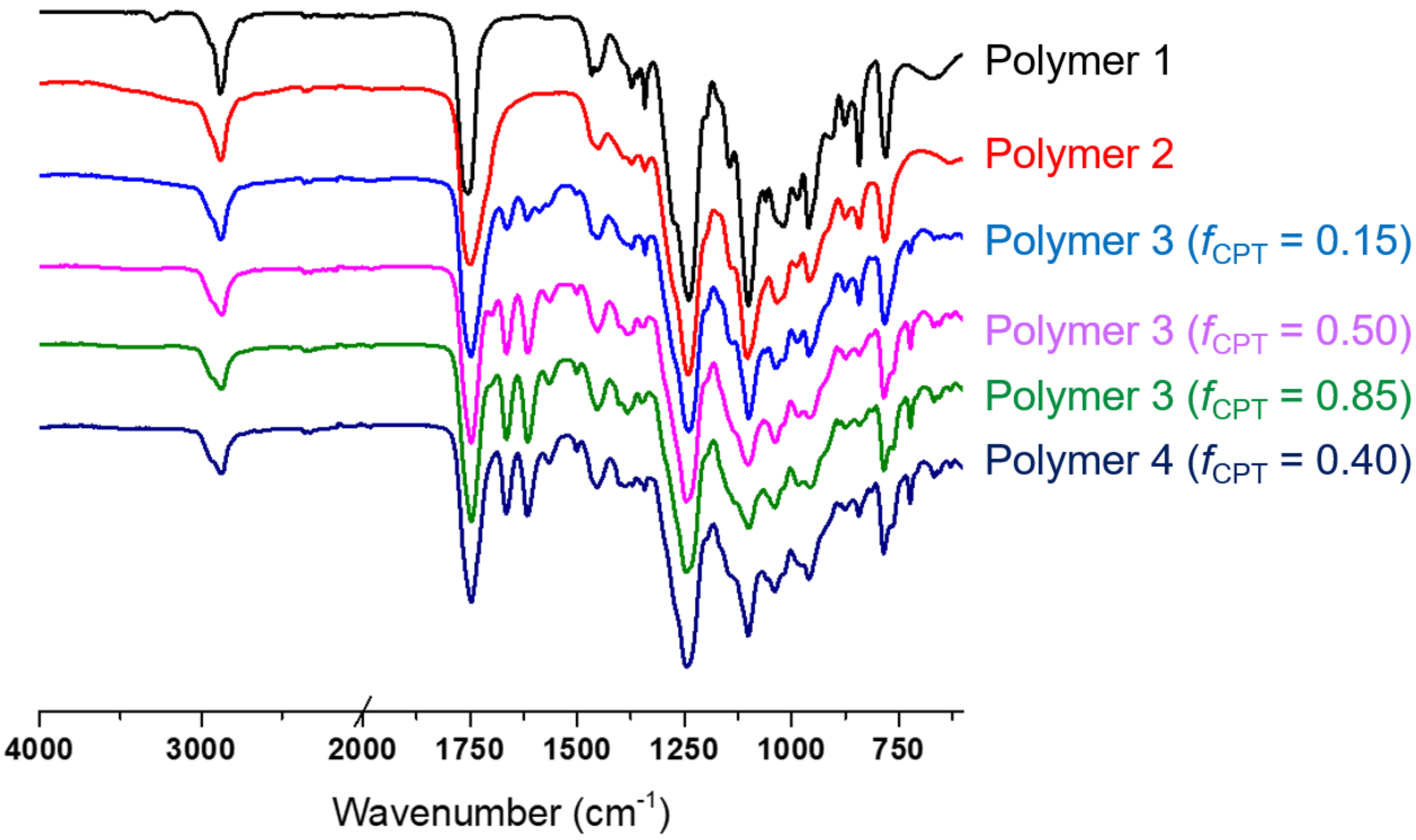

Figure 49. FTIR spectra of polymers 1-4. Reprinted with permission from "A Tale of Drug-Carrier Optimization: Controlling Stimuli Sensitivity via Nanoparticle Hydrophobicity through Drug Loading" by Lin, Y.-N.; Khan, S.; Song, Y.; Dong, M.; Shen, Y.; Tran, D. K.; Pang, C.; Zhang, F.; Wooley, K. L., *Nano Letters* **2020**, 20 (9), 6563-6571. Copyright 2020 American Chemical Society.

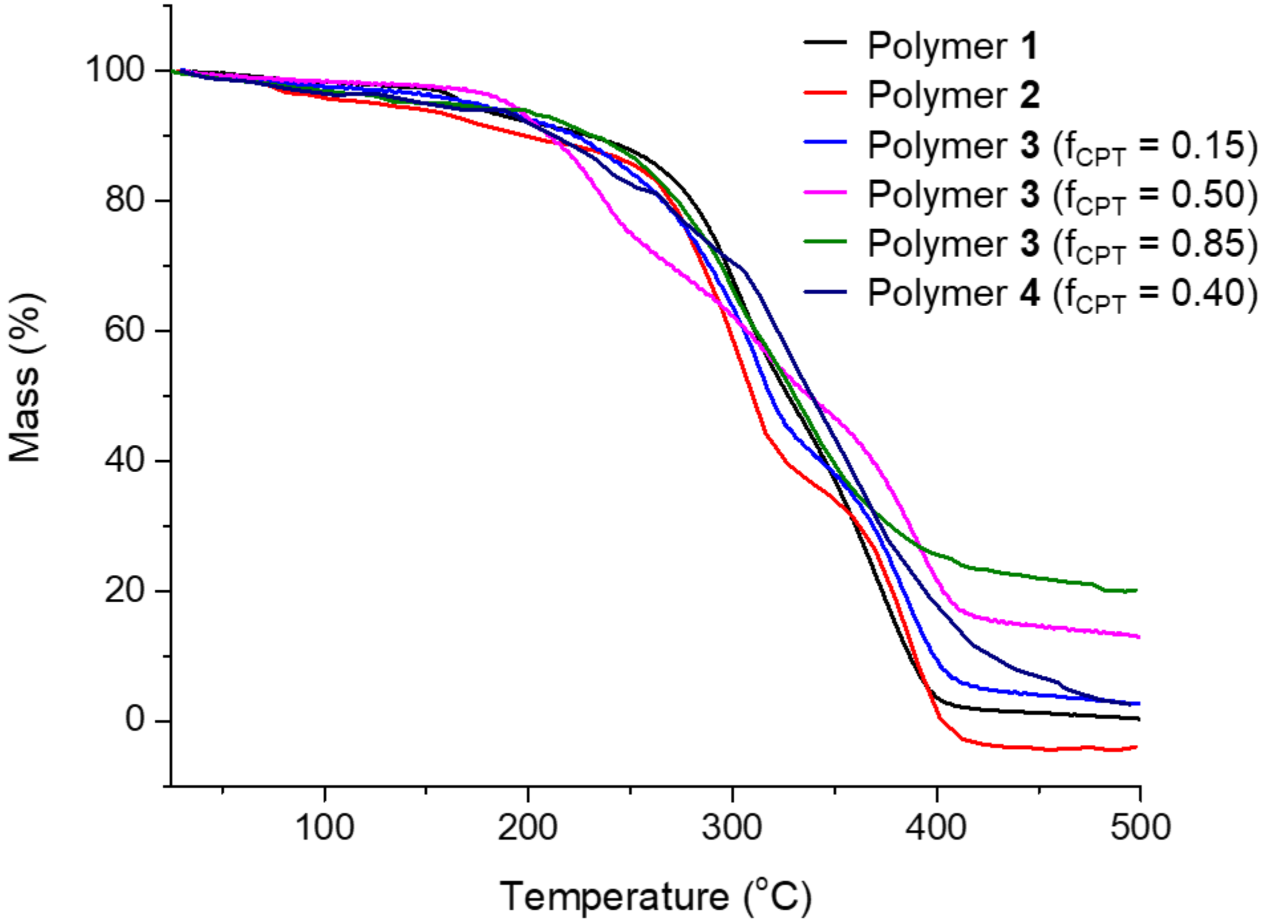

Figure 50. TGA traces of Polymer **1-4**. Reprinted with permission from "A Tale of Drug-Carrier Optimization: Controlling Stimuli Sensitivity via Nanoparticle Hydrophobicity through Drug Loading" by Lin, Y.-N.; Khan, S.; Song, Y.; Dong, M.; Shen, Y.; Tran, D. K.; Pang, C.; Zhang, F.; Wooley, K. L., *Nano Letters* **2020**, 20 (9), 6563-6571. Copyright 2020 American Chemical Society.

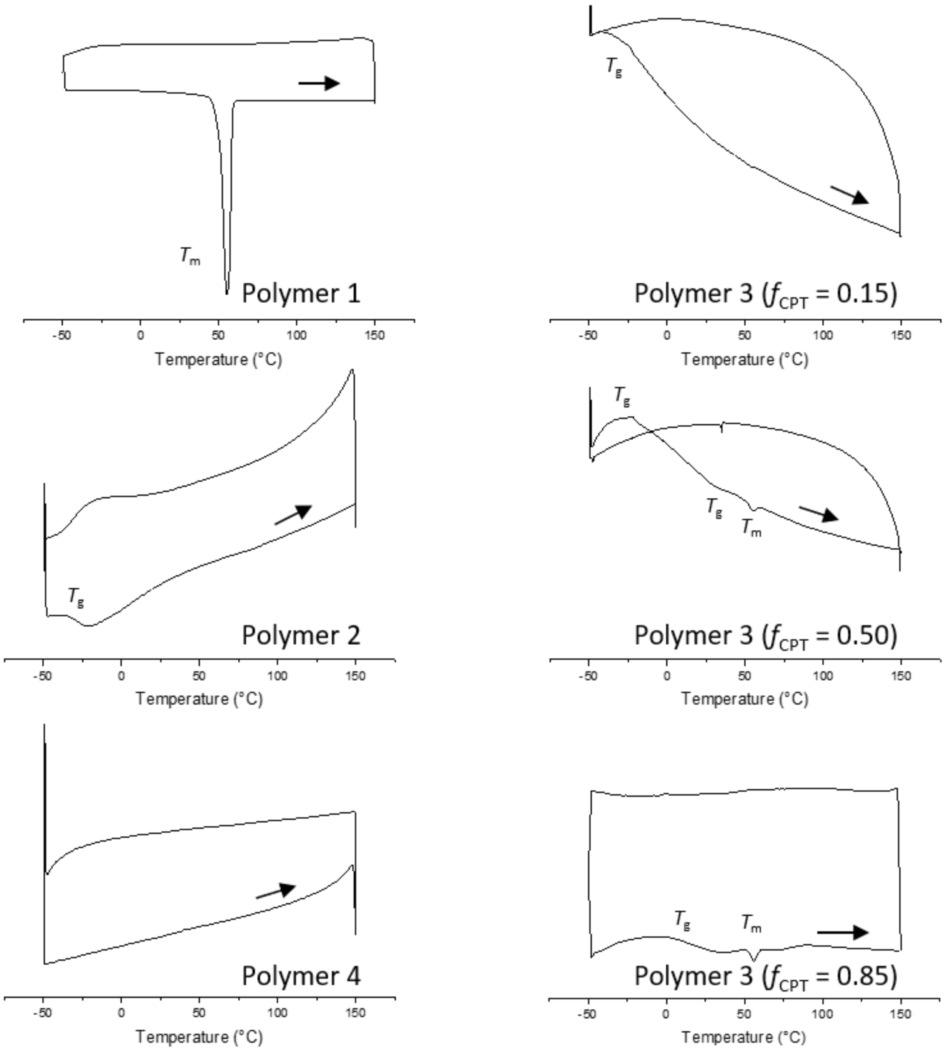

Figure 51. DSC traces for Polymer **1-4**. Glass transition temperature (T_g) and melting transition temperature (T_m) are labeled on the thermograms. Arrows indicate the direction of temperature ramping. Reprinted with permission from "A Tale of Drug-Carrier Optimization: Controlling Stimuli Sensitivity via Nanoparticle Hydrophobicity through Drug Loading" by Lin, Y.-N.; Khan, S.; Song, Y.; Dong, M.; Shen, Y.; Tran, D. K.; Pang, C.; Zhang, F.; Wooley, K. L., *Nano Letters* **2020**, 20 (9), 6563-6571. Copyright 2020 American Chemical Society.

Polymer assemblies (0.5 mg/mL) were prepared by nanoprecipitation from DMSO into nanopure water and then dialyzed against nanopure water for 24 h to remove organic solvent. The number-average hydrodynamic diameters ($D_{h(\text{number})}$) of the polymer nanoconstructs were in the range 20–50 nm (Figure 52). Transmission electron microscopy (TEM) and atomic force microscopy (AFM) analyses of polymer nanoparticles showed globular structures with average diameters in agreement with those obtained from dynamic light scattering (DLS), independent of fCPT.

However, polymer **3** assemblies exhibited significant f_{CPT}-dependent heights and diameter-to-height (D/H) ratios, with number-average heights ranging from 2 to 10 nm and D/H ratios ranging from 4 to 26 (Figure 52). At low CPT conjugation levels, the polymer assemblies exhibited significantly lower heights and greater D/H ratios, with f_{CPT} of 0 and 0.15 having heights that were ca. 4–5-fold lower and D/H ratios that were ca. 4–6-fold higher than those of the polymer assemblies with f_{CPT} of 0.50 and 0.85. These AFM data indicated that the nanomaterials with lower f_{CPT} deformed to a greater extent upon drop deposition from aqueous solution onto the polar mica substrate, suggesting greater water plasticization of the nanostructures. In contrast, the higher f_{CPT} counterparts remained as stable, globular structures (Figure 52), suggesting greater rigidity provided by exclusion of water from the more hydrophobic core domains.

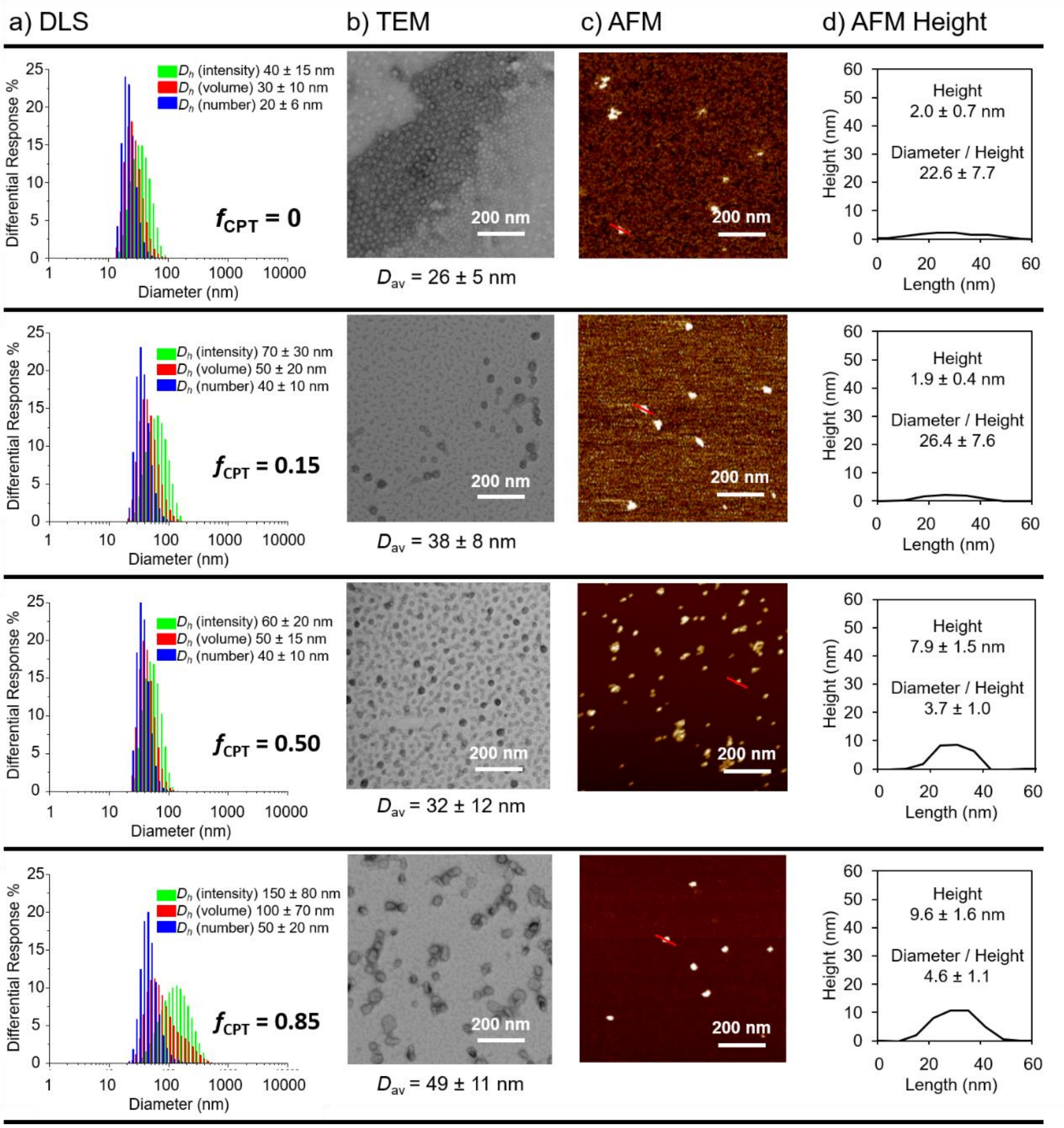

Figure 52. Morphological characterizations of the polymer assemblies using (a) DLS, (b) TEM, (c) AFM, and (d) AFM height profile. From top to bottom: Polymer 2 (f_{CPT} = 0), polymer 3 (f_{CPT} = 0.15), polymer 3 (f_{CPT} = 0.50), and polymer 3 (f_{CPT} = 0.85). Reprinted with permission from "A Tale of Drug-Carrier Optimization: Controlling Stimuli Sensitivity via Nanoparticle Hydrophobicity through Drug Loading" by Lin, Y.-N.; Khan, S.; Song, Y.; Dong, M.; Shen, Y.; Tran, D. K.; Pang, C.; Zhang, F.; Wooley, K. L., *Nano Letters* **2020**, 20 (9), 6563-6571. Copyright 2020 American Chemical Society.

As a measure of the local microenvironment within the polymer nanoassemblies, solution-state ^{1}H NMR spectroscopy was employed to monitor the mobility of the PGC chain segments when packaged within nanoassemblies in D_2O vs as solvated polymer chains in DMSO-d_6, confirming that higher f_{CPT} led to lower water accessibility. The previous literature has reported the importance of the microenvironment adjacent to disulfide bonds for controlling the thiol–disulfide exchange kinetics.[148-149] The NMR signal corresponding to the PGC ethyl carbonate methyl proton resonance (i.e., 1.2 ppm, highlighted in green in Figure 53) was utilized to probe the microenvironment adjacent to the disulfide-linkages in the assembly core. Poor solvation of the relatively hydrophobic PGC segment in the aqueous environment was made evident by the reduction of intensity and broadening of the PGC-associated proton resonances in D_2O, in comparison to protons of the PEG segments (Figure 53a). This phenomenon was quantified by the ratio of the ^{1}H NMR integrations between PEG-associated protons resonating at 3.6 ppm and PGC-associated protons resonating at 1.2 ppm (Figure 53c). The relative change in NMR signal intensity provides insights into the molecular microenvironment. As f_{CPT} increased from 0 to 0.85, the integral ratio (δ 3.6 ppm/δ 1.2 ppm) underwent an ca. 15-fold increase from 25 to 372 in D_2O, indicating reduced solvation of the disulfide-containing PGC segment in aqueous media (Figure 53c). At $f_{CPT} \geq 0.50$, minimal proton resonances from CPT and PGC were observed in the ^{1}H NMR spectra, indicating reduced chain mobility caused by limited aqueous accessibility. CPT influenced the chemical shifts of the methyl protons, presumably due to intramolecular van der Waals interactions, resulting in a slight upfield shift of the PGC ethyl carbonate methyl proton resonance as f_{CPT} increased (Figure 53b).[170-172] The integral ratio (δ 3.6 ppm/δ 1.2–1.1 ppm) remained constant at ca. 11 when any of the four polymers was solvated in DMSO-d_6 (Figure 53b,c) independent of f_{CPT}. The lack of change for proton relaxation in DMSO-d_6 verified that the integral ratio changes in D_2O were due to differential solvation between PEG and PGC segments with a lower aqueous accessibility of the core-forming sugar segment (Figure 53).

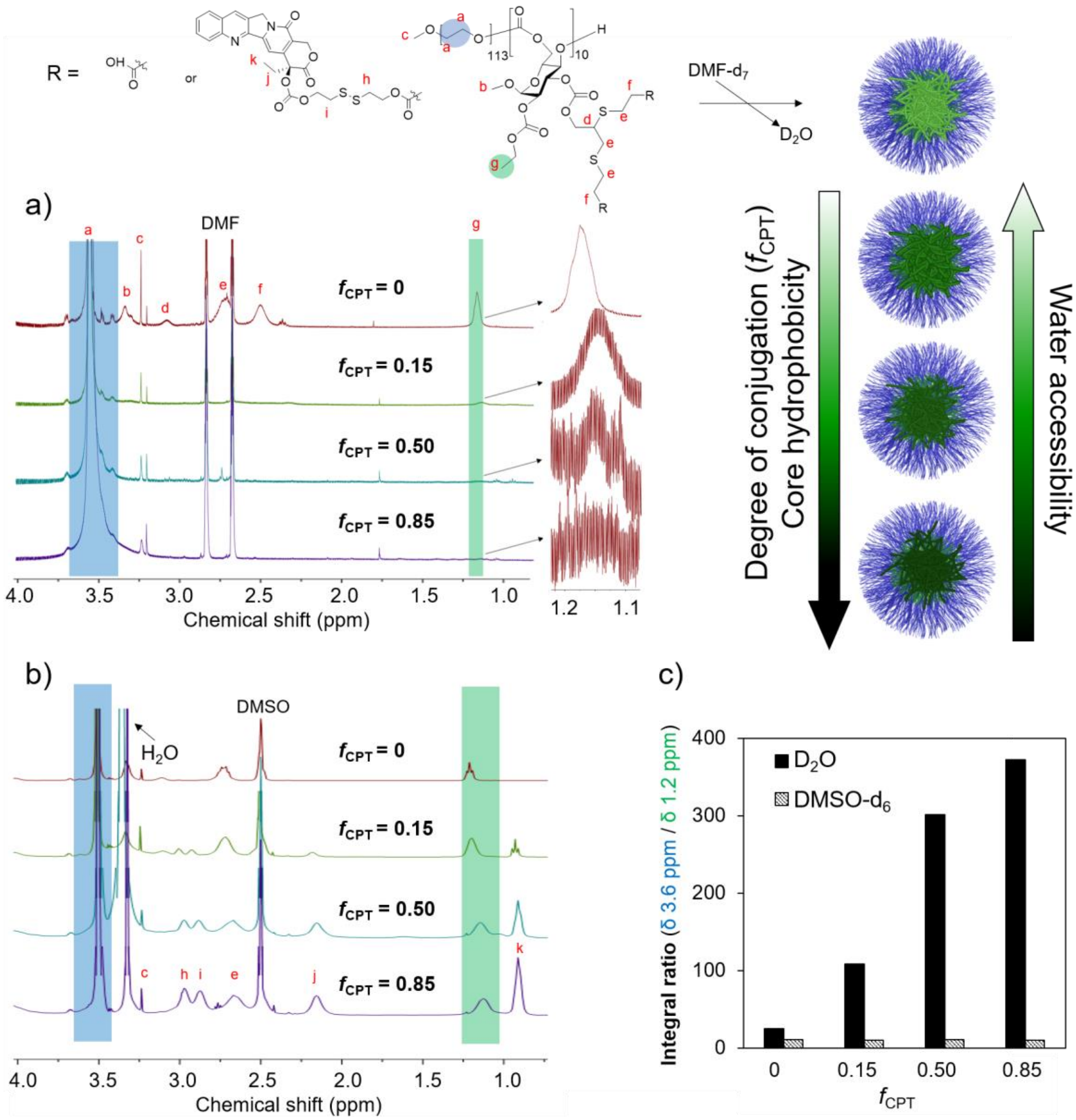

Figure 53. (a) ^{1}H NMR spectra for the assemblies from polymers **2** and **3** in D$_2$O, highlighting the PEG methylene proton resonance (δ 3.6 ppm, blue) and the PGC ethyl carbonate methyl proton resonance (δ 1.2-1.1 ppm, green). (b) ^{1}H NMR spectra for polymers **2** and **3** in DMSO-d$_6$. (c) Integral ratios (δ 3.6 ppm / δ 1.2-1.1 ppm) in D$_2$O *vs.* DMSO-d$_6$. Reprinted with permission from "A Tale of Drug-Carrier Optimization: Controlling Stimuli Sensitivity via Nanoparticle Hydrophobicity through Drug Loading" by Lin, Y.-N.; Khan, S.; Song, Y.; Dong, M.; Shen, Y.; Tran, D. K.; Pang, C.; Zhang, F.; Wooley, K. L., *Nano Letters* **2020**, 20 (9), 6563-6571. Copyright 2020 American Chemical Society.

The higher aqueous accessibility led to an increase in the GSH sensitivity, as revealed by disulfide cleavage experiments in PBS solutions (pH = 7.4) at 37 °C in the presence of GSH (5 mM) as a function of time (Figure 54). Calculations of the % disulfide cleavage were based on the free CPT concentrations in aliquots collected at predetermined time points using high-performance liquid chromatography (HPLC).[173] CPT was released from polymer **3** assemblies upon exposure to GSH, with an initial rapid release followed by sustained release (Figure 54a, c). Higher f_{CPT} led to slower GSH-triggered disulfide cleavage and CPT release. In the presence of 5 mM GSH, polymer **3** assemblies underwent 30%, 20%, and 14% of the total CPT release in the first 4 h with f_{CPT} of 0.15, 0.50, and 0.85, respectively. After 72 h, polymer **3** assemblies with f_{CPT} of 0.15, 0.50, and 0.85 had released 85%, 67%, and 45% of the total CPT, respectively (Figure 54a). Although the lowest f_{CPT} of 0.15 achieved the fastest and greatest % CPT release, it resulted in the lowest CPT concentration due to the limited overall amount of drug loaded (Figure 54c and Table 3). As expected, minimal disulfide cleavage occurred in samples without GSH (Figure 54b, d). As control studies, assemblies of non-redox-responsive CPT-conjugated polymer **4** exhibited minimal CPT release with or without GSH over a period of 72 h (Figure 54). Interestingly, polymer **3** assemblies with f_{CPT} of 0.85 exhibited a similar CPT release profile in comparison to the f_{CPT} of the 0.50 counterpart (Figure 54c, d), despite a greater drug loading that resulted in a higher total amount of loaded CPT at the same 0.5 mg/mL polymer concentration. This phenomenon can be explained as a result of a slower GSH-triggered drug release from nanoparticles with a higher f_{CPT}. These findings indicate that a higher conjugation of hydrophobic drug led to a lower stimuli-responsive sensitivity against water-soluble stimuli (e.g., GSH).

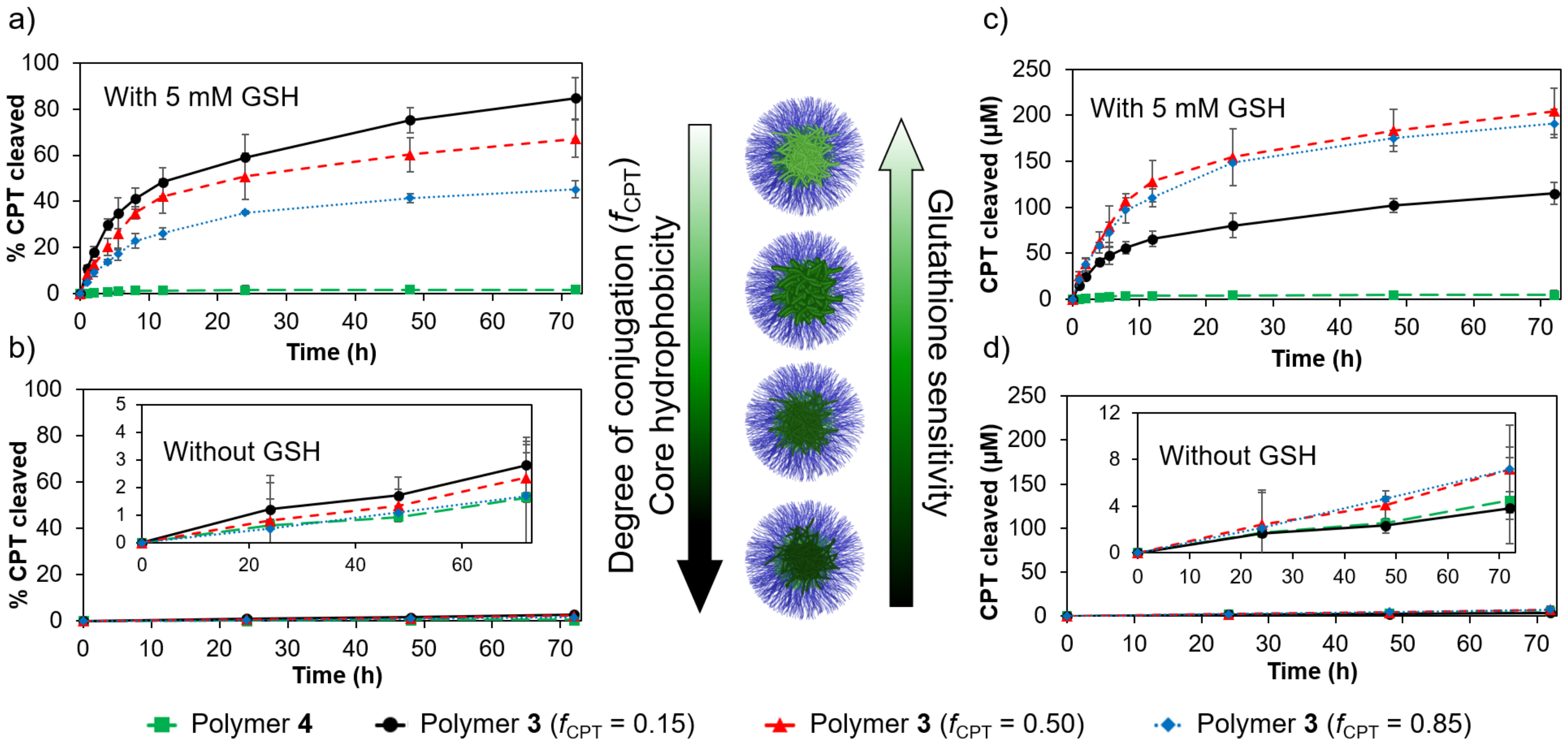

Figure 54. The disulfide cleavages and drug releases of CPT-conjugated polymer nanomaterials (0.5 mg/mL, 2 mL) studied over 3 days at 37 °C in PBS buffer (pH 7.4) in triplicate (a) (c) with 5 mM GSH and (b) (d) without GSH. The results are presented as (a) (b) % CPT release and (c) (d) CPT molar release. Reprinted with permission from “A Tale of Drug-Carrier Optimization: Controlling Stimuli Sensitivity via Nanoparticle Hydrophobicity through Drug Loading” by Lin, Y.-N.; Khan, S.; Song, Y.; Dong, M.; Shen, Y.; Tran, D. K.; Pang, C.; Zhang, F.; Wooley, K. L., *Nano Letters* **2020**, 20 (9), 6563-6571. Copyright 2020 American Chemical Society.

Table 3. Loading capacity and concentration of the CPT during the *in vitro* disulfide cleavage experiment with 0.5 mg/mL polymer concentration. Reprinted with permission from "A Tale of Drug-Carrier Optimization: Controlling Stimuli Sensitivity via Nanoparticle Hydrophobicity through Drug Loading" by Lin, Y.-N.; Khan, S.; Song, Y.; Dong, M.; Shen, Y.; Tran, D. K.; Pang, C.; Zhang, F.; Wooley, K. L., *Nano Letters* **2020**, 20 (9), 6563-6571. Copyright 2020 American Chemical Society.

	CPT Loading capacity (%)	* [CPT] (μM)	* [CPT] (μg/mL)
Polymer 2 (f_{CPT} = 0)	0	0	0
Polymer 3 (f_{CPT} = 0.15)	9.5	140	47
Polymer 3 (f_{CPT} = 0.50)	21	300	110
Polymer 3 (f_{CPT} = 0.85)	29	420	150
Polymer 4 (f_{CPT} = 0.40)	19	280	100

* 0.5 mg/mL polymer solution in PBS (total volume = 2 mL)

The GSH sensitivity was also shown to significantly influence the in vitro cytotoxicities of the redox-responsive CPT-conjugated nanomaterials against OVCAR-3 ovarian cancer cells (Figure 55 and Table 4). Ovarian cancer is the most lethal gynecological cancer in the Western world, with ca. 75% cases that were diagnosed at late stages (III/IV) having a 5 year survival rate <50%.[174] The polymer **3** with f_{CPT} of 0.15 was most efficacious against cancer cells with the lowest IC_{50} value (12 μM) in comparison to f_{CPT} of 0.50 (IC_{50} = 34 μM) and f_{CPT} of 0.85 (IC_{50} = 27 μM) counterparts (Figure 55). When IC_{50} values were determined based on polymer concentrations, rather than CPT concentrations, polymer **3** with the highest f_{CPT} of 0.85 displayed the lowest IC_{50} value, i.e., the highest cytotoxicity against OVCAR-3 cancer cells (Figure 55 b and Table 4). The observed *in vitro* outcomes can be attributed to the complex interplay between nanocarriers and the environment; higher hydrophobic payload reduced diffusion of GSH into and free CPT out from the nanoparticle assemblies, thereby affecting disulfide cleavage and the resulting CPT release kinetics. Moreover, differences in f_{CPT} for the initial polymer chains, and the changing levels of f_{CPT} during CPT cleavage, each could contribute to variations in the polymer chain hydrophilicity, thereby affecting the packing parameters and potentially leading to variable extents of polymer chain assembly and disassembly. Therefore, additional factors, such as slight differences in size, morphologies, and polymer chain packings, could profoundly impact the *in vitro* outcomes. The disulfide-linked CPT-conjugated polymer **3** assemblies displayed reduced cytotoxicities over the free CPT (IC_{50} = 2.1 μM), partly due to a sustained release of CPT, where even after 3 days, polymer **3** assemblies with f_{CPT} of

0.15, 0.50, and 0.85 only cleaved 85%, 67%, and 45% of the total conjugated CPT in the presence of 5 mM GSH in PBS, respectively (Figure 54a). Although having high *in vitro* cytotoxicities, free CPT has poor aqueous solubility and causes severe side effects that have resulted in limited clinical usage.[175] Polymers **3** displayed a significantly higher cytotoxicity while maintaining good water solubility when compared to irinotecan (IR, IC_{50} = 236 μM), a water-soluble CPT analogue that has received FDA-approval for treating colorectal cancers and has been investigated as a candidate for ovarian cancers in clinical trials.[175-177] Furthermore, the GSH-responsive CPT-conjugated polymers **3** were 1 order of magnitude more efficacious against ovarian cancer cells in comparison to the nonresponsive CPT-conjugated polymer **4** (IC_{50} = 287 μM), demonstrating the essential role of the redox-responsive disulfide-linkages in maintaining drug efficacy. It is worth noting that polymer **2** (f_{CPT} = 0) was noncytotoxic at the tested concentration ranges (16–2000 μg/mL, Figure 58).

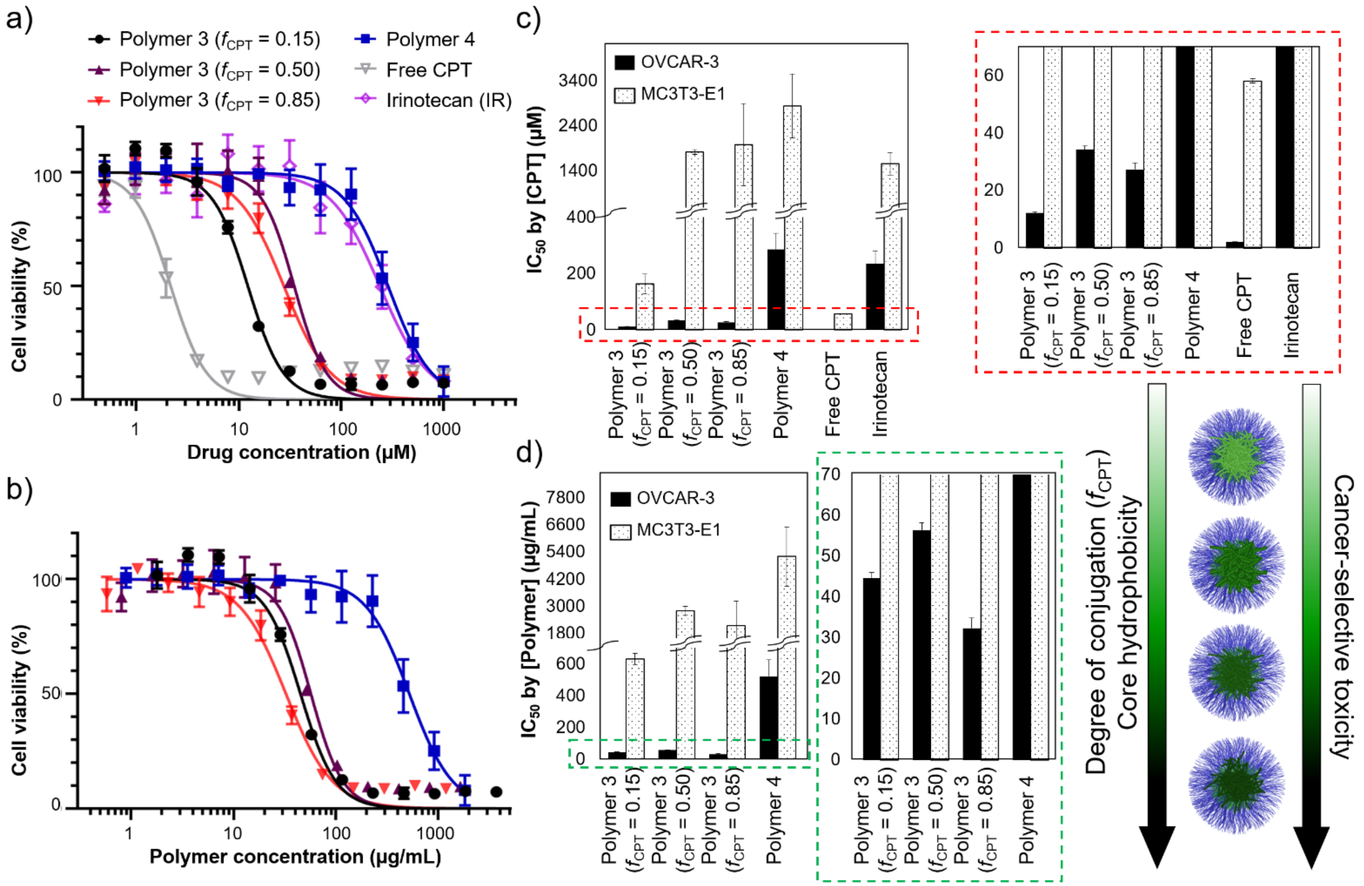

Figure 55. Cytotoxicity evaluation of CPT-conjugated polymers in OVCAR-3 ovarian cancer cells based on (a) CPT concentrations or (b) polymer concentrations. (c) Half maximal inhibitory concentration (IC$_{50}$) obtained from the data plotted in (a), with the red dashed box showing a zoom-in view. (d) IC$_{50}$ obtained from the data plotted in (b), with the green dashed box showing a zoom-in view. Cell viabilities are reported as an average of three measurements, and error bars represent standard deviation. Reprinted with permission from “A Tale of Drug-Carrier Optimization: Controlling Stimuli Sensitivity via Nanoparticle Hydrophobicity through Drug Loading” by Lin, Y.-N.; Khan, S.; Song, Y.; Dong, M.; Shen, Y.; Tran, D. K.; Pang, C.; Zhang, F.; Wooley, K. L., *Nano Letters* **2020**, 20 (9), 6563-6571. Copyright 2020 American Chemical Society.

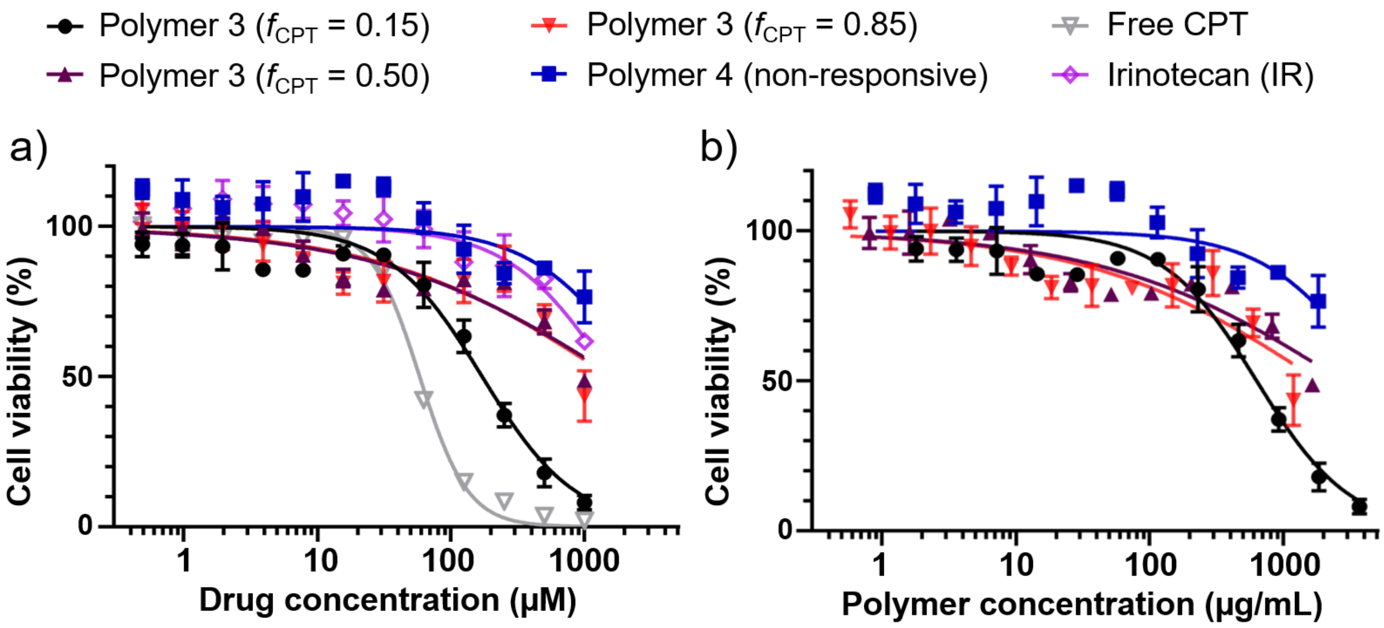

Figure 56. Cytotoxicity evaluation of CPT-conjugated polymers in MC3T3-E1 osteoblast progenitor cells based on (a) CPT concentration or (b) polymer concentration. Reprinted with permission from "A Tale of Drug-Carrier Optimization: Controlling Stimuli Sensitivity via Nanoparticle Hydrophobicity through Drug Loading" by Lin, Y.-N.; Khan, S.; Song, Y.; Dong, M.; Shen, Y.; Tran, D. K.; Pang, C.; Zhang, F.; Wooley, K. L., *Nano Letters* **2020**, 20 (9), 6563-6571. Copyright 2020 American Chemical Society.

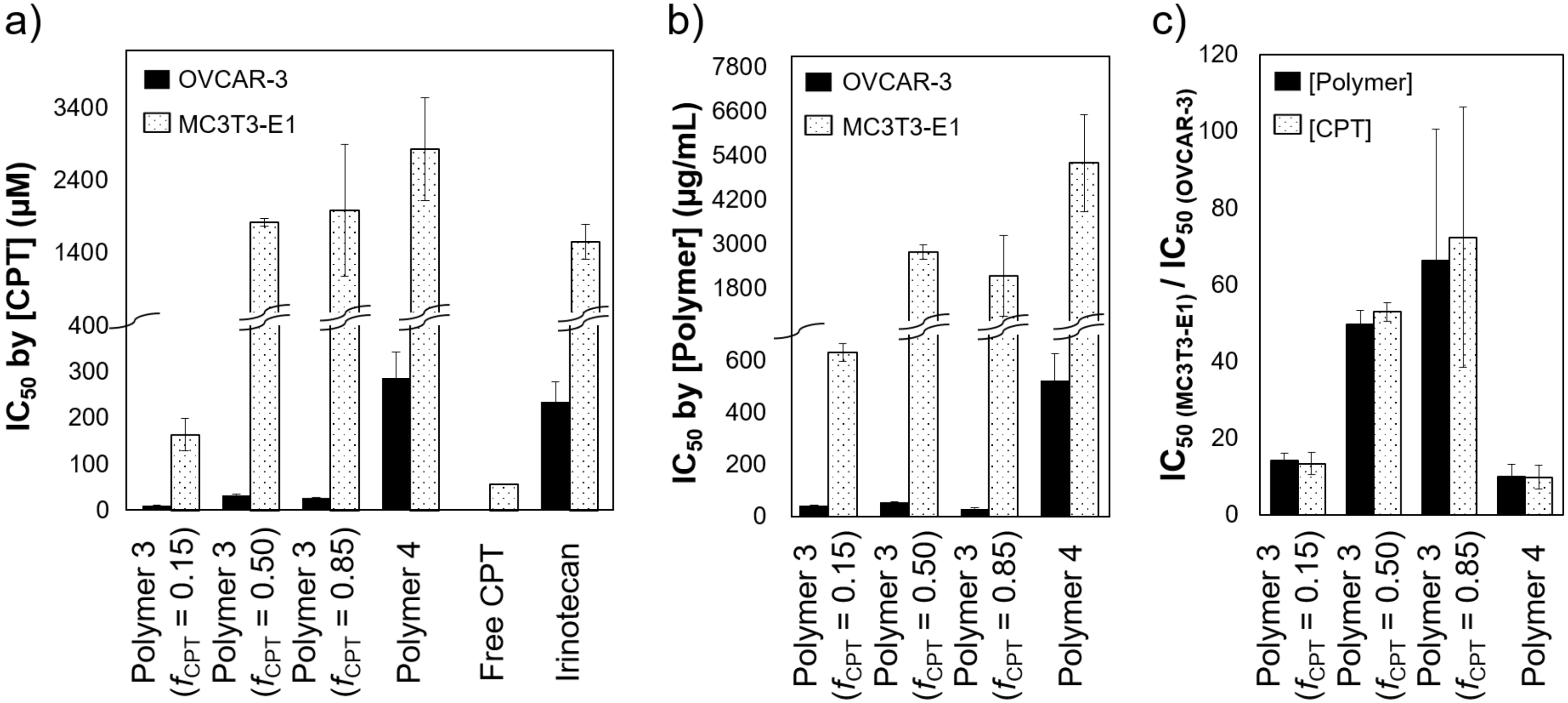

Figure 57. Graphical representations of IC_{50} in (a) CPT concentrations or (b) polymer concentrations. (c) Graphical representation of $IC_{50\ (MC3T3\text{-}E1)}/IC_{50\ (OVCAR\text{-}3)}$ values based on (a) and (b). Reprinted with permission from "A Tale of Drug-Carrier Optimization: Controlling Stimuli Sensitivity via Nanoparticle Hydrophobicity through Drug Loading" by Lin, Y.-N.; Khan, S.; Song, Y.; Dong, M.; Shen, Y.; Tran, D. K.; Pang, C.; Zhang, F.; Wooley, K. L., *Nano Letters* **2020**, 20 (9), 6563-6571. Copyright 2020 American Chemical Society.

Table 4. Summary of IC$_{50}$ and IC$_{50\ (\mathrm{MC3T3\text{-}E1})}$/IC$_{50\ (\mathrm{OVCAR\text{-}3})}$ values for non-cancerous MC3T3-E1 and cancerous OVCAR-3 cell lines. Reprinted with permission from "A Tale of Drug-Carrier Optimization: Controlling Stimuli Sensitivity via Nanoparticle Hydrophobicity through Drug Loading" by Lin, Y.-N.; Khan, S.; Song, Y.; Dong, M.; Shen, Y.; Tran, D. K.; Pang, C.; Zhang, F.; Wooley, K. L., *Nano Letters* **2020**, 20 (9), 6563-6571. Copyright 2020 American Chemical Society.

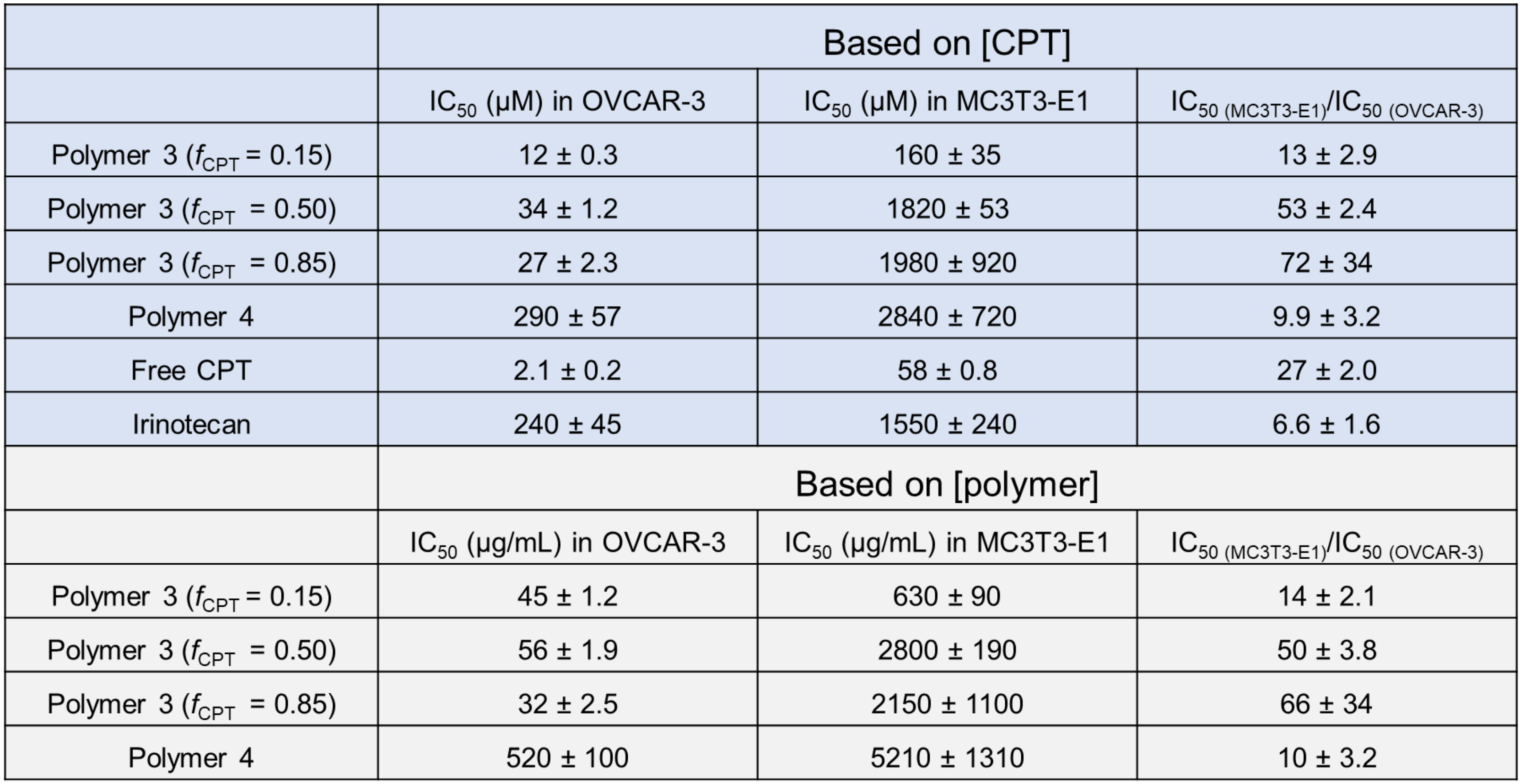

	Based on [CPT]		
	IC$_{50}$ (μM) in OVCAR-3	IC$_{50}$ (μM) in MC3T3-E1	IC$_{50\ (\mathrm{MC3T3\text{-}E1})}$/IC$_{50\ (\mathrm{OVCAR\text{-}3})}$
Polymer 3 (f_{CPT} = 0.15)	12 ± 0.3	160 ± 35	13 ± 2.9
Polymer 3 (f_{CPT} = 0.50)	34 ± 1.2	1820 ± 53	53 ± 2.4
Polymer 3 (f_{CPT} = 0.85)	27 ± 2.3	1980 ± 920	72 ± 34
Polymer 4	290 ± 57	2840 ± 720	9.9 ± 3.2
Free CPT	2.1 ± 0.2	58 ± 0.8	27 ± 2.0
Irinotecan	240 ± 45	1550 ± 240	6.6 ± 1.6
	Based on [polymer]		
	IC$_{50}$ (μg/mL) in OVCAR-3	IC$_{50}$ (μg/mL) in MC3T3-E1	IC$_{50\ (\mathrm{MC3T3\text{-}E1})}$/IC$_{50\ (\mathrm{OVCAR\text{-}3})}$
Polymer 3 (f_{CPT} = 0.15)	45 ± 1.2	630 ± 90	14 ± 2.1
Polymer 3 (f_{CPT} = 0.50)	56 ± 1.9	2800 ± 190	50 ± 3.8
Polymer 3 (f_{CPT} = 0.85)	32 ± 2.5	2150 ± 1100	66 ± 34
Polymer 4	520 ± 100	5210 ± 1310	10 ± 3.2

We further investigated the effect of GSH sensitivity of the redox-responsive CPT-conjugated nanomaterials on the differential cytotoxicity between cancerous and healthy cells (Figure 55-Figure 56). Although chemotherapeutic agents help combat cancers, off-site toxicities for healthy tissues cause adverse effects; for instance, toxicity against bone marrow increases the risks of developing hypoplastic anemia and myelodysplastic syndrome.[178-180] Osteoblasts regulate hematopoietic stem cell niches and are essential for the hematopoietic cell repopulation after chemotherapies.[181] Therefore, the ideal anticancer agents should spare osteoblasts while attacking cancer cells. For this reason, OVCAR-3 ovarian cancer cells and MC3T3-E1 osteoblast progenitor cells were selected to represent cancerous and healthy cells, respectively. The selectivity was calculated as the ratio of the IC_{50} values against noncancerous MC3T3-E1 vs cancerous OVCAR-3 ($IC_{50\text{-(MC3T3-E1)}}/IC_{50\text{-(OVCAR-3)}}$) in order to quantify the differential cytotoxicity. A higher selectivity value ($IC_{50\text{-(MC3T3-E1)}}/IC_{50\text{-(OVCAR-3)}}$) suggests a wider therapeutic window for the formulation.

Polymers **3** with f_{CPT} of 0.15, 0.50, and 0.85 had selectivity values of 13, 53, and 72, respectively: higher than those of nonresponsive polymer **4** (selectivity value = 10) and IR (selectivity value = 7) formulations (Figure 55-Figure 56 and Table 4), indicating a better safety profile for the GSH-responsive CPT-conjugated nanomaterials. The differential cytotoxicities of polymer **3** assemblies possibly arose from higher GSH concentrations in cancer cells vs healthy cells.[129, 132] A similar trend was observed among polymer **3** assemblies when selectivity values were calculated based on polymer concentrations: a higher f_{CPT} led to a greater cancer-selective cytotoxicity (Figure 57).

Although the highest f_{CPT} of 0.85 resulted in reduced cytotoxicity, it led to a ca. 5.5-fold increase in the differential cytotoxicity against ovarian cancer cells in comparison to the f_{CPT} of the 0.15 counterpart (Figure 55,Figure 57 and Table 4). The differences in GSH sensitivities resulted in significant variations in the cancer selectivity, demonstrating the importance of controlling the stimuli sensitivity of smart drug carriers. With the improved differential cytotoxicity, our redox-responsive CPT-conjugated sugar-based polymeric nanomaterials showed great promise for treating ovarian cancers and associated metastatic diseases.

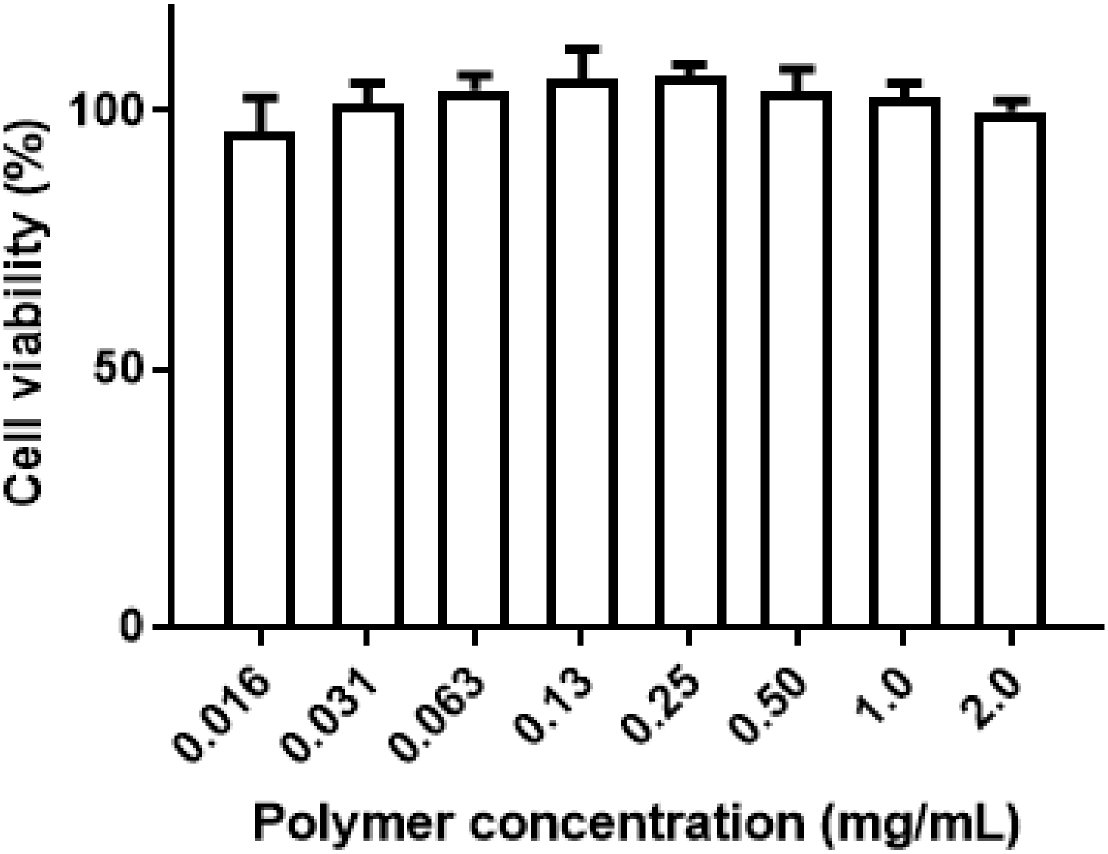

Figure 58. Cell viability as a function of Polymer 2 ($f_{CPT} = 0$) concentration. Cell viabilities are reported as an average of three measurements, and error bars represent standard deviation. Reprinted with permission from “A Tale of Drug-Carrier Optimization: Controlling Stimuli Sensitivity via Nanoparticle Hydrophobicity through Drug Loading” by Lin, Y.-N.; Khan, S.; Song, Y.; Dong, M.; Shen, Y.; Tran, D. K.; Pang, C.; Zhang, F.; Wooley, K. L., *Nano Letters* **2020**, 20 (9), 6563-6571. Copyright 2020 American Chemical Society.

4.3. Experimental Section

4.3.1. Materials

Bicyclic glucose carbonates methyl-2-O-ethyloxycarbonyl-3-O-propargyloxycarbonyl-4,6-Ocarbonyl-α-D-glucopyranoside (GC(EPC)), prodrugs (S)-4-ethyl-3,14-dioxo-3,4,12,14-tetrahydro1H-pyrano[3',4':6,7]indolizino[1,2-β]quinolin-4-yl (2-((2-hydroxyethyl)disulfanyl)ethyl) carbonate (CPT-ss-OH), and (S)-4-ethyl-3,14-dioxo-3,4,12,14-tetrahydro-1H-pyrano[3',4':6,7]indolizino[1,2- b]quinolin-4-yl (6-hydroxyhexyl) carbonate (CPT-cc-OH) were synthesized according to previously reported procedures.[50, 173, 182] 1,5,7-Triazabicyclo[4.4.0]dec-5-ene (TBD) was purchased from TCI chemicals. Dichloromethane (DCM) and N,N-dimethylformamide (DMF) were purified by passing through a solvent purification system from J. C. Meyer Solvent Systems, Inc. (Laguna Beach, CA). Nanopure water (18.2 MΩ·cm) was acquired from a Milli-Q water filtration system (Millipore Corp, USA). Phosphate-buffered saline (PBS, 10x) was purchased from MilliporeSigma (Burlington, MA). Other chemicals and reagents were used as received from Sigma-Aldrich, Co. (St. Louis, MO), unless otherwise noted. Dialysis membrane tubing with a molecular weight cutoff (MWCO) of 6-8 kDa was purchased from Spectrum Laboratories, Inc. (Rancho Dominguez, CA) and soaked in nanopure water for 5 min at room temperature before use. Roswell Park Memorial Institute 1640 (RPMI1640) and Minimum Essential Medium alpha (MEMα) cell media were obtained from the American Type Culture Collection (Manassas, VA), with media additives (10% fetal bovine serum, 1% penicillin/streptomycin) purchased from Sigma-

Aldrich (St. Louis, MO). Cell culture 96-well round bottom plates were purchased from Corning Costar Co. (Corning, NY).

4.3.2. Instrumentation

^{1}H Nuclear magnetic resonance (NMR) and ^{13}C NMR spectra were recorded on a Varian 500 spectrometer (Varian, Inc., Palo Alto, CA) interfaced with a UNIX computer using VNMR-J software. All NMR experiments were performed at ambient temperature. Chemical shifts were referenced to the solvent residual signals. All ^{1}H NMR chemical shifts are reported in parts per million (ppm) relative to the signals for residual $CHCl_3$ (7.26 ppm) or dimethyl sulfoxide (DMSO) (2.50 ppm). All ^{13}C NMR spectra are reported in ppm relative to $CDCl_3$ (77.23 ppm) or DMSO-d_6 (39.51 ppm) and were obtained with ^{1}H decoupling.

Fourier transform infrared (FT-IR) spectra were recorded on an IR Prestige 21 system equipped with a diamond attenuated total reflection (ATR) lens (Shimadzu Corp., Japan) and analyzed using IRsolution v. 1.40 software.

Size exclusion chromatography (SEC) eluting with tetrahydrofuran (THF) was performed on a Waters Chromatography, Inc. (Milford, MA) system equipped with an isocratic pump (model 1515), a differential refractometer (model 2414), and a column set comprised of a PLgel 5 μm guard column (50 × 7.5 mm), a PL$_{gel}$ 5 μm Mixed C column (300 × 7.5 mm, Agilent Technologies) and two Styragel® columns (500 Å and 104 Å, 300 × 7.5 mm, Waters Chromatography, Inc.). The system was operated at 40 °C with a flow rate of 1 mL/min. Data were analyzed using Breeze software from Waters

Chromatography, Inc. (Milford, MA). Molar masses were determined relative to polystyrene standards (580–3,250,000 Da) purchased from Polymer Laboratories, Inc. (Amherst, MA). Polymer solutions were prepared at a concentration of *ca.* 3 mg/mL with 0.05 vol% toluene as the flow rate marker; an injection volume of 200 μL was used.

Thermogravimetric analysis (TGA) was performed under the N_2 atmosphere using a Mettler-Toledo TGA2/1100/464 (Mettler-Toledo, Inc., Columbus, OH), with a heating rate of 10 °C/min, from 25 to 500 °C. Data were analyzed using Mettler-Toledo STAR^e v. 15.00a software.

Glass transition temperature (T_g) and melting temperature (T_m) were measured by differential scanning calorimetry (DSC) on a Mettler-Toledo DSC3/700/1190 (Mettler-Toledo, Inc., Columbus, OH) under N_2. The T_g was taken as the midpoint of the inflection tangent and the T_m was taken as the maximum of the endothermic peak from the second heating scan. Measurements were performed with a heating rate of 10 °C/min, and the data were analyzed using Mettler-Toledo STAR^e v. 15.00a software.

Dynamic light scattering (DLS) measurements were conducted using a Zetasizer Nano ZS instrument (Malvern Panalytical, Inc., Westborough, MA) equipped with a laser diode operating at 632.8 nm. The scattered light was detected at 175° and analyzed using a log correlator for a 0.5 mL sample in a disposable cell (capacity = 0.9 mL). The photomultiplier aperture and attenuator were adjusted automatically. The particle size distribution and distribution averages were calculated using particle size analysis routines in Zetasizer 7.13 software. The measurement duration and number of accumulations were adjusted automatically. The average diameter of the particles was reported as the intensity-, volume-, and number-average hydrodynamic diameter from three measurements.

Transmission electron microscopy (TEM) images were collected on a JEOL 1200EX operated at 100 kV, and micrographs were recorded using a SIA-15C CCD camera. Samples for TEM were prepared by drop deposition of an aqueous polymer solution (20 µL, 0.5 mg/mL) onto a carbon-coated copper grid, and after 1 min, excess solution was quickly wicked away by a piece of filter paper. The samples were then negatively stained with a 1% phosphotungstic acid aqueous solution (20 µL). After 30 s, the excess staining solution was quickly wicked away by a piece of filter paper, and the samples were left to dry under ambient conditions (typically 10-12 h) before imaging.

Atomic force microscopy (AFM) was performed using a Multimode 8 system (Bruker) using a ScanAsyst-Air Silicon Nitride probe (k = 0.4 N/m, f = 70 kHz, Bruker). AFM images were assessed with Nanoscope Analysis (Bruker). For AFM sample preparation, an aqueous polymer solution of nanoparticles in nanopure water (50 µL) at 0.1 mg/mL was deposited onto a freshly-cleaved mica substrate. After 1 min, excess solution was quickly wicked away by a piece of filter paper, and the mica surface was dried under ambient atmosphere (typically 10-12 h) before imaging.

Camptothecin (CPT) concentrations were determined by high-performance liquid chromatography (HPLC) on a Shimadzu Prominence system equipped with a SPD-20AV prominence UV-Vis detector set to 366 nm and a Waters X Bridge C8 column (4.6 × 150 mm, 5 µM, 100 Å) eluting in 45% acetonitrile and 55% aqueous solution (0.1% trifluoroacetic acid) in isocratic mode. The flow rate was set to 0.7 mL/min with a run time of 10 min, and the column temperature was set to 40 °C. The HPLC method employed an external calibration of CPT.

4.3.3. Synthesis

4.3.3.1. Synthetic procedure for PEG_{113}-*b*-$PDGC(EPC)_{10}$ (polymer 1)

Methoxy poly(ethylene glycol) ($mPEG_{113}$) and GC(EPC) were dried under vacuum over P_2O_5 for 2 days before transferring to a glovebox for storage under an Ar atmosphere. Stock solutions were prepared in a glovebox under N_2 atmosphere, while the ring-opening polymerization (ROP) was conducted in a -15 °C sodium chloride ice bath in a fume hood. To a solution of GC(EPC) (508 mg, 1.36 mmol) and $mPEG_{113}$ (523 mg, 104 µmol) in 5 mL of DCM at -15 °C was added organocatalyst TBD (7.1 mg, 51 µmol) in DCM (100 µL) under N_2 atmosphere. After stirring for 8 min, the reaction vial was opened to air and quenched by addition of excess acetic acid. The polymer was purified by precipitation from DCM into diethyl ether (3 ×) and dried under vacuum to afford PEG_{113}-*b*-$PGC(EPC)_{10}$ (polymer **1**) as a white powder (917 mg, yield 89%). ^1H NMR (500 MHz, $CDCl_3$) δ ppm 5.34 (dd, J = 10, 10 Hz), 5.01 (s), 4.87 (dd, J = 10, 10 Hz), 4.78 – 4.64 (m), 4.26 (br), 4.18 (q, J = 10 Hz), 4.01 (br), 3.62 (s), 3.45 – 3.38 (m), 3.37 (s), 2.57 (s), 1.28 (t, J = 10 Hz). ^{13}C NMR (126 MHz, $CDCl_3$) δ ppm 154.1, 153.7, 153.6, 129.4, 128.5, 96.5, 77.5, 77.2, 76.8, 76.3, 74.2, 73.6, 72.0, 70.7, 66.7, 65.9, 64.9, 59.1, 56.0, 55.8, 15.4, 14.2. FT-IR (ATR) 3330 – 3190, 3040 – 2740, 1797 – 1700, 1466, 1371, 1342, 1321 – 1186, 1144, 1101, 1053 – 999, 986, 960, 907, 876, 843, 779, 667 cm^{-1}. TGA in N_2, 282

– 316 °C, 29% weight loss; 316 – 393 °C, 52% weight loss; 19% mass remained at 500 °C. T_m = 55 °C. $M_{n\,SEC}$ = 14.2 kDa, $Đ$ = 1.08.

4.3.3.2. Post-polymerization modification of polymer 1 with mercaptoproprionic acid *via* thiol-yne reaction to afford PEG$_{113}$-*b*-PDGC(COOH)$_{20}$ (polymer 2)

Polymer **1** (497 mg, 50 µmol), mercaptoproprionic acid (364 mg, 3.2 mmol), and 2,2-dimethoxy-2-phenylacetophenone (DMPA, 124 mg, 0.48 mmol) were dissolved in anhydrous DMF (8 mL), deoxygenated under N_2(g) for 30 min, and irradiated under UV light (365 nm) for 2 h. The resulting copolymer solution was transferred to dialysis tubing (MWCO *ca.* 6-8 kDa) and dialyzed against nanopure water at 4 °C for 3 d to remove excess thiol and photoinitiator. The solution was then lyophilized to give the polymer **PEG$_{113}$-*b*-PDGC(COOH)$_{20}$** as a white powder (561 mg, 93 % yield).

4.3.3.3. Post-polymerization modification of polymer 2 with CPT-ss-OH *via* EDC-coupling reaction to afford PEG$_{113}$-*b*-[PDGC(COOH)$_{20\text{-}x}$-*co*-PDGC(CPT)$_x$] (polymer 3)

DMAP (2.1 mg, 17 µmol), polymer 2 (43 mg, 3.6 µmol) and CPT-ss-OH (54.9 mg, 101 µmol) were mixed in 15 mL DCM. EDC HCl (26.6 mg, 139 µmol) in 5 mL was dropwise added over 10 min under stirring. After stirring for 24 h at room temperature, the solution was dialyzed against nanopure water at 4 °C for 3 d, then lyophilized to give the polymer **3** (f_{CPT} = 0.85), PEG$_{113}$-*b*-[PDGC(COOH)$_3$-*co*-PDGC(CPT)$_{17}$], as a white powder. PEG$_{113}$-*b*-[PDGC(COOH)$_{10}$-*co*-PDGC(CPT)$_{10}$] (f_{CPT} = 0.50) and PEG$_{113}$-*b*-

$[PDGC(COOH)_{17}$-*co*-$PDGC(CPT)_3]$ ($f_{CPT} = 0.15$) were synthesized using less CPT-ss-OH equivalents in the coupling reaction. Polymer 3 ($f_{CPT} = 0.85$) (68 mg, 85% yield); Polymer 3 ($f_{CPT} = 0.50$) (27 mg, 76% yield); Polymer 3 ($f_{CPT} = 0.15$) (63 mg, 86% yield).

4.3.3.4. Post-polymerization modification of polymer 2 with CPT-cc-OH *via* EDC-coupling reaction to afford PEG_{113}-*b*-$[PDGC(COOH)_{12}$-*co*-$PDGC(CPT)_8]$ (polymer 4)

DMAP (0.7 mg, 5.6 μmol), polymer 2 (23 mg, 1.9 μmol) and CPT-ss-OH (11.9 mg, 24 μmol) were mixed in 10 mL DCM. EDC HCl (9.3 mg, 48 μmol) in 5 mL was dropwise added over 10 min under stirring. After stirring for 24 h at room temperature, the solution was dialyzed against nanopure water at 4 °C for 3 d, then lyophilized to give the polymer **4** ($f_{CPT} = 0.40$), PEG_{113}-*b*-$[PDGC(COOH)_3$-*co*-$PDGC(CPT)_{17}]$, as a white powder. PEG_{113}-*b*-$[PDGC(COOH)_{10}$-*co*-$PDGC(CPT)_{10}]$ ($f_{CPT} = 0.50$) and PEG_{113}-*b*-$[PDGC(COOH)_{17}$-*co*-$PDGC(CPT)_3]$ ($f_{CPT} = 0.15$) were synthesized using less CPT-ss-OH equivalents in the coupling reaction.

4.3.4. Procedures

4.3.4.1. Preparation of CPT-conjugated NPs

In a typical experiment, polymers were dissolved in DMSO (100 μL), then added dropwise into 9.9 mL nanopure water with vigorous stirring, to afford CPT-conjugated polymeric nanoparticles (0.5 mg/mL) with 1 vol % DMSO. Polymer assembly solutions were dialyzed for 24 h in nanopure water to remove organic solvent, then characterized by DLS, TEM, AFM, and electrophoretic light scattering.

4.3.4.2. Preparation of CPT-conjugated NPs samples for D_2O ^1H NMR studies

Polymers were dissolved in deuterated DMF (2.5 mg/mL), then added 60 uL to the stirring D_2O (540 uL) to afford a series of CPT-conjugated polymeric nanoparticles. Polymer assembly solutions were analyzed by ^1H NMR.

4.3.4.3. *In vitro* disulfide cleavage of the CPT-conjugated NPs

PolyCPT (0.5 mg/mL) assemblies in PBS (pH = 7.4) were transferred into closed vials, with or without 5 mM glutathione, and shake at 37 °C. The disulfide cleavage was monitored by the free CPT increase in polyCPT solutions. Aliquots (100 µL) of the polymer solutions were taken at pre-determined times and analyzed by HPLC. The cleavage study was conducted in triplicate.

4.3.4.4. CPT cleavage from CPT-conjugated NPs *via* incubation method

CPT-conjugated nanoparticles (0.5 mg/mL) were incubated in PBS (pH 7.4) with (5 mM) or without GSH in a closed vial. The formulation solutions were shaking at 37 ºC for 72 h. Aliquots of solution were taken at 2, 4, 8, 12, 24, 48, and 72 h and analyzed by HPLC to monitor the increase of CPT concentration.

4.3.4.5. 2D cytotoxicity assays

Human ovarian adenocarcinoma cells (OVCAR-3) (5×10^3 cells/well) and mouse osteoblast precursor cells MC3T3-E1 (5×10^3 cells/well) were plated in 96-well plates in RPMI1640 medium (20% fetal bovine serum and 1% penicillin/streptomycin) and MEMα media (10% fetal bovine serum, and 1% penicillin/streptomycin), respectively. Cells were incubated at 37 °C in a humidified atmosphere containing 5% CO2 atmosphere. The medium was replaced with a fresh medium 24 h after seeding. Culture medium was replaced with serial dilutions of the polymers (100 µL) in fresh medium (final CPT concentrations ranged from 0.488 µM – 1000 µM). Polymer stock solutions were prepared in DMSO. The cells were incubated for 24 h, and after this period, the media was replaced with 100 µL of the complete medium. Then, 20 µL of the MTS combined reagent was added to each well (Cell Titer 96® Aqueous Non-Radioactive Cell Proliferation Assay, Promega Co.). The cells were incubated with the reagent for 3 h for OVCAR-3 cells, at 37 ˚C in a humidified atmosphere containing 5% CO2 protected from light. Absorbance was measured at 490 nm by using SpectraMax M5 (Molecular Devices Co.). The cell viability was calculated based on the relative absorbance to the control untreated cells. The 0% and 100% cell viabilities were considered as the control medium (no cells) and cells with no treatment, respectively.

4.4. Conclusions

In summary, we demonstrated the impact of hydrophobic drug conjugation on the complex interplay between the level of drug loading on the polymer nanoparticle physicochemical characteristics and the resulting access of molecular stimuli to the internal compartments and subsequent triggered drug release, with a focus on GSH sensitivity of disulfide-linked CPT-conjugated PEG-*b*-PGC nanomaterials. The hydrophobic payload increased the core hydrophobicity, which negatively influenced the aqueous accessibility, lowered the GSH sensitivity, and consequently slowed down the GSH-triggered drug release. Importantly, when compared to the low CPT loading formulation ($f_{\mathrm{CPT}} = 0.15$), the higher CPT-conjugated formulations ($f_{\mathrm{CPT}} = 0.50$ and 0.85) significantly improved selective cytotoxicities against ovarian cancer cells over healthy cells. With an emphasis on the importance of controlling the drug loading, this work represents a significant advancement in the drug carrier design, providing a versatile strategy to tune GSH sensitivity through payload control, with the potential for extending this strategy to other water-borne stimuli, including enzymes, peptides, pH, and other ions.

5. CONCLUSIONS

This dissertation presents facile strategies to precisely control the physicochemical characteristics of biocompatible polymeric materials toward personalized nanomedicine. Individual heterogeneity poses a significant challenge for the clinical translation of nanomedicine. With tailored physicochemical properties for a specific individual's genetic and disease profile, personalized nanocarriers can overcome such a challenge. Therefore, the future of nanomedicine depends on customization, and the development of next-generation nanomedicine requires more precise control over the physicochemical characteristics of nanomaterials. Versatile strategies for controlling size, surface, shape, stimuli-responsiveness, and cargo release were explored and developed in this work. This work has laid a foundation for customization and personalization of the synthetic nanomaterials, providing effective approaches for controlling physicochemical characteristic of nanomaterials, thus facilitating bench-to-bedside translation of nanomedicine.

In Chapter 2, polymer co-assembly has been shown to be a versatile approach to coincidentally tune the size, shape and surface charge of nanoscopic supramolecular assemblies in water, to optimize the stimuli-responsive properties of nanomaterials. Sequential ring opening polymerizations of lactide and an alkynyl-bearing glucose-carbonate monomer afforded reactive block polymers that were conveniently transformed into amphiphilic derivatives having carboxylic acid or histamine side chain groups. Assembly and co-assembly of these block polymers yielded nanoparticles with highly tunable size, zeta potential, and pH-responsive behaviors, while bypassing tedious and time-consuming synthesis. The tailorability derived from co-assembly enables the facile optimization of nanomaterials for different biomedical applications. This work represents a fundamental advance in the design and preparation of glucose-derived acid-responsive amphiphilic block polymeric materials, with potential for these constructs to be useful in a broad range of drug delivery applications.

In Chapter 3, we demonstrated a facile fabrication of RBC-MCNs with tunable PTX release kinetics via controlling the macromolecular stereostructure. Isotactic and atactic PLAs of similar molar masses (M_n = 8.2–8.9 kDa) and dispersities (<1.1) were synthesized via organocatalyzed ROPs. PLA assemblies, with varying polymer tacticity, had comparable hydrodynamic diameters. Significant PLA stereocomplex retention upon loading PTX was evidenced by WAXD and DSC experiments. The PTX release kinetics from the RBC-MCNs was successfully tuned by changing PLA stereochemistry, with a higher degree of stereocomplexation corresponding to slower PTX release. RBC-MCNs were not cytotoxic and displayed lower immunotoxic responses compared to the RBC membrane vesicles. This strategy can be adapted to encapsulate other cargos, such as different chemotherapeutics, radiosensitizers, and growth factors. Although the cytotoxicity against cancer cells was diminished by packaging the drug within the nanoparticle framework, the extended release profile may be attractive for in vivo efficacy. Therefore, this work represents fundamental advances toward a potential personalized nanocarrier technology that would be capable of employing an individual’s RBCs for membrane isolation, together with tuning of cargo loading and release simply via alteration of the biocompatible PLA stereoisomer feed ratio.

In Chapter 4, we demonstrated the impact of hydrophobic drug conjugation on the complex interplay between the level of drug loading on the polymer nanoparticle physicochemical characteristics and the resulting access of molecular stimuli to the internal compartments and subsequent triggered drug release, with a focus on GSH sensitivity of disulfide-linked CPT-conjugated PEG-*b*-PGC nanomaterials. The hydrophobic payload increased the core hydrophobicity, which negatively influenced the aqueous accessibility, lowered the GSH sensitivity, and consequently slowed down the GSH-triggered drug release. Importantly, when compared to the low CPT loading formulation ($f_{\mathrm{CPT}} = 0.15$), the higher CPT-conjugated formulations ($f_{\mathrm{CPT}} = 0.50$ and 0.85) significantly improved selective cytotoxicities against ovarian cancer cells over healthy cells. With an emphasis on the importance of controlling the drug loading, this work represents a significant advancement in the drug carrier design, providing a versatile strategy to tune GSH sensitivity through payload control, with the potential for extending this strategy to other water-borne stimuli, including enzymes, peptides, pH, and other ions.

Given the novel strategies to precisely control nanomaterial physicochemical characteristics presented in this dissertation, future work should include developing polymer-based nanomaterials tailored toward specific disease targets. The remaining challenges in personalized nanomedicine included but were not limited to high cost, quality control, variable responses among individuals. More researches are needed to bring personalized nanomedicine into reality. In conjunction with the in-depth biological understanding of the disease process, this study opened new avenues for tailor-made nanomaterials toward personalized medicine.

REFERENCES

1. Lee, J. H.; Yeo, Y., Controlled Drug Release From Pharmaceutical Nanocarriers. *Chem. Eng. Sci.* **2015,** *125*, 75-84.

2. Nyström, A. M.; Xu, Z.; Xu, J.; Taylor, S.; Nittis, T.; Stewart, S. A.; Leonard, J.; Wooley, K. L., SCKs as nanoparticle carriers of doxorubicin: investigation of core composition on the loading, release and cytotoxicity profiles. *Chemical Communications* **2008,** (30), 3579-3581.

3. Lin, L. Y.; Lee, N. S.; Zhu, J.; Nyström, A. M.; Pochan, D. J.; Dorshow, R. B.; Wooley, K. L., Tuning core vs. shell dimensions to adjust the performance of nanoscopic containers for the loading and release of doxorubicin. *Journal of Controlled Release* **2011,** *152* (1), 37-48.

4. Nyström, A. M.; Wooley, K. L., Construction of thermoresponsive SCKs through tuning the crystalline melting point of the core domain. *Soft Matter* **2008,** *4* (4), 849-858.

5. Zhang, X.; Han, L.; Liu, M.; Wang, K.; Tao, L.; Wan, Q.; Wei, Y., Recent progress and advances in redox-responsive polymers as controlled delivery nanoplatforms. *Mater. Chem. Front.* **2017,** *1* (5), 807-822.

6. Su, L.; Li, R.; Khan, S.; Clanton, R.; Zhang, F.; Lin, Y.-N.; Song, Y.; Wang, H.; Fan, J.; Hernandez, S.; Butters, A. S.; Akabani, G.; MacLoughlin, R.; Smolen, J.; Wooley, K. L., Chemical Design of Both a Glutathione-Sensitive Dimeric Drug Guest and a Glucose-Derived Nanocarrier Host to Achieve Enhanced Osteosarcoma Lung Metastatic Anticancer Selectivity. *J. Am. Chem. Soc.* **2018,** *140* (4), 1438-1446.

7. Shrestha, R.; Elsabahy, M.; Florez-Malaver, S.; Samarajeewa, S.; Wooley, K. L., Endosomal escape and siRNA delivery with cationic shell crosslinked knedel-like nanoparticles with tunable buffering capacities. *Biomaterials* **2012,** *33* (33), 8557-68.

8. Cabral, H.; Nishiyama, N.; Kataoka, K., Supramolecular Nanodevices: From Design Validation to Theranostic Nanomedicine. *Acc. Chem. Res.* **2011,** *44* (10), 999-1008.

9. Nishiyama, N.; Bae, Y.; Miyata, K.; Fukushima, S.; Kataoka, K., Smart polymeric micelles for gene and drug delivery. *Drug Discovery Today: Technol.* **2005,** *2* (1), 21-26.

10. Elsabahy, M.; Wooley, K. L., Design of polymeric nanoparticles for biomedical delivery applications. *Chem. Soc. Rev.* **2012,** *41* (7), 2545-2561.

11. Blanazs, A.; Armes, S. P.; Anthony, R. J., Self-Assembled Block Copolymer Aggregates: From Micelles to Vesicles and their Biological Applications. *Macromol. Rapid Commun.* **2009,** *30* (4-5), 267-277.

12. Zou, J.; Zhang, F.; Zhang, S.; Pollack, S. F.; Elsabahy, M.; Fan, J.; Wooley, K. L., Poly(ethylene oxide)-block-Polyphosphoester-graft-Paclitaxel Conjugates with Acid-Labile Linkages as a pH-Sensitive and Functional Nanoscopic Platform for Paclitaxel Delivery. *Adv. Healthcare Mater.* **2014,** *3* (3), 441-448.

13. Li, D.; Sun, L.; Zhang, Y.; Yu, M.; Guo, J.; Wang, C., Flexible assembly of targeting agents on porous magnetic nano-cargos by inclusion complexation for accurate drug delivery. *Mater. Chem. Front.* **2017,** *1* (3), 521-529.

14. Lim, Y. H.; Heo, G. S.; Cho, S.; Wooley, K. L., Construction of a Reactive Diblock Copolymer, Polyphosphoester-block-Poly(l-lactide), as a Versatile Framework for Functional Materials That Are Capable of Full Degradation and Nanoscopic Assembly Formation. *ACS Macro Lett.* **2013,** *2* (9), 785-789.

15. Putnam, D.; Gentry, C. A.; Pack, D. W.; Langer, R., Polymer-based gene delivery with low cytotoxicity by a unique balance of side-chain termini. *Proc. Natl. Acad. Sci. U. S. A.* **2001,** *98* (3), 1200-1205.

16. Wang, H.; Su, L.; Li, R.; Zhang, S.; Fan, J.; Zhang, F.; Nguyen, T. P.; Wooley, K. L., Polyphosphoramidates That Undergo Acid-Triggered Backbone Degradation. *ACS Macro Lett.* **2017,** *6* (3), 219-223.

17. Zhang, F.; Smolen, J. A.; Zhang, S.; Li, R.; Shah, P. N.; Cho, S.; Wang, H.; Raymond, J. E.; Cannon, C. L.; Wooley, K. L., Degradable polyphosphoester-based silver-loaded nanoparticles as therapeutics for bacterial lung infections. *Nanoscale* **2015,** *7* (6), 2265-2270.

18. Zhang, F.; Zhang, S.; Pollack, S. F.; Li, R.; Gonzalez, A. M.; Fan, J.; Zou, J.; Leininger, S. E.; Pavía-Sanders, A.; Johnson, R.; Nelson, L. D.; Raymond, J. E.; Elsabahy, M.; Hughes, D. M. P.; Lenox, M. W.; Gustafson, T. P.; Wooley, K. L., Improving Paclitaxel Delivery: In Vitro and In Vivo Characterization of PEGylated Polyphosphoester-Based Nanocarriers. *J. Am. Chem. Soc.* **2015,** *137* (5), 2056-2066.

19. Zhang, S.; Wang, H.; Shen, Y.; Zhang, F.; Seetho, K.; Zou, J.; Taylor, J.-S. A.; Dove, A. P.; Wooley, K. L., A Simple and Efficient Synthesis of an Acid-Labile Polyphosphoramidate by Organobase-Catalyzed Ring-Opening Polymerization and Transformation to Polyphosphoester Ionomers by Acid Treatment. *Macromolecules* **2013,** *46* (13), 5141-5149.

20. Zhang, S.; Zou, J.; Elsabahy, M.; Karwa, A.; Li, A.; Moore, D. A.; Dorshow, R. B.; Wooley, K. L., Poly(ethylene oxide)-block-polyphosphester-based paclitaxel

conjugates as a platform for ultra-high paclitaxel-loaded multifunctional nanoparticles. *Chem. Sci.* **2013,** *4* (5), 2122-2126.

21. Kataoka, K.; Harada, A.; Nagasaki, Y., Block copolymer micelles for drug delivery: design, characterization and biological significance. *Adv. Drug Delivery Rev.* **2001,** *47* (1), 113-131.

22. Epps, I. T. H.; O'Reilly, R. K., Block copolymers: controlling nanostructure to generate functional materials - synthesis, characterization, and engineering. *Chem. Sci.* **2016,** *7* (3), 1674-1689.

23. Cui, H.; Chen, Z.; Zhong, S.; Wooley, K. L.; Pochan, D. J., Block copolymer assembly via kinetic control. *Science* **2007,** *317* (5838), 647-50.

24. Chen, Y.; Zhang, K.; Wang, X.; Zhang, F.; Zhu, J.; Mays, J. W.; Wooley, K. L.; Pochan, D. J., Multigeometry Nanoparticles: Hybrid Vesicle/Cylinder Nanoparticles Constructed with Block Copolymer Solution Assembly and Kinetic Control. *Macromolecules* **2015,** *48* (16), 5621-5631.

25. Brendel, J. C.; Schacher, F. H., Block Copolymer Self-Assembly in Solution—Quo Vadis? *Chem. - Asian J.* **2018,** *13* (3), 230-239.

26. Schacher, F. H.; Rupar, P. A.; Manners, I., Functional Block Copolymers: Nanostructured Materials with Emerging Applications. *Angew. Chem., Int. Ed.* **2012,** *51* (32), 7898-7921.

27. Zhu, J.; Zhang, S.; Zhang, F.; Wooley, K. L.; Pochan, D. J., Hierarchical Assembly of Complex Block Copolymer Nanoparticles into Multicompartment Superstructures through Tunable Interparticle Associations. *Adv. Funct. Mater.* **2013,** *23* (14), 1767-1773.

28. Tritschler, U.; Pearce, S.; Gwyther, J.; Whittell, G. R.; Manners, I., 50th Anniversary Perspective: Functional Nanoparticles from the Solution Self-Assembly of Block Copolymers. *Macromolecules* **2017,** *50* (9), 3439-3463.

29. Yan, X.; Delgado, M.; Fu, A.; Alcouffe, P.; Gouin, S. G.; Fleury, E.; Katz, J. L.; Ganachaud, F.; Bernard, J., Simple but Precise Engineering of Functional Nanocapsules through Nanoprecipitation. *Angew. Chem., Int. Ed.* **2014,** *126* (27), 7030-7033.

30. Yan, X.; Ramos, R.; Hoibian, E.; Soulage, C.; Alcouffe, P.; Ganachaud, F.; Bernard, J., Nanoprecipitation of PHPMA (Co)Polymers into Nanocapsules Displaying Tunable Compositions, Dimensions, and Surface Properties. *ACS Macro Lett.* **2017,** *6* (4), 447-451.

31. Black, K. C. L.; Ibricevic, A.; Gunsten, S. P.; Flores, J. A.; Gustafson, T. P.; Raymond, J. E.; Samarajeewa, S.; Shrestha, R.; Felder, S. E.; Cai, T.; Shen, Y.; Löbs, A.-K.; Zhegalova, N.; Sultan, D. H.; Berezin, M.; Wooley, K. L.; Liu, Y.; Brody, S. L., In vivo fate tracking of degradable nanoparticles for lung gene transfer using PET and Ĉerenkov imaging. *Biomaterials* **2016,** *98*, 53-63.

32. Varela-Moreira, A.; Shi, Y.; Fens, M. H. A. M.; Lammers, T.; Hennink, W. E.; Schiffelers, R. M., Clinical application of polymeric micelles for the treatment of cancer. *Mater. Chem. Front.* **2017,** *1* (8), 1485-1501.

33. Elsabahy, M.; Heo, G. S.; Lim, S.-M.; Sun, G.; Wooley, K. L., Polymeric Nanostructures for Imaging and Therapy. *Chem. Rev.* **2015,** *115* (19), 10967-11011.

34. Elsabahy, M.; Zhang, S.; Zhang, F.; Deng, Z. J.; Lim, Y. H.; Wang, H.; Parsamian, P.; Hammond, P. T.; Wooley, K. L., Surface Charges and Shell Crosslinks Each Play Significant Roles in Mediating Degradation, Biofouling, Cytotoxicity and Immunotoxicity for Polyphosphoester-based Nanoparticles. *Sci. Rep.* **2013,** *3*, 3313.

35. Jordan, M. A.; Wilson, L., Microtubules as a target for anticancer drugs. *Nat. Rev. Cancer* **2004,** *4*, 253.

36. Fornari, F. A.; Randolph, J. K.; Yalowich, J. C.; Ritke, M. K.; Gewirtz, D. A., Interference by doxorubicin with DNA unwinding in MCF-7 breast tumor cells. *Mol. Pharmacol.* **1994,** *45* (4), 649-656.

37. Momparler, R. L.; Karon, M.; Siegel, S. E.; Avila, F., Effect of Adriamycin on DNA, RNA, and Protein Synthesis in Cell-free Systems and Intact Cells. *Cancer Res.* **1976,** *36* (8), 2891-2895.

38. Lee, Y.; Ishii, T.; Kim, H. J.; Nishiyama, N.; Hayakawa, Y.; Itaka, K.; Kataoka, K., Efficient Delivery of Bioactive Antibodies into the Cytoplasm of Living Cells by Charge-Conversional Polyion Complex Micelles. *Angew. Chem., Int. Ed.* **2010,** *49* (14), 2552-2555.

39. Lee, Y.; Miyata, K.; Oba, M.; Ishii, T.; Fukushima, S.; Han, M.; Koyama, H.; Nishiyama, N.; Kataoka, K., Charge-Conversion Ternary Polyplex with Endosome Disruption Moiety: A Technique for Efficient and Safe Gene Delivery. *Angew. Chem.* **2008,** *120* (28), 5241-5244.

40. Lee, Y.; Ishii, T.; Cabral, H.; Kim, H. J.; Seo, J.-H.; Nishiyama, N.; Oshima, H.; Osada, K.; Kataoka, K., Charge-Conversional Polyionic Complex Micelles—Efficient Nanocarriers for Protein Delivery into Cytoplasm. *Angew. Chem., Int. Ed.* **2009,** *48* (29), 5309-5312.

41. Lee, Y.; Fukushima, S.; Bae, Y.; Hiki, S.; Ishii, T.; Kataoka, K., A Protein Nanocarrier from Charge-Conversion Polymer in Response to Endosomal pH. *J. Am. Chem. Soc.* **2007,** *129* (17), 5362-5363.

42. Pittella, F.; Zhang, M.; Lee, Y.; Kim, H. J.; Tockary, T.; Osada, K.; Ishii, T.; Miyata, K.; Nishiyama, N.; Kataoka, K., Enhanced endosomal escape of siRNA-incorporating hybrid nanoparticles from calcium phosphate and PEG-block charge-conversional polymer for efficient gene knockdown with negligible cytotoxicity. *Biomaterials* **2011,** *32* (11), 3106-3114.

43. Wang, D.; Lu, X.; Jia, F.; Tan, X.; Sun, X.; Cao, X.; Wai, F.; Zhang, C.; Zhang, K., Precision Tuning of DNA- and Poly(ethylene glycol)-Based Nanoparticles via Coassembly for Effective Antisense Gene Regulation. *Chem. Mater.* **2017,** *29* (23), 9882-9886.

44. Anraku, Y.; Kishimura, A.; Oba, M.; Yamasaki, Y.; Kataoka, K., Spontaneous Formation of Nanosized Unilamellar Polyion Complex Vesicles with Tunable Size and Properties. *J. Am. Chem. Soc.* **2010,** *132* (5), 1631-1636.

45. Fernandez-Trillo, F.; van Hest, J. C. M.; Thies, J. C.; Michon, T.; Weberskirch, R.; Cameron, N. R., Fine-tuning the transition temperature of a stimuli-responsive polymer by a simple blending procedure. *Chem. Commun.* **2008,** *44* (19), 2230-2232.

46. Xiao, R.; Dane, E. L.; Zeng, J.; McKnight, C. J.; Grinstaff, M. W., Synthesis of Altrose Poly-amido-saccharides with beta-N-(1-->2)-d-amide Linkages: A Right-Handed Helical Conformation Engineered in at the Monomer Level. *J. Am. Chem. Soc.* **2017,** *139* (40), 14217-14223.

47. Gregory, G. L.; Lopez-Vidal, E. M.; Buchard, A., Polymers from sugars: cyclic monomer synthesis, ring-opening polymerisation, material properties and applications. *Chem. Commun.* **2017,** *53* (14), 2198-2217.

48. Mikami, K.; Lonnecker, A. T.; Gustafson, T. P.; Zinnel, N. F.; Pai, P.-J.; Russell, D. H.; Wooley, K. L., Polycarbonates Derived from Glucose via an Organocatalytic Approach. *J. Am. Chem. Soc.* **2013,** *135* (18), 6826-6829.

49. Tsao, Y.-Y. T.; Wooley, K. L., Synthetic, Functional Thymidine-Derived Polydeoxyribonucleotide Analogues from a Six-Membered Cyclic Phosphoester. *J. Am. Chem. Soc.* **2017,** *139* (15), 5467-5473.

50. Su, L.; Khan, S.; Fan, J.; Lin, Y.-N.; Wang, H.; Gustafson, T. P.; Zhang, F.; Wooley, K. L., Functional sugar-based polymers and nanostructures comprised of degradable poly(D-glucose carbonate)s. *Polym. Chem.* **2017,** *8* (10), 1699-1707.

51. Song, Y.; Chen, Y.; Su, L.; Li, R.; Letteri, R. A.; Wooley, K. L., Crystallization-driven assembly of fully degradable, natural product-based poly(l-lactide)-block-poly(α-d-glucose carbonate)s in aqueous solution. *Polymer* **2017,** *122*, 270-279.

52. Walba, H.; Isensee, R. W., Acidity Constants of Some Arylimidazoles and Their Cations. *J. Org. Chem.* **1961,** *26* (8), 2789-2791.

53. Shi, J.; Schellinger, J. G.; Johnson, R. N.; Choi, J. L.; Chou, B.; Anghel, E. L.; Pun, S. H., Influence of histidine incorporation on buffer capacity and gene transfection efficiency of HPMA-co-oligolysine brush polymers. *Biomacromolecules* **2013,** *14* (6), 1961-70.

54. Du, J.-b.; Cheng, Y.; Teng, Z.-h.; Huan, M.-l.; Liu, M.; Cui, H.; Zhang, B.-l.; Zhou, S.-y., pH-Triggered Surface Charge Reversed Nanoparticle with Active Targeting To Enhance the Antitumor Activity of Doxorubicin. *Mol. Pharmaceutics* **2016,** *13* (5), 1711-1722.

55. Dogan, I., Radical Cations from Imidazole Derivatives. *Spectrosc. Lett.* **1992,** *25* (1), 1-11.

56. Llano, J.; Eriksson, L. A., Mechanism of Hydroxyl Radical Addition to Imidazole and Subsequent Water Elimination. *J. Phys. Chem. B* **1999,** *103* (26), 5598-5607.

57. Pratt, L. R.; Pohorille, A., Theory of hydrophobicity: transient cavities in molecular liquids. *Proc. Natl. Acad. Sci. U. S. A.* **1992,** *89*, 2995-9.

58. Mai, Y.; Eisenberg, A., Self-assembly of block copolymers. *Chem Soc Rev* **2012,** *41* (18), 5969-85.

59. Discher, D. E.; Ahmed, F., Polymersomes. *Annual review of biomedical engineering* **2006,** *8*, 323-41.

60. Zhang, L.; Eisenberg, A., Multiple Morphologies and Characteristics of “Crew-Cut” Micelle-like Aggregates of Polystyrene-b-poly(acrylic acid) Diblock Copolymers in Aqueous Solutions. *J. Am. Chem. Soc.* **1996,** *118* (13), 3168-3181.

61. Zhang, L.; Eisenberg, A., Formation of crew-cut aggregates of various morphologies from amphiphilic block copolymers in solution. *Polym. Adv. Technol.* **1998,** *9* (10-11), 677-699.

62. Beattie, J. K., The intrinsic charge on hydrophobic microfluidic substrates. *Lab Chip* **2006,** *6* (11), 1409-1411.

63. Marinova, K. G.; Alargova, R. G.; Denkov, N. D.; Velev, O. D.; Petsev, D. N.; Ivanov, I. B.; Borwankar, R. P., Charging of Oil−Water Interfaces Due to Spontaneous Adsorption of Hydroxyl Ions. *Langmuir* **1996,** *12* (8), 2045-2051.

64. Deng, H.; Liu, J.; Zhao, X.; Zhang, Y.; Liu, J.; Xu, S.; Deng, L.; Dong, A.; Zhang, J., PEG-b-PCL Copolymer Micelles with the Ability of pH-Controlled Negative-to-Positive Charge Reversal for Intracellular Delivery of Doxorubicin. *Biomacromolecules* **2014,** *15* (11), 4281-4292.

65. Hu, C. M. J.; Zhang, L.; Aryal, S.; Cheung, C.; Fang, R. H.; Zhang, L. F., Erythrocyte Membrane-Camouflaged Polymeric Nanoparticles as a Biomimetic Delivery Platform. *Proceedings of the National Academy of Sciences of the United States of America* **2011,** *108* (27), 10980-10985.

66. Kroll, A. V.; Fang, R. H.; Zhang, L., Biointerfacing and Applications of Cell Membrane-Coated Nanoparticles. *Bioconjugate Chem.* **2017,** *28* (1), 23-32.

67. Fang, R. H.; Kroll, A. V.; Gao, W.; Zhang, L., Cell Membrane Coating Nanotechnology. *Advanced Materials* **2018,** *30* (23), 1706759.

68. Chen, Y.; Zhang, Y.; Chen, M.; Zhuang, J.; Fang, R. H.; Gao, W.; Zhang, L., Biomimetic Nanosponges Suppress In Vivo Lethality Induced by the Whole Secreted Proteins of Pathogenic Bacteria. *Small* **2019,** *15* (6), 1804994.

69. Luk, B. T.; Zhang, L., Cell Membrane-Camouflaged Nanoparticles for Drug Delivery. *Journal of Controlled Release* **2015,** *220*, 600-607.

70. Fang, R. H.; Hu, C. M. J.; Luk, B. T.; Gao, W. W.; Copp, J. A.; Tai, Y. Y.; O'Connor, D. E.; Zhang, L. F., Cancer Cell Membrane-Coated Nanoparticles for Anticancer Vaccination and Drug Delivery. *Nano Lett.* **2014,** *14* (4), 2181-2188.

71. Hu, C. M. J.; Fang, R. H.; Copp, J.; Luk, B. T.; Zhang, L. F., A Biomimetic Nanosponge that Absorbs Pore-Forming Toxins. *Nat. Nanotechnol.* **2013,** *8* (5), 336-340.

72. Thamphiwatana, S.; Angsantikul, P.; Escajadillo, T.; Zhang, Q.; Olson, J.; Luk, B. T.; Zhang, S.; Fang, R. H.; Gao, W.; Nizet, V.; Zhang, L., Macrophage-like nanoparticles concurrently absorbing endotoxins and proinflammatory cytokines for sepsis management. *Proc. Natl. Acad. Sci. U. S. A.* **2017,** *114* (43), 11488-11493.

73. Koo, J.; Escajadillo, T.; Zhang, L.; Nizet, V.; Lawrence, S. M., Erythrocyte-Coated Nanoparticles Block Cytotoxic Effects of Group B Streptococcus β-Hemolysin/Cytolysin. *Front. Pediatr.* **2019,** *7* (410).

74. Zhang, Q.; Dehaini, D.; Zhang, Y.; Zhou, J.; Chen, X.; Zhang, L.; Fang, R. H.; Gao, W.; Zhang, L., Neutrophil membrane-coated nanoparticles inhibit synovial inflammation and alleviate joint damage in inflammatory arthritis. *Nat. Nanotechnol.* **2018,** *13* (12), 1182-1190.

75. Chen, Z.; Zhao, P. F.; Luo, Z. Y.; Zheng, M. B.; Tian, H.; Gong, P.; Gao, G. H.; Pan, H.; Liu, L. L.; Ma, A. Q.; Cui, H. D.; Ma, Y. F.; Cai, L. T., Cancer Cell Membrane-Biomimetic Nanoparticles for Homologous-Targeting Dual-Modal Imaging and Photothermal Therapy. *ACS Nano* **2016,** *10* (11), 10049-10057.

76. Kroll, A. V.; Fang, R. H.; Jiang, Y.; Zhou, J.; Wei, X.; Yu, C. L.; Gao, J.; Luk, B. T.; Dehaini, D.; Gao, W.; Zhang, L., Nanoparticulate Delivery of Cancer Cell Membrane Elicits Multiantigenic Antitumor Immunity. *Advanced Materials* **2017,** *29* (47), 1703969.

77. Wei, X.; Zhang, G.; Ran, D.; Krishnan, N.; Fang, R. H.; Gao, W.; Spector, S. A.; Zhang, L., T-Cell-Mimicking Nanoparticles Can Neutralize HIV Infectivity. *Advanced Materials* **2018,** *30* (45), 1802233.

78. Park, J. H.; Dehaini, D.; Zhou, J.; Holay, M.; Fang, R. H.; Zhang, L., Biomimetic nanoparticle technology for cardiovascular disease detection and treatment. *Nanoscale Horiz.* **2020,** *5* (1), 25-42.

79. Hu, C.-M. J.; Fang, R. H.; Luk, B. T.; Chen, K. N. H.; Carpenter, C.; Gao, W.; Zhang, K.; Zhang, L., 'Marker-of-self' Functionalization of Nanoscale Particles Through a Top-down Cellular Membrane Coating Approach. *Nanoscale* **2013,** *5* (7), 2664-2668.

80. Nyström, A. M.; Xu, Z.; Xu, J.; Taylor, S.; Nittis, T.; Stewart, S. A.; Leonard, J.; Wooley, K. L., SCKs as nanoparticle carriers of doxorubicin: investigation of core composition on the loading, release and cytotoxicity profiles. *Chem. Commun.* **2008,** (30), 3579-3581.

81. Drumright, R. E.; Gruber, P. R.; Henton, D. E., Polylactic Acid Technology. *Advanced Materials* **2000,** *12* (23), 1841-1846.

82. Nampoothiri, K. M.; Nair, N. R.; John, R. P., An Overview of the Recent Developments in Polylactide (PLA) Research. *Bioresour. Technol.* **2010,** *101* (22), 8493-8501.

83. Tsuji, H., Poly(lactide) Stereocomplexes: Formation, Structure, Properties, Degradation, and Applications. *Macromol. Biosci.* **2005,** *5* (7), 569-97.

84. Kang, N.; Perron, M.-È.; Prud'homme, R. E.; Zhang, Y.; Gaucher, G.; Leroux, J.-C., Stereocomplex Block Copolymer Micelles: Core−Shell Nanostructures with Enhanced Stability. *Nano Lett.* **2005,** *5* (2), 315-319.

85. Worch, J. C.; Prydderch, H.; Jimaja, S.; Bexis, P.; Becker, M. L.; Dove, A. P., Stereochemical enhancement of polymer properties. *Nat. Rev. Chem.* **2019,** *3* (9), 514-535.

86. Shuai, X.; Merdan, T.; Schaper, A. K.; Xi, F.; Kissel, T., Core-Cross-Linked Polymeric Micelles as Paclitaxel Carriers. *Bioconjugate Chem.* **2004,** *15* (3), 441-448.

87. Martinez, A. W.; Caves, J. M.; Ravi, S.; Li, W.; Chaikof, E. L., Effects of Crosslinking on the Mechanical Properties, Drug Release and Cytocompatibility of Protein Polymers. *Acta Biomater* **2014,** *10* (1), 26-33.

88. Guo, Z.; Zhao, K.; Liu, R.; Guo, X.; He, B.; Yan, J.; Ren, J., pH-sensitive polymeric micelles assembled by stereocomplexation between PLLA-b-PLys and PDLA-b-mPEG for drug delivery. *J. Mater. Chem. B* **2019,** *7* (2), 334-345.

89. Feng, C.; Piao, M.; Li, D., Stereocomplex-Reinforced PEGylated Polylactide Micelle for Optimized Drug Delivery. *Polymer* **2016,** *8* (4), 165.

90. Xiao, R. Z.; Zeng, Z. W.; Zhou, G. L.; Wang, J. J.; Li, F. Z.; Wang, A. M., Recent Advances in PEG-PLA Block Copolymer Nanoparticles. *Int J Nanomedicine* **2010,** *5*, 1057-1065.

91. Sun, L.; Pitto-Barry, A.; Kirby, N.; Schiller, T. L.; Sanchez, A. M.; Dyson, M. A.; Sloan, J.; Wilson, N. R.; O’Reilly, R. K.; Dove, A. P., Structural reorganization of cylindrical nanoparticles triggered by polylactide stereocomplexation. *Nat. Commun.* **2014,** *5* (1), 5746.

92. Hu, C. M. J.; Fang, R. H.; Wang, K. C.; Luk, B. T.; Thamphiwatana, S.; Dehaini, D.; Nguyen, P.; Angsantikul, P.; Wen, C. H.; Kroll, A. V.; Carpenter, C.; Ramesh, M.; Qu, V.; Patel, S. H.; Zhu, J.; Shi, W.; Hofman, F. M.; Chen, T. C.; Gao, W. W.; Zhang, K.; Chien, S.; Zhang, L. F., Nanoparticle Biointerfacing by Platelet Membrane Cloaking. *Nature* **2015,** *526* (7571), 118-121.

93. Abu Lila, A. S.; Kiwada, H.; Ishida, T., The accelerated blood clearance (ABC) phenomenon: Clinical challenge and approaches to manage. *Journal of Controlled Release* **2013,** *172* (1), 38-47.

94. Zhang, P.; Sun, F.; Liu, S. J.; Jiang, S. Y., Anti-PEG antibodies in the clinic: Current issues and beyond PEGylation. *Journal of Controlled Release* **2016,** *244*, 184-193.

95. Zhang, J.; Sato, H.; Tsuji, H.; Noda, I.; Ozaki, Y., Infrared Spectroscopic Study of CH3···OC Interaction during Poly(l-lactide)/Poly(d-lactide) Stereocomplex Formation. *Macromolecules* **2005,** *38* (5), 1822-1828.

96. Tsuji, H.; Hyon, S. H.; Ikada, Y., Stereocomplex Formation Between Enantiomeric Poly(lactic acid)s. 4. Differential Scanning Calorimetric Studies on Precipitates from Mixed Solutions of Poly(D-lactic acid) and Poly(L-lactic acid). *Macromolecules* **1991,** *24* (20), 5657-5662.

97. Brizzolara, D.; Cantow, H.-J.; Diederichs, K.; Keller, E.; Domb, A. J., Mechanism of the Stereocomplex Formation between Enantiomeric Poly(lactide)s. *Macromolecules* **1996,** *29* (1), 191-197.

98. Sarasua, J. R.; Prud'homme, R. E.; Wisniewski, M.; Le Borgne, A.; Spassky, N., Crystallization and Melting Behavior of Polylactides. *Macromolecules* **1998,** *31* (12), 3895-3905.

99. Ikada, Y.; Jamshidi, K.; Tsuji, H.; Hyon, S. H., Stereocomplex formation between enantiomeric poly(lactides). *Macromolecules* **1987,** *20* (4), 904-906.

100. Leroux, J.-C.; De Jaeghere, F.; Anner, B.; Doelker, E.; Gurny, R., An investigation on the role of plasma and serum opsonins on the evternalization of biodegradable poly(D,L-lactic acid) nanoparticles by human monocytes. *Life Sci.* **1995,** *57* (7), 695-703.

101. Saeidlou, S.; Huneault, M. A.; Li, H. B.; Park, C. B., Poly(lactic acid) Crystallization. *Prog. Polym. Sci.* **2012,** *37* (12), 1657-1677.

102. Dehaini, D.; Wei, X. L.; Fang, R. H.; Masson, S.; Angsantikul, P.; Luk, B. T.; Zhang, Y.; Ying, M.; Jiang, Y.; Kroll, A. V.; Gao, W. W.; Zhang, L. F., Erythrocyte-Platelet Hybrid Membrane Coating for Enhanced Nanoparticle Functionalization. *Advanced Materials* **2017,** *29* (16), 8.

103. Désilets, J.; Lejeune, A.; Mercer, J.; Gicquaud, C., Nanoerythrosomes, a New Derivative of Erythrocyte Ghost: IV. Fate of Reinjected Nanoerythrosomes. *Anticancer Res* **2001,** *21* (3B), 1741-1747.

104. Himbert, S.; Alsop, R. J.; Rose, M.; Hertz, L.; Dhaliwal, A.; Moran-Mirabal, J. M.; Verschoor, C. P.; Bowdish, D. M. E.; Kaestner, L.; Wagner, C.; Rheinstädter, M. C., The Molecular Structure of Human Red Blood Cell Membranes from Highly Oriented, Solid Supported Multi-Lamellar Membranes. *Sci. Rep.* **2017,** *7* (1), 39661.

105. Elsabahy, M.; Wooley, K. L., Cytokines as Biomarkers of Nanoparticle Immunotoxicity. *Chem. Soc. Rev.* **2013,** *42* (12), 5552-5576.

106. Elsabahy, M.; Wooley, K. L., Data Mining as a Guide for the Construction of Cross-Linked Nanoparticles with Low Immunotoxicity via Control of Polymer Chemistry and Supramolecular Assembly. *Acc. Chem. Res.* **2015,** *48* (6), 1620-1630.

107. Benne, N.; van Duijn, J.; Kuiper, J.; Jiskoot, W.; Slütter, B., Orchestrating immune responses: How size, shape and rigidity affect the immunogenicity of particulate vaccines. *Journal of Controlled Release* **2016,** *234*, 124-134.

108. McRae Page, S.; Martorella, M.; Parelkar, S.; Kosif, I.; Emrick, T., Disulfide Cross-Linked Phosphorylcholine Micelles for Triggered Release of Camptothecin. *Mol. Pharmaceutics* **2013,** *10* (7), 2684-2692.

109. Wang, B.; Ding, Y.; Zhao, X.; Han, X.; Yang, N.; Zhang, Y.; Zhao, Y.; Zhao, X.; Taleb, M.; Miao, Q. R.; Nie, G., Delivery of small interfering RNA against Nogo-B receptor *via* tumor-acidity responsive nanoparticles for tumor vessel normalization and metastasis suppression. *Biomaterials* **2018,** *175*, 110-122.

110. Sun, H.; Yan, L.; Chang, M. Y. Z.; Carter, K. A.; Zhang, R.; Slyker, L.; Lovell, J. F.; Wu, Y.; Cheng, C., A multifunctional biodegradable brush polymer-drug conjugate for paclitaxel/gemcitabine co-delivery and tumor imaging. *Nanoscale Adv.* **2019,** *1* (7), 2761-2771.

111. Meng, F.; Wang, J.; Ping, Q.; Yeo, Y., Camouflaging Nanoparticles for Ratiometric Delivery of Therapeutic Combinations. *Nano Lett.* **2019,** *19* (3), 1479-1487.

112. Saw, P. E.; Yao, H.; Lin, C.; Tao, W.; Farokhzad, O. C.; Xu, X., Stimuli-Responsive Polymer–Prodrug Hybrid Nanoplatform for Multistage siRNA Delivery and Combination Cancer Therapy. *Nano Lett.* **2019,** *19* (9), 5967-5974.

113. Lin, Y.-N.; Elsabahy, M.; Khan, S.; Zhang, F.; Song, Y.; Dong, M.; Li, R.; Smolen, J.; Letteri, R. A.; Su, L.; Wooley, K. L., Erythrocyte-Membrane-Camouflaged Nanocarriers with Tunable Paclitaxel Release Kinetics *via* Macromolecular Stereocomplexation. *ACS Mater. Lett.* **2020,** *2*, 595-601.

114. Qin, H.; Ding, Y.; Mujeeb, A.; Zhao, Y.; Nie, G., Tumor Microenvironment Targeting and Responsive Peptide-Based Nanoformulations for Improved Tumor Therapy. *Mol. Pharmacol.* **2017,** *92* (3), 219-231.

115. Chen, X.; Zhou, W.; Liang, C.; Shi, S.; Yu, X.; Chen, Q.; Sun, T.; Lu, Y.; Zhang, Y.; Guo, Q.; Li, C.; Zhang, Y.; Jiang, C., Codelivery Nanosystem Targeting the Deep Microenvironment of Pancreatic Cancer. *Nano Lett.* **2019,** *19* (6), 3527-3534.

116. Banskota, S.; Saha, S.; Bhattacharya, J.; Kirmani, N.; Yousefpour, P.; Dzuricky, M.; Zakharov, N.; Li, X.; Spasojevic, I.; Young, K.; Chilkoti, A., Genetically Encoded Stealth Nanoparticles of a Zwitterionic Polypeptide-Paclitaxel Conjugate Have a Wider Therapeutic Window than Abraxane in Multiple Tumor Models. *Nano Lett.* **2020,** *20* (4), 2396-2409.

117. Parrish, B.; Emrick, T., Soluble Camptothecin Derivatives Prepared by Click Cycloaddition Chemistry on Functional Aliphatic Polyesters. *Bioconjugate Chem.* **2007,** *18* (1), 263-267.

118. Yang, C.; Tan, J. P. K.; Cheng, W.; Attia, A. B. E.; Ting, C. T. Y.; Nelson, A.; Hedrick, J. L.; Yang, Y.-Y., Supramolecular nanostructures designed for high cargo loading capacity and kinetic stability. *Nano Today* **2010,** *5* (6), 515-523.

119. Samarajeewa, S.; Shrestha, R.; Elsabahy, M.; Karwa, A.; Li, A.; Zentay, R. P.; Kostelc, J. G.; Dorshow, R. B.; Wooley, K. L., *In Vitro* Efficacy of Paclitaxel-Loaded Dual-Responsive Shell Cross-Linked Polymer Nanoparticles Having Orthogonally Degradable Disulfide Cross-Linked Corona and Polyester Core Domains. *Mol. Pharmaceutics* **2013,** *10* (3), 1092-1099.

120. Lv, S.; Wu, Y.; Cai, K.; He, H.; Li, Y.; Lan, M.; Chen, X.; Cheng, J.; Yin, L., High Drug Loading and Sub-Quantitative Loading Efficiency of Polymeric Micelles Driven by Donor–Receptor Coordination Interactions. *J. Am. Chem. Soc.* **2018,** *140* (4), 1235-1238.

121. Ansari, M.; Moradi, S.; Shahlaei, M., A molecular dynamics simulation study on the mechanism of loading of gemcitabine and camptothecin in poly lactic-co-glycolic acid as a nano drug delivery system. *J. Mol. Liq.* **2018,** *269*, 110-118.

122. Jafari, A.; Yan, L.; Mohamed, M. A.; Wu, Y.; Cheng, C., Well-Defined Diblock Poly(ethylene glycol)-b-Poly(ε-caprolactone)-Based Polymer-Drug Conjugate Micelles for pH-Responsive Delivery of Doxorubicin. *Materials* **2020,** *13* (7).

123. Champion, J. A.; Mitragotri, S., Role of target geometry in phagocytosis. *Proc. Natl. Acad. Sci. U. S. A.* **2006,** *103* (13), 4930-4934.

124. Geng, Y.; Dalhaimer, P.; Cai, S.; Tsai, R.; Tewari, M.; Minko, T.; Discher, D. E., Shape effects of filaments versus spherical particles in flow and drug delivery. *Nat. Nanotechnol.* **2007,** *2* (4), 249-255.

125. Petros, R. A.; DeSimone, J. M., Strategies in the design of nanoparticles for therapeutic applications. *Nat. Rev. Drug Discovery* **2010,** *9* (8), 615-627.

126. Sun, T.; Zhang, Y. S.; Pang, B.; Hyun, D. C.; Yang, M.; Xia, Y., Engineered Nanoparticles for Drug Delivery in Cancer Therapy. *Angew. Chem., Int. Ed.* **2014,** *53* (46), 12320-12364.

127. Cheng, K.; Ding, Y.; Zhao, Y.; Ye, S.; Zhao, X.; Zhang, Y.; Ji, T.; Wu, H.; Wang, B.; Anderson, G. J.; Ren, L.; Nie, G., Sequentially Responsive Therapeutic Peptide Assembling Nanoparticles for Dual-Targeted Cancer Immunotherapy. *Nano Lett.* **2018,** *18* (5), 3250-3258.

128. Mohamed, M. A.; Fallahi, A.; El-Sokkary, A. M. A.; Salehi, S.; Akl, M. A.; Jafari, A.; Tamayol, A.; Fenniri, H.; Khademhosseini, A.; Andreadis, S. T.; Cheng, C., Stimuli-responsive hydrogels for manipulation of cell microenvironment: From chemistry to biofabrication technology. *Prog. Polym. Sci.* **2019,** *98,* 101147.

129. Russo, A.; DeGraff, W.; Friedman, N.; Mitchell, J. B., Selective Modulation of Glutathione Levels in Human Normal versus Tumor Cells and Subsequent Differential Response to Chemotherapy Drugs. *Cancer Res.* **1986,** *46* (6), 2845-2848.

130. Raina, S.; Missiakas, D., Making and Breaking Disulfide Bonds. *Annu. Rev. Microbiol.* **1997,** *51* (1), 179-202.

131. Schafer, F. Q.; Buettner, G. R., Redox environment of the cell as viewed through the redox state of the glutathione disulfide/glutathione couple. *Free Radicals Biol. Med.* **2001,** *30* (11), 1191-1212.

132. Kuppusamy, P.; Li, H.; Ilangovan, G.; Cardounel, A. J.; Zweier, J. L.; Yamada, K.; Krishna, M. C.; Mitchell, J. B., Noninvasive Imaging of Tumor Redox Status and Its Modification by Tissue Glutathione Levels. *Cancer Res.* **2002,** *62* (1), 307-312.

133. Saito, G.; Swanson, J. A.; Lee, K.-D., Drug delivery strategy utilizing conjugation *via* reversible disulfide linkages: role and site of cellular reducing activities. *Adv. Drug Delivery Rev.* **2003,** *55* (2), 199-215.

134. Liu, J.; Pang, Y.; Huang, W.; Huang, X.; Meng, L.; Zhu, X.; Zhou, Y.; Yan, D., Bioreducible Micelles Self-Assembled from Amphiphilic Hyperbranched Multiarm Copolymer for Glutathione-Mediated Intracellular Drug Delivery. *Biomacromolecules* **2011,** *12* (5), 1567-1577.

135. Bajpai, A. K.; Shukla, S. K.; Bhanu, S.; Kankane, S., Responsive polymers in controlled drug delivery. *Prog. Polym. Sci.* **2008,** *33* (11), 1088-1118.

136. Zhang, W.; Lin, W.; Zheng, X.; He, S.; Xie, Z., Comparing Effects of Redox Sensitivity of Organic Nanoparticles to Photodynamic Activity. *Chem. Mater.* **2017,** *29* (4), 1856-1863.

137. Thorpe, P. E.; Wallace, P. M.; Knowles, P. P.; Relf, M. G.; Brown, A. N. F.; Watson, G. J.; Knyba, R. E.; Wawrzynczak, E. J.; Blakey, D. C., New Coupling Agents for the Synthesis of Immunotoxins Containing a Hindered Disulfide Bond with Improved Stability *In Vivo*. *Cancer Res.* **1987,** *47* (22), 5924-5931.

138. Arpicco, S.; Dosio, F.; Brusa, P.; Crosasso, P.; Cattel, L., New Coupling Reagents for the Preparation of Disulfide Cross-Linked Conjugates with Increased Stability. *Bioconjugate Chem.* **1997,** *8* (3), 327-337.

139. Kellogg, B. A.; Garrett, L.; Kovtun, Y.; Lai, K. C.; Leece, B.; Miller, M.; Payne, G.; Steeves, R.; Whiteman, K. R.; Widdison, W.; Xie, H.; Singh, R.; Chari, R. V. J.; Lambert, J. M.; Lutz, R. J., Disulfide-Linked Antibody−Maytansinoid Conjugates: Optimization of *In Vivo* Activity by Varying the Steric Hindrance at Carbon Atoms Adjacent to the Disulfide Linkage. *Bioconjugate Chem.* **2011,** *22* (4), 717-727.

140. Zhai, L.; Liang, J.; Guo, X.; Zhao, Y.; Wu, C., Extraordinary Modulation of Disulfide Redox-Responsiveness by Cooperativity of Twin-Disulfide Bonds. *Chem. - Eur. J.* **2014,** *20* (52), 17507-17514.

141. Mirzahosseini, A.; Noszál, B., Species-specific thiol-disulfide equilibrium constants of ovothiol A and penicillamine with glutathione. *RSC Adv.* **2016,** *6* (32), 26757-26764.

142. Liu, J.; Pang, Y.; Huang, W.; Zhu, Z.; Zhu, X.; Zhou, Y.; Yan, D., Redox-Responsive Polyphosphate Nanosized Assemblies: A Smart Drug Delivery Platform for Cancer Therapy. *Biomacromolecules* **2011,** *12* (6), 2407-2415.

143. Zhang, F.; Zhu, G.; Jacobson, O.; Liu, Y.; Chen, K.; Yu, G.; Ni, Q.; Fan, J.; Yang, Z.; Xu, F.; Fu, X.; Wang, Z.; Ma, Y.; Niu, G.; Zhao, X.; Chen, X., Transformative Nanomedicine of an Amphiphilic Camptothecin Prodrug for Long Circulation and High Tumor Uptake in Cancer Therapy. *ACS Nano* **2017,** *11* (9), 8838-8848.

144. Tang, L.; Yu, F.; Tang, B.; Yang, Z.; Fan, W.; Zhang, M.; Wang, Z.; Jacobson, O.; Zhou, Z.; Li, L.; Liu, Y.; Kiesewetter, D. O.; Tang, W.; He, L.; Ma, Y.; Niu, G.; Zhang, X.; Chen, X., Tumor Microenvironment-Activated Ultrasensitive Nanoprobes for Specific Detection of Intratumoral Glutathione by Ratiometric Photoacoustic Imaging. *ACS Appl. Mater. Interfaces* **2019,** *11* (31), 27558-27567.

145. Wang, D.; Jin, Y.; Zhu, X.; Yan, D., Synthesis and applications of stimuli-responsive hyperbranched polymers. *Prog. Polym. Sci.* **2017,** *64*, 114-153.

146. Li, Y.; Wu, Y.; Chen, J.; Wan, J.; Xiao, C.; Guan, J.; Song, X.; Li, S.; Zhang, M.; Cui, H.; Li, T.; Yang, X.; Li, Z.; Yang, X., A Simple Glutathione-Responsive Turn-On Theranostic Nanoparticle for Dual-Modal Imaging and Chemo-Photothermal Combination Therapy. *Nano Lett.* **2019,** *19* (8), 5806-5817.

147. Cheng, R.; Feng, F.; Meng, F.; Deng, C.; Feijen, J.; Zhong, Z., Glutathione-responsive nano-vehicles as a promising platform for targeted intracellular drug and gene delivery. *J. Controlled Release* **2011,** *152* (1), 2-12.

148. Wu, C.; Belenda, C.; Leroux, J.-C.; Gauthier, M. A., Interplay of Chemical Microenvironment and Redox Environment on Thiol–Disulfide Exchange Kinetics. *Chem. - Eur. J.* **2011,** *17* (36), 10064-10070.

149. Wu, C.; Wang, S.; Brülisauer, L.; Leroux, J.-C.; Gauthier, M. A., Broad Control of Disulfide Stability through Microenvironmental Effects and Analysis in Complex Redox Environments. *Biomacromolecules* **2013,** *14* (7), 2383-2388.

150. Zhuang, J.; Zhao, B.; Thayumanavan, S., Cascaded Step-Growth Polymerization for Functional Polyamides with Diverse Architectures and Stimuli Responsive Characteristics. *ACS Macro Lett.* **2019,** *8* (3), 245-249.

151. Jiang, Z.; Thayumanavan, S., Disulfide-Containing Macromolecules for Therapeutic Delivery. *Isr. J. Chem.* **2020,** *60* (1-2), 132-139.

152. Yao, Y.; Xu, H.; Liu, C.; Guan, Y.; Xu, D.; Zhang, J.; Su, Y.; Zhao, L.; Luo, J., Biodegradable multi-blocked polyurethane micelles for intracellular drug delivery: the effect of disulfide location on the drug release profile. *RSC Adv.* **2016,** *6* (11), 9082-9089.

153. Chan, N.; An, S. Y.; Oh, J. K., Dual location disulfide degradable interlayer-crosslinked micelles with extended sheddable coronas exhibiting enhanced colloidal stability and rapid release. *Polym. Chem.* **2014,** *5* (5), 1637-1649.

154. Ghosh, S.; Basu, S.; Thayumanavan, S., Simultaneous and Reversible Functionalization of Copolymers for Biological Applications. *Macromolecules* **2006,** *39* (17), 5595-5597.

155. Ryu, J.-H.; Chacko, R. T.; Jiwpanich, S.; Bickerton, S.; Babu, R. P.; Thayumanavan, S., Self-Cross-Linked Polymer Nanogels: A Versatile Nanoscopic Drug Delivery Platform. *J. Am. Chem. Soc.* **2010,** *132* (48), 17227-17235.

156. Ryu, J.-H.; Jiwpanich, S.; Chacko, R.; Bickerton, S.; Thayumanavan, S., Surface-Functionalizable Polymer Nanogels with Facile Hydrophobic Guest Encapsulation Capabilities. *J. Am. Chem. Soc.* **2010,** *132* (24), 8246-8247.

157. Zhuang, J.; Chacko, R.; Amado Torres, D. F.; Wang, H.; Thayumanavan, S., Dual Stimuli–Dual Response Nanoassemblies Prepared from a Simple Homopolymer. *ACS Macro Lett.* **2014,** *3* (1), 1-5.

158. Xu, H.; Cao, W.; Zhang, X., Selenium-Containing Polymers: Promising Biomaterials for Controlled Release and Enzyme Mimics. *Acc. Chem. Res.* **2013,** *46* (7), 1647-1658.

159. Cao, W.; Wang, L.; Xu, H., Selenium/tellurium containing polymer materials in nanobiotechnology. *Nano Today* **2015,** *10* (6), 717-736.

160. Nuttall, K. L., Evaluating selenium poisoning. *Ann. Clin. Lab. Sci.* **2006,** *36* (4), 409-20.

161. Vinceti, M.; Mandrioli, J.; Borella, P.; Michalke, B.; Tsatsakis, A.; Finkelstein, Y., Selenium neurotoxicity in humans: Bridging laboratory and epidemiologic studies. *Toxicol. Lett.* **2014,** *230* (2), 295-303.

162. Rae, W.; Kitley, J.; Pinto, A., Selenium Toxicity Associated With Reversible Leukoencephalopathy and Cortical Blindness. *JAMA Neurol.* **2018,** *75* (10), 1282-1283.

163. Chen, X.; McRae, S.; Parelkar, S.; Emrick, T., Polymeric Phosphorylcholine−Camptothecin Conjugates Prepared by Controlled Free Radical Polymerization and Click Chemistry. *Bioconjugate Chem.* **2009,** *20* (12), 2331-2341.

164. Xu, Z.; Wang, D.; Xu, S.; Liu, X.; Zhang, X.; Zhang, H., Preparation of a Camptothecin Prodrug with Glutathione-Responsive Disulfide Linker for Anticancer Drug Delivery. *Chem. - Asian J.* **2014,** *9* (1), 199-205.

165. Zhang, Q.; He, J.; Zhang, M.; Ni, P., A polyphosphoester-conjugated camptothecin prodrug with disulfide linkage for potent reduction-triggered drug delivery. *J. Mater. Chem. B* **2015,** *3* (24), 4922-4932.

166. Li, J.; Li, Y.; Wang, Y.; Ke, W.; Chen, W.; Wang, W.; Ge, Z., Polymer Prodrug-Based Nanoreactors Activated by Tumor Acidity for Orchestrated Oxidation/Chemotherapy. *Nano Lett.* **2017,** *17* (11), 6983-6990.

167. Lin, Y.-N.; Su, L.; Smolen, J.; Li, R.; Song, Y.; Wang, H.; Dong, M.; Wooley, K. L., Co-assembly of sugar-based amphiphilic block polymers to achieve nanoparticles with tunable morphology, size, surface charge, and acid-responsive behavior. *Mater. Chem. Front.* **2018,** *2* (12), 2230-2238.

168. Osumi, S.; Felder, S. E.; Wang, H.; Lin, Y.-N.; Dong, M.; Wooley, K. L., Construction of nanostructures in aqueous solution from amphiphilic glucose-derived polycarbonates. *J. Polym. Sci., Part A: Polym. Chem.* **2019,** *57* (3), 432-440.

169. Dong, M.; Song, Y.; Wang, H.; Su, L.; Shen, Y.; Tran, D. K.; Letteri, R. A.; Flores, J. A.; Lin, Y.-N.; Li, J.; Wooley, K. L., Degradable sugar-based magnetic hybrid nanoparticles for recovery of crude oil from aqueous environments. *Polym. Chem.* **2020**.

170. Schaefer, T.; Reynolds, W. F.; Yonemoto, T., Possible Intramolecular Van der Waals Contributions to Proton and Carbon-13 Shifts in Aliphatic and Aromatic Halogen Compounds. *Can. J. Chem.* **1963,** *41* (12), 2969-2976.

171. Gil, V. M. S.; Gibbons, W. A., Effect of intramolecular Van der Waals forces on N.M.R. spectra. *Mol. Phys.* **1964,** *8* (2), 199-200.

172. Li, S.; Chesnut, D. B., Intramolecular van der waals interactions and chemical shifts: A model for β- and γ-effects. *Magn. Reson. Chem.* **1985,** *23* (8), 625-638.

173. Zhang, F.; Ni, Q.; Jacobson, O.; Cheng, S.; Liao, A.; Wang, Z.; He, Z.; Yu, G.; Song, J.; Ma, Y.; Niu, G.; Zhang, L.; Zhu, G.; Chen, X., Polymeric Nanoparticles with a Glutathione-Sensitive Heterodimeric Multifunctional Prodrug for *In Vivo* Drug Monitoring and Synergistic Cancer Therapy. *Angew. Chem., Int. Ed.* **2018,** *57* (24), 7066-7070.

174. Heintz, A.; Odicino, F.; Maisonneuve, P.; Quinn, M.; Benedet, J.; Creasman, W.; Ngan, H.; Pecorelli, S.; Beller, U., Carcinoma of the Ovary. *Int. J. Gynecol. Obstet.* **2006,** *95* (S1), S161-S192.

175. Venditto, V. J.; Simanek, E. E., Cancer Therapies Utilizing the Camptothecins: A Review of the *In Vivo* Literature. *Mol. Pharmaceutics* **2010,** *7* (2), 307-349.

176. Bodurka, D. C.; Levenback, C.; Wolf, J. K.; Gano, J.; Wharton, J. T.; Kavanagh, J. J.; Gershenson, D. M., Phase II Trial of Irinotecan in Patients With Metastatic Epithelial Ovarian Cancer or Peritoneal Cancer. *J. Clin. Oncol.* **2003,** *21* (2), 291-297.

177. Musa, F.; Pothuri, B.; Blank, S. V.; Ling, H. T.; Speyer, J. L.; Curtin, J.; Boyd, L.; Li, X.; Goldberg, J. D.; Muggia, F.; Tiersten, A., Phase II study of irinotecan in combination with bevacizumab in recurrent ovarian cancer. *Gynecol. Oncol.* **2017,** *144* (2), 279-284.

178. Wang, Y.; Probin, V.; Zhou, D., Cancer therapy-induced residual bone marrow injury-Mechanisms of induction and implication for therapy. *Curr. Cancer Ther. Rev.* **2006,** *2* (3), 271-279.

179. Shao, L.; Wang, Y.; Chang, J.; Luo, Y.; Meng, A.; Zhou, D., Hematopoietic stem cell senescence and cancer therapy-induced long-term bone marrow injury. *Transl. Cancer Res.* **2013,** *2* (5), 397-411.

180. Verma, R.; Foster, R. E.; Horgan, K.; Mounsey, K.; Nixon, H.; Smalle, N.; Hughes, T. A.; Carter, C. R. D., Lymphocyte depletion and repopulation after chemotherapy for primary breast cancer. *Breast Cancer Res.* **2016,** *18* (1), 10.

181. Calvi, L. M.; Adams, G. B.; Weibrecht, K. W.; Weber, J. M.; Olson, D. P.; Knight, M. C.; Martin, R. P.; Schipani, E.; Divieti, P.; Bringhurst, F. R.; Milner, L. A.; Kronenberg, H. M.; Scadden, D. T., Osteoblastic cells regulate the haematopoietic stem cell niche. *Nature* **2003,** *425* (6960), 841-846.

182. Wang, H.; Tang, L.; Tu, C.; Song, Z.; Yin, Q.; Yin, L.; Zhang, Z.; Cheng, J., Redox-Responsive, Core-Cross-Linked Micelles Capable of On-Demand, Concurrent Drug Release and Structure Disassembly. *Biomacromolecules* **2013,** *14* (10), 3706-3712.